UNIVERSITÀ DEGLI STUDI DI MILANO

Scuola di Dottorato in Fisica, Astrofisica e Fisica Applicata
Dipartimento di Fisica

Corso di Dottorato in Fisica, Astrofisica e Fisica Applicata
Ciclo XXVI

Quantum effects in Molecular Nanomagnets: from Theory to Applications

Settore Scientifico Disciplinare FIS/03

Supervisore: Prof. Alessandro LASCIALFARI

Co-supervisore: Prof. Paolo SANTINI

Coordinatore: Prof. Marco BERSANELLI

Tesi di Dottorato di:
Elena GARLATTI

Anno Accademico 2013/2014

Commission of the final examination:

External Referee:
Prof. Alberto Parola

External Member:
Prof. Pietro Carretta

External Member:
Prof. Paolo Santini

Final examination:

February 11th 2014,

Università degli Studi di Milano, Dipartimento di Fisica, Milano, Italy

To my Father Andrea and

my Grandfather Gustavo

Cover illustration:

The molecular structure of Ni_7 (red: O, white: H, grey: C, cyan: N, yellow: Cl). The large green spheres represent Ni ions.

Design:

This document was typeset by the author using LATEXmarkup language, with MikTEX2.9 software and TEXnicCenter editor. The file in Portable Document Format was generated with pdfTEX.

MIUR subjects:

FIS/03

PACS:

75.50.Xx, 75.10.Jm, 71.70.Gm, 76.60.Es, 75.30.Sg, 78.70.Nx, 76.60.-k, 76.30.-v

Contents

List of Figures

List of Tables

Introduction

Magnetism is a research field within condensed matter physics which keeps on suggesting new ideas and results both for fundamental physics and technological applications. In the last decades, *molecular magnetism* has allowed physicists and chemists to introduce molecule-based materials among the most investigated systems in magnetism. Indeed molecular magnetism requires an active collaboration between chemists and physicists: The former are driven to synthesize molecular clusters of higher complexity and/or symmetry, while the latter are encouraged to develop new theoretical models and experimental technique in order to investigate magnetic properties of these systems.

In addition, the increasing attention for nanoscience and nanotechnology have moved the attention of the scientific research towards the interface between classical and quantum physics. Molecular magnetism indeed focuses on molecules of the order of the nanometer, whose behavior is at the crossing between classical and quantum regimes. In fact, they can display hysteresis cycles as bulk magnetic materials, but also typical quantum behaviors, such as coherent oscillations of the total-spin.

From a technological point of view, as we will see in the following section, hysteresis cycles at a molecular level could be the starting point for the realization of high density memory devices, by storing one bit of information in each single molecule. Furthermore, due to the quantum nature of molecular magnets, it has been demonstrated that we can define a quantum bit with a single molecule and that it can be implemented for quantum computation algorithms . Molecular nanomagnets can also show an enhanced magnetocaloric effect: Therefore they are considered promising materials for magnetic refrigeration at low temperature.

0.1   State of the Art

Molecular nanomagnets (MNMs) are cluster containing a finite number of paramagnetic ions (typically 3d ions), whose spins are strongly coupled by Heisenberg exchange interactions. Magnetic cores of adjacent molecules are well separated from each other by a surrounding of organic ligands, so that inter-molecular interactions are negligible. Therefore, molecular crystals formed by these kind of metal-organic clusters behave like an ensemble of non-interacting identical molecules and it is possible to obtain magnetic properties of a single molecule from bulk measurements. MNMs present several advantages both from a theoretical and experimental point of view: Not only it is possible to describe their magnetic cores in detail with theoretical models, but it is also possible to have an high degree of control of their chemical structure and resulting magnetic properties.

MNMs are of the order of the nanometer in size and their dimension has several consequence on their magnetization behavior and dynamics. Hysteresis cycles are at

the basis of the implementation of magnetic materials in information storage applications. On the other hand, if we increasingly reduce the size of magnetic systems, we finally reach the so-called superparamagnetic limit. In fact, in a particle with uniaxial anisotropy, two possible orientation of the magnetization and dimensions of the order of the nanometer, the thermal energy is usually of the same order of magnitude of the anisotropy barrier. Therefore the particle can have enough thermal energy to overcome the barrier, showing fluctuations of the magnetization and preventing its implementation for information storage applications. It has been shown [1, 2] that MNMs can show slow magnetization dynamics with hysteresis cycles of pure molecular origin, below a certain blocking temperature T_B. Furthermore in these systems the reorientation of the magnetization can be due not only to thermally activated process described by the Arrhenius law (where the characteristic time is given by $\tau = \tau_0 \exp(U/K_B T)$), but also to other phenomena of quantum origin like the tunneling of the magnetization.

0.1.1 Single-molecule magnets

The first systems showing this peculiar behavior have been Single-Molecule Magnets (SMMs) Mn_{12} and Fe_8. Both systems are characterised by an high spin ground state and uniaxial magnetic anisotropy, which creates an energy barrier for the reorientation of the magnetization. In absence of an applied magnetic field, levels belonging to the ground state multiplet (which are well separated from the excited ones) are arranged within a double-well potential created by the anisotropy barrier (see Fig. 1). Mn_{12} and Fe_8 also show thermally activated reorientation of the magnetization. The energy barrier is overcome with Orbach multi-step relaxation processes [3]: Interactions with phonons can promote the system to higher energy levels with higher quantum number M, towards the top of the barrier. Therefore the energy barrier is overcome due to the absorption and emission of resonant phonons, leading to a reorientation of the magnetization with a characteristic time given by the Arrhenius law.
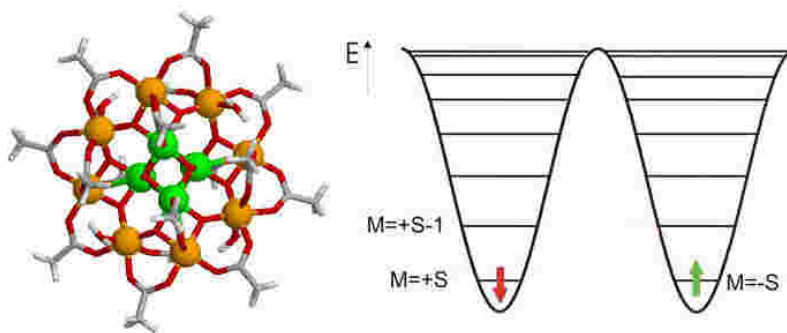
Figure 1: Molecular structure of Mn_{12} SMM (left) and its low-lying energy levels in the double-well approximation (right).

Mn_{12} has been the first system where slow magnetization dynamics at low temperature, which can reach the order of magnitude of a year, have been experimentally observed with AC susceptibility and magnetization measurements. To the slow magnetization dynamics of SMMs is also associated an hysteresis cycle of pure molecular origin

(see Fig. 2), which allow one to store information in one single molecule, overcoming the superparamagnetic limit. Furthermore, in the Fe_8 cluster has been verified that the characteristic time of relaxation becomes temperature independent below T = 0.36 K [4], showing that the relaxation of the magnetization is due to pure quantum tunneling across the anisotropy barrier. In Fig. 2 we report the hysteresis cycles of Fe_8 measured with a magnetic field applied along the easy axis at different temperatures: Indeed hysteresis cycles are temperature independent below T = 0.36 K. From the graphs in Fig. 2 it is possible to notice several jumps in the cycles, separated by plateaux, for specific values of the applied magnetic field with regular spacing. These values of the applied magnetic field correspond to anti-crossing fields, involving states belonging to different sides of the energy barrier. At these anti-crossing fields the magnetization relaxes faster due to pure quantum tunneling phenomena [5].
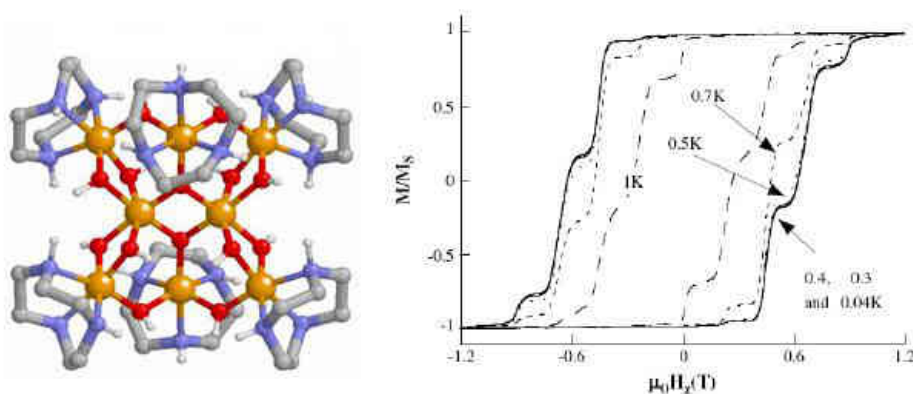
Figure 2: Molecular structure of Fe_8 SMM (left) and its hysteresis cycles measured at different temperatures with the magnetic field applied along the easy axis (right) [5].

SMMs show slow relaxation of the magnetization at very low temperatures (below their so-called blocking temperature [2]), depending on their ground state and anisotropy. Therefore, as far as slow relaxing MNMs are concerned, the competition to obtain higher spin ground states and stronger anisotropy is expected to continue. Recently, after the discovery of SMM behavior in a mononuclear Tb complex [6], an intense research activity has been focused on the design of high-symmetry environments for single lanthanide ions [7, 8, 9] with the aim to reduce the efficiency of the tunneling mechanism of magnetic relaxation and to increase the blocking temperature of the material. Moreover some of these single-ion molecules preserve their SMM behavior also when grafted on surfaces [10].

0.1.2 Beyond Single-Molecule Magnets

New families of MNMs came after SMMs with new and different properties. Among these new species of MNMs, great interest have been raised by even numbered AF rings with N = 6, 8, 10, 12 and 18, which have been synthesized with different transition metal ions, e.g. Fe^{3+} (s = 5/2) [11, 12, 13, 14], Cr^{+3} (s = 3/2) [15], V^{3+} (s = 1) [16] and Cu^{2+} (s = 1/2) [17]. These rings are all characterised by a non-magnetic S = 0 ground state and they can be considered model systems to study AF spin chains. Due to finite size

effects, AF rings have a discrete energy spectrum and the lowest-lying excited states for each total-spin S are known to be approximately given by the so-called Landè interval rule [18]. Heterometallic rings with $S \neq 0$ can be obtained from an $S = 0$ homonuclear ring by chemical substitution of one or two magnetic centers. For instance, Cr_7M rings (M = Zn, Cd, Mn, Ni) are derived from the spin-compensated neutral Cr_8 ring [15] by substitution of one divalent cation M = Zn, Cd, Mn, Ni for a trivalent Cr ion [19]. Cr_7Ni AF ring has been proposed as a good candidate for the implementation of qubits with MNMs. In fact, it is characterised by a $S = 1/2$ doublet ground state and it can be can be manipulated in times much shorter than the measured decoherence time [20, 21]. Furthermore, as we will see in Chapter 5, Cr_7Ni rings can be also successfully grafted on surfaces in an ordered fashion, preserving their magnetic properties. Heterometallic rings have shown that the possibility to change the pattern of exchange interactions and spin values in AF rings with chemical engineering represents a great opportunity to study new quantum phenomena in MNMs. Now the attention is focusing on newly synthesized AF rings, with a particular attention to their frustration-induced properties. Thus, frustrated rings like Cr_8Ni and Cr_9, where frustration is due to the odd number of interacting ions, have been taken into account. Their magnetic behavior can be compared with the even numbered closed ring Cr_8 and open rings Cr_8Cd and Cr_8Zn [22, 23].
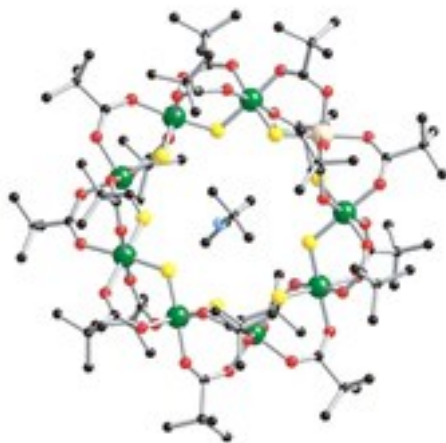
Figure 3: Molecular structure of Cr_8M ring: dark green: Cr, light pink: M (Cr, Zn, Cd, Ni), yellow: F, red: O [23].

Other species of MNMs like the grid Mn[3x3] have allowed us to experimentally observe from macroscopic measurements a pure quantum phenomena like coherent oscillations of the total-spin S, which cause fluctuation not only of the direction (as it happens in Mn_{12} or Fe_8) but also of the modulus of the total-spin S [24]. Recently molecules containing AF triangles have been taken into account for the implementation of quantum gates [25], thus, trimers like Cr_2Cu [26] have been completely characterised. Due to their chirality properties, triangular MNMs like Cu_3 have been also suggested as new component in spintronic devices [27].

Molecular clusters can also show polyhedral structures: In particular, MNMs with highly complex and symmetric structures like $Mo_{72}Fe_{30}$ belong to the family of highly frustrated molecular magnets, where frustration, as we will also see in Chapter 3, is at

the origin of several exotic phenomena [28, 29]. A toroidal arrangement of local magnetic moments has been recently found in lanthanide based MNMs. It was first discovered in Dy_3 triangles [30] and has been recently observed in a Dy_6 ring [31]. As we will see in the following section the toroidal magnetic state seems to be promising for future applications in quantum computing and information storage [32].

0.1.3 Technological Applications

MNMs are also interesting for their envisaged technological applications. For instance, SMMs show hysteresis cycles of pure molecular origin due to their slow relaxation of the magnetization. These features could allow us to store information in one single molecule, with the aim of building high-density memories with nanometric molecules. For future implementations of SMMs in information storage technologies, suppression of quantum tunneling phenomena, which can cause the loss of information, and molecules with higher blocking temperature are needed.

Due to their quantum behavior and properties, MNMs are considered valid candidate to realize qubits, the unit of quantum information, for quantum computation algorithms [33]. Indeed, at low temperature systems like Cr_7Ni exhibit two stable spin states, which can be associated to the two logical states 0 and 1 of the qubit, and long decoherence times [20, 21]. Quantum computation algorithms are based on sequences of elementary logical operations on qubits, the so-called quantum gates, which can be physically implemented with resonant electromagnetic pulses. One-qubit gates can be realized with local magnetic fields, whereas two-qubit gates are based on the electronic control of qubit-qubit interactions. Therefore spin entanglement between two interacting molecules (usually AF rings) is a crucial resource for quantum information processes [21]. It has been also demonstrated that a proper engineering of the intercluster link would result in an effective coupling that vanishes when the system is kept in the computational space, while it is turned on by a selective excitation of specific auxiliary states. These feature would allow the performing of single-qubit and two-qubit gates without an individual addressing of the rings by means of local magnetic fields [34].

Recently a scheme to efficiently exploit chains of MNMs as quantum simulators have been developed, where the quantum simulator state is manipulated by sequences of uniform electromagnetic pulses implementing quantum gates, performed in parallel on the whole array [35]. In addition, the recent demonstrations that MNMs can be self-assembled on surfaces without altering their properties, opened interesting possibilities also for their implementation in superconducting stripline resonators. Indeed, the coupling between the spin of MNMs and a high-finesse cavity resonant mode would pave the way to the implementation of hybrid solid-state devices. A new scheme to perform quantum information processing based on a hybrid spin-photon qubit encoding have already been proposed [36].

Also the toroidal magnetic state seems to be promising for future applications in quantum computing and information storage. A key property of toroidal magnetic moments is their insensitivity to homogeneous magnetic fields [37]. This means that the two components of the toroidal magnetic state, corresponding to circular arrangements of magnetic moments in opposite directions [30] will be much more protected against the action of a magnetic field, compared to the spin projection eigenstates of a true spin $S = 1/2$ [38]. Moreover, the toroidal magnetic moment interacts with a dc current passing through the molecule [39] or a time-varying electric field [40] via magneto-electric coupling [41] and this allows the moment to be controlled and manipulated purely by electrical means. MNMs have been also suggested as new component in spintronic de-
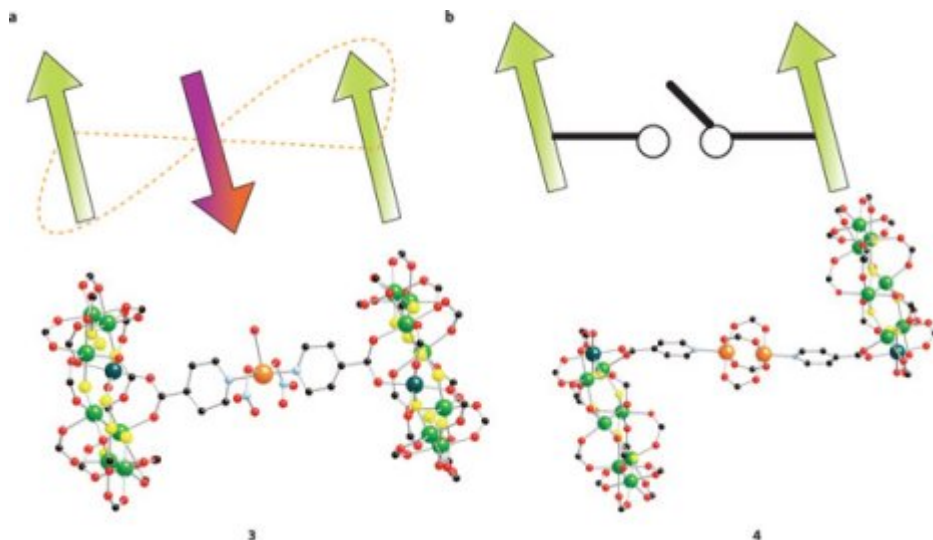
Figure 4: Molecular structure of Cr_7Ni-link-Cr_7Ni dimers: light green: Cr, dark green: Ni, orange: Cu, red: O, yellow: N. Rings linked with a single Cu^{2+} center (right) can be regarded as a three-qubit system. Rings coupled through a dimetallic link (left) implement two-qubit systems with switchable effective coupling [21].

vices, such spin-polarized [42] or magnon transistors [27].

As we will show in Chapter 4, MNMs can show an enhanced magnetocaloric effect at low temperature and therefore are considered promising materials for magnetic refrigeration [43, 44, 45, 46].

0.2 Thesis overview

Main results

As pointed out in the previous sections, MNMs have attracted the attention of the scientific community for two main reasons. First, they represent model systems to study many quantum phenomena, such as quantum tunneling of the magnetization, quantum oscillations of the total-spin, quantum entanglement and decoherence. Second, they are interesting for their envisaged technological applications, including magnetic refrigeration, high-density memory storage and quantum information processing. Driven by these motivations, the present Thesis focuses on the study of magnetic properties and spin dynamics of different classes of molecular nanomagnets, with the purpose to understand their quantum behavior and their potential applications in future technologies.

The main results of the Thesis are summarized below.

Study of frustration induced static and dynamical properties in MNMs: Geometrical magnetic frustration due to competing antiferromagnetic (AF) interactions is at the origin of many exotic phenomena in MNMs. We have theoretically investigated frustration-induced static and dynamical properties in the Ni_7 MNMs and we have shown that the high degree of frustration leads to a magnetic energy spectrum with large degeneracies which result in an unusual behavior of the cluster. In particu-

lar, the relaxation dynamics of the magnetization is characterised by several distinct characteristic times. We have also discussed the possible interest of Ni_7 for magnetocaloric refrigeration. With the study of the three systems Fe_7, Fe_6 an Mn_6 we have demonstrated that even if geometrical frustration is removed by structural distortions in the molecular structure of the cluster, competing AF interactions lead to a low-spin ground state, low-lying excited levels and still to an unusual behavior. In particular competing AF interactions are responsible for a multi-time scale relaxation dynamics at low temperature. This peculiar behavior has been verified in the Fe_7 cluster and probed by ^{1}H-NMR. Indeed, the comprehension of relaxation mechanisms in MNMs is crucial in order to address the implementation of these systems in the fields of quantum information processing or information storage.

Theoretical design of MNMs for magnetic refrigeration: Molecular nanomagnets are promising materials for very-low-temperature magnetic refrigeration due to their enhanced magnetocaloric effect. By explicitly considering Carnot refrigeration cycles, we have theoretically shown that the best molecules for magnetic refrigeration between T = 10 K and the sub-Kelvin region are those made of strongly ferromagnetically coupled magnetic ions, contrarily to the established belief. This recipe will provide a strong stimulus for designing new magnetic molecules for cryogenic technologies.

Study of local magnetic properties and anisotropy in Cr_7Ni green rings: Cr_7Ni is a very promising system to encode a qubit, since it behaves as an effective spin 1/2 at low-T and can be manipulated in times much shorter than the measured decoherence time. ^{53}Cr-NMR spectra collected at low temperature in a single crystal of Cr_7Ni in the S = 1=2 ground state have allowed us to establish the distribution of the local electronic moment in the ring. Indeed the latter plays a key role in the scheme proposed for obtaining time dependent qubit–qubit couplings in the presence of permanent exchange interactions between two AF rings. In addition with XMCD spectroscopic technique and theoretical calculations we have investigated the origin of magnetic anisotropy in Cr_7Ni rings grafted on surfaces.

Complete characterization of Cr_7M purple rings and of entangled Cr_7Ni purple-green dimer: Cr_7M (M = Zn, Mn, Ni) purple rings have been originally synthesized in order to facilitate the linking of two or more AF rings. Furthermore, the substitution of bridging fluorides of green rings with alkoxide groups in purple rings can reduce the hyperfine-induced decoherence, making them attractive candidates for applications in quantum-information processing. Cr_7Zn, Cr_7Mn and Cr_7Ni purple rings have been completely characterised by comparing our theoretical calculations with INS, EPR and specific heat experimental data. The characterization of single purple rings represents a first step in the description of a new family of entangled dimers obtained by linking together one purple and one green ring. EPR and specific heat measurements on Cr_7Ni purple-green dimer have allowed us to demonstrates the presence of an effective interaction between the two rings. These dimers represent model systems to study spin entanglement and its application in the field of quantum computation.

Organizational note

The present Thesis consists of six Chapters. The first two Chapters are devoted to a brief introduction about the main theoretical models and experimental techniques for the investigation of MNMs. The other four Chapters present the main results of this Thesis:

Each Chapter concerns a different sub-group of MNMs or it describes peculiar properties or applications of these systems. Chapter 3, 5 and 6 contains several sections and each section is devoted to the study of a particular system. Sections of Chapter 3, 5 and 6 and Chapter 4 have appeared as refereed publications in scientific journals; co-authors of the relevant articles are mentioned below. Chapter 6 presents results which haven't been published yet. Some variations have been made in the presentation of previously published results, to maintain consistency of style and content structure through the manuscript.

Chapter 1 - Theoretical Framework: In this Chapter we introduce the Spin Hamiltonian approach, which allows us to describe magnetic properties and coherent dynamics of MNMs. The irreducible tensor operator techniques and several diagonalization method are also presented. We also introduce the quantum theory of relaxation and the rate master equation formalism, in order to describe phonon-induced irreversible relaxation dynamics in MNMs.

Chapter 2 - Experimental Techniques: Several experimental techniques are described in this Chapter: Inelastic neutron scattering, nuclear magnetic resonance, electron paramagnetic resonance and X-rays magnetic circular dichroism. We describe each experiment both from a phenomenological and theoretical point of view.

Chapter 3 - Molecular Magnets with Competing AF Interactions: in this Chapter we focus on four different MNMs with competing AF interactions. In Section 3.1 we analyze the static and dynamical magnetic properties of the Ni_7 molecular nanomagnet, which is an excellent model system to investigate the effects of magnetic frustration. This work on Ni_7 has been published on Journal of Physics: E. Garlatti, S. Carretta, M. Affronte, E. C. Sañudo, G. Amoretti, P. Santini, *J. Phys.: Condens. Matter* **24**, 104006 (2012). Section 3.2 is devoted to the magnetic characterization of three different systems, Fe_6, Mn_6 and Fe_7, as it appears on the paper published on Dalton Transaction: K. Mason, J. Chang, A. Prescimone, E. Garlatti, S. Carretta, P. A. Tasker, E. K. Brechin, *Dalton Trans.* **41**, 8777 (2012). In section 3.3 we investigate the phonon-induced relaxation dynamics in Fe_7, which is also probed by measurements of the nuclear spin-lattice relaxation rate $1/T_1$. The results of this last section have been published as an article on Physical Review B: E. Garlatti, S. Carretta, P. Santini, G. Amoretti, M. Mariani, A. Lascialfari, S. Sanna, K. Mason, J. Chang, P. Tasker and E.K. Brechin, *Phys. Rev. B* **87**, 054409 (2013).

Chapter 4 - Design of Molecular Nanomagnets for Magnetic Refrigeration: In this Chapter we perform calculations in ideal model systems to understand the characteristics of a MNM yielding an efficient magnetocaloric effect between T = 10 K and the sub-Kelvin region. By explicitly considering Carnot refrigeration cycles, we theoretically show that the best molecules for magnetic refrigeration between T = 10 K and the sub-Kelvin region are those made of strongly ferromagnetically coupled magnetic ions, contrarily to the established belief. This Chapter is based on the work by E. Garlatti, S. Carretta, J. Schnack, G. Amoretti and P. Santini that will soon be published on *Applied Physics Letters*.

Chapter 5 - Local Magnetic Properties of Cr_7Ni-green AF Ring: In this Chapter we focus on a particular sub-group of MNMs, the so-called AF green rings. In particular in Section 5.1 we present [53]Cr-NMR spectra collected at low temperature in a single crystal of Cr_7Ni in the S = 1/2 ground state, with the aim of establishing

the distribution of the local electronic moment in the ring. This analysis as been published as a refereed paper on Journal of Physics: C. M. Casadei, L. Bordonali, Y. Furukawa, F. Borsa, E. Garlatti, A. Lascialfari, S. Carretta, S. Sanna, G. Timco and R. Winpenny, *J. Phys.: Condens. Matter* **24**, 406002 (2012). Section 5.2 is devoted to the experimental and theoretical determination of magnetic anisotropy of Cr_7Ni grafted on surfaces, using XMCD and theoretical calculations. These results have appeared on Advanced Functional Materials: V. Corradini , A. Ghirri , E. Garlatti, R. Biagi, V. De Renzi, U. del Pennino, V. Bellini, S. Carretta, P. Santini, G. Timco, R. Winpenny, M. Affronte, *Adv. Funct. Mat.* **22**, 3706-3713 (2012).

Chapter 6 - Spin Dynamics of Cr_7M-purple Rings and of Entangled Dimers: In this last Chapter we present a complete characterization of Cr_7M purple AF rings. Magnetic properties and spin dynamics of these systems are investigate with INS, EPR and specific heat measurements and with theoretical calculations. The last section of the Chapter is devoted to the analysis of a super-molecular system belonging to a new family of entangled AF rings. By means of EPR and specific heat measurements we demonstrate the presence of an effective interaction between the on Cr_7Ni purple and one Cr_7Ni green ring in a super-molecular dimer. This work is currently in preparation for submission to scientific journals.

Theoretical Framework

1.1 The Spin Hamiltonian

Magnetic Properties of MNMs can be accurately described by single-molecule Spin Hamiltonians (SHs). The SH formalism is based on the assumption that each magnetic ion in the molecule can be represented by an effective spin s_i and it allows us to express all the contributions to the energy of the system (exchange or dipolar interactions and local crystal fields) in terms of spin operators only [47].

As we will show in the following sections, the irreducible tensor operator (ITO) technique and the Wigner-Eckart theorem [48] simplify the calculation of the Hamiltonian matrix elements on the total-spin basis. The eigenvalues are usually expressed in terms of the parameters characterizing the different contributions to the SH. These parameters can be calculated directly or determined through the comparison with experimental data.

The SH describing a MNM usually has three main contributions:

$$\mathcal{H} = \mathcal{H}_0 + \mathcal{H}_{CF} + \mathcal{H}_{dip}. \tag{1.1}$$

The first term represents the isotropic Heisenberg (super)-exchange interaction, which is usually the dominant one, the second term represents the effects of the local crystal electric fields (CFs), produced by surrounding ligand charges, while the third term is the classical dipole-dipole interaction. A fourth term representing the Zeeman interaction with an external magnetic field can be added to Eq. 1.1. All the possible contribution to the SH are described in the following section.

If the isotropic exchange interactions is largely dominant over all the other contributions (*strong-exchange limit*), the splitting within each total-spin multiplet will be much smaller than the energy difference between two multiplets with different total-spin S. Therefore to describe the behavior of the system we can consider only the ground state multiplet and the SH will have only CFs and Zeeman terms acting on it. This particular SH is called *single-Spin Hamiltonian* and it is easier to manage, since the Hilbert space associated to the molecule is reduced to the dimension of ground state total-spin multiplet, $\dim(H) = 2S + 1$. If the presence of the other excited multiplets cannot be neglected, we have to consider a *generalized* SH, taking into account also the exchange interactions between the magnetic ions.

1.1.1 Main contributions to the Spin Hamiltonian

In the following we briefly report all the possible contribution to the SH describing a MNM with N magnetic centers.

Exchange Interactions

The exchange interaction between the magnetic ions of a MNM can be decomposed in four different contributions [47, 48, 2]:

$$\mathcal{H}_{ex} = \mathcal{H}_0 + \mathcal{H}_{BQ} + \mathcal{H}_{AS} + \mathcal{H}_{AS}, \tag{1.2}$$

where $\mathcal{H}_0$ is the Heisenberg-Dirac isotropic-exchange Hamiltonian, $\mathcal{H}_{BQ}$ is the bi-quadratic exchange Hamiltonian, $\mathcal{H}_{AS}$ represents the antisymmetric exchange and $\mathcal{H}_{AN}$ the anisotropic exchange. In the conventional form these terms are expressed as:

$$\mathcal{H}_0 = \sum_{i>j} J_{ij}\mathbf{s}_i \cdot \mathbf{s}_j, \tag{1.3}$$

$$\mathcal{H}_{BQ} = \sum_{i>j} j_{ij}^{BQ}(\mathbf{s}_i \cdot \mathbf{s}_j)^2, \tag{1.4}$$

$$\mathcal{H}_{AS} = \sum_{i>j} \mathbf{G}_{ij}(\mathbf{s}_i \times \mathbf{s}_j), \tag{1.5}$$

$$\mathcal{H}_{AN} = \sum_{i>j} \sum_{\alpha} J_{ij}^{\alpha} s_i^{\alpha} s_j^{\alpha}, \tag{1.6}$$

where $\mathbf{s_i}$ are spin operators of the ith ion in the molecule. J_{ij} are the isotropic exchange parameters, j_{ij}^{BQ} are the biquadratic exchange interactions, J_{ij}^{α} are the parameters associated to the components of the anisotropic exchange interactions and $\mathbf{G_{ij}}(= -\mathbf{G_{ji}})$ are the antisymmetric parameters, i.e., antisymmetric vectors. For the sake of simplicity, the low-symmetry contributions to $\mathcal{H}_{AN}$ and multi-center interactions in $\mathcal{H}_{BQ}$ are omitted.

Dipolar intra-molecular interaction

When two interacting spins are sufficiently removed one from the other, their magnetic interaction reduces to that of two magnetic dipole. Therefore between the magnetic centers in a MNM there is also a classical dipole-dipole interaction, usually evaluated within this point-dipole approximation [49]. The magnetic dipole of a single ion in the molecule is given by $\mathbf{m}_i = -\mu_B\mathbf{g}_i\mathbf{s}_i$, where μ_B is the Bohr magneton and $\mathbf{g}_i$ is the spectroscopic splitting tensor. The classical form of the interaction between two spins i and j can be written as:

$$\mathcal{H}_{dip} = \sum_{i>j} \mathbf{s}_i \cdot \mathbf{J}_{ij}^{dip} \cdot \mathbf{s}_j, \tag{1.7}$$

where the coefficients $\mathbf{J}_{ij}^{dip}$ are given by:

$$\mathbf{J}_{ij}^{dip} = \frac{\mu_B^2}{R_{ij}^3}[\mathbf{g}_i \cdot \mathbf{g}_j - 3(\mathbf{g}_i \cdot \hat{\mathbf{R}}_{ij})(\mathbf{g}_j \cdot \hat{\mathbf{R}}_{ij})], \tag{1.8}$$

and $\hat{\mathbf{R}}_{ij}$ is a unit vector parallel to the $\overline{s_is_j}$ direction.

From Eq. 1.8 we can see that for each couple of interacting dipoles we have a coefficient matrix, which can be decomposed into an *isotropic*, *anisotropic* and *antisymmetric* part, respectively given by:

$$J_{ij} = \frac{1}{3}Tr(\mathbf{J}_{ij}^{dip}), \tag{1.9}$$

$$D_{ij}^{dip,\alpha\beta} = \frac{1}{2}(J_{ij}^{dip,\alpha\beta} + J_{ij}^{dip,\beta\alpha}) - \delta_{\alpha\beta}\frac{1}{3}Tr(\mathbf{J}_{ij}^{dip}),$$

$$d_{ij}^{dip,\alpha\beta} = \frac{1}{2}(J_{ij}^{dip,\alpha\beta} - J_{ij}^{dip,\beta\alpha}),$$

where $\alpha, \beta = x, y, z$.

It is worth to note that the magnetic dipole-dipole interaction can be taken into account within the exchange contributions described in the previous subsection [1], since both dipolar and exchange terms contain the same dependence on spin operators.

Crystal Fields

The *Crystal field theory* describe the influence of the electric field produced by surrounding ligand charges on the electronic structure of a given ion. The CF SH can be written in terms of *Stevens equivalent operators* $O_k^q(\mathbf{s_i})$[47]: these particular operators can be considered as effective-spin operators acting on a given total-spin multiplet. We have that $k = 2, 4$ for d electrons [3] and $k = 2, 4, 6$ for f electron [50], while $q = -k, ..., k$:

$$\mathcal{H}_{CF} = \sum_{i=1}^{N} \sum_{k,q} b_k^q(i)\hat{O}_k^q, \tag{1.10}$$

For instance, the widely-used second order CF Hamiltonian, corresponding to a crystal field with rhombic symmetry, in terms of the spin operators of the ith ion in the molecule, becomes:

$$\mathcal{H}_{CF} = \sum_{i=1}^{N} \left\{ d_i[\mathbf{s}_{i,z}^2 - \frac{1}{3}s_i(s_1+1)] + e_i(\mathbf{s}_{i,x}^2 - \mathbf{s}_{i,y}^2) \right\}, \tag{1.11}$$

The parameters d_i and e_i are respectively the local *axial* and *transverse* CF parameters.

The general form a CF Hamiltonian acting on a total-spin multiplet S in the *strong-exchange limit* can be written as a quadratic form [2]:

$$\mathcal{H}_{CF} = \mathbf{S} \cdot \underline{\mathbf{D}} \cdot \mathbf{S}, \tag{1.12}$$

where $\underline{\mathbf{D}}$, is a real symmetric tensor called *fine-structure tensor* or *zero-field splitting tensor*. In fact the Hamiltonian in Eq. 1.12 is responsible for the splitting of the $(2S + 1)$ degenerate level of the total-spin multiplet, in absence of an external magnetic field.

If the coordinate axes *x, y, z* of the system are chosen parallel to the three orthogonal eigenvectors of the tensor, $\underline{\mathbf{D}}$ is diagonal and assumes the form:

$$\mathcal{H}_{CF} = D_{xx}\mathbf{S}_x^2 + D_{yy}\mathbf{S}_y^2 + D_{zz}\mathbf{S}_z^2, \tag{1.13}$$

with $D_{xx} + D_{yy} + D_{zz} = 0$. Eq. 1.13 can be rewritten as

$$\mathcal{H}_{CF} = D\mathbf{S}_z^2 + E(\mathbf{S}_x^2 - \mathbf{S}_y^2), \tag{1.14}$$

assuming

$$D = \frac{3}{2}D_{zz} \quad E = \frac{1}{2}(D_{xx} - D_{yy}). \tag{1.15}$$

The values of the parameters D ed E strongly depends on the symmetry of the surrounding ligand charges around the magnetic center:

- *cubic* symmetry: $D_{xx} = D_{yy} = D_{zz} \Rightarrow D = 0, E = 0$;

- *axial* symmetry: $D_{xx} = D_{yy} \neq D_{zz} \neq 0 \Rightarrow D \neq 0, E = 0$;

$$\Rightarrow \mathcal{H}_{CF} = D S_z^2;$$

- *rhombic* symmetry: $D_{xx} \neq 0, D_{yy} \neq 0, D_{zz} \neq 0 \Rightarrow D \neq 0, E \neq 0$.

If the CF has axial symmetry the eigenvectors of Eq. 1.11 are the eigenstates of $\mathbf{S}_z$ with eigenvalues given by:

$$W(E) = Dm^2 - \frac{S(S+1)}{3}. \tag{1.16}$$

If $D > 0$ the levels with lowest $|m_{S_z}|$ are the most stable (*easy plane*), while if $D < 0$ the levels with highest $|m_{S_z}|$ lie lowest (*easy axis*). When also $E \neq 0$, if S is an integer the degeneracy between the $|m_{S_z}\rangle$ and the $|-m_{S_z}\rangle$ states is removed, while they remain degenerate in pairs if S is an half integer. This is due to time reversal symmetry and the pairs of degenerate levels are called *Kramers doublet* [47].

The local crystal field parameters d_i and e_i are connected to the corresponding D and E parameters describing the ground state anisotropy by the following relations:

$$D = \sum_{i=1}^{N} \Gamma_i d_i \tag{1.17}$$

$$E = \sum_{i=1}^{N} \Gamma_i e_i, \tag{1.18}$$

where Γ_i are projection coefficients. The same projection procedure between the local effects of the anisotropy and the strong-exchange limit can be done for the dipolar interactions. All the details are reported in Ref.[51]

Zeeman effect

In presence of an external magnetic field, we have to take into account also the Zeeman effect, which is responsible for further splittings of the energy levels. Within the SH formalism, the Hamiltonian for the Zeeman effect is given by:

$$\mathcal{H}_{Zee}^{spin} = \mu_B \sum_{i=1}^{N} \mathbf{B} \cdot \mathbf{g} \cdot \mathbf{s}_i, \tag{1.19}$$

where μ_B is the Bohr magneton, $\mathbf{g}$ is the spectroscopic splitting tensor and $\mathbf{B}$ represents the external magnetic field.

For instance, if the magnetic field is along the z axis of the coordinate reference system of the molecule, $\mathbf{B} = B_z \hat{z}$, the SH becomes:

$$\mathcal{H}_{Zee} = \mu_B \sum_{i=1}^{z} g B_z s_{zi}. \tag{1.20}$$

otherwise, the external magnetic field is always expressed in spherical coordinates:

$$\begin{cases} B_x = B sin\theta cos\phi, \\ B_y = B sin\theta sin\phi, \\ B_z = B cos\theta, \end{cases} \tag{1.21}$$

where θ represents the azimuthal angle between the z axis of the molecule and the field, while ϕ identify its direction in the x,y plane.

Basis definition

In order to represent all the interactions described above and build the Hamiltonian matrix, we have to choose a suitable basis set. The natural choice is represented by the product states

$$|s_1 m_1\rangle |s_2 m_2\rangle ... |s_N m_N\rangle \tag{1.22}$$

as basis functions. Nonetheless, the Heisenberg-Dirac isotropic exchange is often the dominant term in the SH in Eq. 1.1. Therefore the best basis set to build the Hamiltonian matrix is represented by the eigenstates of the total-spin $\mathbf{S} = \sum_i \mathbf{s_i}$. To obtain the total-spin S we also have to choose an appropriate coupling scheme of the single-site spins s_i. For a cluster with N magnetic ions with spins $s_1, s_2, ..., s_N$ a successive coupling scheme leads to the following basis vectors:

$$|s_1 s_2(\tilde{S}_2) s_3(\tilde{S}_3) ... s_{N-1}(\tilde{S}_{N-1}) s_N S M\rangle = |(\tilde{S}) S M\rangle \tag{1.23}$$

where $(\tilde{S})$ represents the complete set of intermediate spin quantum numbers $\tilde{S}_k$, with $k = 1, ..., N - 1$. The first intermediate spin $\tilde{S}_2 = S_{12}$ is given by the coupling of s_1 with s_2. Then $\tilde{S}_2$ is coupled to s_3 to have $\tilde{S}_3 = S_{123}$ and so on. The best choice for the coupling scheme is the one which reflects the symmetry of the molecular system. Nonetheless, all the possible coupling schemes are equivalent, since the corresponding representative vectors are connected to each other by a given unitary transformation.

1.1.2 Irreducible Tensor Operators (ITOs)

The introduction of the *Irreducible Tensor Operators* (ITOs) simplifies the calculation of the matrix elements on the total-spin basis: The spin operators $\mathbf{s}_i$ in the SH can in fact be rewritten as ITOs $\hat{T}_q^k$ with rank $k = 1$. The three components of the tensor, respectively with $q = 0, \pm 1$, corresponds to appropriate combinations of the operator $\mathbf{s}_i$:

$$\begin{aligned} \hat{T}_0^{(1)} &= \mathbf{s}_z, \\ \hat{T}_{\pm 1}^{(1)} &= \mp \frac{1}{\sqrt{2}} (\mathbf{s}_x \pm \mathbf{s}_y). \end{aligned} \tag{1.24}$$

Therefore in the SH will appear a sum of tensors $\hat{T}_q^k$, originating from the product of single-spin operators. The tensor product between two ITOs with rank k_1 e k_2 produces a set of $(2k_1 + 1)(2k_2 + 1)$ operators:

$$\hat{T}^{(k_1)} \otimes \hat{T}^{(k_2)} = \left\{ \hat{T}_{q_1}^{(k_1)} \hat{T}_{q_2}^{(k_2)} \right\}. \tag{1.25}$$

Starting from this set it is possible to build an ITO with rank k defined as:

$$\left\{ \hat{T}^{(k_1)} \otimes \hat{T}^{(k_2)} \right\}_q^{(k)} = \sum_{q_1, q_2} \langle k_1 k_2 q_1 q_2 | k q \rangle \hat{T}_{q_1}^{(k_1)} \hat{T}_{q_2}^{(k_2)}, \tag{1.26}$$

with $|k_1 - k_2| < k < k_1 + k_2$.

The *Wigner-Eckart Theorem* it is exploited to calculate the matrix elements of ITOs on the basis of the angular momentum. This theorem allows us to express all the matrix

elements in terms of Wigner's 3j symbols and reduced matrix elements, which are both easy to calculate and frequently reported in literature. The Wigner-Eckart theorem states that:

In a standard representation $\{\mathbf{J}, J_z\}$, whose basis vectors are denoted by $|\alpha jm\rangle$, the matrix elements $\langle \alpha jm | \hat{T}_q^k | \alpha' j' m' \rangle$ of the qth standard component of a given k^{th}-order ITO $\hat{T}^k$ is equal to the product of the Clebsch-Gordon coefficients by a quantity independent of m, m' and q:

$$\langle \alpha; jm | \hat{T}_q^{(k)} | \alpha'; j'm' \rangle = \frac{1}{\sqrt{2j+1}} C_{j'km'q}^{jm} \langle \alpha; j || \hat{T}^{(k)} || \alpha'; j' \rangle, \tag{1.27}$$

or, in terms of Wigner's 3j symbols:

$$\langle \alpha; jm | \hat{T}_q^{(k)} | \alpha'; j'm' \rangle = (-1)^{j-m} \begin{pmatrix} j & k & j' \\ -m & q & m' \end{pmatrix} \langle \alpha; j || \hat{T}^{(k)} || \alpha'; j' \rangle, \tag{1.28}$$

where $\langle \alpha; j || \hat{T}^{(k)} || \alpha'; j' \rangle$, called reduced matrix element, *is independent of* m,m',q, *varies from one tensor to another and depends on the indices α, j and α', j'*[48].

Exchange interactions

The SH in Eq. 1.3 represents isotropic exchange interactions as a scalar product between the couples of spins s_i and s_j: each scalar product $\mathbf{s}_i \cdot \mathbf{s}_j$ behaves as a $k = 0$, $q = 0$ tensor (i.e. a scalar quantity) and it has a rotational symmetry. Therefore the isotropic exchange Hamiltonian in terms of ITOs becomes:

$$\mathcal{H}_{Iex} = -\sqrt{3} \sum_{i,j} J_{i,j} \{\hat{T}_1^{(1)}(s_i) \otimes \hat{T}_1^{(1)}(s_j)\}_0^{(0)} = -\sqrt{3} \sum_{i,j} J_{i,j} \hat{T}_0^{(0)}(11|ij) \tag{1.29}$$

Since the ranks of the operators appearing in Eq. 1.29 is $k = 0$, we can expect that for the isotropic exchange interaction the matrix elements will be non-zero only between states with the same values of S and M.

The other exchange interactions Hamiltonians in terms of ITOs become:

$$\mathcal{H}_{BQ} = -\sum_{i>j} j_{ij} \left[\sqrt{5} T_0^{(0)}(22|ij) + \frac{\sqrt{3}}{2} T_0^{(0)}(11|ij) \right] \tag{1.30}$$

$$\mathcal{H}_{As} = -i\sqrt{2} \sum_{i>j} \sum_q (-1)^q G_{q,ij}^{(1)} T_{-q}^{(1)}(11|jj) \tag{1.31}$$

$$\mathcal{H}_{AN} = \sum_{i>j} J_{ij}^a T_0^0(11|ij) + \sum_{i,j} J_{ij}^u \left[T_2^{-2}(11|ij) + T_2^2(11|ij) \right] + \sum_{i,j} J_{ij}^v T_2^0(11|ij) \tag{1.32}$$

where

$$G_{q,ij}^{(1)} = \begin{cases} \mp \frac{(G_{z,ij} \pm G_{y,ij})}{\sqrt{q}} & \text{if } q = \pm 1 \\ \\ G_{z,ij} & \text{if } q = 0 \end{cases}, \tag{1.33}$$

$$J_{ij}^a = -\frac{1}{\sqrt{3}} \left(J_{ij}^x + J_{ij}^y + J_{ij}^z \right) \tag{1.34}$$

$$J_{ij}^u = \frac{1}{\sqrt{2}} \left(J_{ij}^x - J_{ij}^y \right)$$

$$J_{ij}^v = \frac{1}{\sqrt{6}} \left(2J_{ij}^z - J_{ij}^x - J_{ij}^y \right)$$

As it can be seen in Eqs. 1.30 and 1.32, both the biquadratic and the anisotropic Hamiltonians contain a scalar rank-0 contribution, i.e. $T_0^{(0)}(11|ij)$. This two terms can be incorporated in the isotropic exchange Hamiltonian by defining the effective isotropic parameters as $\tilde{J}_{ij} = J_{ij} + \frac{1}{3}(J_{ij}^x + J_{ij}^y + J_{ij}^z)$.

Dipolar Interaction

The dipolar interaction can be expressed as a quadratic form (see Eq. 1.7). Developing this quadratic form, it is possible to demonstrate that it can be rewritten in terms of tensor products of operators with $k = 1$. Following the rules of the tensor product, the Hamiltonian in Eq. 1.7 can be rewritten in terms 2nd-order ITOs:

$$
\begin{aligned}
\mathcal{H}_{dip} =\ & \sum_{i,j=1}^{N} \sqrt{\frac{2}{3}} J_{ij}^{zz} \hat{T}_0^{(2)}(11|ij) + \\
& + \ [-J_{ij}^{xz} + iJ_{ij}^{yy}] \hat{T}_1^{(2)}(11|ij) + [J_{ij}^{xz} + iJ_{ij}^{yy}] \hat{T}_{-1}^{(2)}(11|ij) + \\
& + \ \left\{ \frac{1}{2} [J_{ij}^{xx} - J_{ij}^{yx}] - iJ_{ij}^{xy} \right\} \hat{T}_2^{(2)}(11|ij) + \left\{ \frac{1}{2} [J_{ij}^{xx} - J_{ij}^{yx}] + iJ_{ij}^{xy} \right\} \hat{T}_{-2}^{(2)}(11|ij),
\end{aligned}
\tag{1.35}
$$

where $J_{ij}^{\alpha\beta}$, with $\alpha, \beta = x, y, z$ are the components of the coefficients matrix $\mathbf{J}_{ij}^{dip}$ for each couple $s_i s_j$. Since the tensor operators in Eq. 1.35 have $k = 2$, the dipolar interactions will mix states with different total-spin S following the selection rules: $\Delta S = 0, \pm 1, \pm 2$ and $\Delta M = 0, \pm 1, \pm 2$.

Crystal Fields

The exchange and dipolar contributions to the SH are two-bodies interactions, while the CF Hamiltonian expresses the effect of the local crystal field anisotropy on a single magnetic ion. In fact Stevens equivalent operators in the CF Hamiltonian (see Eq. 1.10) acting on a single site j can be expressed in terms of ITOs with all k_i's equal to zero apart from k_j. For instance, the widely-used second-order Hamiltonian (Eq. 1.11) will only contain 2nd-order ITOs:

$$\mathcal{H}_{CF} = \sum_{i=1}^{N} \left[d_i T_0^{(2)}(2|i) + e_i \left(T_2^{(2)}(2|i) + T_{-2}^{(2)}(2|i) \right) \right]. \tag{1.36}$$

Since the tensor operators in Eq. 1.36 have $k = 2$, the CF, as the dipolar interaction, will mix states with different total-spin S following the selection rules: $\Delta S = 0, \pm 1, \pm 2$ and $\Delta M = 0, \pm 1, \pm 2$.

Zeeman effects

In the SH for the Zeeman effect only appear single-spin operators s_i, which can be written as appropriate linear combinations of 1st-rank ITOs (see Eq. 1.24). The Zeeman Hamiltonian can be therefore expressed as:

$$\mathcal{H}_{Zee} = \mu_B g \sum_{i=1}^{7} \{ B_x [\frac{1}{\sqrt{2}} (\hat{T}_{-1}^{(1)}(1|i) - \hat{T}_{1}^{(1)}(1|i))] + \tag{1.37}$$

$$+ B_y [\frac{i}{\sqrt{2}} (\hat{T}_{-1}^{(1)}(1|i) + \hat{T}_{1}^{(1)}(1|i))] + B_z \hat{T}_0^{(1)}(1|i) \}.$$

Recoupling

The tensor operators in the SHs in Eqs. 1.29, 1.35, 1.36 and 1.37 are the results of tensor products between single-spin operators. It is possible to decompose each operator $\hat{T}_q^{(k)}$ following the chosen coupling scheme for the total-spin S:

$$\hat{T}_q^{(k)} = \left\{ \left\{ \left\{ \hat{T}^{(k_1)}(S_1) \otimes \hat{T}^{(k_2)}(S_2) \right\}^{(k_{12})} \otimes \hat{T}^{(k_3)}(S_3) \right\}^{(k_{123})} \otimes ... \right\}_q^{(k)}. \tag{1.38}$$

The Wigner-Eckart theorem simplifies the calculation of the ITOs matrix elements, which can be expressed in terms of Wigner's 3*j* symbols and reduced matrix elements of the product tensors $\hat{T}_q^{(k)}$ in Eq. 1.38. The *recoupling* technique allows us to rewrite the reduced matrix elements of these operators in terms of single-spin reduced matrix elements and Wigner's 9*j* symbols [52]. In the simple case of a spin dimer we have:

$$\hat{T}_q^{(k)} = \left\{ \hat{T}^{(k_1)} \otimes \hat{T}^{(k_2)} \right\}_q^{(k)} = \sum_{q_1, q_2} \langle k_1 k_2 q_1 q_2 | k q \rangle \hat{T}_{q_1}^{(k_1)} \hat{T}_{q_2}^{(k_2)}, \tag{1.39}$$

whose matrix elements on the total-spin basis can be calculated with the Wigner-Eckart theorem as:

$$\langle s_1 s_2 S M | \hat{T}_q^{(k)} | s_1 s_2 S' M' \rangle = (-1)^{S-M} \begin{pmatrix} S & k & S' \\ -M & q & M' \end{pmatrix} \times \tag{1.40}$$

$$\times \langle s_1 s_2 S || \hat{T}^{(k)} || s_1 s_2 S' \rangle.$$

With the recoupling technique the reduced matrix element can be written as:

$$\langle s_1 s_2 S || \hat{T}^{(k)} || s_1 s_2 S' \rangle = \sqrt{(2S+1)(2k+1)(2S'+1)} \times$$

$$\times \begin{Bmatrix} k & S & S' \\ k_1 & s_1 & s_1 \\ k_2 & s_2 & s_2 \end{Bmatrix} \langle s_1 || \hat{T}^{(k_1)} || s_1 \rangle \langle s_2 || \hat{T}^{(k_2)} || s_2 \rangle,$$

where we find only single-spin reduced matrix elements, which are easy to calculate and often reported in literature. In terms on single-ion spin operators with $k_i = 0, 1, 2$ they can be expressed as:

$$< S || \hat{S}^{(0)} || S > = \sqrt{(2S+1)} \tag{1.41}$$

$$< S || \hat{S}^{(1)} || S > = \sqrt{S(S+1)(2S+1)}$$

$$< S || \hat{S}^{(2)} || S > = \frac{1}{2\sqrt{6}} \sqrt{2S(2S+3)(2S+2)(2S+1)(2S-1)}.$$

1.1.3 Spin Hamiltonian Diagonalization

In the previous sections we have described how to rewrite all the SH contributions in terms of ITOs and how to calculate their matrix elements on the total-spin basis $|(\tilde{S})SM\rangle$ exploiting the Wigner-Eckart theorem and the recoupling technique. Once the Hamiltonian matrix is obtained, we can diagonalize it in order to evaluate the energy spectrum of the molecule. For the calculation of the matrix elements and the diagonalization of the Hamiltonian matrix a specific *Fortan90* code has been written for each analysed system. The code is made of several different subroutines for the implementation of each contribution to the SH and the calculation of reduced matrix elements, Wigner's 3*j* and 9*j* symbols (the latter are obtained through the calculation of 6*j* symbols). In order to diagonalize both real symmetric or complex hermitian SHs, *Lapack* diagonalization subroutines have been included in the code.

The dimension of the Hamiltonian matrices to be diagonalized for MNMs increases dramatically with the increase in the number of magnetic centers. The dimension of the Hilbert space associated to a molecule containing N magnetic ions (and thus the dimension of the Hamiltonian matrix) is in fact given by

$$dim(H) = \prod_{i=1}^{N}(2s_i + 1).\tag{1.42}$$

In the case of isotropic systems the matrices are reduced by classifying the states according to the total-spin values. For a cluster exhibiting high symmetry, this problem can be attacked more efficiently by taking advantage of the point group symmetry of the cluster, which results in an additional reduction of the matrices. For the isotropic systems, the Hamiltonian matrix is block-factorized according to the value of the total-spin S, its projection M and the irreducible representation Γ of the point group of the cluster.

In the previous section we have shown that there are many other contributions to the SH, which mix states with different total-spin S. In order to diagonalize the full matrix of the system, one should exploit algorithms of parallel computing. Nevertheless, this would be quite unuseful since the information contained in the most of experimental data involves only levels thermally occupied at very low temperatures. Indeed, a perturbative approach can be applied, since in magnetic molecules the isotropic exchange is almost always the dominant interaction. As a result, the problem can be solved by a two step procedure. Initially, only the Heisenberg-Dirac Hamiltonian $\mathcal{H}_0$ is considered. The eigenvalues and eigenvectors of the cluster are thus determined: The energy spectrum consists of several spin multiplets separated by the isotropic exchange. The eigenvectors of the isotropic exchange in terms of the basis vectors are:

$$|SM\rangle = \sum_{\tilde{S}}\langle(\tilde{S})SM|SM\rangle|(\tilde{S})SM\rangle = \sum_{\tilde{S}}c_{(\tilde{S})S}|(\tilde{S})SM\rangle\tag{1.43}$$

It follows from the above expression that the generic matrix element in Eq. 1.28 is:

$$\langle S'M'|\quad T_1^{(k)}(k_1, k_2, \tilde{k}_2, ..., k_N)\quad |SM\rangle =\tag{1.44}$$

$$= \quad(-1)^{S'-M'}\sum_{\tilde{S},\tilde{S}'}c_{(\tilde{S})S}c_{(\tilde{S}')S'}\langle\tilde{S}'S'||\hat{T}^{(k)}||\tilde{S}S\rangle\begin{pmatrix} S & k & S' \\ -M & q & M' \end{pmatrix}$$

In order to reduce the dimension of the system representative matrix, a cut in the energy diagram of $\mathcal{H}_0$ can be performed: Only eigenvectors of $\mathcal{H}_0$ with corresponding eigenvalues with energy up to the decided threshold value are to be retained. Within this

reduced spin subspace all magnetic interactions can be evaluated. In fact, by means of Eqs. 1.43 and 1.44 it is straightforward to calculate the matrix elements of anisotropic interactions between any of the eigenvectors of isotropic exchange. Finally, the second step of this procedure is to diagonalize the here determined complete SH with all the anisotropic terms within the above-mentioned reduced spin subspace, where we take into account also S-mixing effect [53]. The only approximation of this method consists in neglecting the S-mixing between levels of the reduced spin subspace and the other levels. This approximation can be always checked to produce an error smaller than the experimental error by a little increase of the reduced spin subspace dimension.

The Lanczos Method

The Lanczos iteration [54] was conceived for tridiagonalizing Hermitian matrices. Actually, the Lanczos method is also particularly suited for the determination of extreme eigenvalues and eigenvectors when the dimension of the Hamiltonian matrix prevents the use of direct diagonalization methods, due to the overcome of computational and storage capabilities. For finding the eigenvalues of a matrix H of dimension N, the Lanczos method requires the evaluation of a matrix-vector product $H \cdot v$ as the only problem-specific step. This matrix-vector product can be calculated particularly efficiently when the matrix H is sparse. Storing such a matrix takes only $\mathcal{O}(N)$ memory and $H \cdot v$ can be evaluated in $\mathcal{O}(N)$ time. Calculating the extreme eigenvalue requires $\mathcal{O}(1)$ iteration, i.e., overall $\mathcal{O}(N)$ time. For comparison, a direct diagonalization takes $\mathcal{O}(N^2)$ for storing a matrix and $\mathcal{O}(N^3)$ time to diagonalize. In the following we illustrate the basic steps of the Lanczos Method.

If we want to determine the ground state $|\Psi_0\rangle$ and its energy E_0 for a Hamiltonian $\mathcal{H}$ we can apply the variational principle. The wavefunction functional is given by:

$$E\left[\Psi\right] = \frac{\langle\Psi|\mathcal{H}|\Psi\rangle}{\langle\Psi|\Psi\rangle}, \tag{1.45}$$

which will be minimized for $\Psi = \Psi_0$ with $E\left[\Psi_0\right] = E_0$. The functional gradient

$$\frac{\delta E\left[\Psi\right]}{\delta\langle\Psi|} = \frac{\mathcal{H}|\Psi\rangle - E\left[\Psi\right]|\Psi\rangle}{\langle\Psi|\Psi\rangle} = |\Psi_\alpha\rangle \tag{1.46}$$

gives the direction of the *steepest-ascent* of the functional from the point $|\Psi\rangle$. Moving in the opposite direction will thus result in a wavefunction with lower energy expectation values: $E\left[\Psi - \alpha\Psi\right] < E\left[\Psi\right]$ for small, positive α. To find the optimum value of α we minimize $E\left[\Psi - \alpha\Psi\right]$. In order to do this, it is useful to introduce an orthogonal basis in the space spanned by the two vectors Ψ and Ψ_α. From Eq. 1.46 we see that *span* $(|\Psi\rangle, |\Psi_\alpha\rangle) =$*span* $(|\Psi\rangle, \mathcal{H}|\Psi\rangle)$. Thus, as first basis vector, we normalize Ψ:

$$|v_0\rangle = \frac{\Psi}{\sqrt{\langle\Psi|\Psi\rangle}}, \tag{1.47}$$

for the second vector we orthogonalize $\mathcal{H}|v_0\rangle$ to $|v_0\rangle$

$$|\tilde{v}_1\rangle = \mathcal{H}|v_0\rangle - |v_0\rangle\langle v_0|\mathcal{H}|v_0\rangle \tag{1.48}$$

and normalize to obtain $|v_1\rangle$. With $a_n = \langle v_n|\mathcal{H}|v_n\rangle$ and $b_1^2 = \langle\tilde{v}_1|\tilde{v}_1\rangle$ we thus have

$$\mathcal{H}|v_0\rangle = a_0|v_0\rangle + b_1|v_1\rangle \tag{1.49}$$

with $b_1 = \langle v_1 | \mathcal{H} | v_0 \rangle$. We can then rewrite any normalized wavefunction in *span* $(|\Psi\rangle, \mathcal{H}|\Psi\rangle)$ as

$$|v\rangle = cos(\theta)|v_0\rangle + sin(\theta)|v_1\rangle. \tag{1.50}$$

To find the low-energy state on the subspace spanned by $|v_0\rangle$ and $|v_1\rangle$ we can diagonalize the Hamiltonian matrix on the two-dimensional subspace, which is given by:

$$H_{span(|\Psi\rangle, \mathcal{H}|\Psi\rangle)} = \begin{pmatrix} a_0 & b_1 \\ b_1 & a_1 \end{pmatrix}. \tag{1.51}$$

The variational state of lower energy

$$|\Psi^{(2)}\rangle = cos(\theta_{min})|v_0\rangle + sin(\theta_{min})|v_1\rangle. \tag{1.52}$$

can of course be used as the starting point for another *steepest-descent* minimization. Doing this repeatedly we obtain a series of vectors with decreasing energy expectation value, which rapidly converge to a minimum. Furthermore, the energy functional in Eq. 1.45 has only minima for the ground states, all the other stationary point are saddle point. We can thus expect a rapid convergence to the ground state.

If we apply the method of the *steepest-descent L* times, starting from a vector $|v_0\rangle$, the resulting vector will lie in

$$\mathcal{K}^L(|v_0\rangle) = span(|v_0\rangle, \mathcal{H}|v_0\rangle, \mathcal{H}^2|v_0\rangle, ..., \mathcal{H}^N|v_0\rangle), \tag{1.53}$$

the so-called $L + 1$ dimensional *Krylov space* of $\mathcal{H}$ over $|v_0\rangle$. Instead of repeatedly minimizing the energy in two-dimensional subspaces, we could directly find the state of lowest energy in $\mathcal{K}^L(|v_0\rangle)$. To implement the idea, we construct on orthonormal basis $|v_n\rangle$ of the Krylov space. We start we the normal vector $|v_0\rangle$, while the second vector is constructed as in the steepest-descent method, with Eq. 1.48:

$$b_1|v_1\rangle = |\tilde{v}_1\rangle = \mathcal{H}|v_1\rangle - a_0|v_0\rangle. \tag{1.54}$$

The next basis vector is likewise constructed as $\mathcal{H}|v_n\rangle$ orthogonalized to all previous vectors and normalized:

$$b_2|v_2\rangle = |\tilde{v}_2\rangle = \mathcal{H}|v_1\rangle - \sum_{i=0}^{1} |v_i\rangle\langle v_i|\mathcal{H}|v_i\rangle = \mathcal{H}|v_1\rangle - a_1|v_1\rangle - b_1|v_0\rangle. \tag{1.55}$$

The construction of the further basis vectors follows the same scheme:

$$b_{n+1}|v_{n+1}\rangle = |\tilde{v}_{n+1}\rangle = \mathcal{H}|v_n\rangle - \sum_{i=0}^{n} |v_i\rangle\langle v_i|\mathcal{H}|v_i\rangle = \mathcal{H}|v_n\rangle - a_n|v_n\rangle - b_n|v_{n-1}\rangle, \tag{1.56}$$

where $a_n = \langle v_n|\mathcal{H}|v_n\rangle$ and $b_n^2 = \langle \tilde{v}_n|\tilde{v}_n\rangle$. The Hamiltonian matrix constructed on this basis set is therefore tridiagonal

$$\mathcal{H}|v_n\rangle = a_n|v_n\rangle + b_n|v_{n-1}\rangle + b_{n+1}|v_{n+1}\rangle, \tag{1.57}$$

and this triadiagonalization is the essence of the Lanczos method. After L-step the Hamiltonian on the $L + 1$-dimensional Krylov space is given by:

$$H_{\mathcal{K}^L(|v_0\rangle)} = \begin{pmatrix} a_0 & b_1 & 0 & 0 & ... & 0 & 0 \\ b_1 & a_1 & b_2 & 0 & ... & 0 & 0 \\ 0 & b_2 & a_2 & b_3 & ... & 0 & 0 \\ 0 & 0 & b_3 & a_3 & ... & 0 & 0 \\ & & ... & & ... & & ... \\ 0 & 0 & 0 & 0 & ... & a_{L-1} & b_L \\ 0 & 0 & 0 & 0 & ... & b_L & a_L \end{pmatrix}. \tag{1.58}$$

The numerical implementation of the whole method only requires keeping two N-dimensional vectors in memory. After tens to hundred iterations, the lowest eigenvalue of the tridiagonal representation of $\mathcal{H}$ on the Krylov space gives an excellent approximation to the ground state energy in the full Hilbert space [55].

Finite-Temperature Lanczos

The Finite-Temperature Lanczos is a method for the evaluation of finite-temperature properties, based on the Lanczos diagonalization technique [56, 57]. This method allows us to avoid the calculation of all eigenfunctions of the system, by applying a procedure where the sampling over all states is reduced to a random partial sampling and only approximate ground state and excited states wave functions, generated by the Lanczos technique, are used for the calculation of the matrix elements.

For the evaluation of thermodynamic properties in MNMs, we have, for instance, to calculate the partition function depending on temperature T and magnetic field B:

$$Z(T,B) = \sum_{\nu} \langle \nu | e^{-\beta \mathcal{H}} | \nu \rangle, \tag{1.59}$$

where $|\nu\rangle$ is a vectors of an orthonormal basis of the molecule's Hilbert space. Within the Finite-Temperature Lanczos framework [56, 57], the unknown matrix elements are approximated as:

$$\langle \nu | e^{-\beta \mathcal{H}} | \nu \rangle \approx \sum_{n=1}^{N_L} \langle \nu | n(\nu) \rangle e^{-\beta \epsilon_n^{(\nu)}} \langle n(\nu) | \nu \rangle. \tag{1.60}$$

In order to implement this approximation, we have to perform N_L Lanczos steps, spanning a respective Krylov space, with $|\nu\rangle$ as initial vector of the iteration. As pointed out in the previous section, with the Lanczos method the Hamiltonian is diagonalized in this Krylov space, yielding N_L Lanczos eigenvectors $|n(\nu)\rangle$ with associated Lanczos energy eigenvalues $\epsilon_n^{(\nu)}$. The number of Lanczos steps N_L is a parameter of the approximation, which have to be large enough to converge to the extremal energy eigenvalues, but not to large in order to avoid problems of numerical accuracy. A typical value is $N_L \approx 100$.

As a further step, the complete and thus very large sum over $|\nu\rangle$ ($\nu = 1, ..., dim(H)$) in Eq. 1.59, is replaced by a summation over a subset of R random vectors. These vectors are truly random and they do not need to belong to any special basis set:

$$Z(T,B) \approx \frac{dim(H)}{R} \sum_{\nu=1}^{R} \sum_{n=1}^{N_L} e^{-\beta \epsilon_n^{(\nu)}} |\langle n(\nu) | \nu \rangle|^2. \tag{1.61}$$

The number of random starting vectors can be chosen rather small, e.g. $R \approx 20$ with $N_L \approx 100$. If we take also into account the symmetries of the system and their irreducible representation Γ, we improve the accuracy of the approximation:

$$Z(T,B) \approx \sum_{\Gamma} \frac{dim(H(\Gamma))}{R_\Gamma} \sum_{\nu=1}^{R_\Gamma} \sum_{n=1}^{N_L} e^{-\beta \epsilon_n^{(\nu,\Gamma)}} |\langle n(\nu,\Gamma) | \nu, \Gamma \rangle|^2, \tag{1.62}$$

where the $H(\Gamma)$ are the mutually orthogonal subspaces of the full Hilbert space. It is worth to stress that the pseudo energy eigenvalues $\epsilon_n^{(\nu,\Gamma)}$ have no spectroscopic meaning in general: Very low-lying energy levels may coincide with the true ones due to the
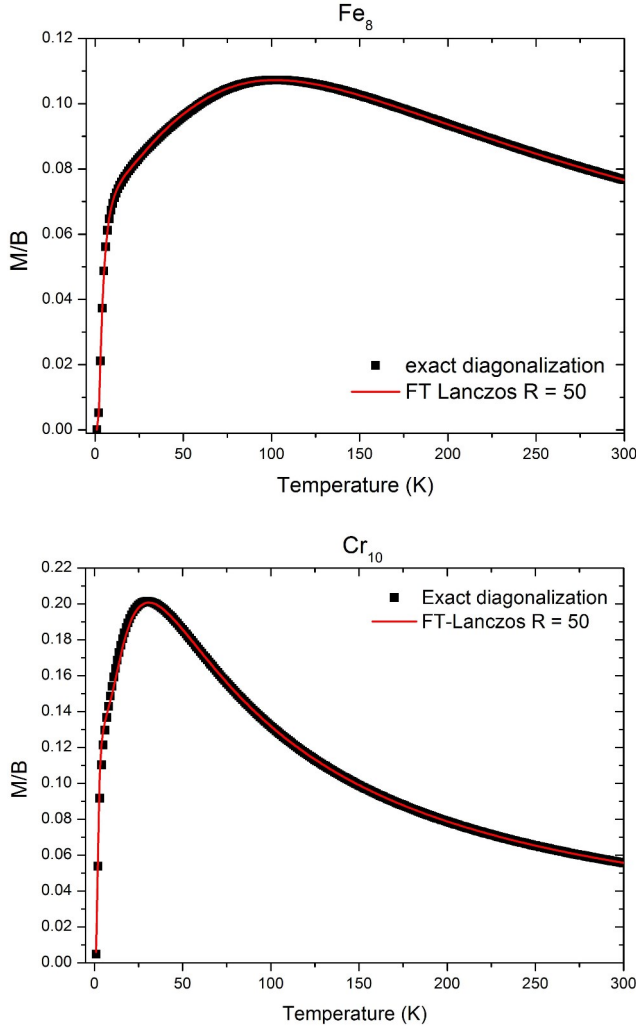
Figure 1.1: Magnetic susceptibility of the two ideal rings Fe_8 (top panel) and Cr_{10} (bottom panel). Simulations obtained with the Finite-Temperature Lanczos Method (red lines) are in excellent agreement with exact calculations (black squares).

rapid convergence of the Lanczos method. However, this discrepancy is miraculously compensated by the weights $\langle n(\nu, \Gamma) | \nu, \Gamma \rangle$.

An observable $\mathcal{A}$ can be calculated as:

$$\mathcal{A}(T, B) \approx \frac{1}{Z(T, B)} \sum_{\Gamma} \frac{dim(H(\Gamma))}{R_{\Gamma}} \sum_{\nu=1}^{R_{\Gamma}} \sum_{n=1}^{N_L} e^{-\beta \epsilon_n^{(\nu, \Gamma)}} \langle n(\nu, \Gamma) | \mathcal{A} | \nu, \Gamma \rangle \langle n(\nu, \Gamma) | \nu, \Gamma \rangle. \quad (1.63)$$

Therefore the Finite-Temperature Lanczos method can be applied to the study of very large MNMs, in order to investigate their finite-temperature magnetic properties. Since

Lanczos iterations consists of matrix-vector multiplications, they can be also parallelized with *OpenMP* directives, in order to reduce the computational time. If we take into account some ideal systems, which are large but still small enough to be diagonalized exactly, we can try out the method and compare it with exact diagonalization techniques. We have performed some tests on ideal Fe_8 and Cr_{10} AF rings, reported in Fig. 1.1. We can see that the agreement between exact calculations and Finite-Temperature Lanczos results is very good, also with a small number of random sampling $R \approx 50$.

1.2 Quantum Theory of Relaxation

The spin dynamics of MNMs can be described by the coherent evolution given by the SH only on sufficiently short time-scales. In fact for time-scales much longer than the characteristic coherence time τ_{coh}, which depends on the specific system and on the temperature, the observables are affected by the interactions of the electronic spins with other degrees of freedom, like nuclear spins or phonons, which often behave like an heat bath. They can cause decoherence of the time-evolution of the observables, leading to an irreversible relaxation dynamics towards equilibrium. It is possible to study these dynamics with the *Master Equations* formalism, which describes the "coarse grained" time-evolution of the matrix elements of the density operator ρ. The comprehension of these decoherence mechanisms it is not only important from the point of view of the fundamental research, but it is also crucial in order address the implementation of MNMs in the envisaged technological applications in the field quantum information processing [58].

1.2.1 Master Equations Formalism

The Density Operator and the Liouville Equation

The macroscopic state of a quantum system can be defined as a *mixed state or mixture* of microscopical pure states:

$$\{|\psi_m\rangle \epsilon H, m = 1, 2, ... Prob(|\psi_m\rangle) = P_m\}, \tag{1.64}$$

where H is the Hilbert space associated with the system and P_m indicates the probability that the systems is in the state $|\psi_m\rangle$. A quantum system, which is initially in a pure quantum state or in a coherent superposition of pure quantum states, if it interacts with an unobserved environment (i.e. phonons), after a characteristic decoherence time it will be found in a mixed quantum state.

All the information about the mixed state are contained in the associated *density operator*, defined as:

$$\hat{\rho} \quad : \quad H \longrightarrow H \tag{1.65}$$
$$\hat{\rho} \quad = \quad \sum_m P_m |\psi_m\rangle\langle\psi_m|,$$

which is a linear combinations of projection operators on the states $|\psi_m\rangle$, weighted with their own probability P_m. In order to obtain the matrix form of $\hat{\rho}$ we have to choose a complete orthonormal basis set $\{|\phi_m\rangle, m = 1, 2, ..., dimH\}$ in H; the *density matrix* will be the representation of the operator $\hat{\rho}$ on this basis set, where the matrix elements are given by:

$$\rho_{ij} = \langle\phi_i|\hat{\rho}|\phi_j\rangle. \tag{1.66}$$

The density matrix is hermitian and of trace one; the diagonal elements ρ_{ii} correspond to the probabilities that the system is found in the corresponding state $|\phi_i\rangle$.

In order to determine the time-evolution of the density matrix we have to define the *time evolution operator*; given a time-dependent Hamiltonian $\mathcal{H}(t)$, the time-evolution operator transform the initial state $|\psi(0)\rangle$ in the state $|\psi(t)\rangle$:

$$|\psi(t)\rangle = U(t)|\psi(0)\rangle. \tag{1.67}$$

The operator $U(t)$ can be obtained solving the equation:

$$i\hbar\frac{\partial U(t)}{\partial t} = \mathcal{H}(t)U(t), \tag{1.68}$$
$$with \; U(0) = \mathbb{I}.$$

If the density matrix at the time $t = 0$ is given by $\rho(0)$, its time-evolution will be obtained through the unitary transformation:

$$\rho(t) = U(t)\rho(0)U^\dagger(t). \tag{1.69}$$

Differentiating Eq. 1.69, we get the *Liouville Equation*:

$$i\hbar\frac{\partial\rho(t)}{\partial t} = [\mathcal{H}(t), \rho(t)]. \tag{1.70}$$

The time-evolution of the density matrix can be determined both from Eq. 1.69 and Eq. 1.70.

Since the Hamiltonian of the investigated systems are often given by $\mathcal{H}(t) = \mathcal{H}_0 + V(t)$, where $\mathcal{H}_0$ is time-independent and $V(t)$ can be considered a small perturbation, it is useful to introduce the *interaction notation*. With this notation it is possible to separate the "fast" time-evolution due to $\mathcal{H}_0$, given by rapidly varying factors as $e^{-\frac{i}{\hbar}E_n^0 t}$, from the "slow" one due to $V(t)$. In the interaction picture we have:

$$|\psi(t)_I\rangle = e^{\frac{i}{\hbar}\mathcal{H}_0 t}|\psi(t)\rangle, \tag{1.71}$$
$$V(t)_I = e^{\frac{i}{\hbar}\mathcal{H}_0 t}V(t)e^{-\frac{i}{\hbar}\mathcal{H}_0 t},$$
$$\rho(t)_I = e^{\frac{i}{\hbar}\mathcal{H}_0 t}\rho(t)e^{-\frac{i}{\hbar}\mathcal{H}_0 t}.$$

The Liouville equation becomes:

$$i\hbar\frac{\partial\rho(t)_I}{\partial t} = [V(t)_I, \rho(t)_I], \tag{1.72}$$

whose integral form is given by:

$$\rho(t)_I = \rho(0)_I - \frac{i}{\hbar}\int_0^\tau [V(\tau)_I, \rho(\tau)_I]d\tau. \tag{1.73}$$

If the perturbation $V(t)$ is small, $\rho(t)_I$ it is not so different from its initial value and it can be replaced with $\rho(0)_I$; thus we obtain the integral form of the Liouville Equation in first-order perturbation theory:

$$\rho(t)_I = \rho(0)_I - \frac{i}{\hbar}\int_0^\tau [V(\tau)_I, \rho(0)_I]d\tau. \tag{1.74}$$

Considering two interacting systems ϕ e φ, if the initial state of the total system is a pure quantum state in the composite space given by $|\psi_{in}\rangle = |\phi_\alpha\rangle|\varphi_\beta\rangle$ (with $|\phi_\alpha\rangle$ and $|\varphi_\beta\rangle$ initial pure states of the single subsystems), after their interaction the final state is a pure state in the composite state, but it is not possible to assign a single state vector to either of the two subsystems (*principle of non-separability*). If we also suppose that the subsystem ϕ it is not observed after the interaction, we'll find that the final state of the subsystem φ will be a mixed quantum state: The non-observation of ϕ results in a loss of coherence in the system φ.

When only one of the two interacting subsystems is observed, it is useful to determine the *reduced matrix density* $\rho(\varphi, t)$, which characterizes only the observed system φ, starting from the density matrix of the total system $\rho(t)$. The matrix $\rho(\varphi, t)$ is obtained projecting the total density matrix $\rho(t)$ on the observed subsystem φ:

$$\rho(\varphi, t) = Tr_\phi \rho(t) = \sum_i \langle \phi_i | \rho(t) | \phi_i \rangle. \tag{1.75}$$

If the reaction of the subsystem φ on the unobserved system ϕ after their interaction cannot be neglected, φ is called *open quantum system*. The time-evolution of these kind of systems, which are in a mixed state after the interaction with the unobserved one, cannot be described by the Liouville Equations: The reduced density matrix of the observed subsystem at a time t $\rho(\varphi, t)$ cannot be expressed as a unitary transformation of the initial matrix $\rho(\varphi, 0)$. Open quantum systems can also have *irreversible* dynamics, as a consequence of the interaction with the unobserved system (which can be, for instance, an heat-bath). The operation described in Eq. 1.75, which consists of taking the trace over all the unobserved variables, can be considered a "quantum source" of irreversibility. It is therefore necessary to introduce a formalism, based on the Liouville Equation, able to describe the time-evolution of the reduced density matrix of an open quantum system, interacting with a unobserved environment [59].

Theory of Relaxation

When a system is in a non-equilibrium state, its gradual evolution towards equilibrium, due to its interaction with the environment, it is called *relaxation process*. All the relaxation phenomena are irreversible processes, which have to be described with a different formalism in respect to the reversible processes described by the Schrödinger or the Liouville Equations.

Consider a system S interacting with an unobserved system R. $\rho(t)$ is the density matrix of the total system and the Hamiltonian is given by $\mathcal{H} = \mathcal{H}_S + \mathcal{H}_R + V(t)$, where $\mathcal{H}_S$ and $\mathcal{H}_R$ describe the two systems R and S, while $V(t)$ represents their interaction. The time-evolution of $\rho(t)$ in the interaction picture is given by Eq. 1.72 or 1.73: Substituting the latter in the former equation we get:

$$\dot{\rho}(t)_I = -\frac{i}{\hbar}[V(t)_I, \rho(0)] - (\frac{i}{\hbar})^2 \int_0^t dt' [V(t)_I, [V(t')_I, \rho(t')_I]]. \tag{1.76}$$

To obtain the reduced matrix density of the observed system S, we take the trace of $\rho(t)$ over all the variables of R:

$$\dot{\rho}(t)_{SI} = -\frac{i}{\hbar} Tr_R [V(t)_I, \rho(0)] - (\frac{i}{\hbar})^2 \int_0^t dt' Tr_R [V(t)_I, [V(t')_I, \rho(t')_I]]. \tag{1.77}$$

In order for an irreversible process to occur further conditions must be imposed on the unobserved system, in order to prevent that the energy initially in the system S returns

from R to S in any finite time.

First key-assumption

It is assumed that R has so many degrees of freedom that the effects of the interaction with S dissipate away quickly and will not react back onto S to any significant extent, so that R remains described by a thermal equilibrium distribution at constant temperature, irrespective of the amount of energy diffusing into it from the system S.

Thus, we have that at any time t:

$$\rho(t)_I \longrightarrow \overline{\rho(t)_I} = \rho(t)_{SI} \cdot \rho(0)_R, \tag{1.78}$$

with $\rho(0)_R$ given by:

$$\rho(0)_R = \frac{1}{Z} e^{-\frac{\mathcal{H}_R}{K_B T}}. \tag{1.79}$$

Therefore the observed system S interacts with an "heat-bath" or energy "reservoir", represented by the system R. The Eq. 1.77 becomes:

$$\dot{\rho}(t)_{SI} = \quad - \frac{i}{\hbar} Tr_R[V(t)_I, \rho(0)_S \cdot \rho(0)_R] + \tag{1.80}$$
$$- (\frac{i}{\hbar})^2 \int_0^t dt' Tr_R[V(t)_I, [V(t')_I, \rho(t')_{SI} \cdot \rho(0)_R]].$$

The integral of Eq. 1.80 contains $\rho(t')_{SI}$: Thus the time-evolution of the system S depends on its past history from $t' = 0$ to $t' = t$. However, in this time interval the motion of the system S is damped by the coupling with the reservoir and damping destroys the knowledge of the past behavior of the system.

Second key-assumption - Markoff approximation

It is assumed that $\dot{\rho}(t)_{SI}$ only depends on $\rho(t)_{SI}$, the value of the reduced density matrix at present time. We therefore suppose that the system loses all memory of its past.

In the Eq. 1.80 it is possible to substitute $\rho(t')_{SI}$ with $\rho(t)_{SI}$:

$$\dot{\rho}(t)_{SI} = \quad - \frac{i}{\hbar} Tr_R[V(t)_I, \rho(0)_S \cdot \rho(0)_R] + \tag{1.81}$$
$$- (\frac{1}{\hbar})^2 \int_0^t dt' Tr_R[V(t)_I, [V(t')_I, \rho(t)_{SI} \cdot \rho(0)_R]].$$

Let us assume that the interaction operator can be written in the form:

$$V(t)_I = \sum_i F(t)_i Q(t)_i, \tag{1.82}$$

where the F_i are reservoir operators and the Q_i are operators acting only on the variables of the dynamic system S. The integral form of the Liouville Equation for the reduced

density matrix of S becomes:

$$
\begin{aligned}
\dot{\rho}(t)_{SI} = \quad - \quad & \frac{i}{\hbar} \sum_i \{ Q(t)_i \rho(0)_{SI} Tr_R(F(t)_i \rho(0)_R) + \\
- \quad & \rho(0)_S Q(t)_i Tr_R(F(t)_i \rho(0)_R) \} + \\
- \quad & (\frac{1}{\hbar})^2 \sum_{ij} \int_0^t dt' \{ (Q(t)_i Q(t')_j \rho(t)_{SI} + \\
- \quad & Q(t')_j \rho(t)_{SI} Q(t)_i) Tr_R(F(t)_i F(t)_j \rho(0)_R) + \\
- \quad & (Q(t)_i \rho(t)_{SI} Q(t')_j - \rho(t)_{SI} Q(t')_j Q(t')_i) Tr_R(F(t')_j F(t)_i \rho(0)_R) \}
\end{aligned}
\tag{1.83}
$$

The expectation values of the operators $F(t)_i$ are given by:

$$
\langle F(t)_i \rangle = Tr_R(F(t)_i \rho(0)_R) = \sum_N \langle N|F(t)_i|N \rangle \sum_N \langle N|\rho(0)_R|N \rangle,
\tag{1.84}
$$

where $|N\rangle$ are eigenstates of $\mathcal{H}_R$ which diagonalize ρ_R. If we assume that all the operators $F(t)_i$ have no diagonal elements in this representation, we have that:

$$
\langle F(t)_i \rangle = Tr_R(F(t)_i \rho(0)_R) = 0,
\tag{1.85}
$$

and the first term in Eq. 1.83 will vanish too.

Let us consider also the *time correlation function*:

$$
\langle F(t)_i F(t')_j \rangle = Tr_R(F(t)_i F(t')_j \rho(0)_R),
\tag{1.86}
$$

which characterize the correlation that exists on average between interactions occurring at time t and t'. Since the reservoir R is assumed to be large enough to dissipate quickly the effects of the interaction, it is expected that R will quickly forget its interaction with the system S. The correlation function $\langle F(t)_i F(t')_j \rangle$ will therefore be non-zero in a time interval $t - t' < \tau$, where τ is typical of the reservoir and it is called *correlation time*. For $t - t' > \tau$ the interactions are progressively less correlated and become uncorrelated for $t - t' \gg \tau$:

$$
\langle F(t)_i F(t')_j \rangle \approx 0.
\tag{1.87}
$$

Thus, the integral in Eq. 1.83 will be effectively non-zero in the time interval $t - t' < \tau$, that is between $t' = t - \tau$ and $t' = t$. The system is able to remember its past states only for time intervals shorter than τ.

If the characteristic time $\tau \ll \frac{1}{\gamma}$, where $\frac{1}{\gamma}$ is the time required for $\rho(t)_{SI}$ to change appreciably on a macroscopic scale, then $\rho(t')_{SI} \approx \rho(t)_{SI}$ and the Markoff Approximation holds. The substitution of $\rho(t')_{SI}$ with $\rho(t)_{SI}$ implies that the time-evolution of the system it is not described in detail for time intervals comparable to τ: Using the Markoff Approximation is like using a "coarse grained" description of the evolution of S:

$$
\frac{\Delta \rho(t)_{SI}}{\Delta t} = \frac{\rho(t + \Delta t) - \rho(t)_{Si}}{\Delta t},
\tag{1.88}
$$

where $\Delta t \gg \tau$, but still sufficiently small that the change of $\rho(t)_{SI}$ is linear in Δt.

All the previous consideration, summarized in Eq. 1.87, allow us to extend the upper limit of the integral in Eq. 1.83 to infinity:

$$
\begin{aligned}
\dot{\rho}(t)_{SI} = \quad - \quad & (\frac{1}{\hbar})^2 \sum_{ij} \int_0^\infty dt'' \{ [Q(t)_i, Q(t - t'')_j \rho(t)_{SI}] \langle F(t'')_i F_j \rangle + \\
- \quad & [Q(t)_i, \rho(t)_{SI} Q(t - t'')_j] \langle F_j F(t'')_i \rangle \}.
\end{aligned}
\tag{1.89}
$$

Secular Approximation

Let us introduce the notations:

$$\Gamma^+_{mkln} = \frac{1}{\hbar^2} \sum_{ij} \langle m|Q_i|k\rangle \langle l|Q_j|n\rangle \times \tag{1.90}$$

$$\times \int_0^\infty dt'' e^{-i\omega_{ln}t''} \langle F(t'')_i F_j\rangle,$$

$$\Gamma^-_{mkln} = \frac{1}{\hbar^2} \sum_{ij} \langle m|Q_j|k\rangle \langle l|Q_i|n\rangle \times \tag{1.91}$$

$$\times \int_0^\infty dt'' e^{-i\omega_{mk}t''} \langle F_j F(t'')_i\rangle,$$

with

$$\omega_{mn} = \frac{i}{\hbar}(E_m - E_n)t. \tag{1.92}$$

The matrix elements of the first derivative of the density operator $\dot{\rho}(t)_{SI}$ on the eigenstates $|m\rangle$ of $\mathcal{H}_S$ can be expressed as:

$$\langle m'|\dot{\rho}(t)_{SI}|m\rangle = \sum_{nn'} < n'|\rho(t)_{SI}|n\rangle \times \tag{1.93}$$

$$\times \left\{ -\sum_k \delta_{mn}\Gamma^+_{m'kkn'} + \Gamma^+_{nmn'm'}\Gamma^-_{mkln} - \sum_k \delta_{n'm'}\Gamma^-_{nkkm} \right\} \times$$

$$\times e^{i(\omega_{m'n'}+\omega_{mn})t} =$$

$$= \sum_{nn'} < n'|\rho(t)_{SI}|n\rangle R_{m'mn'n} e^{i(\omega_{m'n'}+\omega_{mn})t}$$

The equations of motions of the reduced density matrix are called *Generalized Master Equation*, and they describe the irreversible dynamics of the observed system S. $R_{m'mn'n}$ is called *Relaxation matrix*.

In the Eq. 1.93 all the exponentials vanish if

$$E_{m'} - E_m - E_{n'} + E_n = 0; \tag{1.94}$$

and the Eq. 1.93 is often approximated as:

$$\langle m'|\dot{\rho}(t)_{SI}|m\rangle = \sum_{nn'} \langle n'|\rho(t)_{SI}|n\rangle R_{m'mn'n}, \tag{1.95}$$

where the summation runs only on the elements satisfying Eq. 1.94. This approximation is called *Secular Approximation* and means that the "coarse-grained" time derivative in Eq. 1.88 is taken over time intervals Δt which are long compared to a period of free motion of the system:

$$\Delta t \gg \frac{1}{\omega_{mn}}. \tag{1.96}$$

The Secular Approximation also allows us to decouple the time-evolution of the non-diagonal terms of the density matrix from that of the diagonal ones.

When all the indices m, m', n, n' satisfy this approximation, the matrix elements of $\dot{\rho}(t)_{SI}$ become:

$$\langle m'|\dot{\rho}(t)_{SI}|m\rangle = \delta_{m'm}\sum_{n\neq m}\langle |n|\rho(t)_{SI}|n\rangle \cdot W_{mn} - \gamma_{m'm}\langle m'|\rho(t)_{SI}|m\rangle, \qquad (1.97)$$

where

$$\begin{aligned} W_{mn} &= \Gamma^+_{nmmn} + \Gamma^-_{nmmn} \ (real), \qquad &(1.98)\\ \gamma_{m'm} &= \sum_k (\Gamma^+_{m'kkm'} + \Gamma^-_{mkkm}) - \Gamma^+_{nmm'n'} - \Gamma^-_{nmm'n'}. \end{aligned}$$

Within the Secular Approximation, the time-evolution of the non-diagonal elements of the reduced density matrix is given by:

$$\langle m'|\dot{\rho}(t)_{SI}|m\rangle = -\gamma_{m'm}\langle m'|\rho(t)_{SI}|m\rangle, \qquad (1.99)$$

that in Schrödinger notation becomes:

$$\langle m'|\dot{\rho}(t)_S|m\rangle = \frac{i}{\hbar}\langle m'|[\mathcal{H}_S, \rho(t)_s]|m\rangle + \qquad (1.100)$$

$$+\delta_{m'm}\sum_{n\neq m}\langle |n|\rho(t)_S|n\rangle \cdot W_{mn} - \gamma_{m'm}\langle m'|\rho(t)_S|m\rangle,$$

where the first term describes the motion of the unperturbed system.

Rate Master equation

Let us now consider the time-evolution of the diagonal terms of the reduced density matrix, considering only the secular terms. It is worth noting that for the diagonal elements of ρ_S the Schrödinger notation coincides with the interaction notation. Given $\langle m'|\rho(t)_S|m\rangle = \rho(t)_{mm'}$, we have that:

$$\dot{\rho}(t)_{mm} = \sum_{n\neq m}\rho(t)_{nn}W_{mn} - \rho(t)_{mm}\sum_{k\neq m}(\Gamma^+_{mkkm} + \Gamma^-_{mkkm}); \qquad (1.101)$$

substituting the index k with the index n in the second sum term, we obtain:

$$\dot{\rho}(t)_{mm} = \sum_{n\neq m}\rho(t)_{nn}W_{mn} - \rho(t)_{mm}\sum_{n\neq m}W_{nm}. \qquad (1.102)$$

The Eq. 1.102 can be interpreted as follows: The diagonal element $\rho(t)_{mm}$ describe the probability to find the system S in the state $|m\rangle$ at a time t. This probability increases in time owing to transitions from all the other levels $|n\rangle$ to $|m\rangle$. It also decreases due to the transitions from $|m\rangle$ to all the other states $|n\rangle$. Thus the *rate* of change of the diagonal elements of $\rho(t)_S$ must contain two terms. The "gain" term is obtained by multiplying $\rho(t)_{nn}$ by the corresponding transition rate $W_{n\to m}$ summed over all the states $|n\rangle$. The "loss" term is obtained by multiplying $\rho(t)_{mm}$ by the transition rate $W_{m\to n}$ and summing over all n. The parameters W_{mn} in Eq. 1.102 can therefore be interpreted as the probability per unit time that a transition between the levels $|m\rangle$ and $|n\rangle$ of the system S is induced by the interaction with the reservoir. The Eq. 1.102 is called *Rate Master equation*.

1.2.2 The Rate Matrix W

The main source of irreversible relaxation dynamics in MNMs is the interaction of the electronic spins with the "heat-bath" of phonons [60, 61]. The elements of the rate matrix W_{mn} in Eq.1.102 will therefore represent the the probability per unit time that a transition between the levels $|m\rangle$ and $|n\rangle$ of the Spin Hamiltonian is induced by the magneto-elastic coupling with phonons [62, 61].

The main contribution to the spin-phonon coupling is due to the modulation of the 2nd-rank CF terms induced by phonons. Thus, the general form for the spin-phonon coupling potential is given by:

$$V = \sum_{1,N} \sum_{Q=-2,2} \sum_{\mathbf{k},\sigma} C_Q(l,\mathbf{k},\sigma) O_2^Q(\mathbf{s}_l)(c_{\mathbf{k},\sigma} + c_{\mathbf{k},\sigma}^\dagger), \tag{1.103}$$

where $C_Q(l,\mathbf{k},\sigma)$ is the coupling constant between the Q-type electric quadrupole on ion l and phonon modes of wave vector $\mathbf{k}$ and branch index σ. The calculation of all the coupling constants cannot be performed exactly, since we don't know the whole phonons' spectrum. We therefore adopt a Debye model to describe the lattice vibrations and we assume that each magnetic ion in the molecular cluster experiences a spherically symmetric magneto-elastic coupling, due to CF modulations induced by phonons.

The rate matrix in Eq. 1.102 can be then calculated in first-order perturbation theory in terms of the coupling potential V in Eq. 1.103, leading to:

$$W_{nm} = \gamma^2 \pi^2 \Delta_{nm}^3 n(\Delta_{mn}) \sum_{\substack{i,j=1,n \\ q_1,q_2=x,y,z}} \langle m|O_{q_1,q_2}(\mathbf{s}_i)|n\rangle \langle n|O_{q_1,q_2}(\mathbf{s}_j)|m\rangle, \tag{1.104}$$

where $n(x) = (e^{-\beta\hbar x} - 1)^{-1}$, $\Delta_{mn} = \frac{(E_m - E_n)}{\hbar}$ and the quadrupolar operators are calculated as $O_{q_1,q_2}(\mathbf{s}_i) = \frac{1}{2}(s_{q_1,i}s_{q_2,i} + s_{q_1,i}s_{q_2,i})$. The coefficient γ is the only free parameter in Eq. 1.104 and it is proportional to the spin-phonon coupling strength. It will be estimated from the comparison with NMR experimental data.

1.2.3 Correlation Functions

The dynamics of molecular observables near thermal equilibrium can be characterized by the behavior of *two-times correlation functions* $\langle \Delta\mathcal{A}(t)\Delta\mathcal{B}(0)\rangle$, where $\Delta\mathcal{A} = \mathcal{A} - \langle\mathcal{A}\rangle_{eq}$ and $\mathcal{A}$ is a generic observable. The same information on the dynamics of the system can be obtained from their Fourier Transform $S_{\mathcal{A},\mathcal{B}}(\omega)$. In order to calculate these quantities we have to know the time-evolution of the density matrix of the systems $\rho(t)_{mn}$, which can be determined with the Mater Equation formalism, described in the previous sections. The Secular Approximation allows us to decoupled the time-evolution of the non-diagonal terms of the density matrix from that of the diagonal ones (given by Eq. 1.102). Decoupling the evolution of these terms corresponds to separate the *inelastic* (IN) contributions of the spectral composition of $S_{\mathcal{A},\mathcal{B}}(\omega)$ from the *quasi-elastic* (QE) ones.

The fluctuation-dissipation theorem can be exploited in order to calculate the Fourier Transform of the correlation function $S_{\mathcal{A},\mathcal{B}}(\omega)$:

$$S_{\mathcal{A},\mathcal{B}}(\omega) = \frac{2K_B T \chi''_{\mathcal{A},\mathcal{B}}(\omega)}{\omega} = 2K_B T \tilde{R}_{\mathcal{A},\mathcal{B}}(i\omega), \tag{1.105}$$

where $\chi''_{\mathcal{A},\mathcal{B}}(\omega)$ is the imaginary part of the susceptibility and $\tilde{R}_{\mathcal{A},\mathcal{B}}(i\omega)$ is the real part of the Laplace Transform of the relaxation function $R_{\mathcal{A},\mathcal{B}}(t) = lim_{\varepsilon\to 0}\frac{1}{\varepsilon}(\mathcal{A} - \langle\mathcal{A}\rangle_{eq})$. $\varepsilon\mathcal{B}$

is a perturbation which has been "switched-off" at $t = 0$ [50]. It is therefore possible to obtain both the IN and QE part of $R_{\mathcal{A},\mathcal{B}}(t)$ solving the Master Equations system in first-order perturbation theory [59, 63]:

$$R_{\mathcal{A},\mathcal{B}}^{QE}(t) = \beta \sum_{m,n} p_m^{eq}(\mathcal{B}_{mm} - \langle \mathcal{B} \rangle_{eq}) \nu_{mn}(t)(\mathcal{A}_{nn} - \langle \mathcal{A} \rangle_{eq}), \tag{1.106}$$

$$R_{\mathcal{A},\mathcal{B}}^{IN}(t) = \sum_{k \neq l} e^{i\Delta_{kl}t} e^{-\frac{t}{\tau_{kl}}} \frac{p_l^{eq} - p_k^{eq}}{E_k^{(0)} - E_l^{(0)}} \mathcal{B}_{lk}\mathcal{A}_{lk}, \tag{1.107}$$

where the summation runs over the eigenstate $|m\rangle$ of the observed system's Hamiltonian, with eigenvalues $E_m^{(0)}$, $p_m^{eq} = \frac{1}{Z} e^{-\beta E_m}$, $\Delta_{lk} = \frac{E_l^{(0)} - E_k^{(0)}}{\hbar}$ and $\mathcal{B}_{lk} = \langle l|\mathcal{B}|k\rangle$. $\nu(t) = e^{\mathbf{Wt}}$ is the propagator which gives the time evolution of the QE part of the density matrix, where $\mathbf{W}$ is the rate matrix, while the IE propagator is given by

$$\Gamma_{nm}(t) = e^{i\Delta_{nm}t} e^{-\frac{t}{\tau_{nm}}}, \tag{1.108}$$

with $\tau_{nm} = -\frac{1}{2}(\Gamma_{nn} + \Gamma_{mm})$.

Taking the real part of the Laplace Transform of Eq. 1.106 we obtain:

$$\begin{aligned}\tilde{R}_{\mathcal{A},\mathcal{B}}^{QE}(i\omega) &= \beta \sum_{mn} p_m^{eq}(\mathcal{B}_{mm} - \langle \mathcal{B} \rangle_{eq}) \times \\ &\times Re\left[\left(\frac{1}{i\omega - \mathbf{W}}\right)_{nm}\right](\mathcal{A}_{nn} - \langle \mathcal{A} \rangle_{eq}),\end{aligned} \tag{1.109}$$

We can now express the Fourier Transform of the two-times correlation function as:

$$\begin{aligned}S_{\mathcal{A},\mathcal{B}}(\omega) &= \sum_{mn} p_m^{eq}(\mathcal{B}_{mm} - \langle \mathcal{B} \rangle_{eq}) \times \\ &\times Re\left[\left(\frac{1}{i\omega - \mathbf{W}}\right)_{nm}\right](\mathcal{A}_{nn} - \langle \mathcal{A} \rangle_{eq}),\end{aligned} \tag{1.110}$$

which can also be written as:

$$S_{\mathcal{A},\mathcal{B}}(\omega) = \sum_{i=1}^{dim(H)} A(\lambda_i, T, B)\frac{\lambda_i}{\lambda_i^2 + \omega^2} \tag{1.111}$$

where $\lambda_i = \frac{1}{\tau_i^{QE}}$ are the eigenvalues of $-\mathbf{W}$. The Fourier Transform of the two-time correalation function is therefore given by a sum of lorentzians centered at zero frequency and with width $\lambda_i(T, B)$, and decays as a sum of exponentials with characteristic times τ_i^{QE}. Here the $A(\lambda_i, T, B)$ coefficients represent the weights of the possible lorentzians [61]. Each τ_i^{QE} refers to a particular spin-bath relaxation channel, given by the corresponding eigenstate $|w_i\rangle$ of $\mathbf{W}$: The composition of $|w_i\rangle$ in terms of the molecular eigenstates gives the complete relaxation path. Further information on the spin-bath dissipation channels is contained in the N level lifetimes τ_i^{life} defined as $\tau_i^{life} = [-W_{ii}]^{-1} = [\sum_j W_{j \leftarrow i}]^{-1}$: This is the inverse of the sum of all transition rates between the considered i level and all other ones according to the selection rules imposed by spin-bath interaction. The two sets of τ_i^{QE} and τ_i^{life} times contain complementary information on the QE part of relaxation dynamics.

Experimental Techniques

The coherent and time-reversible spin dynamics of MNMs described through Schrödinger equations only occur on very short timescales (usually ns or μs). In this time window, high frequency techniques such as inelastic neutron scattering probe the spin dynamics. Conversely, on longer timescales, the interactions of spins with other degrees of

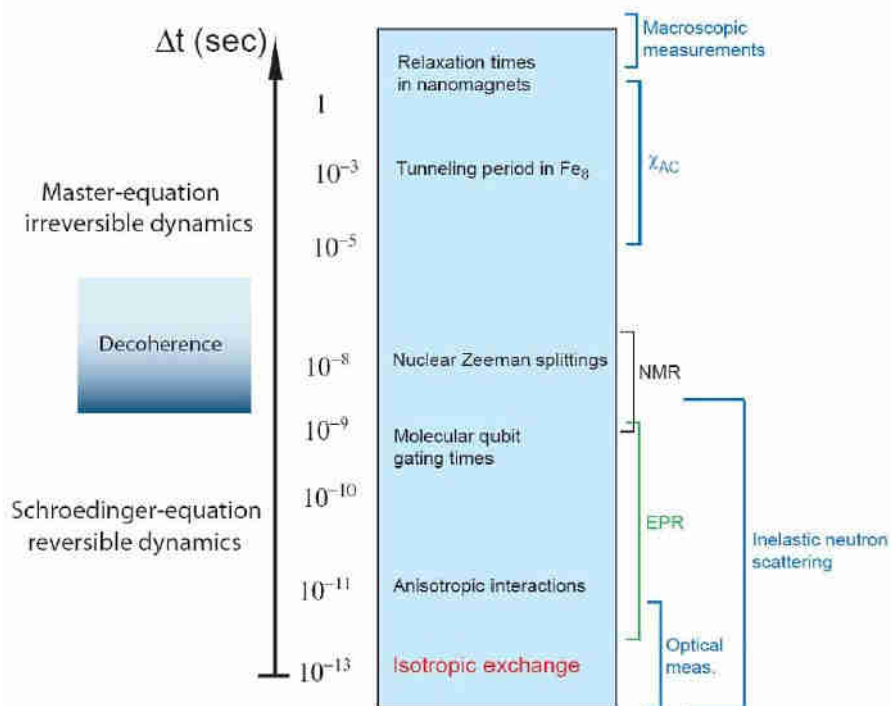**Figure 2.1:** Typical time scales of spin dynamics in MNMs. On the right side we report the main experimental techniques able to probe the spin dynamics in the respective time window.

freedom leads to an irreversible dynamics, described by master equations, and consequently to decoherence and relaxation phenomena. Relaxation dynamics in MNMs are probed by low-frequency techniques such as NMR or AC susceptibility, or, at even

longer timescales, from macroscopic measurements (see Fig. 2.1). In this Chapter we report a brief description of some of the main experimental techniques that can be applied to investigate both statical and dynamical properties of MNMs.

2.1 Inelastic Neutron Scattering

Inelastic Neutron Scattering (INS) is an experimental technique largely used to study spin dynamics of MNMs. It has many advantages respect to other spectroscopy techniques, since the energy spectrum of molecular clusters can be obtained from the transitions induced by interactions with neutrons, without the application of any external magnetic field. It also allows us to observe transition between different total-spin multiplets and the Q-dependence of the cross-section (where Q is the momentum transferred to the neutron during the scattering event) gives also information on the eigenfunctions of the system. From the analysis of INS experimental data is possible to extract all the parameters of the Spin Hamiltonians of MNMs (e.g. isotropic exchange and CF parameters). Furthermore, from high resolution INS experiments it is possible to extract the energy splitting induced by anisotropy effects. They have also proved to be sensitive enough to allow the determination of parameters related to spin operators with rank $k > 2$ [64]. Recently developed INS instruments also yields the four-dimensional inelastic-neutron scattering function in vast portions of reciprocal space and enables the spin dynamics to be determined directly. Indeed, measurements of the scattering function over a large solid angle of wave vectors in high-quality single crystals of MNMs permit to directly determine real-space dynamical two-spin correlations, which are the key quantities characterizing the magnetic dynamics [65].

2.1.1 Scattering by Magnetic Interactions

The magnetic scattering involves the interaction of the magnetic moment of a neutron with the magnetic field generated by the unpaired electrons of an atom. The relationship between the angular momentum of a particle and its magnetic moment is given by:

$$
\begin{aligned}
\hat{\mu}_e &= -\gamma\mu_B\hat{\sigma}, \\
\hat{\mu}_n &= -\gamma\mu_{nm}\hat{\sigma},
\end{aligned}
\tag{2.1}
$$

where μ_B and μ_{nm} are respectively the electronic and nuclear Bohr magnetons, $\underline{\sigma}$ are Pauli operators and γ are the gyromagnetic factors ($\gamma = -2$ for electrons and $\gamma = -1.91$ for neutrons). The unpaired electrons of an atom have both orbital and spin angular momenta. In the INS magnetic theory for MNMs we will only consider the spin angular momentum and *spin-only* magnetic scattering events. In fact magnetic ions in our investigated systems very often show a partial *quenching* of the orbital angular momentum, caused by crystal fields. Furthermore we often consider atoms where the unpaired electrons have wave functions localized around the atomic sites.

In the simple case of a single neutron with magnetic moment μ_n in presence of a magnetic field H, generated by the unpaired electrons of an atom, the Hamiltonian can be expressed as:

$$
\mathcal{H} = \frac{\hat{p}^2}{2m_n} - \hat{\mu}_n \cdot \mathbf{H}.
\tag{2.2}
$$

The first term represents the kinetic energy of the neutron, while the second term, which represents the magnetic interaction, can be written as $-\gamma\mu_{nm}\hat{\sigma} \cdot \mathbf{H}$. The magnetic field

generated by an electron moving with $\mathbf{v}_e$ is given by:

$$\mathbf{H} = \bigtriangledown \times \left(\frac{\hat{\mu}_e \times \mathbf{R}}{|\mathbf{R}|^3} \right) + \frac{-e}{c} \frac{\mathbf{v}_e \times \mathbf{R}}{|\mathbf{R}|^3}, \qquad (2.3)$$

where $\mathbf{R}$ is the distance between the electron and the point where we measure the field. Thus, the magnetic interaction becomes:

$$-\gamma \mu_{nm} \hat{\sigma} \cdot \mathbf{H} = \gamma \mu_{nm} 2 \mu_B \hat{\sigma} \cdot \bigtriangledown \times \left(\frac{\hat{\sigma}_e \times \mathbf{R}}{|\mathbf{R}|^3} \right) - \frac{e}{2 m_e c} \left(\hat{p}_e \cdot \frac{\hat{\sigma} \times \mathbf{R}}{|\mathbf{R}|^3} + \frac{\hat{\sigma} \times \mathbf{R}}{|\mathbf{R}|^3} \cdot \hat{p}_e \right), \quad (2.4)$$

where the first part is a dipolar term, while the second one represents the interaction with the neutron, due to the translational motion of the electron; $\hat{\sigma}_e$ and $\hat{p}_e$ represent respectively the spin and momentum operators of the electron.

   If we therefore take into account an INS experiment where the magnetic ions of the system interact magnetically with the neutron beam, the differential cross-section will be expressed as:

$$\frac{d^2\sigma}{d\Omega dE'} = \left(\frac{m}{2\pi\hbar^2} \right)^2 (2\gamma \mu_{nm} \mu_B)^2 \sum_{\lambda\lambda'\sigma\sigma'} \frac{k'}{k} p_\lambda p_\sigma \mid \langle \mathbf{k}'\lambda'\sigma'| \sum_i \hat{\sigma} \cdot \bigtriangledown \times \left(\frac{\sigma_i \times \mathbf{R}}{|\mathbf{R}|^3} \right) - \quad (2.5)$$

$$- \frac{1}{2\hbar} \left(\hat{p}_i \cdot \frac{\hat{\sigma} \times \mathbf{R}}{|\mathbf{R}|^3} + \frac{\hat{\sigma} \times \mathbf{R}}{|\mathbf{R}|^3} \cdot \hat{p}_i \right) |\mathbf{k}\lambda\sigma\rangle \mid^2 \delta(\hbar\omega + E_\lambda - E_{\lambda'}).$$

k and k' represent respectively the initial and final wave vectors of the neutron, $|\lambda\rangle$ and $|\lambda'\rangle$ are the initial and final state of the system with energies E_λ e $E_{\lambda'}$ and occupation probability of the initial state given by $p_\lambda = \frac{e^{-\beta E_\lambda}}{Z}$. $|\sigma\rangle$ and $|\sigma'\rangle$ are the initial and final polarization states of the neutron with initial occupation probability given by p_σ, while the Dirac Delta guarantees the energy conservation, being $\hbar\omega$ the energy gained/lost by the neutron in the interaction with the system. The summation over i in the interaction potential runs over all the lattice sites and over all the unpaired electrons of the system.

   The matrix elements of the magnetic interaction potential become [66]:

$$\langle \mathbf{k}'|\hat{\sigma} \cdot \bigtriangledown \times (\frac{\sigma_i \times \mathbf{R}}{|\mathbf{R}|^3})|\mathbf{k}\rangle \quad = 4\pi e^{i\mathbf{Q}\cdot\mathbf{r}_i} \sigma \cdot [\tilde{\mathbf{Q}} \times (\sigma_i \times \tilde{\mathbf{Q}})], \qquad (2.6)$$

$$\langle \mathbf{k}'|\hat{p}_i \cdot \frac{\hat{\sigma} \times \mathbf{R}}{|\mathbf{R}|^3}|\mathbf{k}\rangle \qquad = \frac{4\pi}{|\mathbf{Q}|} e^{i\mathbf{Q}\cdot\mathbf{r}_i} \hat{\sigma} \cdot (\tilde{\mathbf{Q}} \times \hat{p}_i),$$

where $\mathbf{r}_i$ is the position vector of the ith electron, $\mathbf{Q} = \mathbf{k} - \mathbf{k}'$ and $\tilde{\mathbf{Q}} = \frac{\mathbf{Q}}{|\mathbf{Q}|}$. If we define the operator:

$$\hat{Q}_\perp = \sum_i e^{i\mathbf{Q}\cdot\mathbf{r}_i} [\tilde{\mathbf{Q}} \times (\sigma_i \times \tilde{\mathbf{Q}}) - \frac{i}{\hbar|Q|} \tilde{\mathbf{Q}} \times \hat{p}_i], \qquad (2.7)$$

which shows how neutrons are sensitive only to the perpendicular component of the exchanged wave vector, the cross-section can be written as:

$$\frac{d^2\sigma}{d\Omega dE'} = \left(\frac{m}{2\pi\hbar^2} \right)^2 (2\gamma \mu_{nm} \mu_B)^2 (4\pi)^2 \sum_{\lambda\lambda'\sigma\sigma'} \frac{k'}{k} p_\lambda p_\sigma \times \qquad (2.8)$$

$$\times \langle \lambda\sigma|(\hat{\sigma} \cdot \hat{Q}_\perp)^+|\lambda'\sigma'\rangle\langle\lambda'\sigma'|\hat{Q}_\perp \cdot \hat{\sigma}|\lambda\sigma\rangle\delta(\hbar\omega + E_\lambda - E_{\lambda'}).$$

Since for non-polarized neutron $\sigma = \sigma'$ and

$$\sum_\sigma p_\sigma \langle|\hat{\sigma}_\alpha \hat{\sigma}_\beta|\sigma\rangle = \delta_{\alpha,\beta}, \qquad (2.9)$$

the differential cross-section becomes:

$$\frac{d^2\sigma}{d\Omega dE'} = \left(\frac{\gamma e^2}{m_e c^2}\right)^2 \frac{k'}{k} \sum_{\lambda\lambda'} p_\lambda \langle\lambda|\hat{Q}_\perp^+|\lambda'\rangle\langle\lambda'|\hat{Q}_\perp|\lambda\rangle \delta(\hbar\omega + E_\lambda - E_{\lambda'}). \tag{2.10}$$

Exploiting the identities:

$$\begin{aligned}
\hat{Q}_\perp &= \tilde{\mathbf{Q}} \times (\hat{Q} \times \tilde{\mathbf{Q}}), \\
\hat{Q}_\perp^+ \hat{Q}_\perp &= \sum_{\alpha\beta}(\delta_{\alpha,\beta} - \tilde{Q}_\alpha \tilde{Q}_\beta)\hat{Q}_\alpha^+ \hat{Q}_\beta,
\end{aligned} \tag{2.11}$$

where α and β run over x, y, z, we finally obtain:

$$\begin{aligned}
\frac{d^2\sigma}{d\Omega dE'} &= \left(\frac{\gamma e^2}{m_e c^2}\right)^2 \frac{k'}{k} \sum_{\alpha\beta}(\delta_{\alpha,\beta} - \tilde{Q}_\alpha \tilde{Q}_\beta) \sum_{\lambda\lambda'} p_\lambda \langle\lambda|\hat{Q}_\alpha^+|\lambda'\rangle\langle\lambda'|\hat{Q}_\beta|\lambda\rangle \times \\
&\times \quad \delta(\hbar\omega + E_\lambda - E_{\lambda'}).
\end{aligned} \tag{2.12}$$

As we have previously pointed out, several systems contain magnetic ions subjected to a *quenching* of the orbital angular momentum caused by the crystal fields, thus we only take into account *spin-only* scattering events. The operator $\hat{Q}$ is therefore given by:

$$\hat{Q} = \sum_d e^{i\mathbf{Q}\cdot\mathbf{R}_d} \sum_{\nu(d)} e^{i\mathbf{Q}\cdot\mathbf{r}_\nu} \hat{\sigma}_\nu, \tag{2.13}$$

where the sum over d runs over all the atomic sites with position vector $\mathbf{R}_d$ and the sum over ν runs over the unpaired electrons within each magnetic ion, with position vector $\mathbf{r}_\nu$. Due to the interactions between the unpaired electrons of the magnetic ions, we can define a total-spin S_d characterizing the state of the molecule. The matrix elements of the operator $\hat{Q}$ are found to be proportional to the total-spin operator $\mathbf{S_d}$:

$$\langle\lambda'|\hat{Q}|\lambda\rangle = \sum_d e^{i\mathbf{Q}\cdot\mathbf{R}_d} F_d(Q)\langle\lambda'|\hat{S}_d|\lambda\rangle, \tag{2.14}$$

where $F_d(Q)$ is the *form factor*, defined as the Fourier Transform of the spin density $\rho_s(\mathbf{r})$ associated to the ion on the dth site of the system:

$$F_d(Q) = \int e^{i\mathbf{Q}\cdot\mathbf{r}} \rho_s(\mathbf{r})d\mathbf{r}. \tag{2.15}$$

Therefore we find that the differential cross-section for the *spin-only* magnetic scattering has the following expression:

$$\begin{aligned}
\frac{d^2\sigma}{d\Omega dE'} &= \left(\frac{\gamma e^2}{m_e c^2}\right)^2 \frac{k'}{k} \sum_{\alpha\beta}(\delta_{\alpha,\beta} - \tilde{Q}_\alpha \tilde{Q}_\beta) \times \\
&\times \quad \sum_{\lambda\lambda'} p_\lambda \sum_{dd'} F_d^*(Q) F_{d'}(Q) e^{i\mathbf{Q}\cdot(\mathbf{R}_{d'}-\mathbf{R}_d)} \times \\
&\times \quad \langle\lambda|\hat{S}_d^\alpha|\lambda'\rangle\langle\lambda'|\hat{S}_{d'}^\beta|\lambda\rangle \delta(\hbar\omega + E_\lambda - E_{\lambda'}).
\end{aligned} \tag{2.16}$$

2.1.2   Cross-section for Powders Samples

INS experiments are often performed on powders samples of MNMs. In order to compare the experimental data with our theoretical calculations it is therefore necessary to find a theoretical expression of the differential cross-section averaged over all the possible orientations of the vector **Q** in respect to the reference system of the molecule. The formula obtained starting from Eq. 2.16 is [67]:

$$\frac{d^2\sigma}{d\Omega dE'} = \frac{A}{N_m}\frac{k'}{k}e^{-2W}\sum_{nn'}\frac{e^{-\beta E_n}}{Z}I_{nn'}(Q)\delta(\hbar\omega - E_{n'} + E_n), \tag{2.17}$$

where A is a constant, N_m the number of magnetic ions and e^{-2W} the Debye-Waller factor. The $I_{nn'}(Q)$ function is defined as:

$$
\begin{aligned}
I_{nn'}(Q) &= \sum_{ij}F_i^*(Q)F_j(Q)\{\frac{2}{3}[j_0(QR_{ij}) + C_0^2 j_2(QR_{ij})]\tilde{s}_{z_i}\tilde{s}_{z_j} + \\[2mm]
&+ \frac{2}{3}[j_0(QR_{ij}) - \frac{1}{2}C_0^2 j_2(QR_{ij})](\tilde{s}_{x_i}\tilde{s}_{x_j} + \tilde{s}_{y_i}\tilde{s}_{y_j}) + \\[2mm]
&+ \frac{1}{2}j_2(QR_{ij})[C_2^2(\tilde{s}_{x_i}\tilde{s}_{x_j} - \tilde{s}_{y_i}\tilde{s}_{y_j}) + C_{-2}^2(\tilde{s}_{x_i}\tilde{s}_{y_j} + \tilde{s}_{y_i}\tilde{s}_{x_j})] + \\[2mm]
&+ j_2(QR_{ij})[C_1^2(\tilde{s}_{z_i}\tilde{s}_{x_j} - \tilde{s}_{x_i}\tilde{s}_{z_j}) + C_{-1}^2(\tilde{s}_{z_i}\tilde{s}_{y_j} + \tilde{s}_{y_i}\tilde{s}_{z_j})]\}.
\end{aligned}
\tag{2.18}
$$

In $I_{nn'}(Q)$, R_{ij} gives the relative position of the magnetic ions i and j, while j_0 and j_2 are the spherical Bessel functions of 0th and 2nd-order respectively:

$$
\begin{aligned}
j_0 &= \frac{sin(QR_{ij})}{QR_{ij}}, \\[2mm]
j_2 &= \left(\frac{3}{QR_{ij}} - 1\right)\frac{sin(QR_{ij})}{QR_{ij}} - \frac{3cos(QR_{ij})}{QR_{ij}}.
\end{aligned}
\tag{2.19}
$$

The C_q^k are given by:

$$
\begin{aligned}
C_0^2 &= \frac{1}{2}\left[3(\frac{R_{ijz}}{R_{ij}})^2 - 1\right], \\[2mm]
C_2^2 &= \frac{R_{ijx}^2 - R_{ijy}^2}{R_{ij}^2}, \\[2mm]
C_{-2}^2 &= 2\frac{R_{ijx}R_{ijy}}{R^2 ij}, \\[2mm]
C_1^2 &= \frac{R_{ijx}R_{ijz}}{R^2 ij}, \\[2mm]
C_{-1}^2 &= \frac{R_{ijy}R_{ijz}}{R^2 ij}.
\end{aligned}
\tag{2.20}
$$

In the Eq. 2.18 there are also the matrix elements of spin operators, written on the basis set $|n\rangle$ of the total Spin Hamiltonian of the system:

$$\tilde{s}_{\alpha_i}\tilde{s}_{\gamma_j} = \langle n|s_{\alpha_i}|n'\rangle\langle n'|s_{\gamma_j}|n\rangle \qquad \alpha, \gamma = (x, y, z). \tag{2.21}$$

The spin operators in Eq. 2.18 are 1st-rank operators: This implies that the selection rules for the allowed magnetic transitions are: $\Delta S = 0, \pm 1$ and $\Delta M = 0, \pm 1$.

Eq. 2.18 represents a general form of the formula reported in [67] and it can be used whatever are the symmetry and the anisotropy of the investigated molecule [68]. If the molecule has an axial symmetry, we can only consider the terms where there are products as $\tilde{s}_{\alpha_i}\tilde{s}_{\gamma_j}$ with $\alpha = \gamma$ [67].

Instrumental resolution and Other Contributions

The implementation of Eq. 2.18 allows us to estimate the Spin Hamiltonian parameters and to find out the eigenstates involved in the detected magnetic transitions, by comparing the data with our theoretical calculations. However we have to take into account the resolution of the instrument, which very often has a gaussian form. We find that:

$$\delta(\hbar\omega - E_{n'} + E_n) \otimes R_{gauss} = R_{gauss}(\hbar\omega) = \frac{1}{\sigma\sqrt{2\pi}}e^{\frac{-(\hbar\omega - E_{n'} + E_n)^2}{2\sigma^2}}, \qquad (2.22)$$

where R_{gauss} is the instrumental resolution. The implemented expression for the cross-section is therefore given by:

$$\frac{d^2\sigma}{d\Omega dE'} = \frac{A}{N_m}\frac{k'}{k}e^{-2W}\sum_{nn'}\frac{e^{-\beta E_n}}{Z}I_{nn'}(Q)\frac{1}{\sigma\sqrt{2\pi}}e^{\frac{-(\hbar\omega - E_{n'} + E_n)^2}{2\sigma^2}}. \qquad (2.23)$$

To each magnetic peak is associated a gaussian function, whose width at half maximum equal to the instrumental resolution. σ is found by fitting the elastic peak with a gaussian function, to each of the considered wave-length:

$$f_{gauss}(x) = \frac{A_0}{\sigma_\lambda\sqrt{2\pi}}e^{\frac{-(x-x_0)^2}{2\sigma_\lambda^2}} + offset. \qquad (2.24)$$

Together with the inelastic peaks, INS data also contain an elastic and a quasi-elastic contributions. The elastic contribution is due to neutron diffraction, i.e. incident neutrons do not transfer/gain momentum Q to/from the sample ($k = k'$). Quasi-elastic neutron scattering is instead characterized by energy transfers being small compared to the incident energy of the scattered neutrons. In order to reproduce the experimental curves, it is therefore necessary to add to the inelastic cross-section a gaussian and a lorentzian function respectively for the elastic and quasi-elastic scattering:

$$f_{fitt}(\hbar\omega) = \frac{d^2\sigma}{d\Omega dE'} + \frac{A_0}{\sigma_\lambda\sqrt{2\pi}}e^{\frac{-(x-x_0)^2}{2\sigma_\lambda^2}} + \frac{P_0}{1 + (\frac{\hbar\omega - P_1}{P_2})^2}.$$

The parameters of the gaussian and lorentzian functions are different for each considered wave-length and temperatures.

2.1.3   IRIS Neutron Scattering Spectrometer @ ISIS

INS experiments have been performed at the ISIS pulsed Neutron and Muon Source of the Rutherford Appleton Laboratory (Didcot, UK) with the IRIS spectrometer. IRIS is a high-resolution quasi/in-elastic neutron spectrometer with high-resolution, long-wavelength diffraction capabilities [69]. It is an inverted or indirect geometry spectrometer, such that neutrons scattered by the sample are energy-analysed by means of Bragg scattering from a crystal-analyzer array. Since the neutron source is a pulsed one, the time-of-flight technique is used for data analysis. IRIS can be considered as consisting of two parts: The *primary* and the *secondary* spectrometer.

The Primary Spectrometer - Beam Transport

The *primary* spectrometer is illustrated in Fig. 2.2. The neutron beam transport from the moderator to the sample position, is achieved using a neutron guide. The majority of the guide section consists of accurately aligned nickel plated glass tubes (approx. 1m long), while it is terminated by a 2.5m-long converging nickel-titanium supermirror. The supermirror component not only helps focus the beam at the sample position, but also serves to increase the incident flux.
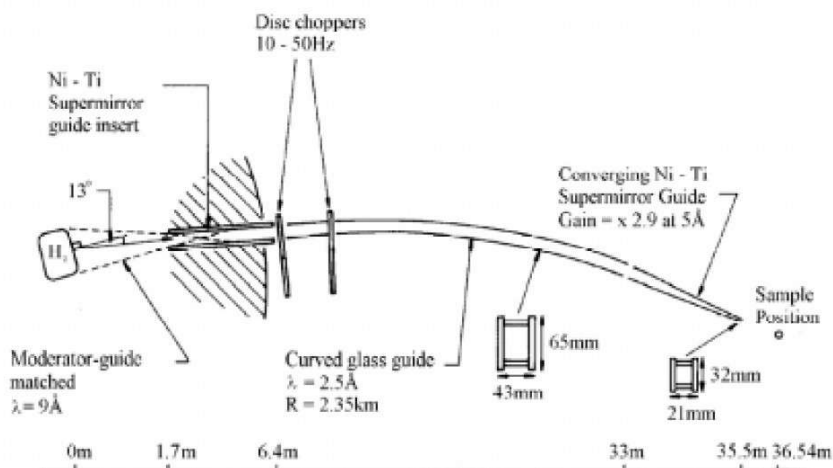
Figure 2.2: The IRIS primary spectrometer [69].

After leaving the moderator and depending upon the incident energy, each neutron either passes or is absorbed by one of the two disc-choppers. The two choppers are used to define the range of neutron wavelengths incident upon the sample during the experiment. They are located at 6.3 m and 10 m from the moderator respectively and operate at either 50, 25, 16.6 or 10Hz. The choppers themselves are constructed from neutron absorbing material, with a small adjustable aperture, through which neutrons may pass. The lower and the upper limits of the incident wavelength band are therefore defined by adjusting the chopper phases, and hence opening times of each aperture, respect to t_0 (the moment at which neutrons are produced by the target). Wavelength-bands selection effectively defines the energy resolution and energy-transfer range covered during an inelastic scattering experiment.

The Secondary Spectrometer

The *secondary* spectrometer (Fig. 2.3) consists of a 2 m diameter vacuum vessel containing two crystal analysers arrays (pyrolytic graphite, muscovite mica or fluorinated mica), two 51-element ZnS scintillator detector banks and a diffraction bank at $2\theta = 170°$ containing ten ^3He gas tubes. Incident and transmitted beam monitors are also located before and after the sample position respectively. The pyrolytic graphite analyzer bank is cooled to ~ 10 K to reduce background contributions from thermal diffuse scattering.
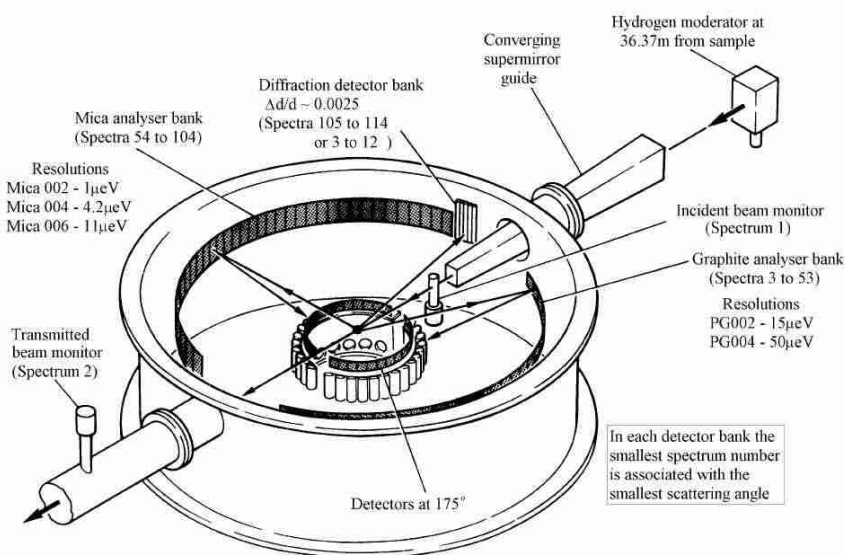
Figure 2.3: The IRIS secondary spectrometer [69].

Principle of Operation

During INS experiments, the scattered neutrons are energy-analysed by means of Bragg-scattering from a large array of single crystals. Only those neutrons with appropriate wavelength/energy to satisfy the Bragg condition are direct towards the detector bank. By recording the time of arrival of each analysed neutron in a detector relative to t_0, we can investigate the energy gain/loss processes occurring within the samples.
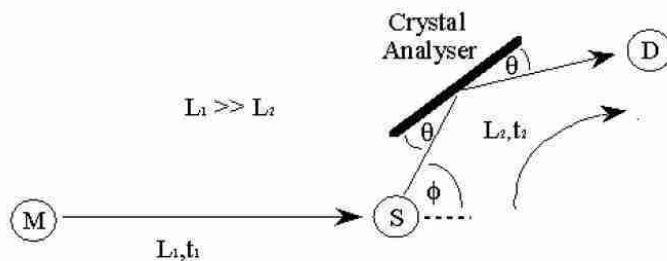
Figure 2.4: An indirect-geometry inelastic neutron scattering spectrometer [69].

The two disc-choppers are used to define the finite range of neutron energies incident

upon the sample (S):

$$E = \frac{1}{2}m_n v^2 \tag{2.25}$$

$$p = m_n v = \frac{h}{\lambda},$$

where m_n is the mass of the neutron. Consequently, the time-of-flight, t_1, of each neutron along the primary flight path L_1, is variable. However, since only those neutrons with a final energy E_2, that satisfy the Bragg condition

$$\lambda = 2dsin(\theta), \tag{2.26}$$

are scattered toward the detector bank D, Eqs. 2.25 and 2.26 can be re-written as:

$$
\begin{aligned}
E_2 &= \frac{1}{2}m_n\left(\frac{L_2}{t_2}\right)^2 = \frac{1}{2}m_n v^2 = \\
&= \frac{l}{2m_n}\left(\frac{h}{\lambda_a}\right) = \frac{l}{2m_n}\left(\frac{h}{2d_a sin(\theta)}\right),
\end{aligned}
\tag{2.27}
$$

where d_a is the d-spacing of the analyzing crystal.

The distance from he sample position to the detector bank (i.e. the secondary flight path L_2) is accurately known. Consequently, the time t_2, which is the time it takes for a detected neutron of energy E_2 to travel a distance L_2, can be calculated using:

$$t_2 = \frac{2m_n L_2 d_a sin(\theta)}{h} \tag{2.28}$$

Interactions within the sample lead to a loss/gain in neutron energy, thus a distribution of arrival times will result. By measuring the total time-of-flight $t = t_1 + t_2$, having an accurate knowledge of t_2, L_1 and L_2, the energy exchange within the sample can be determined:

$$\Delta E = E_1 - E_2 = \frac{1}{2}m_n\left[\left(\frac{L_1}{(t-t_2)}\right)^2 + \left(\frac{L_2}{t_2}\right)^2\right]. \tag{2.29}$$

2.2   Nuclear Magnetic Resonance

Magnetic resonance is a phenomenon found in magnetic systems that possess both magnetic moments and angular momentum. As we will see, the term *resonance* implies that we are in tune with a natural frequency of the magnetic system, in this case corresponding to the frequency of gyroscopic precession of the magnetic moment in an external static magnetic field. Because of the analogy between the characteristic frequencies of atomic spectra, and because the magnetic resonance frequencies fall typically in the radio frequency region (for nuclear spins) or microwave frequency (for electron spins), we often use the terms *radio frequency* for the *nuclear magnetic resonance (NMR)* or *microwave spectroscopy* for the *electronic paramagnetic resonance (EPR)*.

Nuclear moments are much smaller than electronic moments, being $\frac{\mu_B}{\mu_N} \approx 10^3$, where μ_B and μ_N are the Bohr and nuclear magnetons respectively. In fact, if the two-level system given by a single proton with $I = \frac{1}{2}$ is taken into account, the two states $m_I = +\frac{1}{2}$ and $m_I = -\frac{1}{2}$ are separated by an energy $\Delta E = \gamma_N \mu_N B$, with γ_N the proton gyromagnetic ratio, which is tiny. For a proton in a typical laboratory magnetic field $B_0 \approx 1$ T the

splitting between $m_I = +\frac{1}{2}$ and $m_I = -\frac{1}{2}$ would be $\approx 10^{-7}$ eV, which is equivalent to a temperature ≈ 1 mK. Therefore at room temperature and at magnetic fields of the order of 1 T, the nuclei will show only a minute tendency to line up with the applied magnetic field on average, in account of the thermal randomizing energy, much greater than the alignment energy. As a result, any effect due to the magnetism of the nuclei requires a resonance technique such as NMR to be detected.

Spin dynamics in MNMs can be probed by NMR. In fact, as we will see in the following sections, there exists a link between the electronic spins fluctuations due to their interactions with phonons and the measured longitudinal spin-lattice relaxation rate $\frac{1}{T_1}$ of ^{1}H nuclei [70, 71]. Furthermore, due to their hyperfine interactions with all the internal fields generated by the unpaired electrons in the molecule, other nuclei with $I \neq 0$, such us ^{53}Cr and ^{19}F, can be considered a powerful local probe of magnetic properties in MNMs.

In the following we report a brief introduction to magnetic resonance in order to better understand both NMR and EPR phenomena, considering a simple quantum mechanical description [72].

2.2.1 Simple Resonance Theory

A nucleus may consist of many particles coupled together so that in any given state the nucleus posses a total magnetic moment μ and a total angular momentum $\mathbf{I}$, such as:

$$\mu = \gamma \mathbf{I}, \tag{2.30}$$

where γ is the nuclear the gyromagnetic ratio. Within the quantum mechanic framework, μ and $\mathbf{I}$ are treated as (vectors) operators. Thus we can define the angular momentum operator as:

$$\hat{\mathbf{I}} = \hbar \mathbf{I}. \tag{2.31}$$

$\hat{\mathbf{I}}^2$ then has eigenvalues $I(I+1)$, where I can be integer or half-integer. The components I_z commutes with $\hat{\mathbf{I}}^2$ and its eigenvalues m may be any of the $2I + 1$ values $-I, ..., +I$. The relation between the magnetic moment and the nuclear angular momentum can thus be expressed as:

$$\langle Im | \mu_{x'} | Im' \rangle = \gamma \hbar \langle Im | I_{x'} | Im' \rangle, \tag{2.32}$$

where $\mu_{x'}$ and $I_{x'}$ are the components of μ and $\mathbf{I}$ along the arbitrary x' direction.

The application of an external magnetic field $\mathbf{H} = \mathbf{H_0}\hat{\mathbf{z}}$ produces an interaction energy of the nucleus given by the Zeeman Hamiltonian:

$$\mathcal{H} = -\mu \cdot \mathbf{H} = -\gamma \hbar H_0 I_z, \tag{2.33}$$

with eigenvalues

$$E = -\gamma \hbar H_0 m. \tag{2.34}$$

To detect the presence of such a set of energy levels we have to exploit spectral absorption. What is needed is to have an interaction that can cause transitions between levels. To satisfy the conservation of energy, the interaction must be time dependent and of such an angular frequency

$$\hbar \omega = \Delta E, \tag{2.35}$$

where ΔE is the energy difference between the initial and final nuclear Zeeman energies. In order to induce the magnetic resonance, an alternating magnetic field is applied

perpendicular to the static field, which therefore adds a perturbative term to the Hamiltonian:

$$\mathcal{H}_1 = -\gamma \hbar H_x^0 I_x cos(\omega t). \tag{2.36}$$

The operator I_x, being a 1st-rank tensor (vector) operator, permits transitions only between levels adjacent in energy ($m \rightarrow m \pm 1$), holding $\hbar\omega = \Delta E = \gamma \hbar H_0$ or $\omega = \gamma H_0$.

Let us suppose now to have a macroscopic system of $I = \frac{1}{2}$ nuclei. Since there are many nuclei in the system, we specify the number of nuclei in the two possible $m_I = +\frac{1}{2}$ ($|+\rangle$) and $m_I = -\frac{1}{2}$ ($|-\rangle$) states with N_+ and N_- respectively. The probability per unit time of a transition between $|+\rangle$ and $|-\rangle$ induced by $\mathcal{H}_1$ is given by:

$$|\langle +|I_x|-\rangle|^2 = |\langle -|I_x|+\rangle|^2 \tag{2.37}$$

and is independent of whether the transition is from the lower to the upper level or vice versa, and occurs at a rate W which is proportional to the size of the RF power used in $\mathcal{H}_1$ to excite transitions. If $N_-(t)$ is the number of spins in the lower level at a time t, $WN_-(t)$ will be the number of spins excited per unit time to the higher level. A similar consideration can be done for the spins in the higher level, thus having

$$\frac{dN_+}{dt} = WN_-(t) - WN_+(t) \tag{2.38}$$

$$\frac{dN_-}{dt} = WN_+(t) - WN_-(t).$$

By defining $n(t) = N_+(t) - N_-(t)$, the solution of the two equations above can be written as:

$$n(t) = n(0)e^{-2Wt}, \tag{2.39}$$

which means that an initial difference in population tends exponentially towards zero in account of a stimulated electromagnetic transition. At a time t the energy of the system is:

$$E(t) = N_- E_- + N_+(E_- + \hbar\omega) \tag{2.40}$$

with rate of absorption given by

$$\frac{dE}{dt} = WN_+(t)\hbar\omega - WN_-(t)\hbar\omega = \hbar\omega Wn(t) \tag{2.41}$$

and will tend to zero with a time constant of $\frac{1}{2W}$, as the populations of the upper and lower levels become progressively equalized. This implies that it is necessary to have a population difference for the system to absorb energy.

Nuclear spins also interact with the thermal motion and excitations of the sample. Thus, once the perturbation $\mathcal{H}_1$ is switched-off and the absorption of energy is over, the polarization of the spin system will return back to the equilibrium value following a Boltzmann distribution:

$$\left(\frac{N_-}{N_+}\right)_0 = e^{\frac{-\Delta E}{KT}} = e^{\frac{-\gamma \hbar H_0}{KT}}. \tag{2.42}$$

As a result, the polarization would tend to the Boltzmann distribution as

$$n(t) = n_0(1 - e^{\frac{-t}{T_1}}), \tag{2.43}$$

where T_1 is called *spin-lattice relaxation time* and measures the time constant of the interaction of the nuclei with the environment [72, 73].

We may now combine the two rate equations for $n(t)$ to find the transition rate due to both thermal processes and transitions induced by the alternating field:

$$\frac{dn}{dt} = -2Wn(t) + \frac{n_0 - n(t)}{T_1},$$ (2.44)

which has a stationary solution when $dn(t)/dt = 0$, leading to:

$$n(t) = \frac{n_0}{1 + 2WT_1}$$ (2.45)

and

$$\frac{dE}{dt} = n(t)\hbar\omega W = n_0 \hbar\omega \frac{W}{1 + 2WT_1}.$$ (2.46)

From the above equation it follows that the rate of absorption is proportional to W, but for large perturbing alternating field becomes proportional to $\frac{1}{T_1}$ and independent of the precise value of W: This is known as saturation.

In a typical NMR experiment, the weak polarization of nuclear spins produced by an applied magnetic field $\mathbf{H_0}$-e.g. along z-axis- is destroyed by the RF excitations induced by the alternating field in $\mathcal{H}_1$. Once the RF field is switched-off, the weak interactions of the nuclei with the surroundings will force the nuclear magnetization to the equilibrium value with a time constant T_1. As a consequence, we expect that:

$$\frac{dM_z}{dt} = \frac{M_0 - M_z}{T_1},$$ (2.47)

with $M_z = \gamma\hbar n(t)/2$ and M_0 is the thermal equilibrium magnetization. The magnetization M is also driven by torque due to the magnetic field $\mathbf{H_0}$ to precess around its direction, thus having:

$$\frac{dM_z}{dt} = \frac{M_0 - M_z}{T_1} + \gamma(\mathbf{M} \times \mathbf{H}_0)_z.$$ (2.48)

Furthermore we wish to express the fact that in thermal equilibrium under a static field, the magnetization will wish to be parallel $\mathbf{H_0}$. That is, the x- and y-components must have a tendency to vanish. Thus

$$\frac{dM_x}{dt} = \gamma(\mathbf{M} \times \mathbf{H}_0)_x - \frac{M_x}{T_2}$$ (2.49)
$$\frac{dM_y}{dt} = \gamma(\mathbf{M} \times \mathbf{H}_0)_y - \frac{M_y}{T_2},$$

where T_2 is the *spin-spin relaxation time* and causes differences in precession frequency due to interactions of the observed spin with the spins of its neighbors. It can also be due to inhomogeneities of the applied magnetic field $\mathbf{H_0}$. Eqs. 2.48 and 2.49 are known as the *Bloch Equations*. A microscopic explanation of Bloch Equations will be given in Par. 2.2.3.

2.2.2　Nuclear Hamiltonian and Hyperfine Interactions

The generalized Hamiltonian for a system of nuclear magnetic moments in presence of an applied magnetic field is given by:

$$\mathcal{H}_{nuclear} = \mathcal{H}_{Zee} + \mathcal{H}_{n-n} + \mathcal{H}_{n-e} + \mathcal{H}_{EFG},$$ (2.50)

where the first term is the Zeeman coupling between the nuclei and the applied magnetic field. The other three terms represents the so-called sources of *internal fields*, which can cause a sizeable spread and/or shift of the resonance conditions. The second term describes the classical nucleus-nucleus dipolar interaction, given by:

$$\mathcal{H}_{n-n} = \frac{1}{2} \sum_j \sum_k \left[\frac{\mu_j \cdot \mu_k}{r_{jk}^3} - \frac{3\left(\mu_j \cdot \mathbf{r}_{jk}\right)\left(\mu_k \cdot \mathbf{r}_{jk}\right)}{r_{jk}^5} \right], \tag{2.51}$$

where the nuclear moments are $\mu_j = \gamma_N \hbar \mathbf{I}$ and $\mathbf{r}_{jk}$ is the distance between nuclei j and k. The local dipolar field at each nuclear site due to all the other surrounding nuclei may either add or be opposite to the applied magnetic field, resulting in a spread of the resonance condition over a range of $\sim 1 \div 10$ Gauss. The evaluation of the line shape and width in presence of nuclear dipolar interaction is based on the theory of the second and higher moments by Van Vleck [73].

The last two terms account respectively for the *hyperfine interactions*, the coupling between the nuclear and electronic magnetic moments, and the interactions between the nuclear quadrupolar moment (which is non-zero only if $I > 1/2$) and the electric field gradient due to non-spherical charge distribution surrounding the nucleus.

Hyperfine interactions

When the electrons belong to atoms far away form the nuclear site, their contribution to the hyperfine field can be calculated through the classical expression of the magnetic dipolar contribution, evaluated within the point-dipole approximations:

$$H_{n-e}^{dip} = -\frac{\mu_0}{4\pi} \left(\frac{\mu_e \cdot \mu_n}{r^3} - \frac{3\left(\mu_e \cdot \mathbf{r}\right)\left(\mu_n \cdot \mathbf{r}\right)}{r^5} \right), \tag{2.52}$$

where $\mathbf{r}$ is the distance between the moments. Since the two dipole moments are different, this interaction can be described as a local magnetic field generated at the nuclear site by the thermal average of the electronic moment $\langle \mu_e \rangle$ [73]:

$$H_{loc} = \langle \mu_e \rangle \frac{1 - 3\cos^2\theta}{r^3}, \tag{2.53}$$

where θ is the angle between the vector $\mathbf{r}$ and the quantization axis along the applied magnetic field.

When the nuclear and the electronic magnetic moments belong to the same atom or to different atom whose electronic wavefunctions have a non-zero overlap, the point-dipole approximation doesn't hold anymore and the hyperfine interaction term must therefore be averaged over the electronic wavefunction. We have a *direct hyperfine interaction* if the magnetic moments belong to the same atoms and a *transferred hyperfine interaction* if they belong to different atoms. Let us consider the Hamiltonian in Eq. 2.50 for a single nucleus, neglecting the nucleus-nucleus interaction $\mathcal{H}_{n,n}$, the classical dipolar contribution of $\mathcal{H}_{e-n}$ and $\mathcal{H}_{EFG}$:

$$\mathcal{H}_{nuclear} = -\gamma_N \hbar \sum_{i=x,y,z} I_i H_{0,i} + \sum_{j=1}^{N} \mathbf{I} \cdot \mathbf{A}_j \cdot \langle \mathbf{s}_j \rangle. \tag{2.54}$$

The first term is the Zeeman interaction with the external magnetic field, while the second term describes the hyperfine field due to the nearby electronic magnetic moments

(labeled by the index $j = 1, ..., N$). The quantity $\mathbf{A}_j$ is called *hyperfine ctensor* and it represents the strength of the coupling between the nuclear spin and the jth electronic moment. The term $\langle \mathbf{s}_j \rangle$ is the thermal average of the electronic spin of the jth electron. The coupling constant for the direct hyperfine interaction between a nucleus and an electron described by the wavefunction ψ is given by:

$$A_\psi = \frac{2}{5} g \mu_B \gamma_N \hbar \langle \frac{1}{r^3} \rangle_\psi,$$ (2.55)

where $\langle \frac{1}{r^3} \rangle_\psi$ is the expectation value of the operator $\frac{1}{r^3}$ over the electronic state ψ. Eq. 2.55 is characteristic of p-type wavefunctions and doesn't hold for s-type ones. This problem has been overcome by E. Fermi [74] by a renormalization procedure, leading to the *direct contact* hyperfine constant:

$$A_s = \frac{8}{3} \pi g \mu_B \gamma_n \hbar \left| \psi(0) \right|_s^2$$ (2.56)

where $\left| \psi(0) \right|_s^2$ is the normalized probability of finding an s electron at the nuclear site.

The transferred hyperfine interaction occurs when the atom to which the nucleus belongs binds to a magnetic atom. The overlap between the electronic wavefunctions involved in the bond partially polarizes the formerly $S = 0$ electronic shells yielding a non-zero hyperfine field at the nucleus. The ith component of the transferred hyperfine constant can be written as:

$$A_i = A_t + A_\sigma \left(3 \cos^2 \theta_{i,\sigma} - 1 \right) + A_\pi \left(3 \cos^2 \theta_{i,\pi} - 1 \right),$$ (2.57)

where $i = x, y, z$. The constant A_t accounts for the isotropic contribution due to the s-electrons polarization. The anisotropic terms $A_\sigma \left(3 \cos^2 \theta_{i,\sigma} - 1 \right)$ and $A_\pi \left(3 \cos^2 \theta_{i,\pi} - 1 \right)$ describe the contribution due to p_σ and p_π bonds. The angles $\theta_{i,\sigma}$ and $\theta_{i,\pi}$ are the angles between the directional p bonds and i the axis. The anisotropic contribution to the transferred hyperfine field is often much smaller than the isotropic term and it can be therefore often neglected.

For a general review of the hyperfine interactions in magnetic materials we refer the reader to the seminal paper by Freeman and Watson, Ref. [75].

2.2.3   Redfield Theory

Thermal fluctuations of the electronic spins are responsible for fluctuations in the hyperfine dipolar field and thus for the nuclear spin-lattice relaxation. The spin lattice relaxation rate $1/T_1$ is therefore a powerful probe of the electronic relaxation times τ_i^{QE} in MNMs. By the same density matrix formalism applied in Section 1.2 to the spin-phonon coupling, it is possible to describe the behavior of nuclei interacting with electronic spins, in the presence of an external magnetic field, i.e. NMR experiments. We follow the theory of relaxation processes of Redfield [71], which is closely related to the treatment of relaxation due to Wangsness and Bloch [76], to describe an ensemble of non-interacting nuclei in an external static magnetic field, coupled to the perturbative fluctuating field produced by electronic spins. This fluctuating field is different at each nuclear site, thus for each nucleus we have:

$$\mathcal{H}_{nuclear} = \mathcal{H}_0 + \mathcal{H}_1(t) == -\gamma_N \hbar H_0 I_z - \gamma_N \hbar \mathbf{H}_{hyp}(t) \cdot \mathbf{I},$$

where H_0 is the static magnetic field along the z-axis, the Larmor frequency is given by $\omega_L = \gamma_N H_0$ and $\mathbf{H}_{hyp}(t)$ is the fluctuating hyperfine field:

$$\mathbf{H}_{hyp}(t) = -\hbar\gamma_e \sum_{i=1}^{N} \frac{1}{r_i^3} \left[\delta\mathbf{s}_i(t) - 3\mathbf{r}_i \left(\frac{\delta\mathbf{s}_i(t) \cdot \mathbf{r}_i}{r_i^2} \right) \right]. \tag{2.58}$$

The index i labels the N magnetic ions, $\mathbf{s}_i$ represents their spin operators, $\mathbf{r}_i$ their distances from the proton and $\delta\mathbf{s}_i(t) = \mathbf{s}_i(t) - \langle\mathbf{s}_i\rangle$. In Redfield's theory of relaxation processes [71] it is assumed that the ensemble average of the Hamiltonian $\mathcal{H}_1(t)$ vanishes, i.e. $\mathcal{H}_1(t)$ doesn't produce an average frequency shift. If this is not so, it's possible to redefine $\mathcal{H}_0$ in order to include the very-small average shift $\langle\mathcal{H}_1\rangle$. For this reason the Hamiltonian $\mathcal{H}_1(t)$ responsible for the nuclear relaxation in Eq. 2.58 contains fluctuations $\delta\mathbf{s}(t)$ and not $\mathbf{s}(t)$.

To interpret NMR data, we have to describe the time evolution of the expectation values $\langle I_r \rangle$ of the x, y and z components of the nuclear spins:

$$\frac{d\langle I_r\rangle}{dt} = \sum_{\alpha,\alpha'} \frac{1}{\hbar} [\rho, \mathcal{H}_0]_{\alpha\alpha'} \left(\alpha'|I_r|\alpha \right) + \sum_{\alpha,\alpha',\beta,\beta'} R_{\alpha\alpha',\beta\beta'} \rho_{\beta\beta'} \left(\alpha'|I_r|\alpha \right), \tag{2.59}$$

where the first term is the driving term of Bloch equations describing the torque due to the external field, while the second one describes the relaxation dynamics through the relaxation matrix $R_{\alpha\alpha',\beta\beta'}$. By exploiting the secular and Markov approximations, the Redfield theory yields exponential time-decays of the longitudinal and transverse nuclear magnetization with characteristic rates given respectively by [72]:

$$\frac{1}{T_1} = \gamma_N^2 \left[k_{xx}(\omega_L) + k_{yy}(\omega_L) \right], \tag{2.60}$$

$$\frac{1}{T_2} = \frac{1}{2T_1} + \gamma_N^2 k_{zz}(0), \tag{2.61}$$

where $k_{qq}(\omega)$ is the Fourier transform of the correlation function of Eq. 2.58 ($q = x, y, z$) given by

$$k_{qq}(\omega) = \frac{1}{2} \int_{-\infty}^{+\infty} \overline{H_{hyp,q}(t)H_{hyp,q}(t+\tau)} e^{-i\omega t} d\tau, \tag{2.62}$$

which can be calculated in terms of the Fourier transform of the cross correlation functions in Eq. 1.111). These formulas hold if $T_1, T_2 \gg 2\pi/\omega_L$ (secular regime) and T_1, T_2 are longer than the electronic relaxation times (Markov regime). In addition, fluctuations of the three components of $\mathbf{H}_{hyp}$ are assumed independent. The last assumption is not correct when the hyperfine field has a dipolar origin as in the present case. We have calculated the generalized coupled differential equations for the decay of the nuclear magnetization. We have numerically checked that in the experimental conditions of this work it is still possible to decouple the equations as in Redfield's theory and calculate the relaxation rates as in Eqs. 2.60 and 2.61. Taking as inputs the positions of the magnetic ions and nuclei in the molecule, we can calculate the $1/T_1$ and $1/T_2$ of a MNM as:

$$\frac{1}{T_1} = \sum_{\substack{i,j=1,N \\ p,p'=x,y,z}} C_{i,j}^{p,p'} \left[\mathcal{S}_{s_i^p,s_j^{p'}}(\omega_L) + \mathcal{S}_{s_i^p,s_j^{p'}}(-\omega_L) \right], \tag{2.63}$$

$$\frac{1}{T_2} = \frac{1}{2T_1} + \sum_{\substack{i,j=1,N \\ p,p'=x,y,z}} K_{i,j}^{p,p'} \left[\mathcal{S}_{s_i^p,s_j^{p'}}(0) \right], \qquad (2.64)$$

where the $C_{i,j}^{p,p'}$ and $K_{i,j}^{p,p'}$ are geometric coefficients of the hyperfine dipolar interaction between magnetic ions and nuclei [70].

2.3 Electron Paramagnetic Resonance

Electron paramagnetic resonance (EPR) is a powerful spectroscopic technique to study systems containing atoms or molecules with unpaired electrons (such as transitions ions, lanthanides and radicals) [3]. It is very similar to the NMR technique, since both deal with the interaction between electromagnetic radiation and magnetic moments, but in the case of EPR, the magnetic moments arise from electrons rather than nuclei. EPR spectroscopy induces transitions between $|SM\rangle$ states of the Spin Hamiltonian of a MNM, which have been split by an external magnetic field. It provides information on the chemical environment of the paramagnetic center(s) in the molecule, which are associated to the spectroscopic splitting tensor $\mathbf{g}$, the zero-field splitting tensor $\mathbf{D}$ and its related local parameters d_i and e_i, described in Chapter 1. An important information which can be obtained from the EPR spectra is the anisotropy of these tensors. It can be obtained directly not only from experiments performed on single crystals but also from systems in which the tumbling rate of the paramagnetic centers is slow compared to the EPR time-scale and all the orientations of the magnetic molecules are present (as in polycrystalline powders). Furthermore, we will consider only the EPR spectra of magnetically non-diluted systems, where the hyperfine structure is wiped out by the dipolar and exchange interactions between the magnetic centers and is not experimentally available.

In order to understand EPR experiments we can refer to the simple resonance theory described in Section 2.2.1, substituting the nuclear magnetic moments with those of the electrons. For a static magnetic field parallel to the z axis of the $\mathbf{g}$ tensor, in the case of an electronic spin multiplet with S = 1/2, the transition energy between the levels with $m = -1/2$ and $m = 1/2$ is given by:

$$\hbar\omega = g_z \mu_B H. \qquad (2.65)$$

The resonances are in the microwave range, and in this spectral region it is difficult to continuously sweep frequency over a large range. Therefore the resonance is measured by using a fixed frequency and sweeping the magnetic field. In general an EPR spectrum is rather complex, with lines due to different electronic transitions. The magnetic field at which these lines occur alter with the frequency of the applied radiation and, if anisotropy is present, it will also depend on the orientation of the the external magnetic field with respect to the crystal axes. Therefore the Spin Hamiltonian formalism, which was originally introduced to understand EPR spectra, is a powerful theoretical model which gives a complete description of the experimental data taking into account both the magnetic field dependence and anisotropy effects.

Eq. 2.65 is sufficient for multiplets S if the zero field splitting is absent. In Fig. 2.5 we show the spectra of polycrystalline powders of a compound with $S = 1/2$ and anisotropic $\mathbf{g}$.

For $g_x = g_y = g_z$ only one line is observed like in a single crystal. For $g_x = g_y = g_\perp; g_z = g_{//}$ two features are observed, that corresponding to $g_{//}$ being less intense because the crystallites with the z axis parallel to the applied field are less numerous than
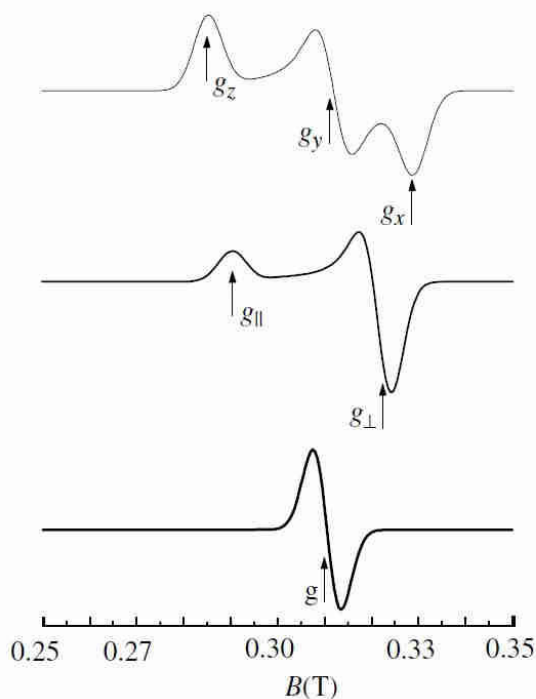
Figure 2.5: Polycrystalline powder EPR spectra of a system with $S = 1/2$ characterised by $g_x \neq g_y \neq g_z$ (top), $g_x = g_y \neq g_z$ (middle), and isotropic g value (bottom)[2].

those with the x or y axes parallel to the field. For $g_x \neq g_y \neq g_z$ three lines are observed. The three g values are easily obtained from the spectra, but it is impossible to know their orientation in the molecular frame. For this, single-crystal experiments are needed. When $S \geq 1$ additional splitting of the energy levels and consequently additional lines in the EPR spectra may appear, due to the effects of the crystal field. Furthermore, if we are not in the strong exchange limit, we have to consider the generalized Spin Hamiltonian in order to take into account also those electronic transitions which involve levels belonging to different total-spin multiplets.

2.3.1   Interpretation of EPR Spectra

Following the linear-response theory [50], given a time-dependent perturbation $\mathcal{H}_1 = -\hat{A}f(t)$ with $\hat{A}$ hermitian operator, we find that the absorption observed in a resonance experiment is proportional to the imaginary or absorptive part of the susceptibility:

$$\chi''_{AA} = \pi \sum_{\alpha,\alpha'} \langle\alpha|A^\dagger|\alpha'\rangle\langle\alpha'|A|\alpha\rangle(n_\alpha - n_{\alpha'})\delta(\hbar\omega - \Delta_{\alpha\alpha'}), \qquad (2.66)$$

where $\Delta_{\alpha\alpha'} = E_{\alpha'} - E_\alpha$ and n_α is the Boltzmann population of the eigenstate $|\alpha\rangle$ of the unperturbed Hamiltonian $\mathcal{H}_0$. The term $\langle\alpha|A^\dagger|\alpha'\rangle\langle\alpha'|A|\alpha\rangle$ in Eq. 2.66 represents the *transition intensity* between the energy levels α and α'. In an EPR experiment the time-dependent perturbation $\mathcal{H}_1$ is the microwave oscillating magnetic field, perpendicular

to the applied static magnetic field **H**. EPR measurements are very often performed on polycrystalline powders. An EPR powder spectrum can be considered as the summation of the spectra corresponding to every orientation $\{\theta, \phi\}$ of the applied magnetic field direction with respect to the principal coordinate system of the EPR center. If we take into account this orientation dependence, the transition intensities between two energy levels n and m are given by [77, 78]:

$$
\begin{aligned}
I_{nm} &= (1 - \sin^2\theta \cos^2\phi) S^*_{x,nm} S_{x,nm} + \\
&- \sin^2\theta \sin\phi \cos\phi \left[S^*_{x,nm} S_{y,nm} + S^*_{y,nm} S_{x,nm} \right] + \\
&- \cos\theta \sin\theta \cos\phi \left[S^*_{x,nm} S_{z,nm} + S^*_{z,nm} S_{x,nm} \right] + \\
&+ (1 - \sin^2\theta \sin^2\phi) S^*_{y,nm} S_{y,nm} + \\
&- \cos\theta \sin\theta \sin\phi \left[S^*_{y,nm} S_{z,nm} + S^*_{z,nm} S_{y,nm} \right] + \\
&+ (\sin^2\theta) S^*_{z,nm} S_{z,nm},
\end{aligned}
\tag{2.67}
$$

with $S_{k,nm} = \langle n|S_k|m \rangle$, where $|n\rangle$ and $|m\rangle$ are the eigenvectors corresponding to levels n and m respectively and S_k is a total-spin operator S_x, S_y or S_z. With Eq. 2.67 we can reproduce the EPR absorbance spectrum of our system for a given $\{\theta, \phi\}$ direction as a function of the applied magnetic field. In order to compare the powders data with our theoretical calculations we have to spherically average over all the possible directions $\{\theta, \phi\}$. Furthermore, the experimental data are usually reported as the derivative of the absorbance, thus we have to derive the so obtained results. We will therefore find the resonance fields where the derivative of absorbance shows a zero (corresponding to a peak in the absorbance spectrum). The broadening of the lineshape of EPR resonance peaks is mainly due to hyperfine interactions of electronic spins with the surrounding nuclei, which decrease the life times of the initial and final states of the transitions through relaxation mechanisms. If for instance we consider a gaussian line-shape LS_{gauss} we have:

$$
\delta(\hbar\omega - \Delta_{\alpha\alpha'}) \otimes LS_{gauss} = LS_{gauss}(\hbar\omega) = \frac{1}{\sigma\sqrt{2\pi}} e^{\frac{-(\hbar\omega - \Delta_{\alpha\alpha'})^2}{2\sigma^2}},
\tag{2.68}
$$

2.4   X-Rays Magnetic Circular Dichroism

Due to its high sensitivity and its chemical selectivity, X-rays absorption (XAS) and X-ray magnetic circular dichroism (XMCD) are powerful techniques to measure the magnetic properties of MNMs also grafted on surfaces as thin or monolayers. XAS provide a unique probe of the electronic and magnetic properties of transition-metal ions with sensitivity down to sub monolayer coverage. The intensity, lineshape and polarization dependence of dipole-allowed 2p→3d transitions give element-selective information about the spin state, oxidation and crystal field. Therefore XMCD is a very powerful tool to study magnetic anisotropy in MNMs. In the following a simple X-ray absorption theory is provided.

The properties of 3d-electrons are best probed in an X-ray absorption experiment by excitation of 2p core electrons to unfilled 3d states as illustrated in Fig. 2.6. In principle, L-edge X-ray absorption spectra contain contributions from both p→d and p→s transitions, but in practice the p→d channel dominates. The sum of the line intensities, denoted I(L$_3$) and I(L$_2$), respectively, is directly proportional to the number of d holes (see Fig. 2.6-a), through the so-called sum rules (see following section).

The use of circularly polarized X-rays allows to study anisotropy effects of transition metal ions. The underlying physics is usually explained within the framework of
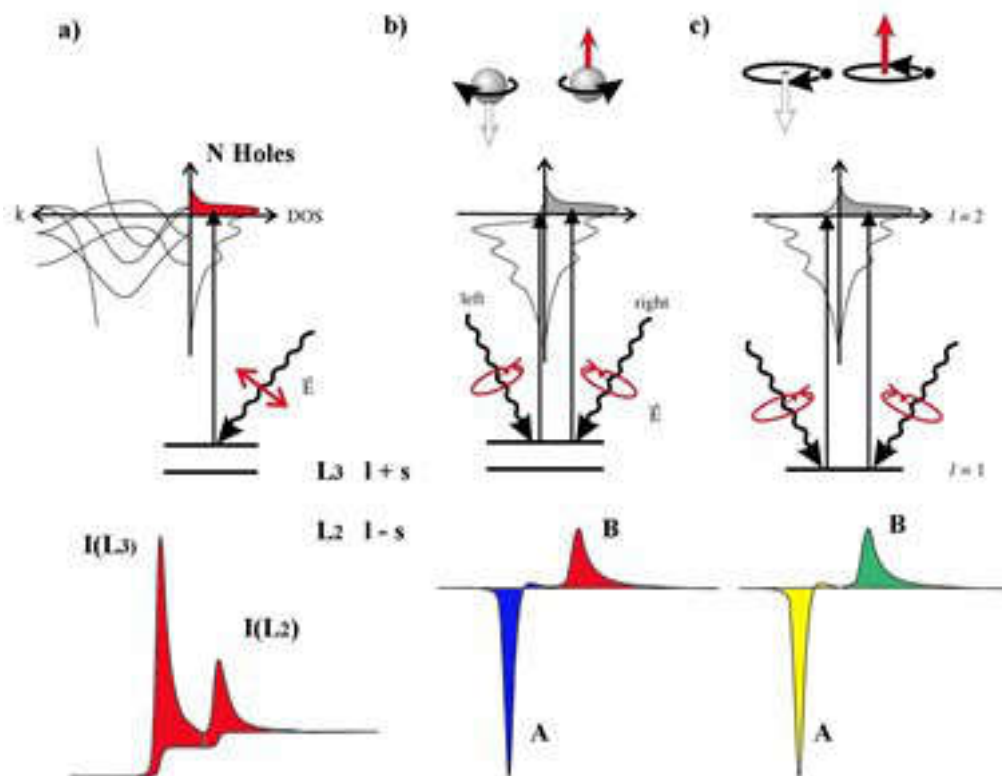
Figure 2.6: Electronic transitions in conventional L-edge X-ray absorption, (b) and (c) X-ray magnetic circular dichroism for spin and orbital moments respectively, illustrated in a one-electron model [79].

the following two-step picture. In the *first step*, right or left circularly polarized photons transfer their angular momentum, $+\hbar K$ and $-\hbar K$, respectively, to the excited photoelectron. If the photoelectron originates from a spin-orbit split level, e.g. the $p_{3/2}$ level (L_3 edge), the angular momentum of the photon can be transferred in part to the spin through the spin-orbit coupling. Right circularly polarized photons transfer the opposite momentum to the electron than left circularly polarized photons, and hence photoelectrons with opposite spins are created in the two cases. Since the $p_{3/2}(L_3)$ and $p_{1/2}(L_2)$ levels have opposite spin-orbit coupling (l+s and l-s, respectively), the spin polarization will be opposite at the two edges. In the first (absorption) step, spin-up and spin-down are defined relative to the photon helicity or photon spin.

The magnetic properties enter in the *second step*. Since spin flips are forbidden in electric dipole transitions, spin-up (spin-down) photoelectrons from the p core shell can only be excited into spin-up (spin-down) d hole states. Therefore, the spin-split valence shell acts as a detector for the spin of the excited photoelectron. The quantization axis of the detector is given by the magnetization direction which, for maximum dichroism effect, needs to be aligned with the photon spin direction. As illustrated in Fig. 2.6 we

shall denote the differences of the line intensities recorded with right and left circular polarization, i.e. the XMCD intensities, as A (L_3 edge) and B (L_2 edge), respectively. Note that A and B have opposite sign, reflecting the opposite spin-orbit coupling of the $p_{3/2}$ and $p_{1/2}$ levels. Sum rules link the spin moment quantitatively to the measured intensity A-2B, as discussed below. Similarly, if the d valence shell possesses an orbital moment, as shown in Fig. 2.6-c, it will act as an orbital momentum detector for the excited photoelectron. By summing over the L_3, i.e. (l+s), and L_2, i.e. (l-s), intensities it is apparent that the spin s is eliminated and one measures the orbital moment of the valence shell. This is expressed by the orbital moment sum rule which links the orbital moment in the d shell to the dichroism intensity A+B. For more detailed reviews on XAS and XMCD refer to Ref.[79].

2.4.1   Sum Rules

The usual XMCD analysis is based on the exploitation of the so-called sum rules, which, in principle, enable the element- and shell-specific measurement of the orbital and of the spin moments separately. Yet, the effective application of these rules faces several drawbacks: The non-negligible presence of the magnetic dipole term, the evaluation of the correct number of 3d holes, and the problem of the j-j mixing effect [80, 81, 82]. Therefore, in order to verify the applicability of sum rules to MNMs, it is important to test them on benchmark samples and to compare with theoretical results. For instance, the validity of the sum rules for Cr_8 [82], Cr_7Ni [83], Cr_xInNi [84] and Cr_2Cu [26] has already been discussed and verified. The mean value of the spin (m_S) and orbital (m_O) moments (along the z direction) from XMCD data can be calculated as:

$$
\begin{aligned}
\frac{m_O}{\mu_B} &= -\frac{4qN_{eff}}{3r} \\
\frac{m_S}{\mu_B} &= -\frac{(6p-4q)N_{eff}}{r}Sc + \frac{7\langle T_Z \rangle}{\mu_B},
\end{aligned}
\tag{2.69}
$$

where r is the integral of the whole absorption spectrum, A and B are the intensities of the dichroic signal at the L_3 and L_2 edges, respectively, and p = A and q = A + B, N_{eff} is the number of effective 3d-holes and $\langle T_Z \rangle$ takes into account magnetic dipolar effects [80]. S_C is a spin correction factor which takes into account the partial L_2 and L_3 mixing.

Molecular Magnets with Competing AF Interactions

A new route in molecular magnetism is based on magnetically frustrated MNMs. In fact, geometrical magnetic frustration is at the origin of many exotic phenomena [85]. It occurs when the presence of competing interactions forbids the simultaneous minimization of all individual two-spin terms [86], as it happens in an antiferromagnetically-coupled system of three spins in a triangle. MNMs with competing antiferromagnetic (AF) interactions can display geometrical frustration, but the effects of frustration on their static and dynamical properties are still largely unexplored. They also represent ideal systems to study the interplay between frustration and quantum effects due to their zeroth-dimensional character [87]. Magnetically frustrated MNMs have also been proposed for technological applications in magnetocaloric refrigeration (see Chapter 4), due to their large energy degeneracies and hence large field-induced entropy variations.

An interesting example is provided by the "Moebius strip" odd-membered Cr_8Ni AF ring [88], where a large number of frustrated classical spin configurations coalesce quantum mechanically into a single nondegenerate ground state, with the spins resonating among these energetically equivalent classical states. Another famous example of frustrated MNMs is Fe_{30}, a large molecule where the 30 Fe^{3+} (s = 5/2) ions occupy the vertices of an icosadodecahedron and experience nearest-neighbor AF coupling. Interesting physical properties characterize this mesoscopic system [28, 29], but unfortunately exact calculations are not possible because of the large Hilbert space.

In this Chapter we focus on four different MNMs with competing AF interactions: Ni_7 (Sec. 3.1), Fe_6, Mn_6 (Sec. 3.2) and Fe_7 (Sec. 3.3). A great advantage of these clusters is their relatively small Hilbert space compared to other frustrated clusters (e.g. Fe_{30}), which allow us to perform exact calculations. In these systems a complex spectrum with low-spin ground state, large degeneracies and/or many low-lying excited levels results from competing AF interactions [87]. The consequences on their static magnetic behavior are discussed in the following. We also investigate the effect of frustration on relaxation dynamics of Ni_7 and Fe_7.

3.1 Magnetic Properties and Relaxation Dynamics of a Frustrated Ni_7 Molecular Nanomagnet

In this Section we focus on Ni_7 [89], a frustrated MNM, whose core consists of a pair of corner-sharing tetrahedra (see Fig. 3.1). Its structure resembles a piece of bulk pyrochlores, which are characterised by spins on a lattice of corner-sharing tetrahedra, and where frustration may lead to large ground state degeneracies [90, 91]. As we will show, also in Ni_7 frustration leads to large degeneracies in the energy spectrum which cause unusual static and dynamical magnetic properties. The consequences of the spectral

structure on the magnetocaloric effect will also be discussed in view of possible applications of frustrated MNMs in magnetic refrigeration.
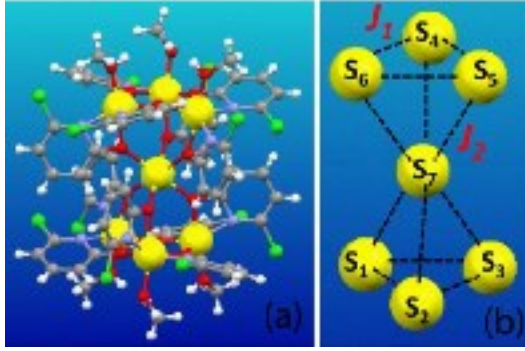

Figure 3.1: (a) The molecular structure of Ni$_7$ (red: O, white: H, grey: C, cyan: N, green: Cl). The large yellow spheres represent Ni ions. Oxygen ions transmit antiferromagnetic superexchange interactions between adjacent Ni ions. (b) The magnetic core of Ni ions arranged on two corner-sharing tetrahedra. Dashed lines represent exchange interactions. Two different exchange constants characterize the interaction between spins in the external triangles (J$_1$) and between the central and the external spins (J$_2$).

Each Ni^{2+} ion in the Ni$_7$ cluster is described in terms if its total spin s = 1 (the orbital moment being nearly quenched) and in the Hamiltonian 1.1 only the leading interactions are considered: Anisotropic terms are neglected and isotropic exchange is limited to nearest neighbors, for which oxygen bonds provide effective superexchange bridges. Anisotropy is expected to produce fine effects, some of which are discussed in Section 3.1.3 assuming a typical strength for local crystal fields. The exchange interaction is parametrized by two constants J$_1$ and J$_2$ describing respectively the coupling within the two external triangles and with the central spin (Fig. 3.1). The gyromagnetic tensors g$_i$ are assumed diagonal and isotropic, which is normally a good approximation. The Hamiltonian then reduces to:

$$\mathcal{H} = J_1 \left[\mathbf{s}_1 \cdot \mathbf{s}_2 + \mathbf{s}_2 \cdot \mathbf{s}_3 + \mathbf{s}_1 \cdot \mathbf{s}_3 \right] + J_1 \left[\mathbf{s}_4 \cdot \mathbf{s}_5 + \mathbf{s}_5 \cdot \mathbf{s}_6 + \mathbf{s}_4 \cdot \mathbf{s}_6 \right] + \tag{3.1}$$
$$+ J_2 \left[\mathbf{s}_7 \cdot \sum_{i=1}^{6} \mathbf{s}_i \right] - g\mu_B \mathbf{B} \cdot \sum_{i=1}^{7} \mathbf{s}_i,$$

and can be analytically diagonalized by choosing the following basis states:

$$|S_{12} S_A S_{45} S_B S_{AB} S M\rangle = |\tilde{S} S M\rangle. \tag{3.2}$$

The quantum numbers in this coupling scheme refer to the total squared spin of the pairs (1, 2) and (4, 5) (e.g. $\mathbf{S_{12}^2} = [\mathbf{s_1} + \mathbf{s_2}]^2 = \mathbf{S_{12}}(\mathbf{S_{12}} + \mathbf{1})$, the total squared spin of the upper triangle (S$_A$), of the lower triangle (S$_B$), of the two triangles (S$_{AB}$) and of the whole molecule (S), whereas M refers to the z component of the total spin. On the basis of the molecule's structure we expect J$_1$ and J$_2$ to be positive (antiferromagnetic) and of a similar order of magnitude. The gyromagnetic factor for Ni^{2+} is usually slightly larger than 2.

3.1.1   Magnetization

The temperature dependence of the magnetic susceptibility was measured on microcrystalline powders (squares in Fig. 3.2). A fitting of the calculated magnetic susceptibility χ to experimental data yields J_1 = 18 K, J_2 = 26 K and g = 2.2, and in the following we will use these values. For the fitting procedure we have exploited the *Van Vleck* formula [47]:

$$\chi(T) = \frac{1}{Z}\frac{\mu_B^2 N_A g}{3K_B T} \sum_i e^{-\beta E_i} S_i \left(S_i + 1\right) \left(2S_i + 2\right),\qquad (3.3)$$

where Z is the partition function, E_i are the eigenvalues of Eq. 3.1 with total-spin S_i.
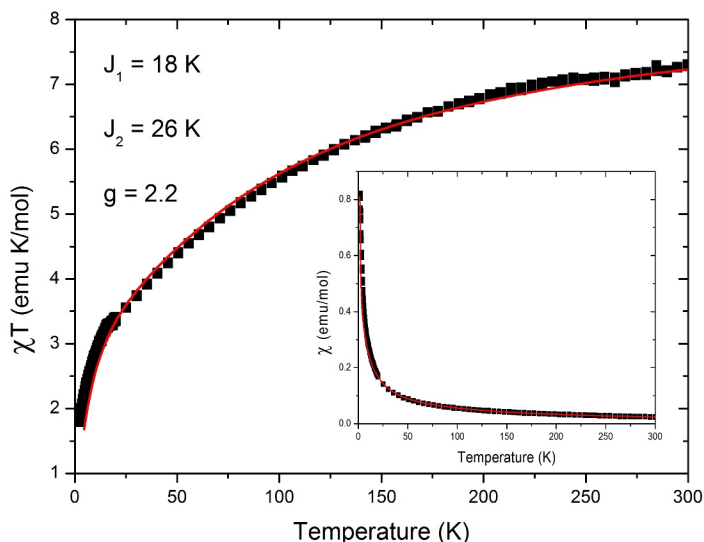

Figure 3.2: Calculated (line) and measured (squares) temperature dependence of χT and χ (inset). The parameters used in Eq. 3.1 are J_1 = 18 K, J_2 = 26 K and g = 2.2.

The corresponding spectrum is shown Fig. 3.3. The ground manifold comprises nine multiplets of total spin S = 1, for a total 27 levels. At high T the square of the effective molecular moment χT tends to that of seven non-interacting spins. The decrease by lowering T reflects the AF character of the couplings, and as T $\rightarrow$ 0 the molecule responds like a single moment $g\mu_B S$ with S = 1.

While the zero-field susceptibility does not display any specific feature associated with the frustrated geometry, the latter causes an unusual magnetization process in finite fields. The field splits the multiplets into their M components as illustrated in Fig. 3.4.

While in nanomagnets field-induced crossings usually involve a pair of levels, resulting in a staircase magnetization process with equal jumps, a characteristic feature of frustrated systems like Ni$_7$ is the presence of ground state level crossings involving more than two levels. For instance, 25 levels cross at $B_C \approx 6.8$ T: Nine $|S = 1, M = 1\rangle$, twelve $|S = 2, M = 2\rangle$ and four $|S = 3, M = 3\rangle$ states. This situation is caused by the linear dependence on S of the zero-field energies of the lowest S = 1–3 manifolds (Fig. 3.3). The resulting magnetization experiences a double jump by $2g\mu_B$ at B_C (see Fig. 3.5), while the usual two-level crossings yield jumps by $g\mu_B$.
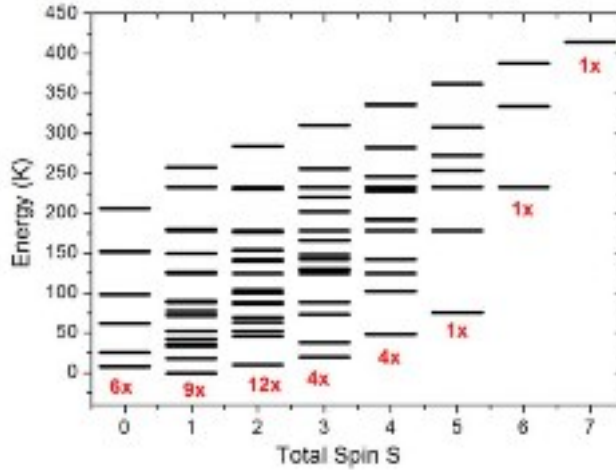
Figure 3.3: Spectrum of Eq. 3.1 for $J_1 = 18$ K, $J_2 = 26$ K and $B = 0$. The $3^7 = 2187$ energy levels are arranged into multiplets of given total spin S with degeneracy $2S + 1$. Several distinct multiplets with the same value of S are degenerate due to frustration. The numbers indicate the number of these multiplets for the lowest group of states for any given S. For instance, the ground manifold has S = 1 and includes nine distinct multiplets, for a total degeneracy of 27.
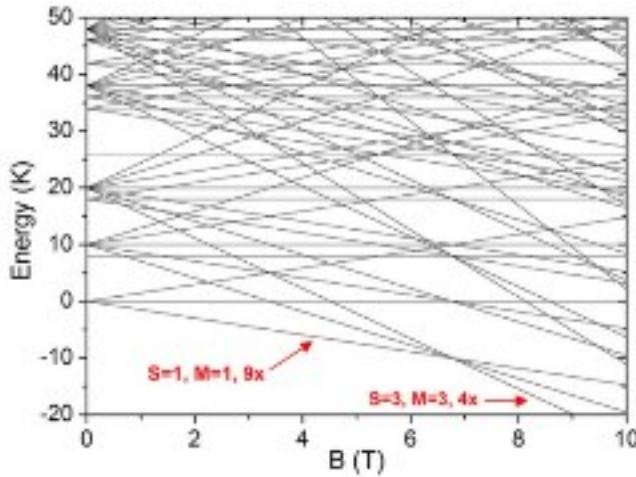
Figure 3.4: Field dependence of the lowest-lying levels of Eq. 3.1. The field removes the degeneracy on M, but not that between different multiplets. Thus, the ground state between 0 and 6.8 T is ninefold-degenerate.

We have also calculated the magnetization of the cluster as a function of the applied magnetic field: :

$$M(B) = -\mu_B \sum_{i=1}^{7} g_i \left(\langle s_{i,x} \rangle \sin(\theta) \cos(\phi) + \langle s_{i,y} \rangle \sin(\theta) \sin(\phi) + \langle s_{i,z} \rangle \cos(\theta) \right), \qquad (3.4)$$

Figure 3.5: Calculated field dependence of the magnetization per molecule at T = 0 K. Note the two anomalous jumps by $2g\mu_B$ at B = 6.8 and 19 T. The inset focuses on the first of these jumps and shows that it is still well recognizable in a realistic experimental condition, T = 0.3 K.

where the thermal average of single-ion spin operators are evaluated as

$$\langle s_{i,k}\rangle = \frac{1}{Z}\sum_{j=1}^{N}\langle j|s_{i,k}|j\rangle e^{-\beta E_j(B)}. \tag{3.5}$$

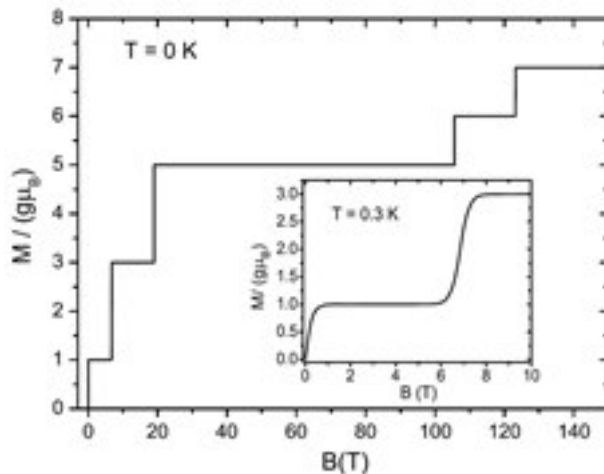We would like to stress that for the an isotropic Hamiltonian as the one in Eq. 3.1 the magnetization doesn't depend on the orientation (θ, ϕ) of the applied magnetic field. Ni_7 magnetization displays a plateau between B = 19 and 105 T. This plateau also exists for $J_1 = J_2$, and it is wider the larger J_2/J_1. It is associated with the large exchange gap between the lowest S = 5 and the lowest S = 6 sets of manifolds (Fig. 3.3). The plateau is a sort of molecular counterpart of the well-known plateaus characterizing some bulk systems with magnetic frustration such as pyrochlores [87, 92]. It is interesting to compare the behavior of Ni_7 with that of the highly studied frustrated nanomagnets with icosado-decahedral symmetry. For the latter a triple jump in the magnetization is theoretically predicted for large fields close to the saturation field [29] and it can be interpreted in terms of a multiple crossing between a set of states with independent localized magnons (in a ferromagnetic background) and the fully ferromagnetic state. In Ni_7 this type of multiple crossing near saturation is missing, the double jumps occur at low field and do not correspond to a simple picture of localized excitations.

3.1.2 Magnetocaloric effect

The method of adiabatic demagnetization has been successfully used over the last decades to reach temperatures in a sub-Kelvin range. This technique relies on the thermal response of a magnetic system to an adiabatic variation of the applied field. Such a response can be quantified in terms of the so-called cooling rate:

$$\mathcal{R} = \left(\frac{\partial T}{\partial B}\right)_S = -\frac{T}{C(T,B)}\left(\frac{\partial S(T,B)}{\partial B}\right)_T, \tag{3.6}$$

where C is the magnetic specific heat. In the simplest case of an ideal paramagnetic salt, isentropic curves in a T–B plane are straight lines (S = S(T/B)) and $\mathcal{R}$ = T/B. Hence, during adiabatic demagnetization T decreases linearly with B. In order to obtain a large cooling power the density and the size of these paramagnetic moments should be maximized, but residual interactions between different moments set a limit to the reachable power. Interactions alter the simple shape of the paramagnetic isentropic curves and, for large-enough densities, eventually cause magnetic phase transitions. The transition temperature sets a lower bound to the lowest temperatures achievable with paramagnetic salts.
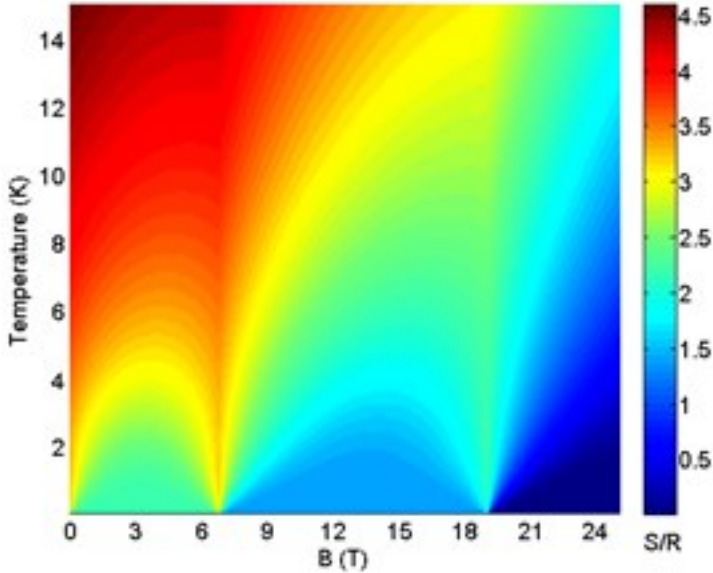

Figure 3.6: Intensity plot showing the value of the magnetic entropy S as a function of T and B. The two crossings causing double magnetization jumps at B_C = 6.8 and 19 T lead to a large cooling rate $\mathcal{R}$ for B_C. $\mathcal{R}$ can be visually estimated by the slope of isentropic (i.e. isocolour) lines.

The main objective in the field of magnetic refrigeration is to find an optimal material with high cooling rate down to very low temperatures, where this technique has its major applications. One possibility is to consider bulk compounds with frustrated magnetic interactions, as frustration may keep the system a paramagnet (albeit not a simple one) as T → 0 [93]. Another possibility is to exploit the superparamagnetism of nanosized magnetic particles [94]. Magnetically frustrated nanomagnets may offer at the same time the advantages of general frustrated systems (i.e. the large degeneracies and hence the potentially large field-induced entropy variations) and those of nanomagnets (i.e. the lack of complex cooperative behavior and the high degree of flexibility in the chemical synthesis). This issue has been investigated in [45] for model Hamiltonians describing nanomagnets of icosahedral symmetry, for which an enhanced magnetocaloric effect with high cooling rates is predicted in the vicinity of the saturation field. In the case of Ni_7 one might exploit the crossings involving double magnetization jumps (e.g. the one at B_C = 6.8 T in Fig. 3.4), where several levels meet and hence a large modulation of the entropy is produced by a small variation of B near Bc. Indeed, Fig. 3.6 shows that $\mathcal{R}$ is particularly large close to B_C = 6.8 T and 19 T, for instance $\mathcal{R}$ = 6.3 K T^{-1} on the

isoentropic path with S = 3 (values of $\mathcal{R}$ for paramagnetic salts are typically below 2 K T^{-1}). With respect to systems like Fe$_{30}$, for which the fields useful for magnetocaloric applications are large, being near the saturation field [45], here relatively small fields are exploited. Thus, the system looks promising even if a precise estimation of the actual usefulness would require fixing the precise type and size of the small anisotropic terms in the Spin Hamiltonian, which have been neglected here. Indeed, such terms may produce fine splittings dependent on the direction of B (see Section 3.1.3) which modify the shape of the isoentropic curves as T $\to$ 0. By tentatively assuming the form of anisotropy described in Section 3.1.3 one finds that cooling rates remain satisfactory, of the order of a few K T^{-1}, and depend on the field direction.

For a deeper investigation on the magnetocaloric effect in MNMs and their applications for magnetic refrigeration see Chapter 4.

3.1.3 Quantum oscillations of the total spin

Small anisotropic terms in the Spin Hamiltonian, which have been neglected in Eq. 3.1, may produce remarkable quantum effects at field-induced level crossings. There is at present no experimental determination of the anisotropy in Ni$_7$ as large-enough single crystals have not yet been produced. Considering the C$_3$ symmetry of the molecule, the dominant effects of magnetic anisotropy can be described by adding to Eq. 3.1 an axial term of the form

$$\mathcal{H}_{CF} = d_1 \sum_{i=1}^{6} s_{i,z}^2 + d_2 s_{7,z}^2 \tag{3.7}$$

where the z axis is parallel to the C$_3$ axis. Higher-order single-ion axial terms have vanishing matrix elements because s = 1 for the Ni^{2+} ions. In the following we assume d$_1$ = d$_2$ = d$_{CF}$ = -1 K, which is a reasonable value for Ni^{2+} in a distorted octahedral environment. Fig. 3.7 illustrates the effect of this axial term on the energy levels of Ni$_7$. Each multiplet is split into a singlet (M = 0) and one or more doublets (M = $\pm$q) and the degeneracy between different spin multiplets is partially removed. In particular, the presence of CF anisotropy has important consequences close to the ground state crossing fields B$_c$. Fig. 3.7 shows that for a generic direction of B these crossings turn into anti-crossings (ACs). The AC splittings reflect the fact that at the AC field the involved states are superpositions of different total-spin states. Physically, quantum oscillations of the length of the total spin take place [95], i.e. at the AC field the total spin of each molecule oscillates along the direction of the applied field. These oscillations occur also at zero temperature and are absent in the classical version of the model. Interestingly, the frequency of these quantum oscillations can be tuned by changing the direction of the applied field and can be made much larger than the expected decoherence frequency. This phenomenon has been investigated in AF rings [95] and grids [24] where it involves a conventional crossing between a single pair of levels whose total spin S differs by one. Here, conversely, at B$_C$ = 6.8 and 19 T the ACs involve many levels belonging to spin multiplets with S differing also by two. For instance, Fig. 3.7 shows that the AC at 6.8 T involves many degenerate levels having total spin ranging from S = 1 to 3. The presence of these ACs could be demonstrated by macroscopic single-crystal torque measurements as the ACs cause marked peaks in the field dependence of the magnetic torque at the B$_c$ [96]. Fig. 3.8 demonstrates that in Ni$_7$ these peaks could be easily detected experimentally. Torque is the tendency of the magnetic field to rotate the magnetization and it's given by

$$\tau = \mathbf{M} \times \mathbf{B}. \tag{3.8}$$
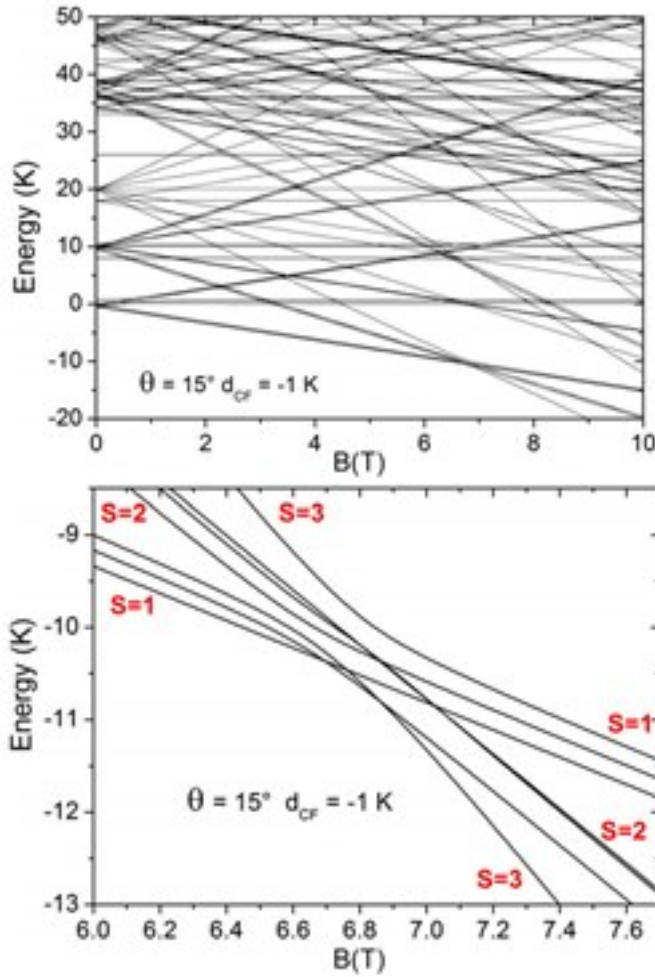
Figure 3.7: Field dependence of the lowest-lying levels of Eq. 3.1 in presence of the crystal field term in Eq. 3.7. The field makes an angle of 15° with the anisotropy axis. The bottom panel shows a zoom onto the anticrossing region. Labels identify the dominating component of eigenfunctions.

In the case of Ni$_7$ we assume to apply the field in the xz-plane, thus the torque is given by:

$$\tau_y = B\left(M_z \sin(\theta) - M_x \cos(\theta)\right) \tag{3.9}$$

Torque measurements allow one to have a macroscopic evidence of the quantum oscillations of the length of the total-spin at the ACs fields, since it is proportional to the magnetic response perpendicular to the direction of the applied magnetic field. If the field is applied along the z-axis, the torque is proportional to $\langle S_x \rangle$, the thermal average of the x component of the total-spin of the cluster. Since oscillations of the length of the total-spin do reflect on $\langle S_x \rangle$ and thus on the magnetization, the torque will display a peak at the ACs fields.

Figure 3.8: Field dependence of the magnetic torque calculated for different directions of B. θ is the angle between the applied field and the anisotropy axis z (see the main text).
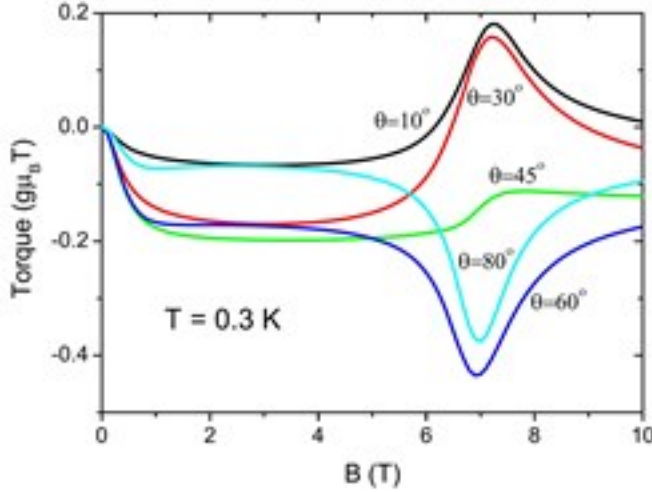
3.1.4 Relaxation dynamics

The relaxation dynamics in MNMs is described by Eqs. 1.102 and 1.104 (see Section 1.2), which imply a multi-exponential relaxation to equilibrium with n possible characteristic times $\tau_i = \frac{1}{\lambda_i}$, n being the dimension of the Hilbert space (n = 2187 in Ni$_7$) [61]. The frequencies λ_i are the eigenvalues of the rate matrix in Eq. 1.104. The specific relaxation paths which characterize the dynamics depend on the starting out-of-equilibrium configuration (setting the initial condition $\rho_{mm}(t=0)$ in Eqs. 1.102), but also on the specific observable monitored during relaxation. We have already discussed in Section 1.2.3 that relaxation dynamics can be described in terms of the equilibrium dynamical cross-correlation between the fluctuations of two generic observables $\mathcal{A}$ and $\mathcal{B}$. A particularly important case in MNMs is $\mathcal{A} = \mathcal{B} = \mathcal{M}$, with $\mathcal{M}$ the total molecular magnetization. Its time autocorrelation could be directly probed by macroscopic AC-susceptibility measurements, which can sense relaxation times longer than about 10^{-4}s. Relaxation times in a generic MNM are usually too fast for AC susceptibility, but system-specific dynamical correlation functions can be sensed indirectly by μSR or NMR techniques through the longitudinal relaxation time of nuclear (or muon) spins (see Section 2.2). In the following we focus on the case $\mathcal{A} = \mathcal{B} = \mathcal{M}$. A multi-exponential relaxation yields in frequency space a sum of Lorentzians as in Eq. 1.111:

$$S_{\mathcal{M},\mathcal{M}}(\omega) = \sum_{i=1}^{dim(H)} A(\lambda_i, T, B) \frac{\lambda_i}{\lambda_i^2 + \omega^2} \qquad (3.10)$$

Fig. 3.9 shows that, for a typical value of γ in Eq. 1.104 [61], for B $\rightarrow$ 0 and T between 1 and 10 K the frequencies having appreciable weights $A(\lambda_i, T, B)$ in Eq. 3.10 are roughly in the range 10^{-10}– 10^{-5} THz, corresponding to times τ_i between 10 ms and 100 ns. The large degeneracies associated with frustration make the spectrum in Fig. 3.9 atypical. In most MNMs a single frequency dominates at low T, meaning that fluctuations in $\mathcal{M}$ decay through a single relaxation path. By increasing T, more and more frequencies get

appreciable weight. Conversely, Ni$_7$ displays already at low T a band of nearly equally weighted frequencies whose value increases by increasing T as $\omega_0 exp\left(-\Delta/K_BT\right)$. This is a fingerprint of a multi-step Arrhenius relaxation process crossing an energy barrier Δ. Unlike SMMs, where Δ in the (single) Arrhenius process is the anisotropy barrier, here $\Delta = 10$ K is the exchange energy gap between the set of S = 1 ground states and the set of S = 2 excited states with lowest energy (Fig. 3.3). Indeed, fluctuations of $\mathcal{M}$ for $K_BT \ll \Delta$ decay by a two-phonon process in which the molecule first absorbs a phonon bringing it from S = 1 to 2 states, and then emits a phonon by decaying back to the S = 1 manifold. Intra-S = 1 spin–phonon processes involve vanishing gaps (or very small gaps if anisotropy is included Fig. 3.7) and hence there are no phonons to activate them (the phonon density of states vanishes for E $\rightarrow$ 0). The presence of many distinct S = 1 and 2 multiplets involved in the two-phonon process leads to several distinct frequencies with the same T dependence but with slightly different prefactors ω_0. For K_BT approaching Δ excited sets of states become increasingly populated, and more frequencies λ_i acquire appreciable weight.
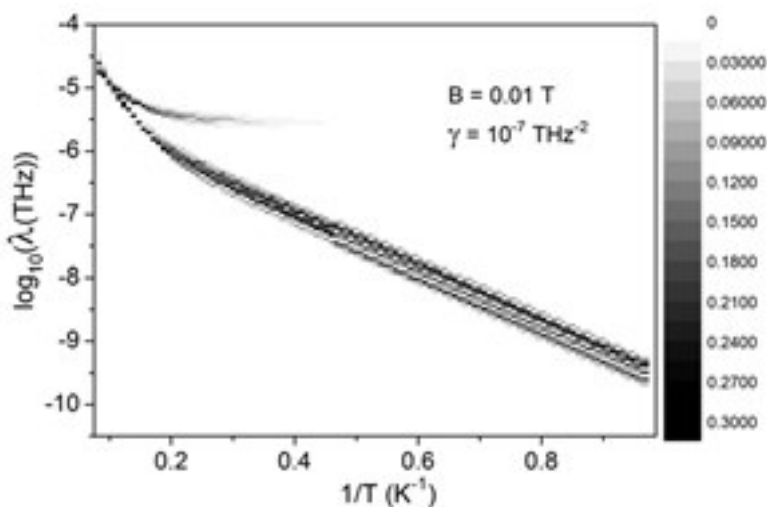

Figure 3.9: Intensity plot showing the calculated weights $A\left(\lambda_i, T, B\right)$ of the magnetization autocorrelation (Eq. 3.10) for B $\rightarrow$ 0 versus 1/T (x axis). The y axis is $\log_{10}\left(\lambda_i\right)$ (in THz). The plot maps $A\left(\lambda_i, T, B\right)/\chi T$, i.e. for each value of T the spectra have been normalized by χT (Fig. 3.2), which is proportional to the size of equilibrium fluctuations. Frequencies weighting less than 1.5% at the given T do not appear. The parameter describing the spin–phonon coupling strength in Eq. 1.104 sets the timescale of the relaxation dynamics. Thus, changing γ produces a vertical translation of the plot. Here we have chosen $\gamma = 10^{-7}$ THz^{-2}.

The effect of a finite field B is shown in Fig. 3.10. The field produces a Zeeman splitting of the various sets of degenerate multiplets in their $\mathcal{M}$ components. The T dependence of the relaxation for B = 3 T shows an overall increase of the rates λ_i at low T, where the Arrhenius T dependence is lost. This is due to the activation of spin–phonon processes involving direct transitions within the set of low-lying S = 1 states. Such processes become likely in finite B because the phonon density of states at the Zeeman splittings becomes sizeable. The spectrum remains anomalous for the presence of a whole band of relevant frequencies at low T from which a single mode tends to emerge at

higher T. This is opposite to what is usually expected in MNMs. Fig. 3.10 also shows how the band of processes relevant at low-T evolves for fixed T = 0.5 K as a function of B. One can clearly see how B first accelerates and then decelerates the dynamics, which becomes again slow at the crossing (B_C = 6.8 T). Indeed Fig. 3.4 shows that the spectrum at B_C is structured into well-separated groups of levels as for B = 0 and hence a similar slow dynamics is recovered.
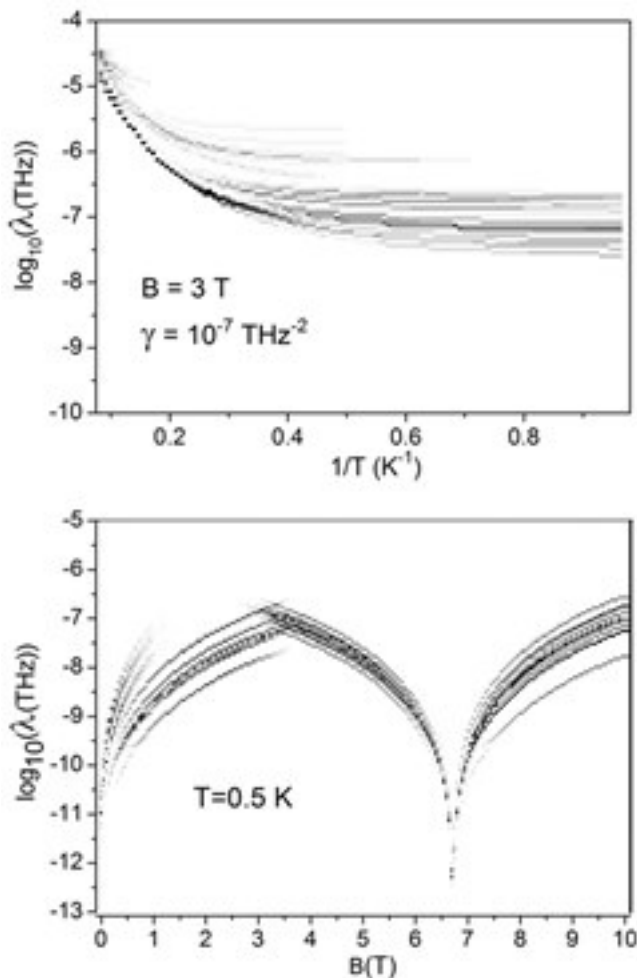
Figure 3.10: Top: intensity plot showing the calculated weights $A(\lambda_i, T, B)/\chi T$ of the magnetization autocorrelation (Eq. 3.10) for B = 3 T versus 1/T (see caption of Fig. 3.9). Bottom: the same weights as a function of B for fixed T = 0.5 K.

3.1.5 Conclusions

We have analysed the static and dynamical magnetic properties of the Ni_7 MNM, which is an excellent model system to investigate the effects of magnetic frustration. The latter leads to a magnetization process displaying two double jumps and a large plateau.

These jumps are associated with multiple level crossings induced by the external field, and involve states with three different total-spin quantum numbers. If a realistic degree of anisotropy is included, the crossings turn into anticrossings for a generic orientation of the field. Physically this effect corresponds to quantum oscillations of the total-spin length among the three different values, which could be detected by measuring the macroscopic torque at the anticrossing fields. We have discussed the possible interest of Ni_7 for magnetic refrigeration, and we have analysed its relaxation dynamics induced by the spin–phonon coupling. The temperature and field dependence of these dynamics is again atypical and reflects the large degeneracies of the underlying energy levels.

3.2 $[M_3^{III}]$ Triangles Linked with "Double-Headed" Phenolic Oximes

Magnetic properties of three different compounds, Fe_7, Fe_6 and Mn_6, characterised by competing AF interactions are reported in this section. In each compound the metallic skeleton of the cluster is based on a trigonal prism in which two $[M_3^{III}O]$ triangles are tethered together via three helically twisted double-headed oximes. Both the identity of the metal ion (Fe^{3+} or Mn^{3+}) and the length of ligands units have a major impact on the nuclearity and topology of the resultant cluster. Fe_7 magnetic core consists of seven AF-coupled Fe^{3+} ions arranged on two corner-sharing tetrahedra. Fe_6 and Mn_6 cores contain two AF triangles weakly interacting with each other (only in the case of Fe_6 the two triangles are parallel). Even if in these three clusters geometrical frustration is removed by structural distortions of their molecular structure, there are still many competing AF interactions. For further details on the structures of these cluster see insets in Figs. 3.11, 3.13, 3.14.

3.2.1 Magnetic Measurement

The magnetic properties of Fe_7, Fe_6 and Mn_6 have been investigated by measuring the temperature-dependence of their magnetic susceptibilities (Figs. 3.11, 3.13, 3.14). All the compounds are characterised by a monotonic decrease of χT down to low temperatures, suggesting the presence of sizeable AF interactions. Indeed this is also reflected in the fact that the room temperature values of χT are significantly smaller than that corresponding to non-interacting ions, especially in Fe_7 and Fe_6. As a first approximation, the magnetic properties of Fe_7, Fe_6 and Mn_6 can be modeled by the isotropic Heisenberg Spin Hamiltonian:

$$\mathcal{H} = \sum_{i>j} J_{ij}\mathbf{s}_i \cdot \mathbf{s}_j + g\mu_B \mathbf{B} \cdot \sum_i \mathbf{s}_i \tag{3.11}$$

($\mathbf{s_i}$ = 5/2 for Fe^{3+} and $\mathbf{s_i}$ = 2 for Mn^{3+}). The last term accounts for the Zeeman interaction with the applied magnetic field B. The patterns of exchange constants are illustrated in the insets of Figs. 3.11, 3.12, 3.13, 3.14. Given that Fe^{3+} is characterised by a half-filled d-electron shell, anisotropic exchange and crystal field interactions in Fe_7 and Fe_6 are expected to be small and Eq. 3.11 should provide a very good description of these molecules. Conversely, further anisotropic terms could be important in Mn_6, especially to describe the low-temperature behavior. In the Zeeman term we have assumed g = 2, consistent with the typical behavior of Fe^{3+} (for Fe_7 and Fe_6) and with the values observed in a family of structurally related Mn_6^{III} compounds (for Mn_6) [97]. The simplest conceivable models of these molecules are characterised by two exchange constants only, one describing intra-triangle exchange coupling and one describing the other bonds (see

insets in Figs. 3.11, 3.13, 3.14). However, these models are not adequate to describe the observed magnetic behavior. Indeed, the structures of Fe_7, Fe_6 and Mn_6 allow for several distinct exchange parameters. In the following we therefore describe the simplest models that allow for a satisfactory fit of the temperature-dependence of magnetic susceptibility.

Fe_7
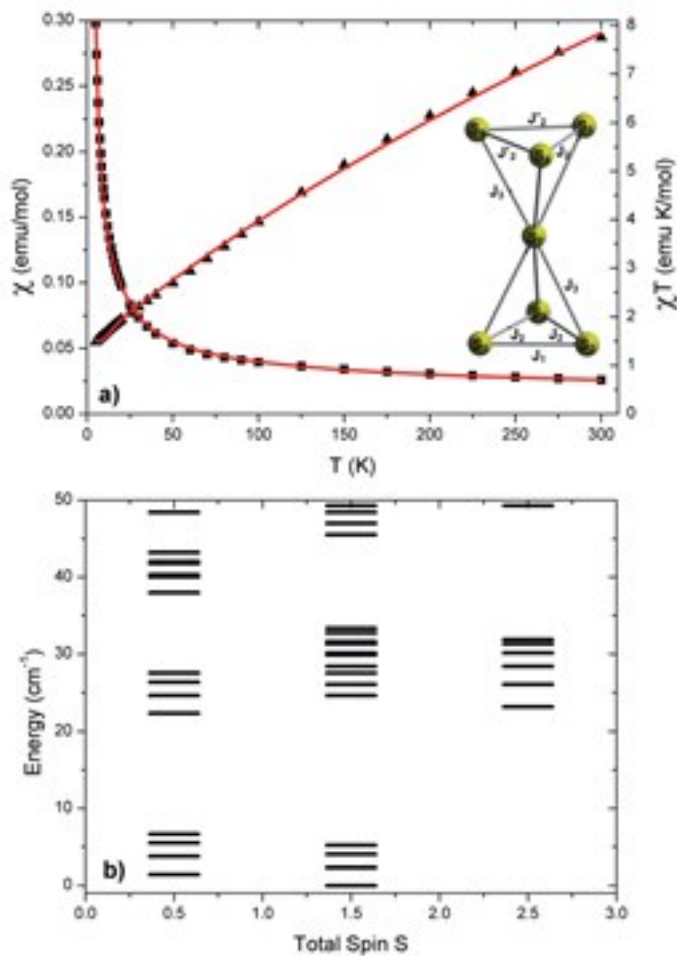
Figure 3.11: (a) Measured temperature dependence of the magnetic susceptibility of Fe_7 (black squares), also reported as χT (black triangles). Red lines represent calculations with $J_1 = 58$ cm^{-1}, $J_2 = 63.2$ cm^{-1}, $J'_2 = 63.8$ cm^{-1}, $J_3 = 53.3$ cm^{-1} and g = 2. Inset: schematic representation of the seven Fe^{3+} ions and of the exchange couplings. (b) Exchange energy of the lowest total spin multiplets calculated with the Spin Hamiltonian in Eq. 3.11 and the above exchange constants. The ground state energy is set to zero.

The low temperature value of χT in Fe_7 points to a low total-spin S ground state and to the presence of low-lying excited states. Indeed the measured values are smaller

Figure 3.12: Top-panel: Measured field-dependence of the magnetization of Fe$_7$ (squares) at different temperatures. Lines represent calculations with J$_1$ = 58 cm^{-1}, J$_2$ = 63.2 cm^{-1}, J'$_2$ = 63.8 cm^{-1}, J$_3$ = 53.3 cm^{-1} and g = 2. Bottom panel: Fe$_7$ magnetization at T = 4.2 K as a function of the applied magnetic field up to 15 T.
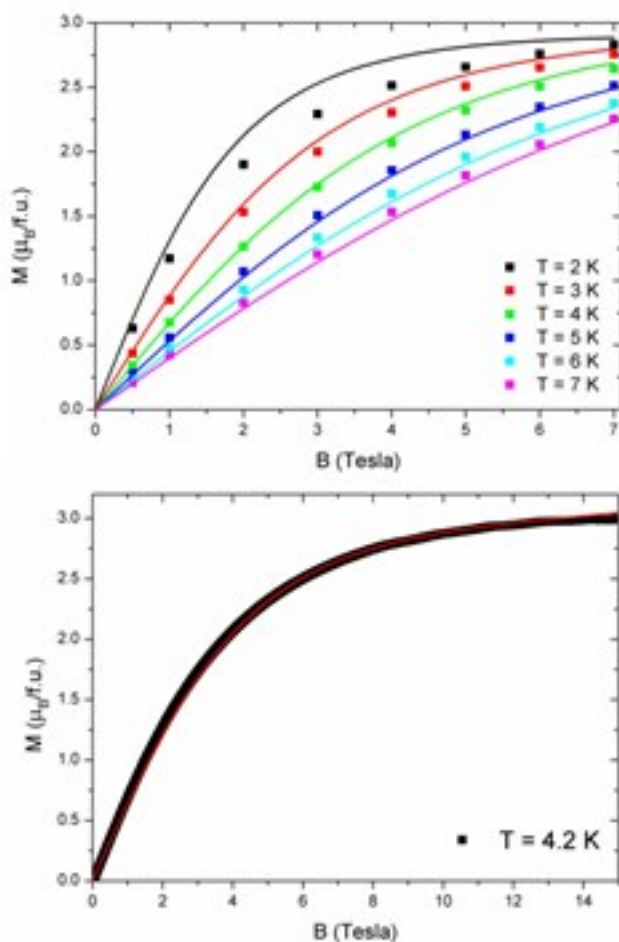
than those corresponding to an isolated $|S = 3/2\rangle$ multiplet, but higher than those of an isolated $|S = 1/2\rangle$ doublet. In addition, the $\chi T(T)$ curve at low temperature has a nearly linear behavior. Fig. 3.11 shows that magnetic measurements can be well reproduced by a model characterised by strong AF exchange couplings both within the upper and lower Fe triangles and between these triangles and the central Fe ion. Indeed the presence of these competing interactions leads to a low-spin ground multiplet and to several low-lying excited manifolds (Fig. 3.11-b). The fitting of the magnetic data of Fe$_7$ within the present model is not unique and the parameters are correlated; indeed the data can be acceptably reproduced by several regions of the parameter space. For instance, a very good agreement with the data is obtained with J$_1$ = 58 cm^{-1}, J$_2$ = 63.2 cm^{-1}, J'$_2$ = 63.8 cm^{-1}, J$_3$ = 53.3 cm^{-1}. For this particular family of parameters the order of magnitude of the Fe–Fe superexchange couplings are consistent with the model introduced by C.

Cañada-Vilalta et al. [98] (see also [99, 100]) to explain magneto-structural correlations in molecular clusters containing Fe^{3+} ions.

For Fe_7 also magnetization measurements have been performed. Within the model base on Eq. 3.11 it is possible to reproduce field-dependent magnetization curves at different temperatures (Fig. 3.12 top panel). Small deviations from experimental data at very low temperature could be due to small anisotropy effects. Low temperature magnetization data saturates to $3\mu_B$ until high fields (Fig. 3.12 bottom panel), confirming the large energy gap between the lowest S = 5/2 sextet and the ground state. Therefore from these magnetic measurements we can conclude that the energy spectrum of Fe_7 has a low-spin ground state $|S = 3/2\rangle$ with a very small gap (of a few K) with the first excited doublet $|S = 1/2\rangle$, low-lying $|S = 3/2\rangle$ excited multiplets and a very large gap (higher than 30 K) with the first excited $|S = 5/2\rangle$ multiplet.

As already pointed out, the fitting of the magnetic data of Fe_7 within the model of Eq. 3.11 is not unique. The Table below reports the different regions of the parameters space where it is possible to find acceptable fits. To better understand the relationships between inter- and intra-triangle parameters, the exchange constant J_1 is taken as a reference and the other parameters are reported as ratios of J_1 (see inset of Fig. 3.11). In order to have a low-spin ground multiplet (S = 1/2 or S = 3/2) as suggested by the low temperature value of χT, $J_3/J_1 < 2$ is required. Due to the small structural differences within each triangle, we have constrained the ratios between intra-triangle constants J_2/J_1 and J'_2/J_1 between 0.5 and 2. In all the regions it is possible to adjust parameters and ratios in order to fit both susceptibility and magnetization data. The set of parameters reported in the main article belongs to region 2, where there is the best overall agreement between the values of the exchange constants and the expectations based the model of C. Cañada-Vilalta et al. [98].

	J_1	J_3/J_1	J_2/J_1	J'_2/J_1
Region 1	30 - 36 cm^{-1}	1.1 - 1.4	1.7 - 2	1.7 – 1.2
Region 2	47 – 70 cm^{-1}	0.6 – 0.9	0.8 – 1.3	0.8 – 1.2
Region 3	100 – 120 cm^{-1}	0.2	1.7 – 1.8	0.6 – 0.7
Region 4	50 – 70 cm^{-1}	0.4 – 0.6	1 – 1.6	0.5 – 0.8
Region 5	40 – 55 cm^{-1}	0.5 – 0.6	0.9 – 1.4	1.6 - 2
Region 6	90 – 110 cm^{-1}	0.2 – 0.3	0.5	0.6 – 0.8
Region 7	70 – 90 cm^{-1}	0.2	1.2 – 1.3	0.8 – 1.3

Table 3.1: Regions of the parameters space where it is possible to find acceptable fits of magnetic data of Fe_7.

Investigations on relaxation dynamics of Fe_7 probed by NMR will be discussed in Section 3.3

Fe_6 and Mn_6

The low temperature value of χT in Fe_6 suggests a non-magnetic S = 0 ground state very close to a magnetic S = 1 triplet. The observed magnetic behavior of Fe_6 is reproduced
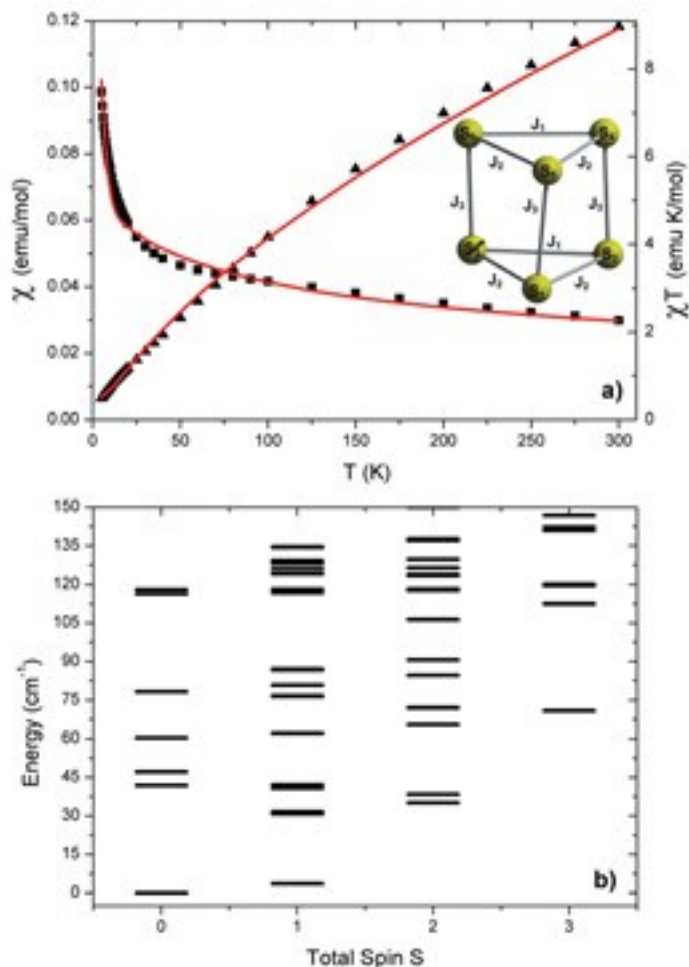
Figure 3.13: (a) Measured temperature dependence of the magnetic susceptibility of Fe_6 (black squares), also reported as χT (black triangles). Red lines are obtained with $J_1 = 43$ cm^{-1}, $J_2 = 56$ cm^{-1}, $J_3 = 0.6$ cm^{-1} and $g = 2$. Inset: schematic representation of the six Fe^{3+} ions and of the exchange couplings. (b) Exchange energy of the lowest total spin multiplets calculated with the Spin Hamiltonian in Eq. 3.11 and the exchange constants reported above. The ground state energy is set to zero.

by assuming strong AF coupling within the two triangles and weak intertriangle interactions (see Fig. 3.13). Best fits are obtained with a unique set of parameters: $J_1 = (43 \pm 4)$ cm^{-1}, $J_2 = (56 \pm 5)$ cm^{-1}, $J_3 = (0.6 \pm 0.05)$ cm^{-1}. The order of magnitude of intratriangle exchange couplings are again in agreement with the Cañada-Vilalta model [98]. The inter-triangle interaction is small, but consistent with other clusters with similar Fe–Fe superexchange bridges [101, 102]. Hence, this system is also characterised by the presence of competing interactions. The presence of strong AF interactions in both Fe_7 and Fe_6 explains the large room temperature reduction of the effective moment in these compounds with respect to that of uncoupled ions. Fig. 3.13-b shows that the present model

is characterised by a singlet ground state and by an excited triplet well separated from
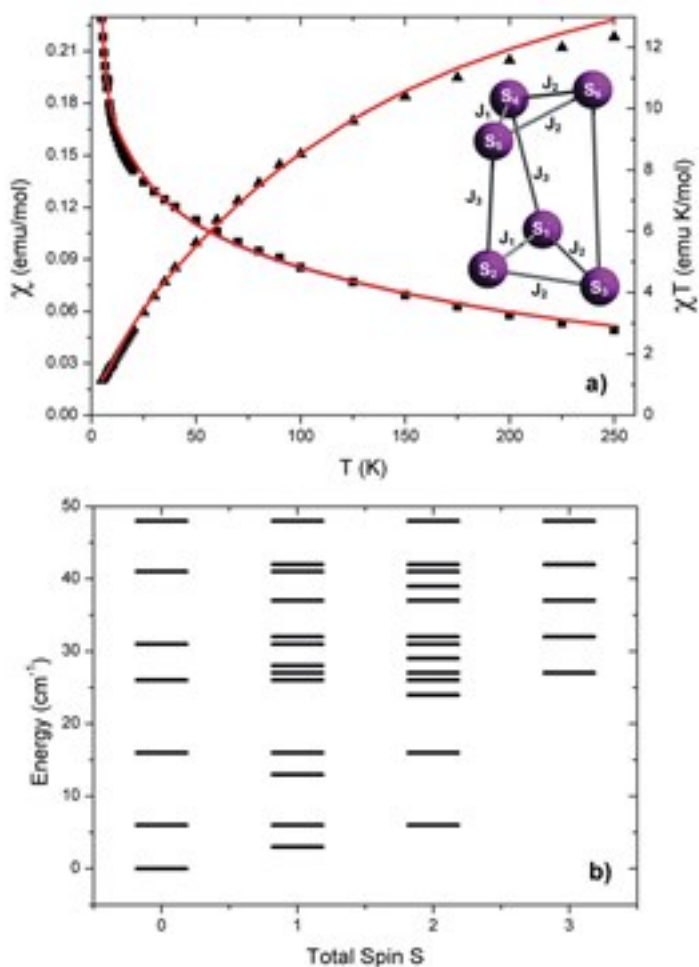the other excited levels.

Figure 3.14: (a) Measured temperature dependence of the magnetic susceptibility of Mn$_6$ (black
squares), also reported as χT (black triangles). Red lines are calculated with J$_1$ = 18 cm^{-1}, J$_2$ =
13 cm^{-1}. Inset: schematic representation of the six Mn^{3+} ions and of the exchange couplings. (b)
Exchange energy of the lowest total spin multiplets calculated with the Spin Hamiltonian in Eq.
3.11 and the above exchange constants. The ground state energy is set to zero.

The temperature dependence of the magnetic susceptibility of Mn$_6$ can be repro-
duced with Eq. 3.11 with a unique set of parameters, as shown in Fig. 3.14-a. The model
is characterised by sizeable AF exchange interactions within the two Mn triangles, J$_1$ =
18 ($\pm$2) cm^{-1}, J$_2$ = 13 ($\pm$2) cm^{-1}, and by vanishing coupling between the triangles. The
use of g-values other than 2 does not improve the fit. The resulting energy of the lowest-
lying multiplets is reported in Fig. 3.14-b as a function of their total spin. The presence
of low-lying magnetic states is necessary to account for the measured low temperature
susceptibility. As stated above, sizeable anisotropic interactions can be expected in Mn$_6$,

but single-crystal measurements are needed to address this issue.

3.3   Relaxation Dynamics in a Fe$_7$ Nanomagnet

In this Section we investigate the spin dynamics of the Fe$_7$ molecular nanomagnet. As explained in the previous section, its magnetic core consists of seven AF-coupled Fe^{3+} ions arranged on two corner-sharing tetrahedra(see inset of Fig. 3.11). We have theoretically predicted frustration effects in a similar system, Ni$_7$, reported in Section 3.1, which displays a large ground state degeneracy and unusual static and dynamical magnetic properties. A great advantage of these two clusters is the relatively small Hilbert space compared to other frustrated clusters. Indeed, this makes (virtually) exact calculations feasible. The possibility to neglect the effects of anisotropies on Fe^{3+} ions makes Fe$_7$ even more appealing than Ni$_7$ in order to study frustration-induced properties. Unfortunately, the magnetic core of the Fe$_7$ cluster shows small structural distortions (the upper and the lower triangles are not exactly equilateral and they are slightly different from each other). Even if these distortions lead to a removal of frustration, there are still many competing AF interactions leading to a low-spin ground state multiplet with a complex pattern of low-lying excited levels (see Fig. 3.11-b) This yields a multiple-time-scale relaxation dynamics at low temperatures. Such behavior is one of the main features we expect in a frustrated MNM, as we have seen in the case of Ni$_7$. Conversely, single-molecule magnets like Fe$_8$ [61] and AF rings like Cr$_8$ [103] are characterised by a single dominant relaxation time.

Phonon-induced relaxation dynamics in MNMs can be probed by the proton spin-lattice relaxation rate $1/T_1$, measured by nuclear magnetic resonance (NMR) [61, 104]. In fact the interpretation of ^{1}H nuclear magnetic resonance measurements allows the determination of the coupling strength of the magneto-elastic interaction and to calculate, for instance, magnetization relaxation times. In this work we have measured the temperature dependence of $1/T_1$ for two different values of the applied magnetic field. NMR measurements on MNMs are often affected by the so-called wipeout effect [105]: At low-temperatures it is possible to have an NMR signal loss, due to the enhancement of the protons transverse relaxation rate $1/T_2$ over the limit of the experimental signal detection capability. As a consequence, not all the protons contribute to the molecular $1/T_1$. Within our theoretical framework it is possible to reproduce this wipeout effect by a novel approach, identifying which protons are probed by NMR.

3.3.1   Theoretical model

The magnetic properties of the Fe$_7$ cluster can be described by the Spin Hamiltonian in Eq. 3.11 and the exchange parameters have been determined by magnetic measurements of susceptibility and magnetization (see Section 3.11). To explain the observed magnetic behavior, four distinct exchange couplings are needed, reflecting the small structural distortions in the cluster (see Fig. 3.15-b). As already pointed out in the previous section, we have found that the energy spectrum of Fe$_7$ must have precise characteristics in order to reproduce the features of the magnetic data (see Section 3.11). As we will show in the following, these characteristics are the same responsible for the multiple-time scale relaxation dynamics of the cluster. As shown in Fig. 3.11-b, Fe$_7$ energy spectrum has a low-spin ground state $|S = 3/2\rangle$ with a very small gap (of a few K) with the first excited doublet $|S = 1/2\rangle$, low-lying $|S = 3/2\rangle$ excited multiplets and a very large gap (higher than 30 K) with the first excited $|S = 5/2\rangle$ multiplet. Fig. 3.16 shows the calculated magnetic field dependence of the lowest lying energy levels.
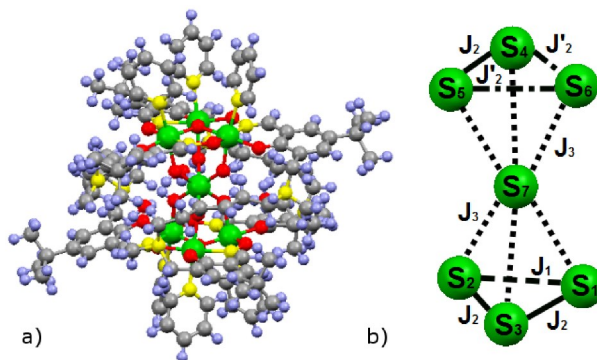
Figure 3.15: a) Molecular structure of Fe_7 (red: O, cyan: H, grey: C, yellow: N). The large green spheres are Fe^{3+} ions. b) Magnetic core of Fe_7. Lines represent exchange interaction; the four different exchange parameters J_1 (Dashed line), J_2 (Solid line), J_2' (Dash-Dotted line) and J_3 (Dotted line) reflect the different Fe-Fe superexchange paths.

To study the relaxation dynamics of Fe_7, we focus on the quasi-elastic components which can be probed by NMR measurements [61, 106]. Within this framework, the coarse-grained time evolution of the cluster is given by the master equations in Eqs. 1.102, where the rate matrix is given by Eq. 1.104 (see Section 1.2). As pointed out in Section 1.2.2, the spin-phonon coupling strength γ is the only free parameter of our model and it can be determined from NMR experimental data[1].

In Section 1.2.3 we have seen that relaxation dynamics towards equilibrium can be described in terms of dynamical correlation functions between the fluctuations of molecular observables. We have also shown that in the theoretical framework given by Eq. 1.102, the Fourier transform of the correlation function can be expressed as a sum of Lorentzians [61], as in Eq. 1.111.

3.3.2 Relaxation Dynamics

Within the theoretical framework illustrated in the previous section, we can investigate the relaxation dynamics of the Fe_7 cluster by applying Eq. 1.111 to the most interesting observables. Here we focus on the relaxation of the cluster magnetization ($\mathcal{A} = \mathcal{B} = \mathcal{M} = \sum_i s_i^z$) and on single-site spin observables s_{iz}, where z is the direction of the external field. In Fig. 1.2 we report the calculated relaxation rates spectra of $\mathcal{M}$ as a function of temperature for three different values of the applied fields (0.01 T and the two fields used in NMR measurements).

The only free parameter of the model, the spin-phonon coupling strength γ, has been determined from the analysis of $1/T_1$ NMR data, that will be discussed in the next section. It is worth to stress that this parameter merely fixes the overall scale factor of the relaxation dynamics timescales (a change of γ only leads to rigid vertical shifts in Figs. 3.17, 3.18), whereas the temperature and field dependence of the relaxation rates comes directly from the calculations.

The rates $\lambda_i(T)$ having appreciable weight in the spectra are roughly in the range

---

[1]A magneto-elastic coupling with a single site-independent parameter γ leads to a non-ergodic spin dynamics. Thus, we have chosen slightly different coupling constants for each Fe^{3+} ion and we have checked that the results don't depend qualitatively on the choice of the specific pattern of coupling constants [107].
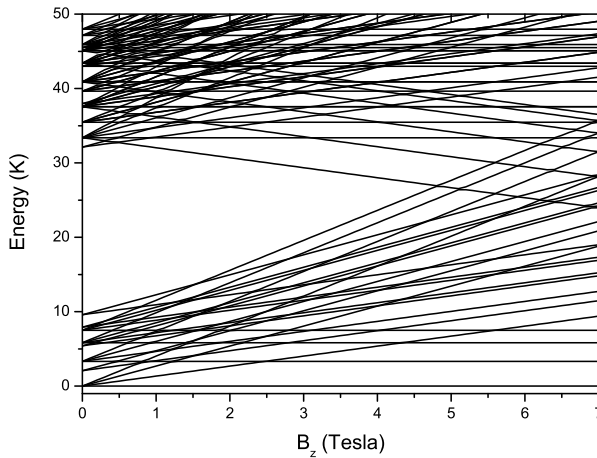
Figure 3.16: Magnetic field dependence of the lowest lying energy levels of the Fe$_7$ calculated with Eq. 3.11. The magnetic field is applied along the z-axis. The ground state energy is set to zero for each value of B_z.

10^{-9} - 10^{-1} THz up to $T = 30$ K, corresponding to relaxation times between 1 ms and 10 ps. Relaxation dynamics become faster as the applied magnetic field increases, especially at low temperature. The most interesting feature of the Fe$_7$ relaxation dynamics is that several rates have appreciable weights, even at rather low temperatures. Conversely, in most MNMs a single rate dominates at low temperature. This multiple-time scale dynamics is a peculiar characteristic of Fe$_7$, due to the effects of AF competing interactions on the energy spectrum. Since there is a complex pattern of low-lying excited levels, the spin-phonon interactions can induce many relaxation processes, with different paths and different characteristic times $\tau_{rel}^{(i)}$. For different values of the applied field, we have analysed the dominant relaxation processes at low temperatures by inspecting the eigenvectors of Eq. 1.102 and the matrix elements of Eq. 1.104. In fact, the former give information about the starting and the final levels of the processes and the latter are the transition probabilities. In small field (Fig. 3.17 top panel) we have found that the two dominant relaxation rates at $T \lesssim 2.5$ K follow the Arrhenius law $\lambda = \lambda_0 \exp(-\Delta/k_B T)$, where the amplitude λ_0 sets the time-scale and reflects the magneto-elastic coupling strength γ and Δ/k_B is the height of the barrier hampering the relaxation of $\mathcal{M}$. These two relaxation processes involve levels of the ground state manifold $S = 3/2$ and of the lower-lying $S = 1/2$ and $S = 3/2$ multiplets. In fact, the dominant relaxation time has $\Delta/k_B \approx 5.8$ K and it corresponds to an Orbach process [3] involving the ground state and the third excited manifold with $S = 3/2$, which has energy ≈ 5.8 K in zero field (see Fig. 3.11-b). The second important relaxation process is characterised by a smaller energy barrier $\Delta/k_B \approx 4.4$ K and it involves levels belonging to the third excited multiplet with $S = 3/2$ and $E_3 = 3.3$ K and to the sixth excited one with $S = 3/2$ and $E_6 = 7.5$ K in zero field. At 2.5 K $< T < 4$ K the rate corresponding to the slowest relaxation process follows an Arrhenius law with $\Delta/k_B \approx 35$ K. This corresponds to an Orbach relaxation process involving the first excited multiplet with $S = 1/2$ and energy $E_1 = 2.1$ K and
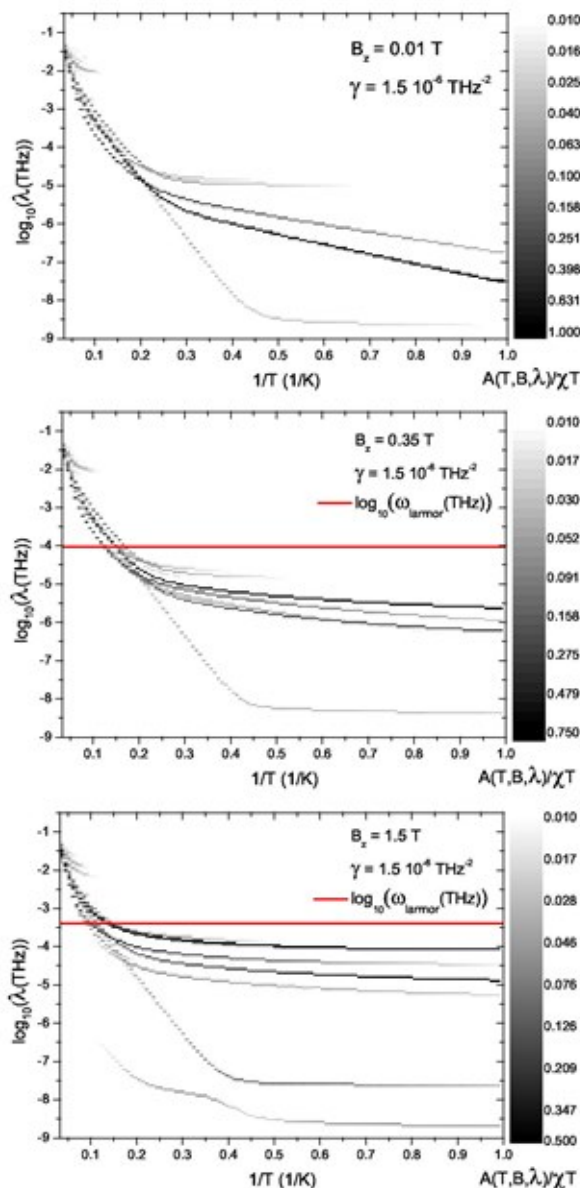
Figure 3.17: Calculated weights $A(\lambda_i, T, B)$ of the magnetization autocorrelation as a function of the inverse temperature for the three values of the applied magnetic field, $B = 0.01$ T, $B = 0.35$ T and $B = 1.5$ T respectively. The y-axis is $log_{10}(\lambda_i)$, the greyscale shows the weights $A(\lambda_i, T, B)/\chi T$. When ω_L (red line) intersects the rates λ_i with significant weight, $1/T_1$ displays a peak (see Fig. 3.19).

the $S = 3/2$ multiplet lying at about $E_{13} = 37.5$ K in zero field (see Fig. 3.11-b). This process gives a very small contribution to the relaxation dynamics of the Fe$_7$ cluster, at odds with many MNMs where the slowest relaxation process is the dominant one. At

higher temperatures several characteristic rates have an appreciable weight and the temperature dependence is not of the Arrhenius type. By increasing the applied field (see
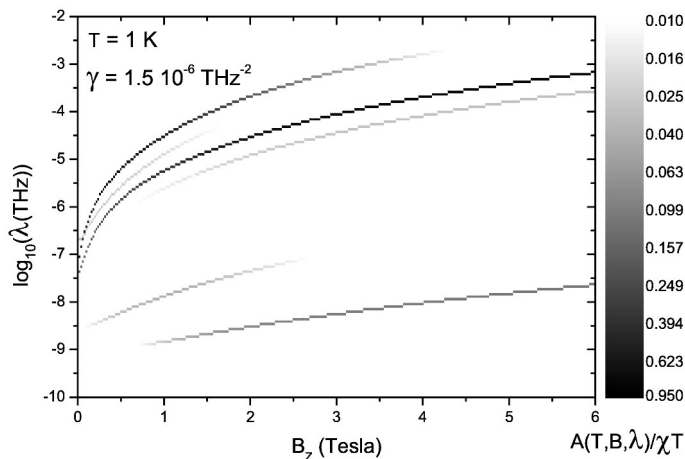

Figure 3.18: Calculated weights $A(\lambda_i, T, B)$ of the magnetization autocorrelation as a function of the applied magnetic field at $T = 1$ K. The y-axis is $log_{10}(\lambda_i)$, the greyscale shows the weights $A(\lambda_i, T, B)/\chi T$.

Fig. 3.17 bottom panels), the multiple-times character of the relaxation dynamics become more pronounced. Moreover, the Arrhenius T-dependence of the dominant rates is lost even at low temperatures, while in most MNMs relaxation times at low temperatures follow the Arrhenius law even in a moderate applied magnetic field[61, 103]. We have found that the two dominant relaxation rates at low temperatures correspond to direct processes involving levels of the ground multiplet, split by the Zeeman interaction with the field. The slowest relaxation process is still of the Arrhenius type and has a slightly larger weight. At $B = 1.5$ T an even slower relaxation process occurs, but it doesn't follow the Arrhenius law. We have also calculated the magnetic field dependence of the relaxation rates at $T = 1$ K, reported in Fig. 3.18. We have confirmed that the multiple-times scale dynamics at low temperature is still present even with high applied magnetic fields (e.g. up to $B = 6$ T as shown Fig. 3.18), with the two dominant relaxation rates increasing with the magnetic field.

We have verified that the multiple-time-scale relaxation dynamics is found also using sets of exchange parameters belonging to other regions of the parameters space, where it is possible to find acceptable fits of Fe$_7$ susceptibility and magnetization (see Section 3.11). In fact, as already mentioned in Section 3.3.1, the characteristics that the energy spectrum must have in order to reproduce the magnetic data are the same responsible for the multiple-time scale relaxation dynamics. Indeed, the two dominant frequencies in the spectrum of fluctuations of the cluster magnetization correspond to relaxation processes involving levels of the ground state manifold $S = 3/2$ and of the lower-lying multiplets. We can therefore conclude that the multiple-time scale dynamics does not depend on the specific choice of the parameter set used to interpret magnetic data.

3.3.3 NMR Experiments

The phonon-induced relaxation dynamics of the Fe_7 cluster has been probed by NMR. The theoretical model reported in the previous sections depends on the single free parameter γ, the spin-phonon coupling strength, which fixes the scale factor of the relaxation dynamics timescales. This parameter can be determined from the interpretation of the proton spin-lattice relaxation rate $1/T_1$, obtained from NMR experiments. In fact, thermal fluctuations of the electronic spins generate fluctuations in the local hyperfine field at the nuclear site, causing relaxation of the nuclear spins. Thus from ^{1}H NMR measurements it is possible to probe the relaxation dynamics of the cluster and determine the parameter γ.

We have measured the nuclear spin-lattice relaxation rate $1/T_1$ on a polycrystalline sample of Fe_7 as a function of temperature and for two values of the applied magnetic field, $B = 0.35$ T and $B = 1.5$ T. Experimental results are shown in Fig. 3.19. The temperature dependence of $1/T_1$ shows a peak at about $8 - 10$ K, whose height and position depends on the applied magnetic field. As shown in Fig. 3.19, the peak lowers and moves to higher temperatures by increasing the field. The quantity $M_{xy}^H(0)T$, determined at $B = 0.35$ T from the $M_{xy}^H(t)T$ relaxation curve, is proportional to the number of protons resonating at the irradiation frequency. Results as a function of temperature are shown in the inset of Fig. 3.19. $M_{xy}^H(0)T$ decreases by lowering the temperature due to the so-called wipeout effect, experimentally observed in other MNMs and qualitatively explained in Ref. [105].
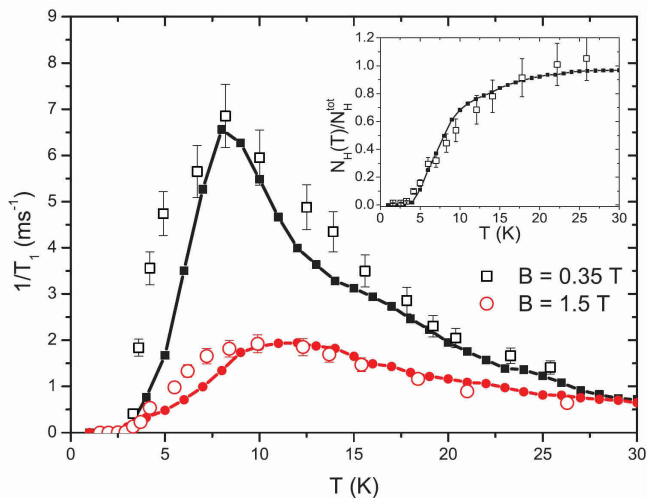
Figure 3.19: Scatter: ^{1}H NMR $1/T_1$ data on Fe_7 powders as a function of temperature at two different applied magnetic fields. Line&Scatter: calculations exploiting equation (2.63) and taking into account the wipeout effect. Inset: fraction of protons probed by NMR (scatter) deduced by the initial transverse nuclear magnetization at $B = 0.35$ T (see Section 3.3.3). Line: fraction of protons taken into account in our calculations determined as described in Section 3.3.3.

The theoretical model illustrated in Section 1.2 and in Section 2.2.3 has been applied to the interpretation of ^{1}H NMR data on Fe_7. In order to reduce the computational effort, a truncation in the molecule Hilbert space is necessary to perform the diagonalization

of the rate matrix $\mathbb{W}$. The reduction to the subspace spanned by the lowest total-spin manifolds (up to 200 K) allows us to calculate the temperature dependence of $1/T_1$ in the most interesting region, i.e. where it displays a peak, up to $T = 30$ K. Since $1/T_1$ measurements have been made on Fe$_7$ powders, to reproduce the experimental data we average over all the possible orientations of the applied external field.

From our theoretical model it is also possible to understand the origin of the peak in the temperature-dependence of $1/T_1$, which has been experimentally observed in the Fe$_7$ nanomagnet as in other MNMs. First of all, we have also investigated the relaxation of single-site observables (s_i^z) and the decay of the hyperfine field fluctuations. We have found that the corresponding spectra are very similar to those of the cluster magnetization $\mathcal{M}$ in Fig. 3.17 and are characterised by the same dominant relaxation times. We can now exploit Eq. 1.111 to rewrite (for each hydrogen) the autocorrelation of the transverse components of the hyperfine field fluctuation (Eqs. 2.60 and 2.61) as a sum of lorentzians evaluated at the Larmor frequency ω_L. In the case of homometallic AF rings only a single lorentzian dominates the sum [61, 106] and $1/T_1$ displays a peak at the temperature at which the relaxation rate of this lorentzian matches ω_L. In the present case the relaxation dynamics is not mono-lorentzian but the different relevant rates are close to one another when they approach ω_L at T close to 10 K (see Fig. 3.17). Therefore, a single-peak in the $1/T_1$ curve results also in the present case. Since the spin-phonon coupling strength γ sets the range of the characteristic relaxation times, it is possible to determine its value by fitting the position of the peak in $1/T_1(T)$.

As mentioned above, $1/T_1$ data on Fe$_7$ are also affected by the wipeout effect [105], i.e., a gradual loss of the ^{1}H NMR signal intensity is observed on decreasing the temperature. This signal loss is associated with the enhancement of the transverse relaxation rates of the probed protons over the limit fixed by the experimental setup; they become so fast that the transverse nuclear magnetization decays irreversibly before it can be observed in a pulsed NMR experiment. In our experimental conditions the minimum T_2 that we can measure in the investigated range of frequencies can be considered around $10 - 12$ μs. We have taken into account the wipeout effect in our calculations by mimicking what actually happens in the NMR experiments. For each hydrogen in the molecule we use Eqs. 2.63 and 2.64 to calculate $1/T_1$ and $1/T_2$ as a function of the temperature, the orientation and the modulus of the applied magnetic field. Then, to determine the experimental $1/T_1$, i.e. averaged over all the protons in the molecule not affected by wipeout, we take into account only the hydrogen nuclei whose transverse relaxation rate is lower than a fixed threshold, $1/T_2 < 1/T_2^{thresh}$. Thus, in the calculation of $1/T_1$ we consider only the protons actually probed by NMR measurements. We let vary the T_2 threshold by an amount of 20%, with the aim of improving the final fits, thus obtaining $1/T_2^{thresh} = 86.6$ ms^{-1}, corresponding to $T_2^{threshold} = 11$ μs, a value that falls perfectly in the experimentally estimated range. By fitting the peak position of $1/T_1(T)$ at $B = 0.35$ T, it is possible to determine the spin-phonon coupling strength, yielding $\gamma = 1.5 \times 10^{-6}$ THz^{-2}. With the same parameter we have also reproduced the position and height of the peak in $1/T_1(T)$ at $B = 1.5$ T, confirming the correctness of the value of γ. Fig. 3.19 demonstrates the good agreement between the experimental results and our calculations. To check the reasonableness of our approach for mimicking the wipeout effect, we have estimated the temperature-dependence of the fraction of probed hydrogens by measuring the transverse nuclear magnetization at time 0, obtained by the extrapolation at zero time of the transverse nuclear magnetization $M_{xy}^H(t)$ recovery curve (see the inset of Fig. 3.19). Indeed, the product $M_{xy}^H(0)T$ is proportional to the number of probed nuclei and can be compared with the number of ^{1}H included in our calculation by the

method described above. These measurements have been performed at 0.35 T because wipeout is generally known to be stronger at small fields. The inset of Fig. 3.19 shows that our modeling captures the wipeout effect. It is worth noting that the conditions for the validity of the approximations underlying the present calculations (see Section 2.2.3) are fulfilled except for the very low temperature region.

3.3.4 Conclusions

We have investigated the phonon-induced relaxation dynamics of the Fe_7 cluster, an excellent model system to study the effects of competing AF interactions on the spin dynamics of MNMs. We have found that several relaxation times $\tau_{rel}^{(i)}$ contribute to the decay of the molecular magnetization even at low temperature. We have also verified the multiple-times character of the relaxation dynamics is a direct consequence of the structure of the energy spectrum and that it is due to the topology of the competing AF interactions.

We have measured the temperature dependence of the spin-lattice relaxation rate $1/T_1$ by ^{1}H NMR measurements. The interpretation of these data has allowed us to determine the spin-phonon coupling strength γ and to set the scale factor of the relaxation dynamics timescales. By means of Redfield's approach [71] to the theory of relaxation processes, we have developed a model to calculate the nuclear spin-lattice relaxation rate $1/T_1$ taking into account also the wipeout effect. Our calculations are in very good agreement with experimental results.

In order to probe the multiple-times character of the relaxation dynamics of the Fe_7 cluster at low temperature, AC susceptibility experiments could be preformed. In fact, the graph in Fig. 3.18 shows that the low temperature relaxation times can be detected by AC susceptibility measurements with very high frequency (of the order of 100 KHz) performed in small magnetic field, thus stimulating further experimental works on the cluster.

Design of Molecular Nanomagnets for Magnetic Refrigeration

MNMs are now considered promising materials for very-low temperature magnetic refrigeration, since they exhibit an enhanced magnetocaloric effect (MCE) [43, 44, 45, 46]. The MCE observed in these systems is in fact significantly larger than that displayed by other envisaged candidates, like lanthanide alloys and garnet [108] or superparamagnetic nanoparticles [94]. In addition, the possibility of grafting MNMs to surfaces opens the perspective of building micron- and submicron-sized cooling devices for all those instruments where local refrigeration down to very low temperatures is needed [109, 110, 111].

The temperature range where MNMs display a large magnetic entropy variation upon application of a magnetic field of few Tesla is below $T \simeq 10$ K. This feature makes them appealing for low temperature cryogenic applications. In fact, they have been suggested as a valid alternative to the expensive ^{3}He -^{4}He dilution refrigerators, thus covering a temperature range below that achieved with liquid Helium cryostats (i.e., $T < 4.2$ K or $T < 2$ K) [112, 46]. However, this temperature range could in principle be expanded up to about 10 K. If magnetic refrigeration with MNMs could be used for cooling applications starting from these temperatures, refrigeration techniques based on liquid ^{4}He could be completely bypassed, with resulting technological and economical advantages. During the last years, the pivotal idea in the search for new magnetocaloric materials based on MNMs has been to increase the maximal entropy difference between zero and applied field $\Delta S_{\mathrm{max}} = \mathrm{Max}_T(S_0(T) - S_\mathbf{B}(T))$. The established recipe is to synthesize molecules characterised by negligible magnetic anisotropy, by a high-spin ground state and by low-lying excited multiplets [112, 46, 113]. These features guarantee a very large field-induced entropy variation at low temperature. Magnetic anisotropy can be controlled through the use of isotropic metal ions (like Mn^{2+}, Fe^{3+} or Gd^{3+}), whereas optimal multiplet structures can be obtained if the interactions between spins in the cluster are either weakly ferromagnetic or with competing antiferromagnetic (AF) terms [114, 115], like in the Fe_{14} molecule [116]. The most recent works on the MCE in MNMs involve clusters containing 4f ions or 3d-4f heterometallic complexes [117, 118, 119, 109, 120]. In these systems it is possible to exploit the large magnetic moments of Rare Earths (RE) ions and it is also easy to have weak ferromagnetic interactions. A crucial point is that even if ΔS_{max} is large it is not obvious that this entropy difference can be really exploited in refrigeration cycles (typically non-regenerative Carnot cycles at low temperatures). Indeed, the performance of the cycles that can be actually implemented with a given magnetic material also largely depends on the shape of the zero-field and in-field $S(T)$ curves.

In this Chapter we explicitly consider Carnot cycles and perform calculations for ideal

model systems to understand the characteristics of a MNM yielding an efficient MCE between $T \simeq 10$ K and the sub-Kelvin region. Temperatures much larger than 10-15 K cannot be achieved because at these temperatures the vibrational part of the specific heat overwhelms the magnetic one in this kind of systems. We show that, contrarily to the common belief, the best molecular MCE refrigerants in this temperature range are those based on molecules containing magnetic ions so strongly ferromagnetically interacting to reach the so-called *strong-exchange limit*. One important consequence of this result is that molecules without RE ions can be excellent magnetocaloric materials. This is particularly important in view of the fact that 4f elements are increasingly rare and expensive. Indeed, the research for "RE-free" materials for magnetic refrigeration is an increasing trend also in room-temperature applications [121], where 3d transition metals are the natural (and cheaper) alternative to REs.

4.0.5 The Magnetocaloric Effect

As already explained in Section 3.6, the MCE consists of a thermal response of a magnetic material to an isothermal/adiabatic variation of the applied magnetic field. In the first case the system responds with an isothermal magnetic entropy variation $\Delta S(T, \Delta H)$, while in the second case it responds with an adiabatic temperature change $\Delta T_{ad}(T, \Delta H)$. For magnetic refrigeration it is necessary to subject the refrigerant to a cyclic repetition of magnetization and demagnetization processes. For applications below about $T = 20$ K, a non-regenerative Carnot cycle is the most efficient [122]. It consists of an adiabatic (1-2) and an isothermal magnetization at T_{hot} (2-3), followed by an adiabatic (3-4) and an isothermal demagnetization at T_{cold} (4-1) (Fig. 4.1) [123].
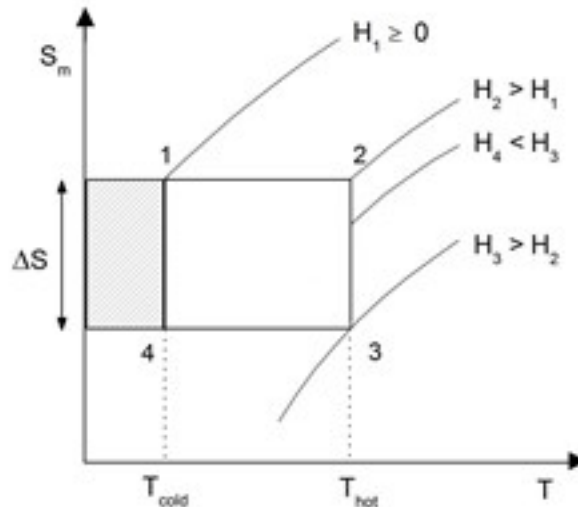

Figure 4.1: Schematic representation of a Carnot cycle in a (S,T,H) phase diagram. The grey area represent the heat absorbed by the refrigerant during the isothermal demagnetization Q_c.

During this last process the refrigerant absorbs heat from the so-called load. The performance of a Carnot cycle can be therefore described by its temperature span $\Delta T_{span} =$

$T_{hot}-T_{cold}$ (coinciding with the modulus of ΔT_{ad} in the cycle) and by the heat absorbed by the refrigerant during the isothermal demagnetization $Q_c=T_{cold}\Delta S_{cold}$ [124]. In fact, a large Q_c guarantees an high cooling power of the thermodynamic cycle. In addition, an useful Carnot cycle must have a relevant ΔT_{span}, since T_{cold} represent the temperature at which it is possible to cool down the load (in cryogenic applications it should be in the sub-Kelvin region), while T_{hot} must be reached by another refrigeration technique (the higher T_{hot} the better). Clearly, these two observables strongly depend on the characteristics of the material and on its state diagram (S, T, H).

4.1   Ideal Model systems

As explained before, the two classes of systems which are currently considered for magnetic refrigeration with MNMs are: i) clusters with competing antiferromagnetic interactions like the Fe_{14} molecule [116]; ii) clusters with weak ferromagnetic interactions like the compounds involving RE [117, 109, 120]. Both kinds of systems are characterised by a high-spin ground multiplet with low-lying excited manifolds leading to a large value of ΔS_{max}. To rationalize the efficiencies of these different classes in realizing Carnot refrigeration cycles, we have studied several ideal models containing all the key characteristics common to the large variety of real molecules which can be of interest for MCE. We have considered as a starting point the real cluster Fe_{14}: In fact in this system the competition between many AF interactions and a negligible anisotropy provide an unusually large MCE [116]. Our ideal models represent the building blocks of the Fe_{14} magnetic core, but, to reduce the computational effort and to calculate exactly both the energy spectra and MCE observables, they have $s = 3/2$ (instead of Fe^{3+} $s = 5/2$) and a lower number of magnetic centers. The Hamiltonian has only two exchange parameters and no magnetic anisotropy (as in Eq. 4.1). In Fig. 4.2 we report the scheme of the exchange interactions of all the investigated model systems.
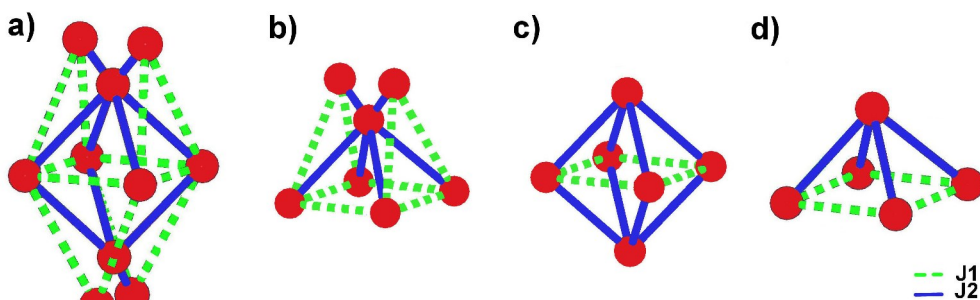

Figure 4.2: Scheme of the exchange interactions of the four ideal model systems.

Model a) has a topology which is equivalent to that of Fe_{14} cluster, since it has an analogous exchange interaction scheme which produces a qualitatively similar spectrum. Even if in model a) the number of involved ions is lower (10 instead of 14 in order to reduce the computational effort), we can still identify the same key 3D graph-theoretic motifs as in Fe_{14}: 1) the "bipyramid" (square-based instead of hexagonal-based), where the ions in the base are arranged on a ring and they all interact with the two vertices; 2) the upper and the lower dimeric (instead of triangular) caps, orthogonal to each other,

where each ion of the dimer interacts with two ions of the base and with the respective vertex of the bipyramid. The other models (Fig. 4.2-b÷d) have simpler and simpler exchange interactions schemes.

In the following section we focus on the simplest model, model d), which allows us to explore quantitatively the different regimes as a function of only two parameters, exploiting exact calculations. The model system is a square-based pyramid composed of five spins $s = 3/2$ connected by two distinct exchange interactions J_1 and J_2 (see Fig. 4.3). The corresponding Hamiltonian is

$$H = J_1 \sum_{i=2,5} \mathbf{s}_i \cdot \mathbf{s}_{i+1} + J_2 \sum_{i=2,5} \mathbf{s}_1 \cdot \mathbf{s}_i + g\mu_B B S_z, \tag{4.1}$$

where in the first sum $\mathbf{s_6} = \mathbf{s_2}$, S_z is the z-component of the total spin, B is the applied magnetic field and μ_B is the Bohr magneton. Since molecules with negligible anisotropy are the best candidates for MCE [46, 112], the single-ion zero-field splitting terms have been neglected.
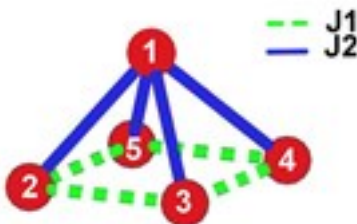

Figure 4.3: Scheme of the exchange interactions of the model d).

When J_1 is positive and both J_1 and J_2 are sizeable, the model displays competing interactions (case i)). Conversely, when J_1 and J_2 are both small and negative the model system is representative of case ii). In addition, the ferromagnetic strong-exchange limit corresponds to J_1 and J_2 large and negative. All the results discussed in Section 4.2 for this simple model are sound, they do not qualitatively depend on the value of the spins and are analogous to those obtained with all the other more complex model systems that we have investigated (see Section 4.2.1).

4.2   Results on Model d)

Fig. 4.4 shows the calculated value of ΔS_{max} as a function of J_1 and J_2. It is evident that the largest entropy variations are achieved for the two classes of systems i) and ii) mentioned above. It is important to note that when there are competing interactions large values of ΔS_{max} occurs only close to defined ratios of the exchange parameters (see the straight dark regions in the right half of Fig. 4.4). The ferromagnetic strong-exchange limit (bottom-left part of the figure) is characterised by a value of ΔS_{max} which is significantly smaller than those of the two previous cases.

This picture would suggest that systems i) and ii) are the ideal candidates for MCE. However, as discussed above, the shape of the $S(T)$ curves plays a key role in determining the actual cycles which can be implemented with these systems. In particular, the
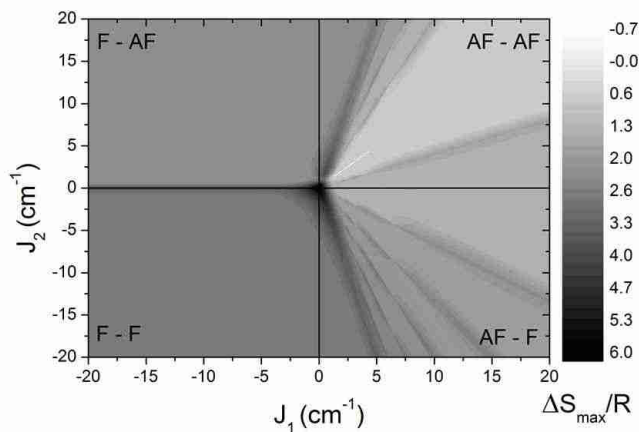
Figure 4.4: Calculated dependence of ΔS_{max} on the two exchange parameters J_1 and J_2. The darkest regions correspond to the largest maximal entropy variations.

entropy variation ΔS_{max} can be fully exploited only in cycles with very narrow temperature span ΔT_{span} centered at the temperature corresponding to ΔS_{max}, because otherwise it is not possible to perform the two adiabatic paths of the Carnot cycle. The actual entropy variation ΔS_{cold} that can be induced in a cycle (proportional to Q_c) and the ΔT_{span} can only be evaluated by considering the whole $S(0, T)$ and $S(\mathbf{B}, (\mathbf{T})$ curves. Fig. 4.5 reports the study of the main MCE observables as a function of J_1 and J_2. Panel a) displays the calculated entropy variation which can be exploited in an optimized Carnot cycle with $T_{cold} = 1$ mK [1] and $T_{hot} = 10$ K. It is evident that the heat Q_c ($\propto \Delta S_{cold}$) absorbed by the refrigerant in each cycle is large when both J_1 and J_2 are strong and negative, i.e., in the ferromagnetic strong-exchange limit (hereafter iii)). Conversely, in the regions corresponding to i) and ii) the entropy variation is very small or zero, implying that the Carnot cycle is inefficient or cannot be implemented at all. We stress that the really non-interacting case ($J_1 = J_2 = 0$) provides the best thermodynamic cycles, but it is extremely fragile with respect to J_1 and J_2. In fact, even small values the exchange parameters strongly deteriorates its refrigeration performances [2].

This behavior can be understood by inspecting Fig. 4.6, where the $S_0(T)$ and $S_{\mathbf{B}}(T)$ curves are reported for three representatives sets of parameters. Even if the zero-field entropy and ΔS_{max} are much larger for the parameter sets belonging to families i) and ii), the slope of the $S_{\mathbf{B}}(T)$ curve is significantly smaller in iii) yielding to much more efficient Carnot cycles. This different behavior is due to the presence of a large number of low-lying excited levels in i) and ii). Indeed, on the one hand they lead to large values of the low temperature entropy and of ΔS_{max}, but on the other hand these levels strongly affect and increase the slope of $S_{\mathbf{B}}(T)$. Fig. 4.6 also reports the best Carnot cycles for cases i) and iii), while for case ii) the cycle in the considered temperature interval cannot be even implemented. The parameter region $J_1 \ll 0$ and $J_2 \gg 0$ corresponds to the strong-exchange limit in which spin number 1 is locked antiparallel to the others. Hence, it is

---

[1]$T_{cold} = 1$ mK has been assumed as a reference value for ultra-low temperatures, the actual achievable value of T_{cold} depends also on the here-neglected magnetic anisotropy and inter-molecular dipolar interactions.

[2]The dimension of the central black point is indeed smaller than the width of the axes.
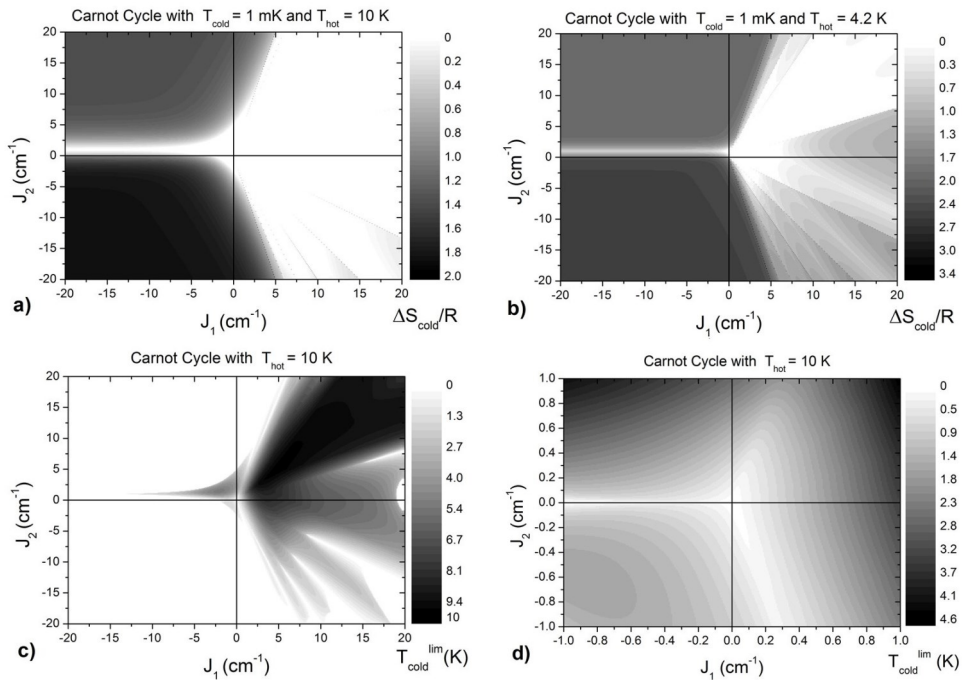
Figure 4.5: Study of the main MCE observables as a function of J_1 and J_2 with $\Delta B = 7$ T. The greyscale reports the values of a) the entropy variation for a Carnot cycle with $T_{cold} = 1$ mK and $T_{hot} = 10$ K; b) the same with $T_{cold} = 1$ mK and $T_{hot} = 4.2$ K c) the minimal value of T_{cold} for a Carnot cycle with $T_{hot} = 10$ K; d) zoom of panel c near the non-interacting limit.

analogous to the case iii) but the efficiency is significantly smaller because the total spin of the ground multiplet is diminished by $2s$ with respect to the fully ferromagnetic case.

By considering cycles with a smaller ΔT_{span} ($T_{cold} = 1$ mK and $T_{hot} = 4.2$ K) the qualitative picture does not change but the performance of i) and ii) improves (see Fig. 4.5-b)), because the smaller temperature variation allows one to use a larger part of the maximal entropy variation. It is worth to note that in this case, efficient MCE systems would be found also in presence of competing interactions, but only for specific values of the ratio $\frac{J_2}{J_1}$ (see the very narrow lines in the bottom right part of Fig 4.5-b)). These situations require an extreme degree of chemical control and thus are probably unrealistic. Conversely, the performance of molecular nanomagnets with strong ferromagnetic interactions does not depend on the precise values of the parameters. Figs. 4.5-c) and 4.5-d) show the lowest value of T_{cold} which can be reached in a Carnot cycle with $T_{hot} = 10$ K as a function of J_1 and J_2. While in the ferromagnetic strong exchange limit it is possible to have $T_{cold} \to 0$, in the case of competing interactions or in the presence of small ferromagnetic couplings this is generally not true because of the shape of the $S_{\mathbf{B}}(T)$ curves.
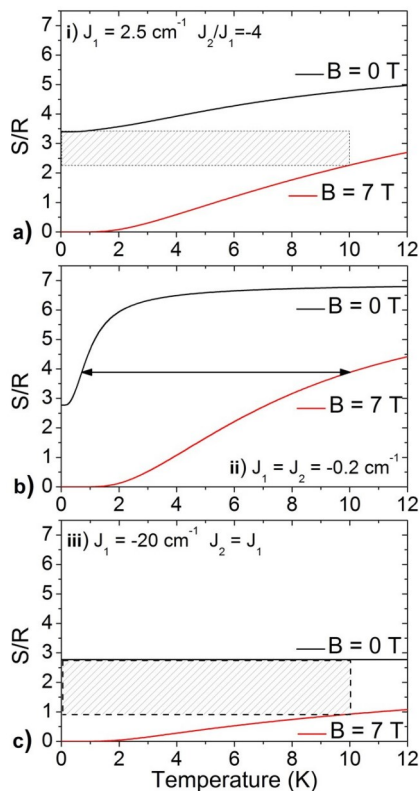
Figure 4.6: $S(T)$ curves for cases i) (panel a)), ii) (panel b)) and iii) (panel c)) with B = 0 T and B = 7 T. The shaded areas in panel a) and c) represent the best Carnot cycles with $T_{cold} = 1$ mK and $T_{hot} = 10$ K for cases i) and iii) respectively. The horizontal arrow in panel b) shows that for case ii) it is not possible to build a closed Carnot cycle able to reach $T_{cold} = 1$ mK from $T_{hot} = 10$ K.

4.2.1 Results on Other Model Systems

The same calculations reported in the previous section have been performed for all the other ideal systems. Fig. 4.7, Fig. 4.8 and Fig. 4.9 show some of the main MCE observable calculated as a function of J_1 and J_2 for the model systems in Fig. 4.2-a, 4.2-b and 4.2-c respectively. In panel a) we report the value of ΔS_{max}, while panel b) shows the entropy variation ΔS_{cold} which can be exploited in an optimized Carnot cycle with T_{cold} and T_{hot} = 10 K (both with $\Delta B = 7$ T). Calculations for model a) are particularly time consuming, due to its larger Hilbert space. In order to reduce the computational efforts we have also exploited the finite-temperature Lanczos method (see Section 1.1.3) to calculate its observables. Calculations on model b), c) and d) can be performed exactly. The results shown in Fig. 4.7, Fig. 4.8 and Fig. 4.9 confirm the conclusions reported in Section 4.2 for the 5-sites simple model. The largest entropy variations are always found for systems with competing AF interactions with defined ratios of the exchange parameters (class i)), or with weak ferromagnetic interactions (class ii)). On the other hand, the largest Q_c (proportional to ΔS_{cold}) which can be exploited in Carnot cycle with T_{cold} = 1 mK and T_{hot} = 10 K are obtained in the ferromagnetic strong-exchange limit. As

pointed out in Section 4.2, the truly non-interacting case ($J_1 = J_2 = 0$) provides the best thermodynamic cycles, but it is extremely fragile with respect to J_1 and J_2 in every model systems. Indeed, the dimension of the central black point is indeed smaller than the width of the axes in Figs. 4.7-b, 4.8-b and 4.9-b.

4.2.2   Analysis of $\Delta S_{\mathbf{max}}$ graphs

Figs. 4.4, 4.7-a, 4.8-a and 4.9-a show that in the AF-F and AF-AF quarters of the $\Delta S_{\max}$ graphs as a function of J_1 and J_2 there are many "dark lines". We have verified that these regions of the parameter space correspond to ratios J_2/J_1 in which the ground state multiplet is degenerate with the first excited one (the multiplets involved always have consecutive total-spin values, S and S+1). In these particular configurations the large number of degrees of freedom, due to degenerate low-lying levels, increases the total magnetic entropy of the system, leading to an enhanced entropy variation $\Delta S_{\max}$. The darkest line in the AF-F quarter of each $\Delta S_{\max}$ graph corresponds to the ratio $-r_{\max}$ = J_2/J_1 leading to the maximum possible degeneracy in the ground state, i.e. when the two highest total spin multiplets are degenerate. This maximum possible degeneracy can't be achieved in the AF-AF quarter, but we anyway find high degeneracy and a large $\Delta S_{\max}$ at the same $r_{\max}$. Fig. 4.10 shows the energy of the ground state of each total-spin multiplet as a function of the ratio J_2/J_1, respectively for model a), b), c) and d) (for the sake of simplicity one of the parameters has been set to $J_1 = 1$ cm^{-1}).

As expected, the number of line/ number of degenerate configurations in the AF-F and in the AF-AF quarters strongly depends on the topology of the exchange interactions, on the number of sites and on the local spin value (and therefore on the Hilbert space dimension and on the number of total-spin multiplets). The starting point to predict the number of lines is the determination of the ground state multiplet when $J_2 = 0$ ($S_{GS}^{J_2=0}$), which depends on the local spin value and on the exchange interactions scheme. In the AF-F configuration, we know that it is possible to have the highest total-spin multiplet $S_{\max}$ as a ground state, when the ferromagnetic parameter J_2 is stronger than the AF J_1, $J_2 \geq -r_{\max}J_1$ (leading to configurations where all the spins are parallel). Therefore the number of "lines" $N_{\text{AF-F}}$ in the AF-F quarter is given by:

$$N_{AF-F} = S_{max} - S_{GS}^{J_2=0}, \tag{4.2}$$

(if the ground state with $J_2 = 0$ is degenerate, we take $S_{GS}^{J_2=0}$ equal to the highest value of the total-spin). Thus the number of lines corresponds to the number of degenerate configurations between two consecutive total-spin multiplets S and S+1 occurring from the ground state $S_{GS}^{J_2=0}$ to $S_{\max}$ when increasing the ratio J_2/J_1.

In the AF-AF configuration the highest total-spin multiplet in the ground state S_{max}^{AF-AF} is achieved when the AF parameter J_2 is stronger enough than the AF parameter J_1, $J_2 \geq r_{\max}J_1$ (in model d) this situation corresponds to a configuration where all the spins in the squared base are anti-parallel to the vertex spin and parallel to each other). Therefore the number of "lines" in the AF-F quarter is given by:

$$N_{AF-AF} = \left(S_{max}^{AF-AF} - S_{GS}^{J_2=0}\right) - 2\left(S_{GS}^{J_2=0} - S_{min}\right) = S_{max}^{AF-AF} + S_{GS}^{J_2=0} - 2S_{min}, \tag{4.3}$$

where the term $2\left(S_{GS}^{J_2=0} - S_{min}\right)$ takes into account the degenerate configurations involving the $S_{GS}^{J_2=0}$ and multiplets with lower total-spin values (which occur twice).

Model a) has a higher degree of frustration and a higher number of ions in respect of all the other models, leading to a much more complex behavior of the low-lying levels
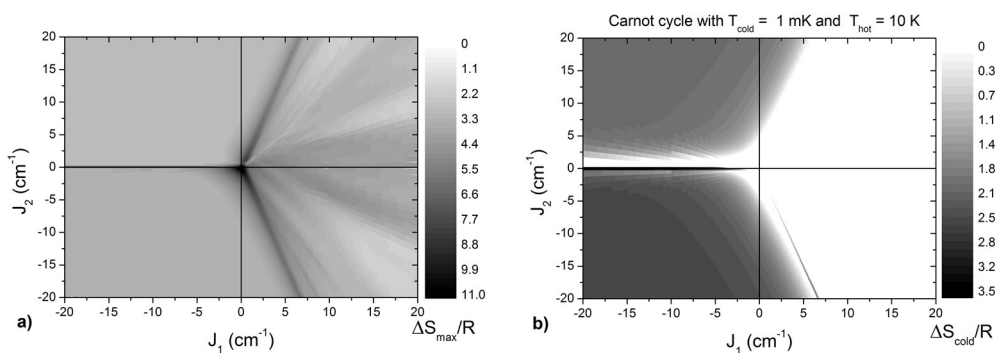
Figure 4.7: Study of some MCE observables as a function of J_1 and J_2 for the 10-sites ideal model system (Fig. 4.2-a). The greyscale reports a) ΔS_{max} and b) the entropy variation ΔS_{cold} for a Carnot cycle with $T_{cold} = 1$ mK and $T_{hot} = 10$ K, both calculated with $\Delta B = 7$ T.

Figure 4.8: Study of some MCE observables as a function of J_1 and J_2 for the 7-sites ideal model system (Fig. 4.2-b). The greyscale reports a) ΔS_{max} and b) the entropy variation ΔS_{cold} for a Carnot cycle with $T_{cold} = 1$ mK and $T_{hot} = 10$ K, both calculated with $\Delta B = 7$ T.
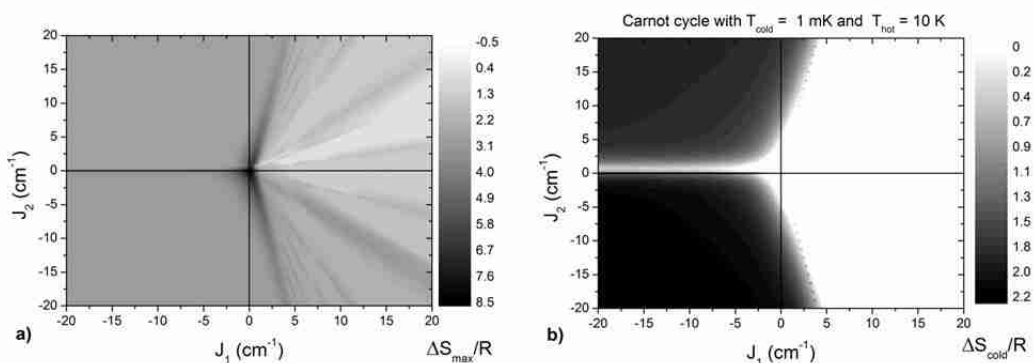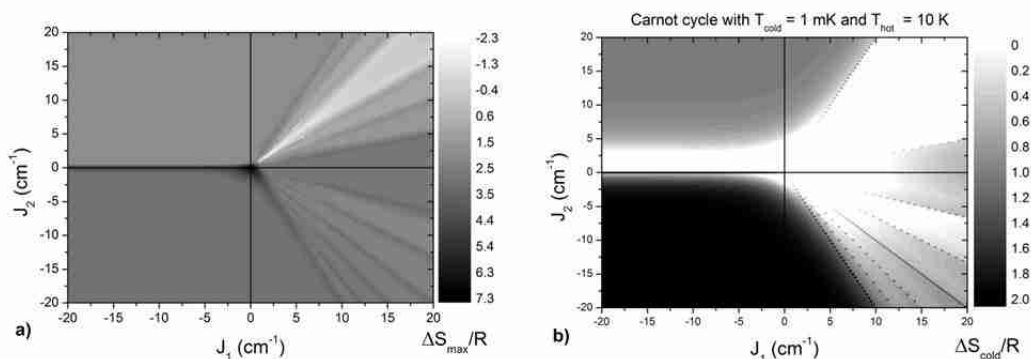

Figure 4.9: Study of some MCE observables as a function of J_1 and J_2 for the 6-sites ideal model system (Fig. 4.2-c). The greyscale reports a) ΔS_{max} and b) the entropy variation ΔS_{cold} for a Carnot cycle with $T_{cold} = 1$ mK and $T_{hot} = 10$ K, both calculated with $\Delta B = 7$ T.
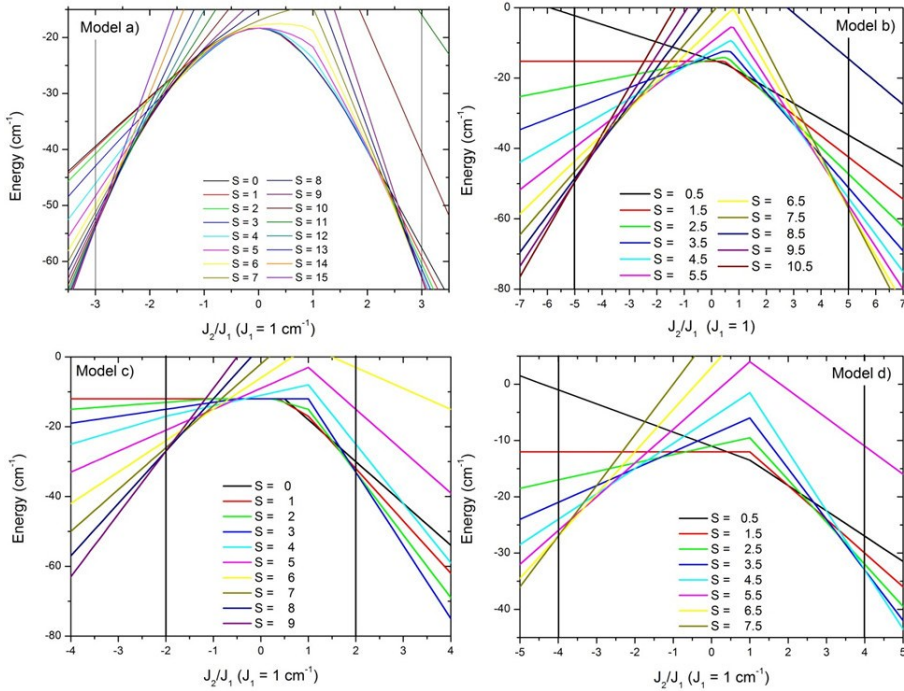
Figure 4.10: Energy of the ground state of each total-spin multiplet as a function of the ratio J_2/J_1 respectively for model a), b), c) and d). The straight black lines indicate the ratios $\pm r_{max}$.

as a function of J_2/J_1. In fact, different degenerate configurations have similar parameter ratios and they also have excited multiplets very close in energy (see Fig. 4.10 for model a)). This "band-like" behavior of the ground states of the total-spin multiplets leads to very close and often unresolved lines in the ΔS_{max} graph (the "darkest lines" corresponding to $\pm r_{max} = 3$ are anyway well recognizable in the ΔS_{max} graph, see Fig. 4.7-a).

4.3   Fe$_{14}$ and Fe$_{14}$-like systems

In order to understand the behavior of the reference system Fe$_{14}$, whose large Hilbert space makes almost impossible to diagonalize its Hamiltonian, we have also studied two ideal clusters with $s_i = 1$ and $s_i = 3/2$, Ni$_{14}$ and Cr$_{14}$. Even if they have a smaller Hilbert space than Fe$_{14}$, we have to use Lanczos diagonalization techniques to study their energy spectrum (see Sec. 1.1.3), in order to speed up our calculations. DFT and Monte-Carlo calculations show that Fe$_{14}$ has four distinct antiferromagnetic exchange interactions, whose competition leads to an high spin ground state and low-lying excited levels (for further details see Ref.[125]).

We study the ideal systems Ni$_{14}$ and Cr$_{14}$ with a two exchange parameters model: $J_1 = J_3$ for the weak interactions (within the 6-sites ring and between the triangular caps and the ring) and $J_2 = J_4$ for the strong ones (apical ions with the ring and with the triangular caps respectively), as shown in the inset of Fig. 4.11. This choice is justified by the values obtained with DFT and Monte-Carlo calculations [125] and it has already
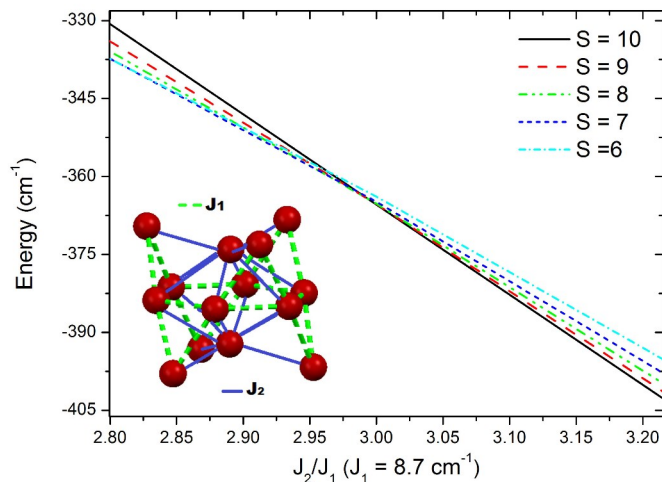
Figure 4.11: Particular of the ground state of the total-spin multiplets of Ni_{14} (from S = 6 to S = 10) as a function of J_2/J_1. We highlight the region around $J_2/J_1 = 3$ where we find the best RCP. Inset: exchange interaction scheme of Fe_{14} with the two parameters model.

been used in the two parameters model of Ref.[116], to explain experimental data. We keep $J_1 = 8.7$ cm^{-1}, corresponding to the strongest between the two weak interactions in Fe_{14}[125], in order to evaluate the MCE in the worst possible case. Then we study the ground state of each total-spin multiplet as a function of J_2/J_1. We report our results for Ni_{14} in Fig. 4.11. The graph shows that when $J_2/J_1 = 3$ the ground states of the total-spin multiplets S = 10 and S = 9 are degenerate and they have the lowest energy. Thus the system has an highly-degenerate ground state. In addition, as we can see from Fig. 4.11, for a range of values around $J_2/J_1 = 3$, the ground states of some high spin multiplets (from S = 6 to S = 10) are really close in energy to each other (the gaps are less than 1 cm^{-1}). Thus the system also has low-lying excited states. We have confirmed this result with Cr_{14}, where the total-spin multiplets S =15 and S = 14 form an highly degenerate ground state when $J_2/J_1 = 3$. This behavior is also similar to that shown by our model a) in Fig. 4.10, which indeed has a topology which is equivalent to that of Fe_{14} cluster. Therefore we can conclude that this "band-like" behavior of the energy spectrum is due to the topology of the exchange interactions and it doesn't depend on the value of the local spin s_i and on the number of magnetic ions. Thus we can expect Fe_{14} to have a similar structure of the energy spectrum and we can consider model a) as a good ideal model system to better understand the effects of the topology on the MCE.

4.4 Discussion and Conclusions

All the results discussed above have been obtained by assuming a magnetic field variation range 0-7 T, but we have checked that the same conclusions can be drawn if the maximum field is restricted to 1 T. In addition, the presented findings do not depend on the values of the local spin s, indeed the increasing of s only leads to an overall improvement of the performances of these systems for magnetic refrigeration. Increasing the

number of magnetic ions allows to boost the entropy variations and thus to improve the performances of the refrigerant. The precise topology of the exchange interaction does not play a key role in classes of systems ii) and iii), while it is crucial in the case of MNMs with competing interactions. We have checked that the conclusions drawn in this work are confirmed also by increasing the number of spins (see Sec. 4.2.1). It is worth to note that an increase in the number of spins per molecule also rises the magnetic contribution to the specific heat.

As already discussed in literature [46], the presence of magnetic anisotropy is harmful for exploiting MNMs for MCE applications, hence S ions (with orbital angular momentum L=0) like Mn^{2+} or Fe^{3+} have to be used in the design of molecules for magnetocaloric applications. An alternative possibility would be to exploit magnetic organic radicals, which are magnetically isotropic and are typically characterised by very strong exchange couplings. In addition, anisotropy effect due to Dzialoshinski-Moriya interaction can also be controlled by choosing systems with exchange bonds characterised by inversion symmetry. Anyway, in S ions the Dzialoshinski-Moriya energy scale is of the order of $0.1 \div 1\%$ of Heisenberg one, and it can therefore be considered as a small perturbation. The presence of inter-molecular dipolar interactions may limit the value of the achievable T_{cold}, since it is not possible to go below the temperature range set by the order of magnitude of these interactions via adiabatic demagnetization. If the energy scale of the dipolar coupling is too large for the specific MCE application, one can diluted the molecular cooler by mixing it with a non-magnetic analog or by using bulkier ligands [126].

In conclusion, we have considered explicitly Carnot cycles and performed calculations in ideal model systems to understand the characteristics of a MNM yielding an efficient MCE between $T \simeq 10$ K and the sub-Kelvin region. We have demonstrated that the best molecular MCE refrigerants in this temperature range are those based on molecules containing magnetic ions strongly ferromagnetically coupled, contrarily to the common belief. Hence, molecules without RE ions can be excellent magnetocaloric materials. This recipe will be a stimulus for designing new MNMs for magnetic refrigeration, which represents an intriguing field requiring a close collaboration between physicists and chemists.

Local Magnetic Properties of Cr_7Ni-green AF Ring

In this Chapter we focus on a particular subgroup of MNMs, the so-called antiferromagnetic (AF) rings [127, 11]. They have an almost coplanar ring shape with a number N of transition metal ions connected by bridging ligands, which mediate nearest-neighbor superexchange interaction J. Even numbered AF rings with N = 6, 8, 10, 12 and 18 have been synthesized with different transition metal ions, e.g. Fe^{3+} (s = 5/2) [11, 12, 13, 14], Cr^{+3} (s = 3/2) [15], V^{3+} (s = 1) [16] and Cu^{2+} (s = 1/2) [17]. A common feature of all even numbered AF rings is to have a spin singlet S = 0 ground state since they have dominant AF exchange couplings. Due to the finite size effects, AF rings have a discrete energy spectrum and the lowest-lying excited states for the total-spin S are known to be approximately given by the so-called Landè interval rule [18]. An external magnetic field lifts the degeneracy of the M_S levels thus inducing successive ground-state crossovers. Furthermore, intramolecular anisotropic interactions lead to uniaxial anisotropy and zero field splitting of the total spin multiplets.

One of the most studied AF ring is the homometallic Cr_8. It is formed of eight Cr^{3+} ions (s = 3/2) which indeed display at low temperature a total S = 0 ground state with zero expectation value of the local spins. When one Cr^{3+} ion is replaced by a diamagnetic ion (e.g. Cd^{2+}) or by a different magnetic ion (e.g. Ni^{2+} with s = 1) the ground state becomes magnetic and there is a redistribution of the local spin density. There exist two main families of these AF rings. The first one and the most studied is that of AF Cr_7M *green* rings, where M is a divalent ion, e.g. Ni^{II}, Mn^{II}, Zn^{II}, Co^{II}, Cu^{II}). They are indeed green in colour, and the transition metal ions form an almost regular octagon, with the divalent metal site disordered about the eight sites. Each edge of the octagon is bridged by one fluoride and two pivalates [19]. The other family is that of AF Cr_7M *purple* rings, which are indeed purple in solution and solid state. The main difference with the green ones is that purple rings have five bridging alkoxide groups within the ring, with only three bridging fluorides. Seven of the eight edges of the octagon have two bridging pivalate ligands attached, however the eighth edge has only a single bridging pivalate and a bridging fluoride [128].

In this Chapter we investigate magnetic properties of AF green Cr_7Ni rings. Local spin density in the Cr_7Ni is studied with ^{53}Cr-NMR and we also investigate the the origin of the magnetic anisotropy in Cr_7Ni clusters grafted on surfaces. Spin dynamics of Cr_7M purple rings will be discussed in the following Chapter.

5.1 Local Spin Density in the Cr_7Ni AF Molecular Ring and ^{53}Cr-NMR

In this section we present ^{53}Cr-NMR spectra collected at low temperature in a single crystal of the heterometallic AF ring Cr_7Ni in the S = 1/2 ground state, with the aim

of establishing the distribution of the local electronic moment in the ring. ^{53}Cr-NMR has been measured in a previous work on Cr_7Cd and the local spin density in the ring has been determined unambiguously with excellent agreement with theory [129]. In this cluster, where the Heisenberg interaction between nearest-neighbor magnetic centers is interrupted by the s = 0 Cd^{2+} ion, the local spin density in the ground state turned out to be rather uniformly distributed over the ring with an alternated staggered orientation due to the AF coupling. Thus it appears of interest to investigate how the single Cr^{3+} ion spin moment is distributed in an heterometallic ring where one Cr ion is replaced by a different magnetic ion rather than a diamagnetic one, like Cr_7Ni heterometallic ring. During the last few years it has been shown that Cr_7Ni is a very promising system to encode a qubit [20]. Indeed, it behaves as an effective spin 1/2 at low-T and can be manipulated in times much shorter than the measured decoherence time [21]. These molecular rings can be linked to each other either directly or through magnetic ions to form dimers; the resulting inter-ring magnetic coupling is sizeable and can be tuned by choosing the linker [34]. The site dependence of the local spin density plays a key role in the scheme proposed for obtaining time dependent qubit–qubit couplings in the presence of permanent exchange interactions [20].

Figure 5.1: Schematic representation of the Cr_7Ni heterometallic ring. Only the Cr^{3+} magnetic ions and the F^- bridging ligands are shown for simplicity.

In this work ^{53}Cr-NMR signals in Cr_7Ni in its S = 1/2 ground state have been observed, which give a determination of the local spin density of each ion. However, due to intrinsic difficulties of the ^{53}Cr-NMR measurement (low gyromagnetic ratio and low sensitivity), only one out of the three expected ^{53}Cr-NMR signals was detected down to 100 mK while the ^{61}Ni signal was too weak to be detected at any temperature. Nevertheless, the distribution of the local spin moments could be calculated theoretically as a function of the external magnetic field at low temperature and we could prove that the observed ^{53}Cr-NMR spectrum arises from three almost equivalent ^{53}Cr nuclei in the ring. The comparison with the theoretical results gave an excellent agreement by assuming a core polarization hyperfine field slightly smaller than the one observed in Cr_7Cd. In particular, since the measurements were performed in a good quality single crystal, we could verify the theoretical prediction about anisotropy which yields different local spin densities for different orientations of the external field. This result gives total con-

fidence about the theoretical calculations which show that the redistribution of the local spin density in the heterosubstituted Cr_7Ni ring is similar to the one observed in the heterometallic Cr_7Cd ring where the heterocenter is diamagnetic.

5.1.1 Experimental Results

The ^{53}Cr-NMR spectrum was collected at 1.6 K with a homemade high power pulsed NMR spectrometer. Typical spectra measured at several resonance frequencies and by applying the magnetic field perpendicular to the plane of the ring (H // molecular z-axis) are shown in Fig. 5.2-a. Increasing the resonance frequency the peak position in the spectrum shifts to higher magnetic field. In Fig. 5.2-b the resonance frequency is plotted as a function of the peak position in terms of the magnetic field. This figure reports the data collected by applying the magnetic field perpendicular to the plane of the ring (H // z-axis) and parallel to the plane of the ring (H ⊥ z-axis) (Cr_7Ni crystals have one ring for unit cell, thus all the rings in the crytsalline sample are coplanar). Different data sets are shown, corresponding to different experimental runs. The data for both orientations show a linear behavior with slope given by the gyromagnetic ratio of the ^{53}Cr nuclear isotope (9.54% abundance), i.e. $\gamma/2\pi = 2.406$ MHzT^{-1}.
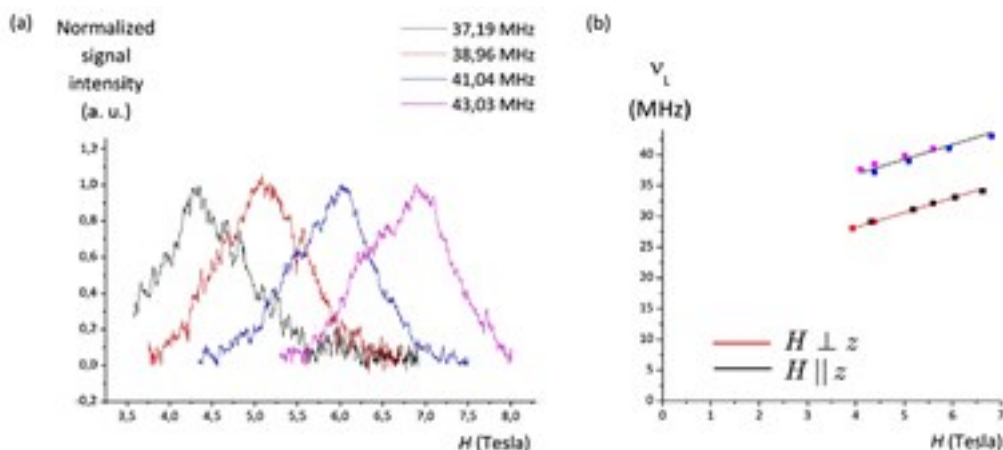

Figure 5.2: (a) Representative ^{53}Cr-NMR spectra at 1.6 K obtained by sweeping the magnetic field at constant frequency. The field is applied perpendicular to the ring's plane. (b) Plot of the resonance frequency versus magnetic field at the center of the NMR line. We plot the data for two orientations of the magnetic field with respect to the plane of the ring in the single crystal. The straight lines are the best fits used to determine the slope of the curve.

The NMR line is very broad and the width slightly increases with increasing magnetic field (Fig. 5.2-a). In these experiments we have measured the central line transition ($I_z = +1/2 \rightarrow -1/2$) of the ^{53}Cr (I = 3/2) NMR spectrum which is shifted only in second order by the quadrupolar interaction, whereby the shift is inversely proportional to the applied magnetic field [130]. Thus the second order quadrupole broadening would be inversely proportional to the applied field. The observed slight increase of the NMR width in Fig. 5.2-a indicates that a magnetic rather than quadrupole broadening mechanism is dominant at high magnetic fields. The magnetic broadening mechanism is most likely due to non-negligible contributions from the anisotropic hyperfine fields at the nuclear

sites which can be different for the different ^{53}Cr sites in the ring and for different rings in the crystal. It is also possible that the broadening of the lines is due to a mosaic spread of our single crystals, often present in nanomagnets. The NMR signal at 1.6 K can be observed only at high fields. In fact, at low temperatures Cr$_7$Ni behaves as an effective spin S = 1/2 and if a high external field is applied along the z-axis only one level of the doublet $|S = 1/2; M = \pm 1/2\rangle$ is thermally populated [95]. Thus, low temperatures and high fields are required to stabilize the local spin configuration and to observe the NMR signal in the magnetic ground state [129, 131].

5.1.2 Analysis of the Data and Discussion

The ^{53}Cr-NMR frequency is expected to be proportional to the vector sum of the external magnetic field H and the internal field due to the hyperfine interaction (see Section 2.2.2). By considering the case of the internal field being parallel (or antiparallel) to the external field and by considering only the dominant isotropic core polarization hyperfine contact term A one can write:

$$\nu_L = \frac{\gamma}{2\pi} \left(H + g\langle s \rangle A \right), \tag{5.1}$$

where γ is the ^{53}Cr nuclear gyromagnetic ratio, g is the Cr^{3+} Landè factor and $\langle s \rangle$ is the local expectation value of the Cr^{3+} electronic moment. If $\langle s \rangle$ is field independent, Eq. 5.1 predicts the linear H dependence of the resonance frequency observed in Fig. 5.2.

In order to compare the experimental data to the local spin density in the ring we turn now to the theoretical calculation of the local spin density $\langle s \rangle$ in the ground state of the ring. Low-temperature properties of the Cr$_7$Ni AF ring can be described by the following Spin Hamiltonian:

$$\mathcal{H} = \sum_{i=1}^{N} J_{i,i+1} \mathbf{s}_i \cdot \mathbf{s}_{i+1} + \sum_{i=1}^{N} d_i \left[s_{i,z}^2 - \frac{1}{3} s_i (s_i + 1) \right] + \tag{5.2}$$
$$+ \sum_{i>j=1}^{N} D_{ij} \left[2 s_{i,z} s_{j,z} - s_{i,x} s_{j,x} - s_{i,y} s_{j,y} \right] - \mu_B \sum_{i=1}^{N} g_i \mathbf{H} \cdot \mathbf{s}_i,$$

where $\mathbf{s_i}$ is the spin operator of the ith magnetic ion (s_i = 3/2 for Cr^{3+} ions and s_i = 1 for the Ni^{2+} ion). The first term represents the Heisenberg nearest-neighbor exchange interaction, with the usual cyclic boundary condition N + 1 =1, N being the number of ions in the molecule (here N = 8). The second term accounts for uniaxial local crystal fields (z being the axis perpendicular to the plane of the ring) and the third term is the axial contribution to the dipolar anisotropic intracluster spin–spin interaction, where D_{ij} is evaluated within the point-dipole approximation. The last term is the Zeeman coupling to an external field. The parameters of the above Hamiltonian were determined by means of inelastic neutron scattering and thermodynamic measurements (J$_{Cr-Cr}$ = 16.9 K; J$_{Cr-Ni}$ = 19.6 K; d$_{Cr}$ = -0.35 K and d$_{Ni}$ = -4 K) [95, 68, 132].

In AF rings the dimension of the spin Hilbert space is large (e.g., 49152 for Cr$_7$Ni). Thus, in order to diagonalize the Hamiltonian in Eq. 5.2, we have followed the two-step perturbative technique described in Section 1.1.3, also including the often-neglected S-mixing effects [53]. Our calculations show that the reduction to the subspace spanned by the lowest spin exchange manifolds (up to 150 K) allows us to reproduce properly the low-temperature properties, reducing the computational effort. The calculated eigenstates and eigenvalues of the Hamiltonian in Eq. 5.2 have been used to evaluate the magnetic field dependence of the thermal averages of the local spin operators $s_{i,\alpha}$ (α =

x, y, z), as in Eq. 3.5. If the magnetic field is applied along the z-axis perpendicular to the ring's plane ($\theta = 0$) only $\langle s_{i,z} \rangle \neq 0$, while if the magnetic field is applied parallel to the ring's plane ($\theta = \pi/2$) only $\langle s_{i,k} \rangle \neq 0$, where k denotes the magnetic field in-plane direction.

Theoretical calculations are summarized in Fig. 5.3. The decrease of the local spin density at 1.6 K for fields below about 4 T is due to the reduction of the Zeeman splitting and to the consequent increasing population of the higher energy level of the S = 1/2 doublet ($|S = 1/2; M = -1/2\rangle$). The results at T = 0.1 K (see the dashed lines in Fig. 5.3) show a nearly constant $\langle s \rangle$ value down to low fields. From the inspection of Eq. 5.1 and of the experimental data in Fig. 5.2 it is clear that the observed ^{53}Cr-NMR signal must be ascribed to the nuclear sites 2, 4, 6 of Fig. 5.1. In fact the core polarization field is opposite to the local spin direction (A is negative in Eq. 5.1). Thus, since the local field of the observed NMR line adds to the external field (Fig. 5.2-b) it must arise from a negative (i.e. opposite to H) g$\langle s \rangle$ value in Fig. 5.3. Note that in the present convention g$\langle s \rangle$ (not -g$\langle s \rangle$) is the magnetic moment in Bohr magnetons (see equation Eq. 5.1).
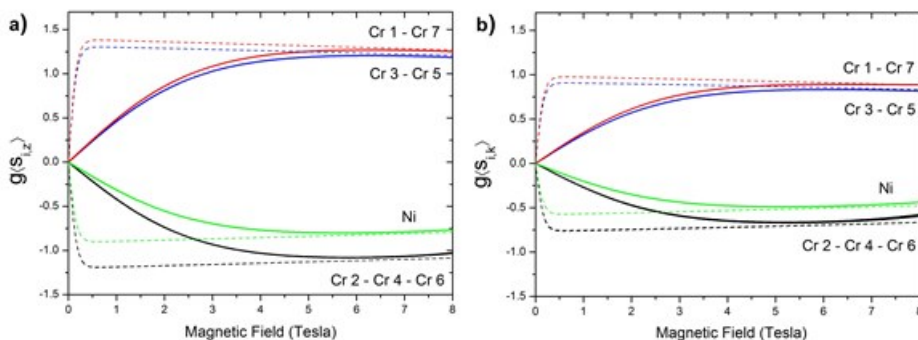

Figure 5.3: Theoretical results regarding the local spin density in the Cr$_7$Ni heterometallic ring at T = 1.6 K (solid lines) and T = 0.1 K (dashed lines) obtained by assuming in the Hamiltonian Eq. 5.2 the following parameters: J$_{Cr-Cr}$ = 16.9 K; J$_{Cr-Ni}$ = 19.6 K; d$_{Cr}$ = -0.35 K and d$_{Ni}$ = -4 K (previously determined by means of inelastic neutron scattering and thermodynamic measurements [95, 68, 132]). The numbering of the sites is shown in Fig. 5.1. Fig. a) shows the local spin values in the case of the magnetic field oriented perpendicular to the plane of the ring while Fig. b) refers to the case of the applied field oriented parallel to the plane of the ring.

The calculated electronic magnetic moments g$\langle s \rangle$ expressed in Bohr magnetons at T = 1.6 K are reported in Tab. 5.1 for the cases of the magnetic field applied parallel and perpendicular to the molecular ring plane. The comparison between results with two orthogonal directions of the applied magnetic field directly shows that the Cr^{3+} spins are characterised by a sizable local easy-axis anisotropy. The orientation dependence of the local spin moment for each Cr^{3+} ion originates from single-ion and dipolar anisotropies (d and D$_{ij}$ terms in the Hamiltonian) and reflects the mixing between different total spin multiplets (S-mixing) [53]. Indeed, even if the ground state is an isotropic S = 1/2 , the S-mixing mixes it with an anisotropic S = 3/2. One can object that the S-mixing of Cr$_7$Ni ground state is small, and indeed it is of the order of 1%. However, the contribution of the S-mixing to expectation values of the local spin operators on the eigenstates of the total Hamiltonian (which are ingredients in calculating the local magnetic moments, as w can see from Eq. 3.5) is larger. We can write expectation values on the basis of total

Hamiltonian $\{|j\rangle\}$ as:

$$\langle j|s_k|j\rangle = \sum_{\alpha,\beta} c_\alpha c_\beta \langle \alpha|s_k|\beta\rangle, \tag{5.3}$$

where $|\alpha\rangle$ and $|\beta\rangle$ states belong the total-spin basis and c_α and c_β are the components of the state $|j\rangle$ on the states $|\alpha\rangle$ and $|\beta\rangle$. Thus, c_α, c_β and $\langle\alpha|s_k|\beta\rangle$ are the three ingredient to be inspected in order to quantify the contribution of the S-mixing to the expectation values of the local spin operators. Therefore this contribution isn't of the order of magnitude of the S-mixing: Indeed it depends both on the matrix element $\langle\alpha|s_k|\beta\rangle$ and on the components (and not their squared modulus) of the ground state on the total-spin basis. It is also worthwhile to observe that the anisotropy effects responsible for S-mixing do not lead to an anisotropy barrier hampering the reversal of the molecular magnetization at low temperatures, like, e.g., in molecular nanomagnets such as Mn_{12} and Fe_8 [2].

	H $\perp$ z	H // z
Cr_1	0.88	1.25
Cr_2	-0.67	-1.07
Cr_3	0.82	1.19
Cr_4	-0.66	-1.07
Cr_5	0.82	1.19
Cr_6	-0.67	-1.07
Cr_7	0.88	1.25
Ni	-0.49	-0.80

Table 5.1: Theoretical electronic magnetic moment expectation values in Cr₇Ni at T = 1.6 K and H = 5 T corresponding to Fig. 5.3. The values listed are the electronic magnetic moments expressed in Bohr magnetons (g = 1.98 for the Cr^{3+} ions and g = 2.2 for the Ni^{2+} ion).

In Fig. 5.4 we have plotted the experimental results for the two orientations of the magnetic field by including the data obtained on different samples and in different runs. We also show the theoretical curves obtained by using Eq. 5.1 (at two different temperatures) and the theoretical values of $\langle s \rangle$ in Fig. 5.3. The only fitting parameter is the core polarization constant A. By choosing A = -11 T/μ_B the agreement is very satisfactory for both field orientations.

The value of the core polarization field A = -11 T/μ_B obtained for ^{53}Cr in Cr₇Ni can be compared to the one obtained in C₇Cd (i.e. A = -11.05 T/μ_B) by fitting the data of [129], in the case of the field being applied perpendicular to the plane of the ring, in the same way as done here. The two values are practically identical in agreement with the notion that the 3d wavefunction of the Cr^{3+} ion is not affected by the heterometallic substitution. It should be noticed that a higher value (i.e. A = -12.38 T/μ_B) was obtained in Cr₇Cd directly from the NMR data without using the theoretical results for the g$\langle s \rangle$ distribution in the ring [129]. This higher value is very close to the estimated theoretical value for a 3d core polarization field in the isolated Cr atom, i.e. A = -12.5 T/μ_B [130, 75]. We suggest that the smaller value (i.e. A = -11.05 T/μ_B) obtained by using the theoretically calculated spin densities is an indication of a slight delocalization of the
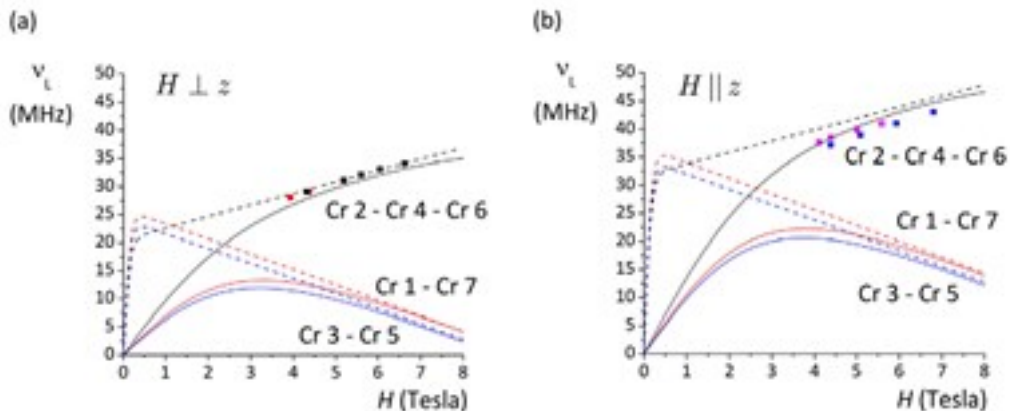
Figure 5.4: ^{53}Cr-NMR of a Cr$_7$Ni single crystal at T = 1.6 K: Resonance frequency versus applied magnetic field. (a) The magnetic field is applied perpendicular to the crystallographic z axis, namely parallel to the plane of the ring. (b) The magnetic field is applied parallel to the crystallographic z-axis, namely perpendicular to the plane of the ring. Solid lines show the theoretical predictions at T = 1.6 K obtained by using Eq. 5.1 with A = -11 T/μ_B and the g$\langle s \rangle$ calculated in Fig. 5.3. Dashed lines represent the theoretical predictions at T = 0.1 K.

3d wavefunction of the Cr^{3+} ion in the ring. Finally, one can compare our results with the first principle calculations of the contact field for Cr^{3+} reported in [58], namely -25 T/3μ_B = -8.3 T/μ_B. By comparing the results for the Cr 2, 4, 6 sites in the two different orientations of the magnetic field in the single crystal (see Fig. 5.4), it was also possible to experimentally confirm the easy-axis anisotropy for the local spin moments of Cr^{3+} predicted by the theoretical calculations based on the Hamiltonian previously determined by neutron spectroscopy and magnetic measurements (Tab. 5.1). In fact, the ^{53}Cr-NMR frequency is higher when the magnetic field is applied parallel to the crystallographic z-axis, due to the larger absolute value of the local spin density (see Eq. 5.1). From the inspection of Fig. 5.4 it is also clear that the signals due to sites 1, 7, 3, 5 (see Fig. 5.1) are difficult to detect at T = 1.6 K since the expected resonance frequency is low in the whole magnetic field range. At very low temperature, where the spin density $\langle s \rangle$ remains constant down to low values of H, the expected resonance frequency would be higher (see the dashed lines in Fig. 5.4). We did try to detect the signals at T = 100 mK by using a dilution refrigerator but the radiofrequency probe head did not have sufficient sensitivity. Furthermore, it would be interesting to be able to follow the NMR signal at low fields where the $\langle s \rangle$ values decrease due to the thermal population of the first excited level. Unfortunately, thermal fluctuations are likely to decrease the nuclear spin lattice, T_1, and spin–spin, T_2, relaxation times making the signal too broad to be observed. Also, second order quadrupole effects may shift and broaden the signal at low magnetic fields [130]. One possibility would be to synthesize ^{53}Cr isotopically enriched samples to improve the S/N ratio of the NMR signal.

5.1.3 Conclusions

In conclusion we have shown that the ^{53}Cr-NMR signal observed at high magnetic field values and at T = 1.6 K in Cr$_7$Ni is in excellent agreement with the local spin density

distribution calculated theoretically including effects due to the anisotropy, which could be evidenced by using a single crystal in the NMR experiment. The core polarization hyperfine constant turns out to be almost the same in Cr$_7$Cd and Cr$_7$Ni indicating that the heterometallic substitution in the Cr$_8$ ring does not affect the local 3d wavefunction at the Cr^{3+} site. The main result appears to be the fact that the local spin density redistribution in the heterometallic rings is rather uniform for both the diamagnetic substitution (i.e. Cr$_7$Cd) and the magnetic substitution (i.e. Cr$_7$Ni). However, although we have similar staggered spin moment distributions for both cases, the absolute values of the spin moments are different. In the case of Cr$_7$Cd the spin moments of the Cr^{3+} ions are slightly smaller ($\sim$2 μ_B) than 3 μ_B which is the value expected for Cr^{3+} isolated ions [129]. On the other hand, for Cr$_7$Ni each Cr^{3+} spin moment is much smaller ($\sim$1 μ_B) than 3 μ_B. This indicates that the disconnection of the magnetic interaction due to a diamagnetic ion leads to a larger perturbation that destroys the spin singlet state of the mother material, i.e. Cr$_8$, with S = 0 ground state characterised by local $\langle s \rangle$ = 0 values.

5.2   Magnetic Anisotropy of Cr$_7$Ni Spin Clusters Grafted on Surfaces

In this section we address the problem of the experimental and theoretical determination of magnetic anisotropy in isolated molecular spin clusters. To this end, the case of molecular Cr$_7$Ni rings sublimated in ultrahigh vacuum conditions and assembled in an ordered fashion on Au(111) surface is addressed and investigated using X-ray magnetic dichroism (XMCD) and theoretical calculations.
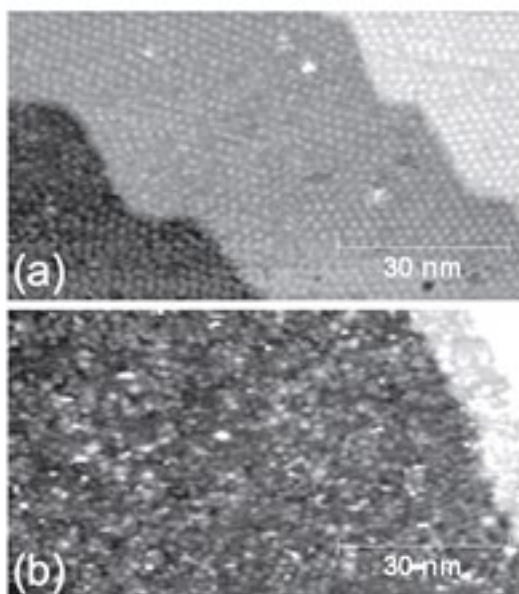

Figure 5.5: STM image of one complete self-assembled monolayer of Cr$_7$Ni-bu (upper panel) and Cr$_7$Ni-thiobu (lower panel) deposited by sublimation on Au(111) surface. Tunneling conditions: 2 V and 20 pA. Scan area 90 × 50 nm 2 .

Since we investigate Cr$_7$Ni magnetic properties, we can take advantage of several

special conditions. Firstly, the extra magnetic ion (Ni^{2+}) unbalances the Cr ring magnetization and acts as local probe inside the ring, as demonstrated in previous works [95]. So far XMCD has been used to measure the total molecular magnetization, i.e., considering the features of the ground state multiplet of the whole molecule [133, 134]. Yet, X-ray photons interact with single transition metal ions having their own local magnetic anisotropy projected on the molecular states that, in turns, may have different type of anisotropy one to another. So, the actual alignment of the magnetization of single ion depends on the features of the dominant multiplets at working conditions and it indirectly reflects the characteristics of the whole spin cluster, besides the local environment. This issue is somehow masked in homometallic molecules but it can be properly addressed in heterometallic ones, such as Cr$_7$Ni rings [135] and Fe$_3$Cr [136, 137]. Interestingly, the chemical specificity of XMCD allows to elucidate this interplay between the magnetization of the single ion and that of the entire molecule. While the importance of magnetic anisotropy for large spin single molecule magnets is well recognized, it is worth noting that the control and the understanding of magnetic anisotropy is also relevant for the spin manipulation in molecular qubits like the F Cr$_7$Ni.

Secondly, Cr$_7$Ni rings can now be successfully assembled in ordered fashion on Au(111) surface by UHV sublimation [138]. Namely, no changes are observed on the chemical features and only minor variations are observed on magnetism of isolated Cr$_7$Ni rings that lay all flat and well packed (hexagonal arrangement) on gold surface (Fig. 5.5) [138]. Moreover, for the experimental investigation different types of molecule-surface interaction have been used, namely two different functionalizations of the rings deposited on Au(111) and HOPG substrates.

Since the ground state of Cr$_7$Ni is an isotropic doublet, experiments have been performed at finite temperature and magnetic field in such a way that the first excited S = 3/2 multiplet, with in-plane anisotropy, is the dominant one. Spin Hamiltonian simulations are then used to clarify the alignment of the Ni magnetization and the interplay between the local and the molecular magnetic anisotropy.

5.2.1 Experimental Results

In Fig. 5.6 the Cr and Ni L$_{2,3}$ XAS and XMCD spectra for the two monolayers (MLs) (i.e., Cr$_7$Ni-bu and Cr$_7$Ni-thiobu) on Au(111) and the Cr$_7$Ni-bu ML on the HOPG surface are compared with those of the corresponding microcrystalline thick film (TF). Remarkably, both the XAS and XMCD spectral line-shapes for MLs perfectly resemble those of the TFs, demonstrating that deposition by sublimation does not affect the valence electronic structure of the Cr and Ni ions, namely oxidation state, local environment and crystalfield intensity at the Cr and Ni sites. More specifi cally, for all samples the Cr absorption spectra present eight features characteristic of Cr3+ in a nearly O$_h$ environment, whereas Ni spectra present two peaks at the L$_3$ edge and a partially resolved doublet structure at the L$_2$ edge, characteristic of a high-spin Ni^{2+} ion in nearly O$_h$ symmetry [139]. In these molecular rings, when an external magnetic field H is applied, there is a competition between the antiferromagnetic coupling between nearest-neighboring ions and the Zeeman interaction, tending to align the magnetic moments along the field direction. The XMCD spectra of Fig. 5.6-b provide information on this competition. The negative dichroic signal at the Cr L$_3$ edge and the positive one at the L$_2$ edge [L$_3(-)$, L$_2(+)$] implies that the total magnetic moment of the Cr ions is parallel to H. Conversely, the opposite behavior of Ni [L$_3(+)$, L$_2(-)$], for either powders and MLs, implies that at 8K the magnetic moment of the Ni ion is antiparallel to H.

Fig. 5.7-a,b show the Cr-L$_{2,3}$ and Ni-L$_{2,3}$ absorption spectra taken using both photon
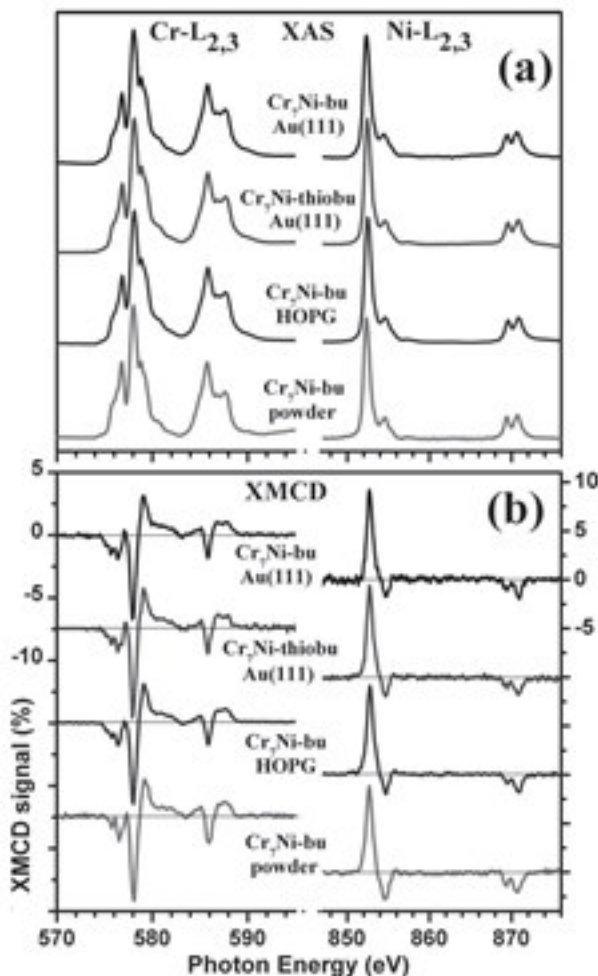
Figure 5.6: Cr (left) and Ni (right) $L_{2,3}$ XAS (a) and XMCD (b) spectra, measured at 8 K and 5 T on 1 ML of Cr_7Ni-bu and Cr_7Ni-thiobu on Au(111), 1 ML of Cr_7Ni-bu on HOPG deposited by sublimation. The spectrum of Cr_7Ni-bu powders is also shown for comparison.

helicities (upper panel), the relative dichroic signal and its integral (lower panel) measured for 1 monolayer (ML) of Cr_7Ni-bu on Au(111) at 8 K and 5 T. In Fig. 5.7-c,d, the XMCD spectra of Cr and Ni are displayed at three temperatures: 8 K, 15 K, and 25 K. Similar measurements were performed also for the other ML samples and for the TFs. We observe that, while the total Cr magnetic moment is always parallel to H , for Ni the magnetic moment is antiparallel to H at 8 and 15 K but it becomes parallel to H at 25 K (see Fig. 5.7-d). These results can be quantitatively analysed exploiting XMCD sum rules for each type of magnetic ion, as in Eq. 2.69. Here a spin correction factor S_C= 1.75 (as in Ref. [82, 83, 84, 26]), and for what concerns the 3d-hole numbers, the nominal values N_{eff} = 7 for Cr^{3+} and N_{eff} = 2 for Ni^{2+} have been used. For the general case of 3d metals, the dipolar term T_Z is expected to be different from zero, however, in the case of Cr^{3+} ions

in O_h symmetry, it results negligible [80] allowing the application of the isotropic sum rules for Cr. On the contrary, for 3d^8 metal, e.g., Ni^{2+} ions, T_Z is not negligible even in O_h symmetry. On the basis of theoretical calculations [80] in the spin moment sum rule we consider a negative $7T_Z$ term of -0.06μ_B , which is about 1/30 of the m$_S$ value: $7T_Z$ / m$_S$ = -0.03.
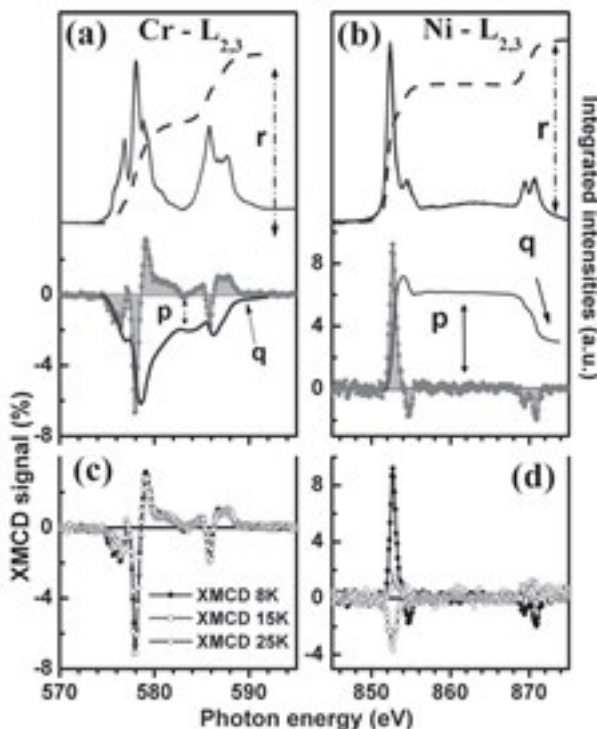

Figure 5.7: Upper panels: Cr (a) and Ni (b) L$_{2,3}$ XAS spectra taken with $\sigma^{\uparrow\uparrow}$ and $\sigma^{\uparrow\downarrow}$ circularly polarized light and the XAS integral (dashed line) at 5 T and 8 K for 1 ML Cr$_7$Ni-bu on Au(111). XMCD spectra ($\sigma^{\uparrow\downarrow}$-$\sigma^{\uparrow\uparrow}$) and their integrals (continuous lines). The parameters p , q , and r are the values used for the sum rules analysis. Lower panels: Cr (c) and Ni (d) XMCD spectra measured at 8 K, 15 K, and 25 K in 5 T magnetic field.

The q value of the dichroic signal at the Cr-L$_{2,3}$ edges is related to the orbital moment m$_O$ of the Cr^{3+} ions. Its vanishing value indicates a complete quenching of m$_O$ due to crystal field effects. On the contrary m$_O$ of Ni^{2+} ions is only partially quenched. This occurs for all the MLs and powders investigated. For all systems the m$_O$ value derived by the sum rules is about 10÷15% of m$_S$, for all the spanned temperatures and magnetic field H . Thus Cr ions have a nearly spin-only gyromagnetic factor (g$_{Cr}$ = 2.0), whereas for Ni g$_{Ni}$ = 2.25 $\pm$ 0.05. These values are very close to the ones derived for the pristine (bulk) Cr$_7$Ni-piv derivative and, incidentally, confirm that neither thermal sublimation nor the interaction with the Au surface affects the degree of quenching of the orbital momentum.

Fig. 5.8 displays the behavior of the Cr and Ni magnetic moments, for 1 ML of Cr$_7$Ni-bu on Au(111) and the corresponding thick films (TF), as a function of an external magnetic field H at different temperatures. It is worth noting that the Cr total magnetic

moment is larger in the ML than in the TF and it is parallel to H, at all the temperatures considered. A different behavior is observed for Ni in the ML: Negative values, i.e., moment antiparallel to H , are observed at 8 and 15 K, while as temperature increases, an inversion in the sign of the Ni dichroism at 25 K occurs. This behavior reproduces that observed in the TF, and shows that the increasing temperature induces different alignment of the Ni magnetization to the external field. A very similar behavior has been observed also for 1ML of Cr_7Ni-thiobu on Au(111) and ofCr_7Ni-bu on HOPG.

5.2.2 Spin Hamiltonian and Numerical Simulations

We can describe the magnetic properties of each Cr_7Ni ring by the Spin Hamiltonian (s_{Cr} = 3/2 and s_{Ni} = 1):

$$\mathcal{H} = \sum_{i=1}^{7} J_{i,i+1}\mathbf{s}_i \cdot \mathbf{s}_{i+1} + \sum_{i=1}^{7} d_i \left[s_{i,z}^2 - \frac{1}{3} s_i \left(s_i + 1 \right) \right] + \mu_B \sum_{i=1}^{7} g_i \mathbf{H} \cdot \mathbf{s}_i, \qquad (5.4)$$

where the first term represents the dominant isotropic nearest-neighbor antiferromagnetic exchange interaction, the second term accounts for axial anisotropy (being z' the axis perpendicular to the ring plane) and the last one is the Zeeman coupling to an external field $\mu_0 H$. Since XMCD results show that the degree of orbital momentum quenching is the same as in the original Cr_7Ni-piv molecule, the gyromagnetic factors g_i have been fixed to 1.98 (Cr^{3+}) and 2.2 (Ni^{2+}) [139, 140].
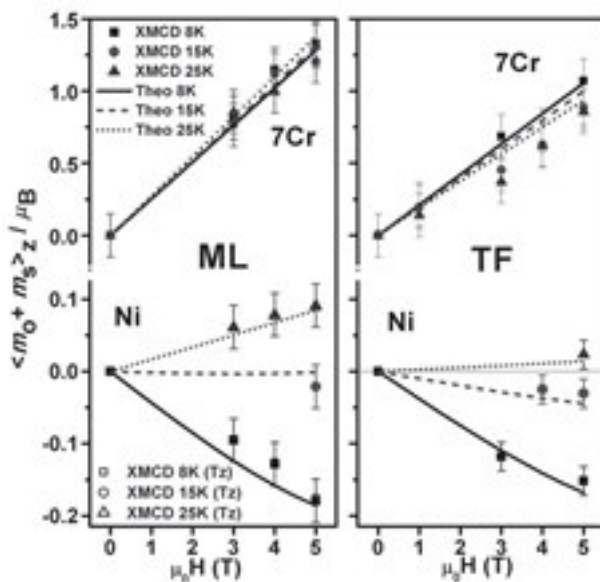

Figure 5.8: Total magnetic moments derived by using the sum rules for 7Cr and 1 Ni with (open symbols) and without (filled symbols) considering Tz, plotted as a function of the applied magnetic field at 8 K, 15 K, and 25 K and compared with the results of spin-Hamiltonian calculation (continuous lines). 1ML Cr_7Ni-bu on Au(111) (left panel) and Cr_7Ni-bu powders (right panel) are reported.

As shown in Fig. 5.8 , the experimental results on TF samples (right panel) are well reproduced by Eq. 5.4 , using J$_{Cr-Cr}$ = 1.46 meV = 16.9 K and J$_{Cr-Ni}$ = 1.69 meV = 19.6 K, values obtained from bulk measurements [95, 68, 132]. The temperature dependence of magnetic moments measured on the ML is slightly different: Reasonably the direct interaction of molecules with the gold surface induces a slight change in the J's constants. So, the experimental data for 1 ML of Cr$_7$Ni-bu on Au(111) in the left panels of Fig. 5.8 are well fitted by using exchange constants J$_{Cr-Cr}$ = 1.14 meV = 13.2 K and J$_{Cr-Ni}$ = 1.32 meV = 15.3 K in Eq. 5.4 , which present a small but sizeable reduction (22%) for both J's constant with respect to the (TF) bulk. The uncertainty on the TF and ML fitting parameters is of the order of 10% as variations within this range keep the fit acceptable. It is important to note that both TF and ML data are well reproduced by assuming the same d$_{Cr}$ = -0.03 meV = -0.35 K and d$_{Ni}$ = -0.35 meV = -4 K in Eq. 5.4 , as derived from bulk measurements[1], i.e., changes in d's values make the fit systematically worse.

It is worth to stress that the structure of the low-energy levels of the grafted rings, shown in Fig. 5.9 , is not modified by the reduction of the exchange coupling constants and it remains practically the same as in the original Cr$_7$Ni rings in bulk crystals. This small reduction of J's values only leads to a small compression of the spectrum (e.g., the ground-doublet to first excited-quartet gap $\Delta_{1/2-3/2}$ becomes about 11 K instead of 14 K).
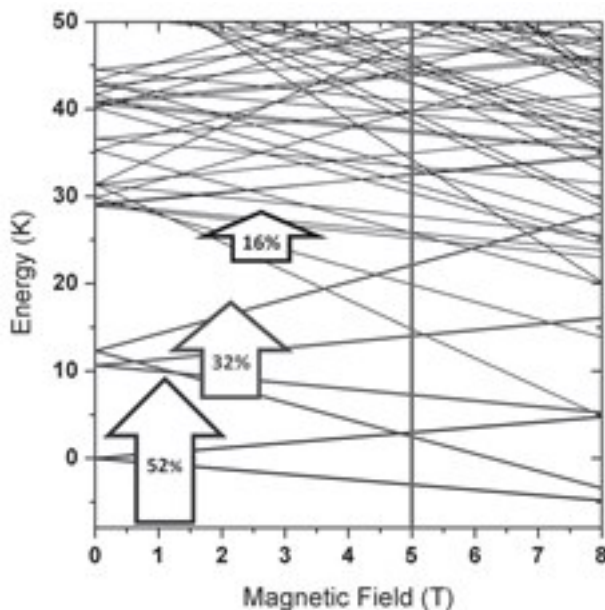

Figure 5.9: Zeeman plot (magnetic field dependence) of the low-lying energy levels calculated for 1 ML of Cr$_7$Ni-bu on Au(111). Parameters used in calculations are J$_{Cr-Cr}$ = 1.14 meV and J$_{Cr-Ni}$ = 1.32 meV. Arrows indicate the occupancy calculated at 5 T and 8 K for different multiplet.

---

[1]The axial dipole-dipole interaction and single ion axial anisotropies have similar effects: Therefore, d parameters have been rescaled to d$_{Cr}$ = -0.037 meV = -0.43 K and d$_{Ni}$ = -0.43 meV = -5 K, in order to reproduce the effects of the whole anisotropy.

Diagonalization of Spin Hamiltonian

The theoretical evaluation of the temperature and magnetic field dependence of Cr and Ni magnetic moments required the diagonalization of Eq. 5.4. If the magnetic field $\mu_0 H$ was along the z'- axis ($\theta = 0$), the total spin operator $S_{z'}$ commuted with the Spin Hamiltonian. Thus Eq. 5.4 could be exactly diagonalized within each block with fixed M, where M is the eigenvalue of $S_{z'}$. However when the magnetic field $\mu_0 H$ was along a different direction ($\theta \neq 0$), $[\sum_i g_i \mathbf{s_i} \cdot \mathbf{H}, \mathbf{S_{z'}}] \neq 0$ and diagonalization of Eq. 5.4 was obtained by a solution scheme based on an irreducible tensor operators (ITOs) formalism (see Section 1.1.2). Using these two diagonalization methods it is possible to obtain both eigenvalues and eigenstates of Eq. 5.4 at the different θ's from which one can estimate the local magnetization at single Cr and Ni sites. It was verified that for $\theta = 0$ both methods yield the same results.

5.2.3   Angular Dependence of X-Rays Dichroism

In the experimental setup the magnetic field direction is always parallel to the beam, whereas the angle θ between the surface normal and H can be varied between 0° and 75° (Fig. 5.10-b). The dependence of the XAS and XMCD spectral shape on θ has been studied for all MLs and for the TFs, and it is shown in Fig. 5.10-a for Cr and in Fig. 5.10-c÷e for Ni. The information on the magnetic moment anisotropy of Cr (Fig. 5.10-a) is averaged over seven ions and it results practically zero. Conversely, the Ni XMCD signal shows a clear dependence on θ: In the case of 1 ML of Cr$_7$Ni-bu and 1 ML of Cr$_7$Ni-thiobu (Fig. 5.10-c,d) on Au(111), a strong angular dependence is observed with 40% reduction passing from $\theta = 0°$ to $\theta = 75°$, while for Cr$_7$Ni-bu on HOPG a modest angular dependence (12% reduction) is observed. No dependence on θ is observed in the case of randomly oriented polycrystalline thick film. These findings confirm that, in the case of deposition on gold, the molecular rings lay flat on the surface, with their z'- axis perpendicular to the latter [138]. In the case of graphite, the molecular rings tend to be less oriented, representing an intermediate situation between gold and bulky powders, where rings are randomly oriented.

Again, XMCD sum rules have been used to derive the m$_S$ and m$_O$ moments for each type of magnetic ion as a function of θ. The results are reported in Table 1 and Fig. 5.11. As expected the m$_S$ of the 7Cr ions does not change with θ whereas the Ni magnetic moment decreases as θ increases indicating the magnetic moment of Ni preferentially aligns along the z'- axis. Summing up the 7Cr and the Ni magnetic moments, the total magnetization of the Cr$_7$Ni ring results lower at $\theta = 0°$ than at $\theta = 75°$ (see Table 1), indicating an easy plane anisotropy for the ring magnetization in this experimental conditions, i.e., T = 8K and $\mu_0 H = 5$ T. The angular dependence of the different magnetic moments for the Ni ion, each Cr site, the 7Cr complex and the whole Cr$_7$Ni ring, have been theoretically evaluated by Eq. 5.4 at T = 8 K as a function of the applied magnetic field (Fig. 5.12). These calculations show that single ion magnetic moments have alternating signs with a negative sign for Ni (meaning that the Ni moment is anti-parallel to the field direction). The absolute value of the magnetic moment for each Cr ion depends on its distance from the Ni one (see inset in Fig. 5.12). For instance, the two Cr ions right next to it have the largest moments. In summary, Fig. 5.11-a÷c shows a very good agreement between calculations and experimentally derived θ dependence of the different moments.

Exploiting the parameters obtained by fitting the sum rule results, it is possible to understand the origin of the easy plane anisotropy of the Cr$_7$Ni ring. The effective magnetic anisotropy of each total-spin multiplet in molecular nanomagnets can be evaluated
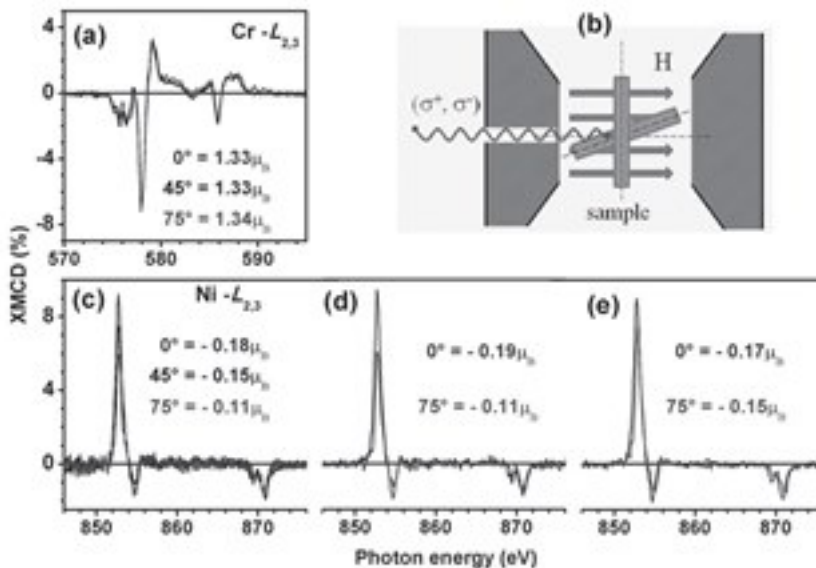
Figure 5.10: XMCD spectra at the Cr (a) and Ni (c) $L_{2,3}$ edges measured on 1 ML of Cr₇Ni-bu on Au(111) for different angles θ of the applied magnetic field; (d) 1 ML of Cr₇Ni-thiobu on Au(111) and (e) 1 ML of Cr₇Ni-bu on HOPG. The values indicated are the total magnetic moments derived by sum rules (the error bar is $\pm 0.05 \, \mu_B$ ($\pm 0.02 \, \mu_B$) for Cr (Ni) edge). b) Experimental geometry with the two limit situations: $\theta = 0$ (H and beam normal to the surface) and $\theta = 75°$.
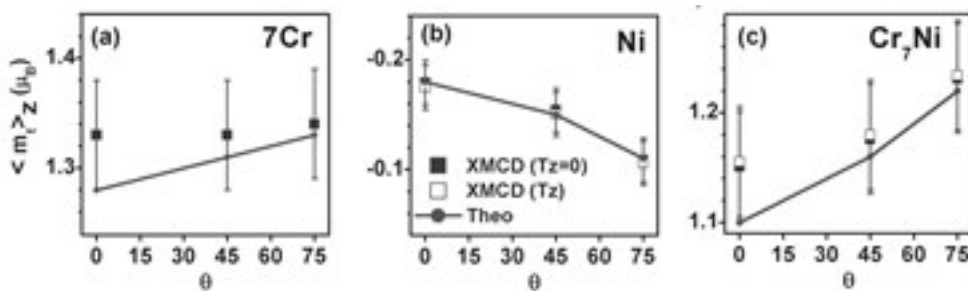

Figure 5.11: Total magnetic moment derived by the sum rules for 7Cr (a), Ni (b), and the whole Cr₇Ni (c) with (open symbols) and without (filled symbols) considering Tz, compared with the results of the spin-Hamiltonian calculations (continuous lines).

by projecting single-ion crystal field terms on the chosen multiplet, thus evaluating their effective zero-field splitting parameter D:

$$D = d_{Cr} \sum_{i=1}^{7} \Gamma_i + d_{Ni} \Gamma_{Ni},\qquad(5.5)$$

(see Section 1.1.1). In the experimental conditions ($\mu_0 H = 5$ T and T = 8 K) the two mainly populated multiplets are the ground S = 1/2 doublet and the first-excited S = 3/2 quartet

	Sum rules	Angle θ			Summary
		0°	45°	45°	
	m_S	-0.16	-0.135	-0.1	
	m_O	-0.02	-0.015	-0.01	
Ni	m_t	-0.18	-0.15	-0.11	easy axis
7Cr	m_t	1.33	1.33	1.34	
Cr₇Ni	m_t	1.15	1.18	1.23	easy plane

Table 5.2: Ni and 7Cr spin, orbital and total magnetic moments, experimentally derived by the sum rules for 1 ML of Cr₇Ni-bu on Au(111) as a function of θ, the angle between the direction of the beam (which coincides with H) and the normal to surface at 8 K and magnetic field 5 T.

(see Fig. 5.9). Our calculations indicate that for the S = 3/2 multiplet all Γ_i coefficients are negative while they vanish in the ground doublet for the time-reversal symmetry (indeed the ground state S = 1/2 doublet is isotropic, only the S-mixing with the S = 3/2 excited multiplets can lead to some anisotropy effects (see Section 5.1.2). Hence, the resulting easy plane anisotropy of the whole Cr₇Ni ring at T = 8 K and H = 5 T is mainly determined by the effective magnetic anisotropy of S = 3/2 multiplet for which D > 0 (all the d parameters and projection coefficients in Eq. 5.5 are negative). Indeed, in zero field, anisotropies cause a splitting between the $|3/2, \pm 1/2\rangle$ and the $|3/2, \pm 3/2\rangle$ states with a gap of 0.15 meV (or 1.7 K) and the $|3/2, \pm 1/2\rangle$ state is the lower in energy (see Fig. 5.9).

5.2.4   Conclusions

Deep analysis of the angular dependence of XMCD spectra of ordered MLs of Cr₇Ni molecular rings allowed us to elucidate the relationship between the magnetization of the single ions and that of the entire molecule. This study is in line with the recent use of XMCD technique on heterometallic molecular systems [133, 134] but here we can exploit the advantage that the deposition by sublimation induces an ordered self-assembling with an alignment of the Cr₇Ni rings on the surface. Experimentally, at 8 K and 5 T, the magnetic moment of Ni tends to align along the z'- axis perpendicular to the ring plane, whilst the total magnetic moment of the molecule prefers to align within that plane. This apparent discrepancy is reconciled as follows: Both Ni and single-Cr magnetic moments have easy-axis anisotropy [weak for Cr: d_{Cr} = -0.03 meV and stronger for Ni: d_{Ni} = -0.35 meV in Eq. 5.4]. Projecting these anisotropies on the S = 3/2 multiplet, which dominates in our experimental conditions, we obtain an easy-plane anisotropy for the magnetization of the whole molecule, in perfect agreement of our experimental findings. These results evidence that X-ray dichroism probe magnetic features of single ion whilst the magnetic anisotropy of molecular cluster results from projection of these anisotropies on the dominant multiplet at fixed experimental conditions (temperature and magnetic field). Whilst this finding is probably not particularly surprising, our description of this interplay involves the use of the XMCD sum rules, diagonalization of Spin Hamiltonian, projection of local anisotropies on molecular multiplets and ab initio DFT calculations (for details on DFT calculations see Ref. [141]). So, remarkably the overall theoretical
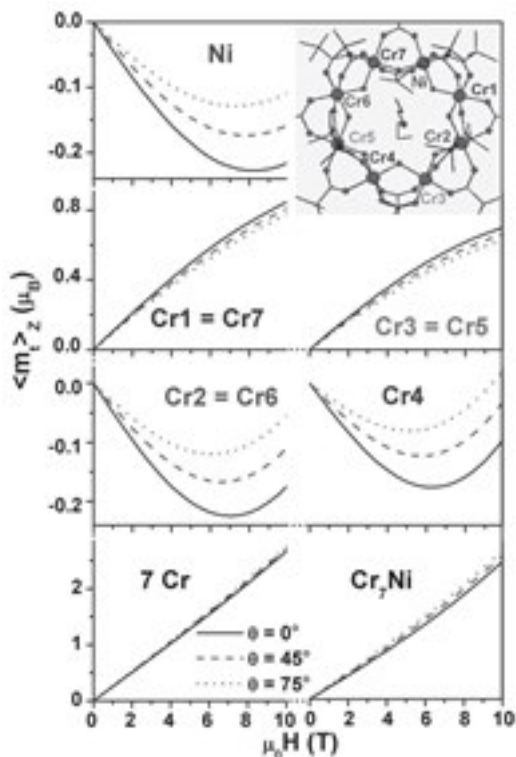
Figure 5.12: Angular dependence of the total magnetization calculated by Spin Hamiltonian at 8 K for the Ni, for each Cr site, for the 7Cr and for the whole Cr$_7$Ni ring. Inset: the ring structure showing the different Cr positions with respective numbers.

description turns out to be self-consistent and perfectly fits the experimental results that, in turns, provide, to our knowledge, the first direct observation of such interplay. More specifically this work elucidates the origin of magnetic anisotropy in antiferromagnetic Cr$_7$Ni, evidencing a weak anisotropy of the magnetic moments at the Cr sites, that is a further element for the easy manipulation of the molecular spin as required for the use of these molecular spin clusters for quantum information processing.

Spin Dynamics of Cr$_7$M purple Rings and of Entangled Dimers

In this Chapter we investigate magnetic properties and spin dynamics of Cr$_7$M *purple* rings. As already explained in the introduction of Chapter 5 the main differences between purple rings and the green ones are in the super-exchange paths between neighbouring 3d ions. Indeed purple rings have five bridging alkoxide groups within the ring, with only three bridging fluorides (see Fig. 6.1). Seven of the eight edges of the octagon have two bridging pivalate ligands attached, however the eighth edge has only a single bridging pivalate and a bridging fluoride [128]. Thus purple rings have a lower number of super-exchange paths involving magnetic ions F$^-$. The substitution of bridging fluorides with alkoxide groups can reduce the hyperfine-induced decoherence, making them attractive candidates for applications in quantum-information processing [58].
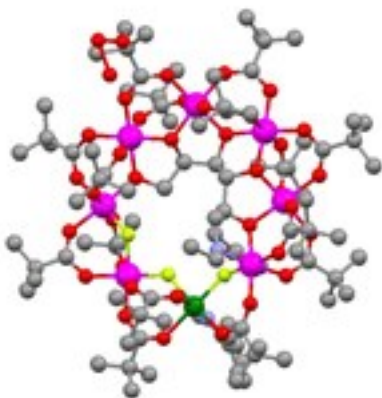

Figure 6.1: Molecular structure of a Cr$_7$M purple ring: magenta = Cr, green = M (Zn, Mn, Ni), red = O, yellow = F.

In this Chapter we also introduce a new family of entangled dimers formed by one AF purple ring and one green ring. The AF exchange coupling between two such rings is tailored by super-molecular chemistry and is small enough to leave unaltered the magnetic properties of each ring but sufficiently large to induce finite-temperature entanglement in experimentally reachable conditions. Spin entanglement between two Cr$_7$Ni purple rings has been experimentally demonstrated, for example, through magnetic susceptibility as an entanglement witness [142, 143]. In addition these rings represent model

systems to study spin entanglement and its application in the field of quantum computation [21].

In Section 6.1 we first characterize Cr_7M ($M = Zn^{2+}, Mn^{2+}, Ni^{2+}$) purple rings through inelastic neutron scattering (INS) and confirm our results with specific heat and electron paramagnetic resonance (EPR) measurements. The comparison with these experimental results allows us to determine the Spin Hamiltonian parameters and to study the spin dynamics of the rings. In Section 6.2 we also study specific heat and EPR spectra of an entangled Cr_7Ni purple - Cr_7Ni green dimer, demonstrating the presence of an effective entanglement between the two rings.

6.1 Spin dynamics of Cr$_7$M purple Rings

Cr_7M ($M = Zn^{2+}, Mn^{2+}, Ni^{2+}$) *purple* AF rings represent a valid alternative to green rings in the field of quantum information processing, since the substitution of bridging fluorides with alkoxide groups can reduce the hyperfine-induced decoherence. Cr_7M purple rings have been originally synthesized in order to facilitate the linking of two or more AF rings. Indeed the presence of a terminal ligand in purple rings, which could either be a fluoride or a water molecule, represents a new opportunity for linking AF rings [128]. A hydroxide-bridged version of Cr_8 rings was first synthesized, which is purple in color due to replacing of all fluoride bridges with alkoxide within the coordination sphere of Cr^{3+} ions [144]. In Cr_7M purple rings a Cr^{3+} ion is replaced by a divalent ion M^{II} ($M = Zn^{2+}, Mn^{2+}, Ni^{2+}$) and only five bridging fluorides are replaced by alkoxide groups. The replacement of a magnetic ion in a cyclic structure allows one to modify the topology of the exchange interactions, which plays a key role in determining the macroscopic behavior of the system [132].

In the following we investigate magnetic properties and spin dynamics of Cr_7M purple rings with INS, specific heat and EPR. Experimental data have been interpreted within the Spin Hamiltonian formalism.

6.1.1 Spin Hamiltonian

Magnetic properties and spin dynamics of Cr_7M ($M = Zn, Mn, Ni$) purple rings can be described by the Spin Hamiltonian ($s_{Cr} = 3/2$, $s_{Zn} = 0$, $s_{Mn} = 5/2$ and $s_{Ni} = 1$):

$$
\begin{aligned}
\mathcal{H} &= \sum_{i=1}^{7} J_{i,i+1}\mathbf{s}_i \cdot \mathbf{s}_{i+1} + \sum_{i=1}^{7} d_i \left[s_{i,z}^2 - \frac{1}{3} s_i\left(s_i+1\right) \right] + \sum_{i=1}^{7} e_i \left(s_{i,x}^2 - s_{i,y}^2 \right) + \quad (6.1) \\
&+ \sum_{i>j=1}^{N} D_{ij} \left[2s_{i,z}s_{j,z} - s_{i,x}s_{j,x} - s_{i,y}s_{j,y} \right] + \mu_B \sum_{i=1}^{7} \mathbf{B} \cdot \mathbf{g}_i \cdot \mathbf{s}_i.
\end{aligned}
$$

The first term represents the dominant isotropic nearest-neighbor antiferromagnetic exchange interaction, the second term accounts for axial crystal field anisotropy (being z the axis perpendicular to the ring plane) while the third one for the rhombic crystal field anisotropy. The last two terms are the axial contribution to the dipolar anisotropic interaction, where D_{ij} is evaluated within the point-dipole approximation, and the Zeeman coupling to an external field, where we take into account the possible anisotropy of the g tensor. The Spin Hamiltonian in Eq. 6.1 has been used to have a first insight into purple rings magnetic properties: Future and more detailed studies will be performed taking into account different couplings constants J for O-based and F-based exchange bridges. In this model we only distinguish between Cr-Cr and Cr-M exchange interactions.

As already pointed out for Cr$_7$Ni in Chapter 5, the large Hilbert space of AF rings forces us to implement the two-step perturbative technique described in Section 1.1.3 in order to diagonalize the Spin Hamiltonian in Eq. 6.1. This technique allows us to include also the often-neglected S-mixing effects [53]. Our calculations show that the reduction to the subspace spanned by the lowest spin exchange manifolds (up to 150 K) allows us to reproduce properly INS data, specific heat and EPR spectra.

6.1.2 Inelastic Neutron Scattering

INS experiments on Cr$_7$Zn and Cr$_7$Mn purple rings have been performed at ISIS pulsed Neutron and Muon Source of the Rutherford Appleton Laboratory (Didcot, UK) with the IRIS spectrometer (see Section 2.1.3), which works in indirect geometry and with time-of-flight techniques. In our experiments we have fixed the final energy of the neutrons to E_2 = 1.843 meV and set the frequency of the two disc choppers to 25 Hz ($-0.7 < E < 3.54$ meV). The explored scattering vector range is $0 < Q < 3.5$ $\mathring{A}$. The two different crystal analysers arrays have allowed us to perform both lower-resolution (pyrolytoc graphite analysers σ = 0.22 μeV) and higher-resolution (mica analysers σ = 0.11 μeV) measurements. Data have been collected at three different sample temperatures: T =1.6-1.8 K, 7 K and 20 K. INS experiments on Cr$_7$Ni have been performed at the Institute Laue-Langevin in Grenoble. On Cr$_7$Mn and Cr$_7$Ni we have also performed measurements of the Q-dependence of the main inter-multiplet transitions. These data allow us to distinguish between magnetic and vibrational transitions, and also to characterize the magnetic transition itself.
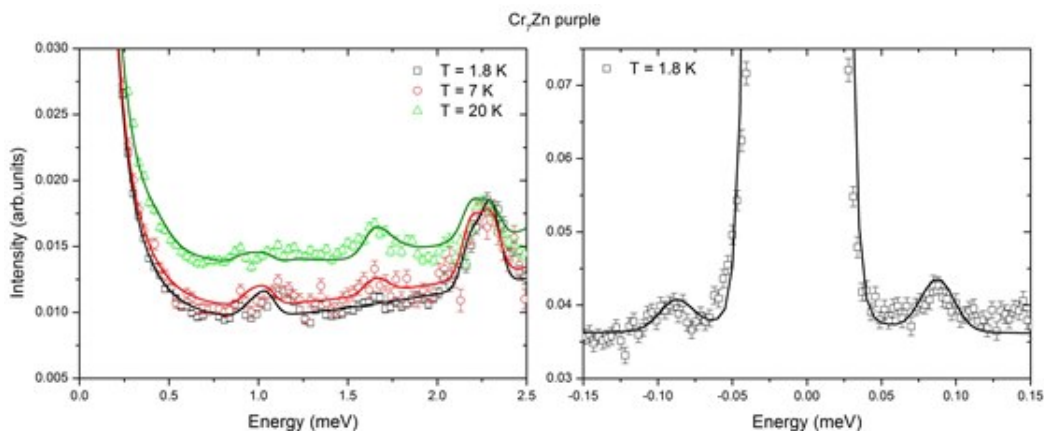

Figure 6.2: INS data (scatter) and calculations (solid lines) on Cr$_7$Zn purple ring. Left panel: low-resolution/high energy spectrum at T = 1.8, 7, 20 K; right panel: high-resolution/low-energy spectrum at T = 1.8 K.

In Figs. 6.2, 6.3 and 6.4 we report experimental data (scatter) and our calculations (solid lines) of INS on Cr$_7$Zn, Cr$_7$Mn and Cr$_7$Ni respectively. Left panels show low-resolution/high energy spectra, where the peaks at E > 0 correspond to inter-multiplet magnetic transitions, due to neutrons that have transferred energy to the system. From the interpretation of these data it is possible to determine the coupling constants of the dominant Heisenberg exchange interaction (first term in Eq. 6.1), which are responsible for the inter-multiplet energy gaps. Peaks in low temperature spectra (T = 1.6-1.8 K) are

due to transitions involving the ground state as the initial state, while new peaks appear at higher temperature (T = 7, 20 K), corresponding to transitions involving excited levels as initial states. Right panels in Figs. 6.2 and 6.3 show high-resolution/low-energy spec-
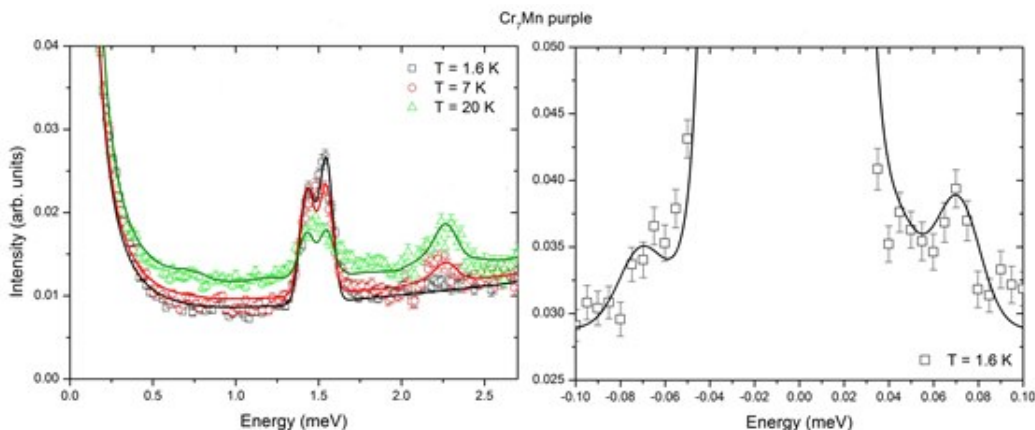

Figure 6.3: INS data (scatter) and calculations (solid lines) on Cr$_7$Mn purple ring. Left panel: low-resolution/high energy spectrum T = 1.6, 7, 20 K; right panel: high-resolution/low-energy spectrum at T =1.6 K.
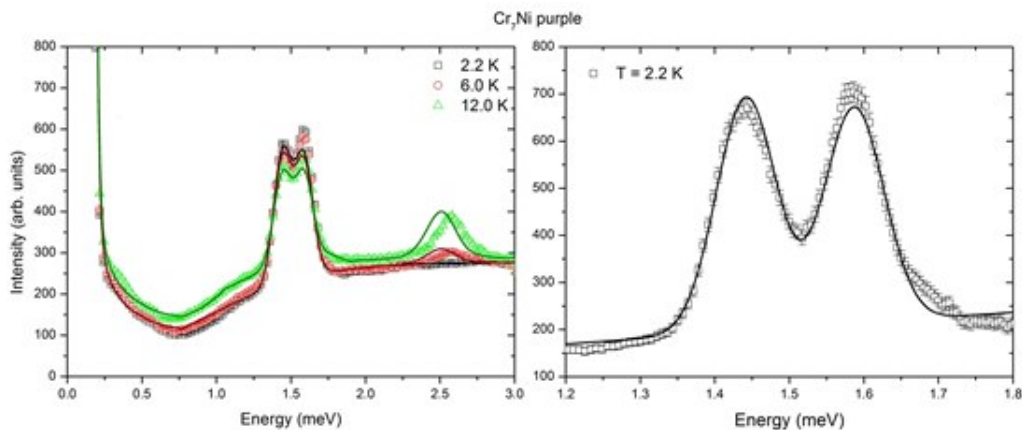

Figure 6.4: INS data (scatter) and calculations (solid lines) on Cr$_7$Ni purple ring. Left panel: low-resolution/high energy spectrum at T =2.2, 6, 12 K; right panel: high-resolution/low-energy spectrum T = 2.2 K.

tra of Cr$_7$Zn and Cr$_7$Mn respectively, where the peaks are due to intra-multiplet magnetic transitions in the ground state. In these spectra at E $\sim$ 0 we can see the elastic peak (usually gaussian-shaped with σ given by the instrumental resolution), whereas magnetic transitions can be found at both E $>$ 0 and E $<$ 0. In the latter case the transition is due to neutrons that have gained energy from the system. From the comparison of these data with our calculations it is possible to determine the zero-field splitting parameters of the Spin Hamiltonian in Eq. 6.1, such as local crystal field parameters d_i. In the right panel of Fig. 6.4 we show an high-resolution/high-energy spectrum of Cr$_7$Ni purple. In fact, since Cr$_7$Ni has a S = 1/2 Kramer's doublet as a ground state, its INS spectra at B =

0 T don't show any intra-multiplet magnetic transition at low energy. Therefore we have investigated the main peak at $E \sim 1.5$ meV with an higher resolution, in order to resolve the transitions involving the ground state doublet as the initial state and the split levels of the $S = 3/2$ excited multiplet as final states.

Since our INS experiments have been performed on powders samples, we have exploited Eq. 2.18, integrated over the Q interval corresponding to the experimental conditions, to simulate the spectra at different temperatures. The analysis of the experimental data have started with the simulation of low-resolution/high-energy spectra, which has allowed us to fix the exchange coupling constants J_{Cr-Cr} and J_{Cr-Ni} in Eq. 6.1 by fitting the peak positions of the inter-multiplet magnetic transitions. Then, from the comparison of our calculations with high-resolution spectra, we have determined the zero-field splittings due to local crystal fields. The latter and in particular the rhombic parameters e_i have been determined from a simultaneous fitting of high-resolution INS and EPR spectra, reported in the following section. Indeed INS doesn't allow us to distinguish between zero-field splittings induced by d_i or e_i. For INS simulations we have assumed isotropic **g** tensor for both Cr and M ions: $g_{Cr} = 1.98$, $g_{Mn} = 2$ and $g_{Ni} = 2.2$. First of all we have determined the parameters of the Spin Hamiltonian in Eq. 6.1 relative to Cr^{3+} ions, J_{Cr-Cr} and d_{Cr}, from the data on Cr_7Zn ring. In fact, since Zn^{2+} is a non-magnetic ion, all the magnetic properties of Cr_7Zn come from Cr^{3+}. In the analysis of Cr_7Mn and Cr_7Ni we have kept the same values of J_{Cr-Cr} and d_{Cr}, and determined J_{Cr-M} and d_M from the comparison of INS data with our calculations. All the parameters of the Spin Hamiltonian in Eq. 6.1 for Cr_7M purple rings are reported in Tab. 6.1. Our calculations are shown as solid lines in Figs. 6.2, 6.3 and 6.4 and are in very good agreement with experimental data. Small differences between the peak positions of our simulated spectra and INS data are due to the fact that in our model we are not taking into account different coupling constants for O-based and F-based exchange bridges.

Cluster	J_{Cr-Cr} (K)	J_{Cr-M} (K)	d_{Cr} (K)	e_{Cr} (K)	d_M (K)	e_M (K)
Cr_7Zn	20	╱	-0.26	-0.09	╱	╱
Cr_7Mn	20	12	-0.26	-0.09	0.06	-0.008
Cr_7Ni	20	30	-0.26	-0.09	-6	╱

Table 6.1: Spin Hamiltonian parameters of Cr_7M rings from INS and EPR.

In order to simulate properly the measured spectra we have also take into account the instrumental resolution (see Section 2.1.2): High-resolution data can be effectively described by gaussian-shaped peaks with σ given by the instrumental resolution, whereas in high-energy data the J-strain[1] leads to an increase of the width of the magnetic peaks.

In Fig. 6.5 we report the energy spectra of Cr_7Zn, Cr_7Mn and Cr_7Ni respectively, calculated with Eq. 6.1 taking into account exchange interactions only. From the spectra we can see that all the rings have the same magnetic ground state as their green analogues: $S = 3/2$ for Cr_7Zn, $S = 1$ for Cr_7Mn and $S = 1/2$ for Cr_7Ni, well separated in energy (more than 10 K) from the first excited muliplet. We can also easily identify a parabolic band, formed by states with minimal energy for each S value. The levels belonging to

---

[1]The J-strain is due to the presence in the sample of slightly different rings with slightly different exchange constants J.
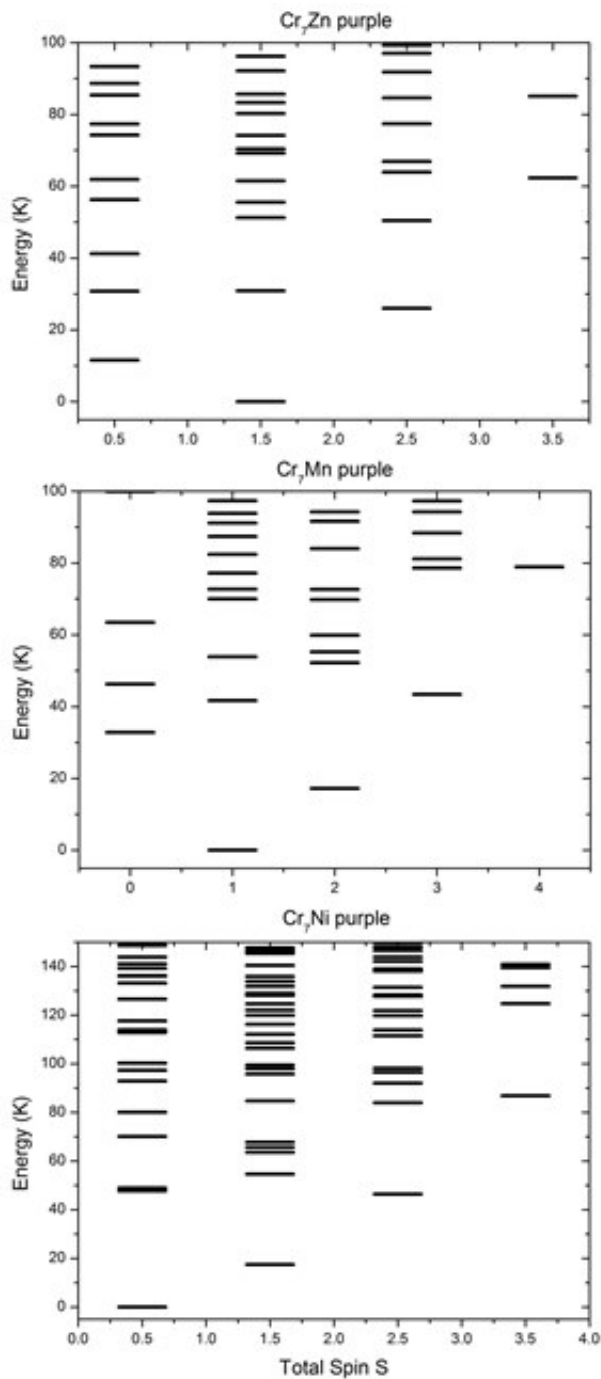
Figure 6.5: From top to bottom: energy spectra of Cr_7Zn, Cr_7Mn and Cr_7Ni purple rings, calculated with Eq. 6.1 taking into account exchange interactions only.
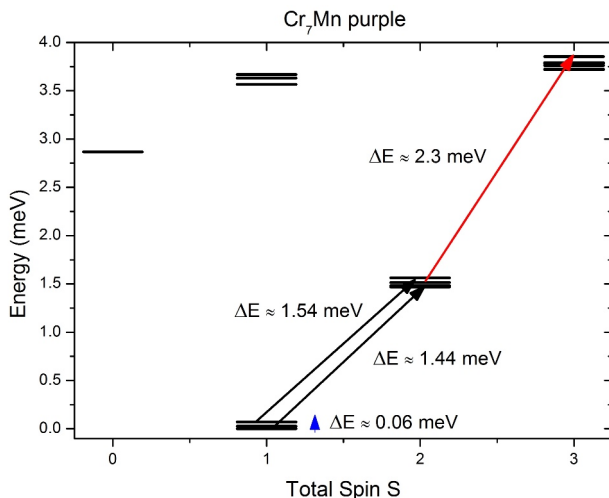
Figure 6.6: Energy spectrum obtained with Eq. 6.1 and the parameters in Tab. 6.1 for Cr_7Mn purple ring. The arrows identify the the transitions extracted from INS spectra labeled with the corresponding energy.

this parabolic band have energies that closely follow the Landé interval rule:

$$E_S = \Delta_{10} \left[S(S+1) - S_0(S_0+1) \right] / \left[S_1(S_1+1) - S_0(S_0+1) \right], \tag{6.2}$$

where S_0 is the spin of the ground state and Δ_{10} is the energy of the first excited multiplet, with spin $S_1 > S_0$.

Figure 6.7: Energy spectrum obtained with Eq. 6.1 and the parameters in Tab. 6.1 for Cr_7Ni purple ring. The arrows identify the the transitions extracted from INS spectra labeled with the corresponding energy.
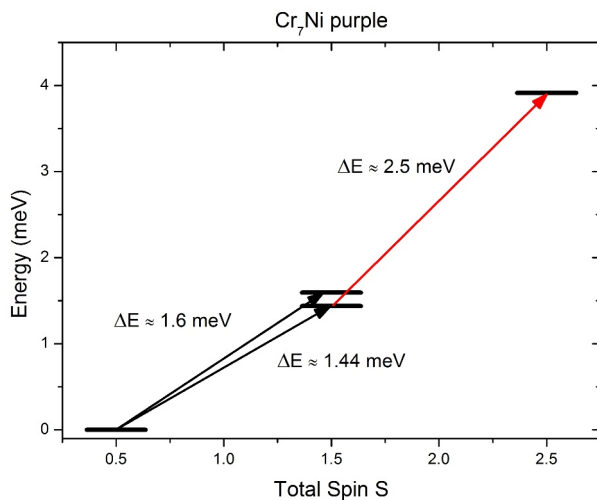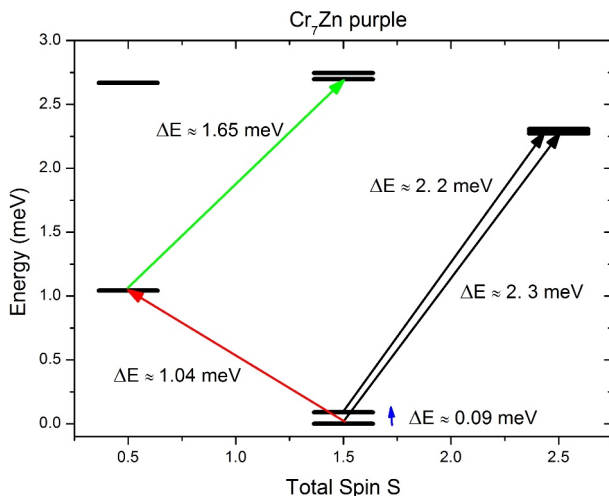
Figure 6.8: Energy spectrum obtained with Eq. 6.1 and the parameters in Tab. 6.1 for Cr₇Zn purple ring. The arrows identify the transitions extracted from INS spectra labeled with the corresponding energy.

If we also take into account the splittings due to local crystal field anisotropy we can identify the initial and the final state of each magnetic transition in the INS spectra. In Figs. 6.6 and 6.7 we report the low-energy spectra of Cr₇Mn and Cr₇Ni respectively, where we have also labeled the transitions extracted from INS spectra with the corresponding energy. Indeed, Cr₇Mn and Cr₇Ni have very similar high-energy spectra. In both rings the most intense peak corresponds to a transition involving the ground state and the first excited multiplet of the parabolic band (black arrows). The main peak in the Cr₇Mn spectrum is at $E \sim 1.5$ meV = 17.4 K and it involves levels of the S = 1 ground state and of the S = 2 first excited multiplet, which are both split by anisotropy effects (see Fig. 6.3-left panel). Cr₇Mn also has an intra-multiplet transition at $E \sim 0.06$ meV = 0.7 K within the S = 1 ground state (blue arrow). The main peak of Cr₇Ni spectrum is at about E = 1.5 meV = 17.4 K too (see Fig. 6.4) and it involves the S = 1/2 ground state doublet and the two levels of the S = 3/2 multiplet (respectively with M = ±1/2 and M = ±3/2), which are split by crystal field anisotropy effects, as we can easily see from the high-resolution spectrum in Fig. 6.4-right panel. In both Cr₇Mn and Cr₇Ni spectra other peaks at higher energies (E = 2.3 meV = 26.7 K and E = 2.5 meV = 72.5 K respectively) appear by increasing the temperature, involving the first excited and the second excited multiplet of the parabolic band (red arrows).

Fig. 6.8 reports the low-energy spectra of Cr₇Zn and the transitions extracted from INS spectra. Cr₇Zn low-resolution/high-energy spectrum (see Fig. 6.2-left panel) shows a main transition at $E \sim 2.3$ meV = 26.7 K, involving the S = 3/2 ground state and the first excited multiplet of the parabolic band with S = 5/2, which are both split by anisotropy effects and separated by an high energy gap (black arrow in Fig. 6.8). There is another transition at $E \sim 1.04$ meV ~ 12 K (red arrow in Fig. 6.8), involving the ground state and the the first excited multiplet with S = 1/2. By increasing the temperature another peak appears in the spectrum, involving the first excited multiplet with S = 1/2 and the first excited one with S = 3/2 ($E \sim 1.65$ meV ~ 19.15 K, green arrow). Cr₇Zn also has an

intra-multiplet transition at E $\sim$ 0.09 meV = 1.04 K within the S = 3/2 ground state (blue arrow).

A stringent test for the spectroscopic assignment of the observed transitions is provided by the Q dependence of their intensity, which is essentially determined by the geometry of the cluster and the composition of the spin wave functions. In Figs. 6.9 and 6.10 we report the Q dependence of the main magnetic transition of Cr$_7$Mn and Cr$_7$Ni respectively. Experimental data (scatter) are compared with our calculations (solid lines) obtained with Eq. 2.18. In both rings peaks at E $\sim$ 1.5meV correspond to excitations in-

Figure 6.9: Q dependence of the main peak at E = 1.5 meV appearing in the Cr$_7$Mn inelastic spectra shown in Fig. 6.3-left panel, compared with theoretical estimates (solid lines) at two different temperatures T = 1.8, 7 K.
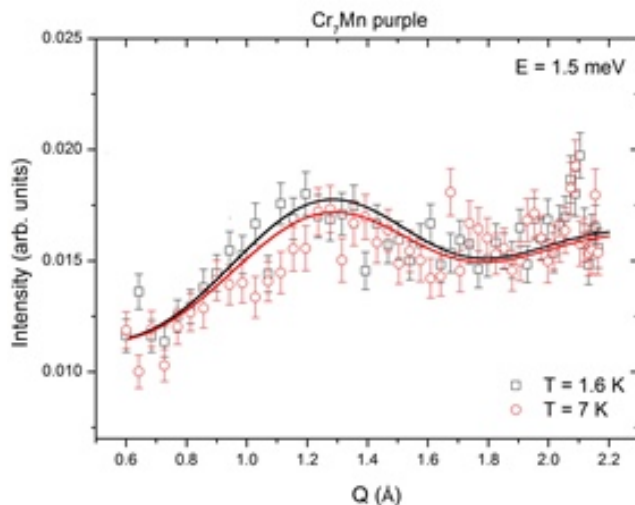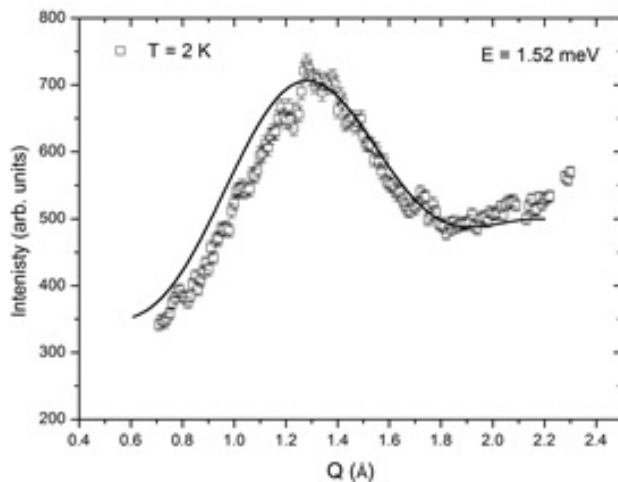

Figure 6.10: Q dependence of the main peak at E = 1.52 meV appearing in the Cr$_7$Ni inelastic spectra shown in Fig. 6.4-left panel, compared with theoretical estimates (solid lines) at T = 2 K.

volving adjacent levels of the parabolic band. Indeed they have similar Q dependencies,

with an oscillatory behavior and a pronounced maximum at a Q value related to the radius of the ring [145, 67]. Q dependencies data are well reproduced by our calculations, obtained with the parameter reported in Tab. 6.1, thus confirming our description and the assignment of the observed magnetic transitions.

6.1.3   Specific Heat and EPR

The description of AF purple rings obtained with Eq. 6.1 and the parameters in Tab. 6.1 from the comparison with INS data have been refined by comparing our calculations with EPR measurements and confirmed by specific heat data (specific heat experiments have been performed on Cr$_7$Zn and Cr$_7$Mn only, data on Cr$_7$Ni purple ring have already been published in Ref.[143]). In Figs. 6.11 and 6.12 we report both EPR (left panel) and specific heat (right panel) data for Cr$_7$Zn and Cr$_7$Mn respectively. In Fig. 6.13 Cr$_7$Ni purple ring EPR data (left panel) are compared with Cr$_7$Ni green ring EPR results.

   EPR measurements on polycrystalline powders of Cr$_7$M purple rings (see Figs. 6.11, 6.12 and 6.13, left panels) are well reproduced by the Spin Hamiltonian in Eq. 6.1 and parameters in Tab. 6.1 exploiting Eq. 2.67, as we can evince from the comparison of experimental data (black lines) and our calculations (red lines). Analysis of the EPR data allows an estimate of local crystal field parameters, in particular the rhombic ones reported in Tab. 6.1, and of the gyromagnetic tensor components. 5.1 and 5.2

   Cr$_7$Zn purple Q band spectrum can be well reproduced considering an isotropic Cr gyromagnetic tensor $g_{Cr}^{xx} = g_{Cr}^{yy} = g_{Cr}^{zz} = 1.98$, as expected for Cr^{3+} ions. The Q band spectrum (ν = 34.1212 GHz) contains a large number of features, showing contributions from ground state and first excited total-spin multiplets, with a sharp resonance at B $\sim$ 1.2 T, close to g = 2. To reproduce all the features of the spectrum it is necessary to assume a rhombic parameter e_{Cr} = -0.09 K $\sim$ 1/3 d$_{Cr}$. The large rhombic character which emerges from the fit of EPR data was not found in green rings, where local crystal fields have axial symmetry (see results reported in Sections 5.1 and 5.2). This difference is likely to reflect a different site-dependence of the actual principal axes of the local crystal field, rather than an intrinsically larger local rhombicity. These axes are assumed to be site-independent in our model Hamiltonian. This is a good approximation in green rings, where the local easy-axis of Cr ions is always close to z. Conversely, the environment of Cr ions in purple rings is much less regular, and local easy-axes are likely to lie along very different directions. In our Hamiltonian principal axes are assumed site-independent and with easy-axis perpendicular to the ring. The large rhombic terms which we find in this common reference frame might then simply reflect a large tilt of some of the actual local easy axes with respect to z. Thus, our model Hamiltonian must not be seen as an actual faithful representation of the local crystal fields. but rather as an effective model with the minimal number of free parameters. In fact, in EPR data anisotropy is sensed mainly through the first-order splitting of the low-lying S = 3/2 multiplet, and two parameters are enough to fully characterize this splitting. Considering only one d$_{Cr}$ and one e$_{Cr}$, our results represent an "averaged" anisotropy, coming from ligand cages of the "green type" (e$_{Cr}$ = 0) and other possible local configurations where e$_{Cr}$ can be similar or even larger than d$_{Cr}$. In addition, the EPR spectrum of Cr$_7$Zn shows contribution from the ground state multiplet S = 3/2 and from the first excited one with S = 1/2. The latter, since S-mixing effects are small, is an isotropic multiplet and is not affected by crystal fields effects due to d$_{Cr}$ or e$_{Cr}$. Thus, anisotropy effects in low temperature properties of Cr$_7$Zn come from the ground state anisotropic quartet S = 3/2. When we take into account a single total-spin multiplet, EPR spectra can be calculated including crystal field effects with the weighted sum given by Eq. 5.5 and thus
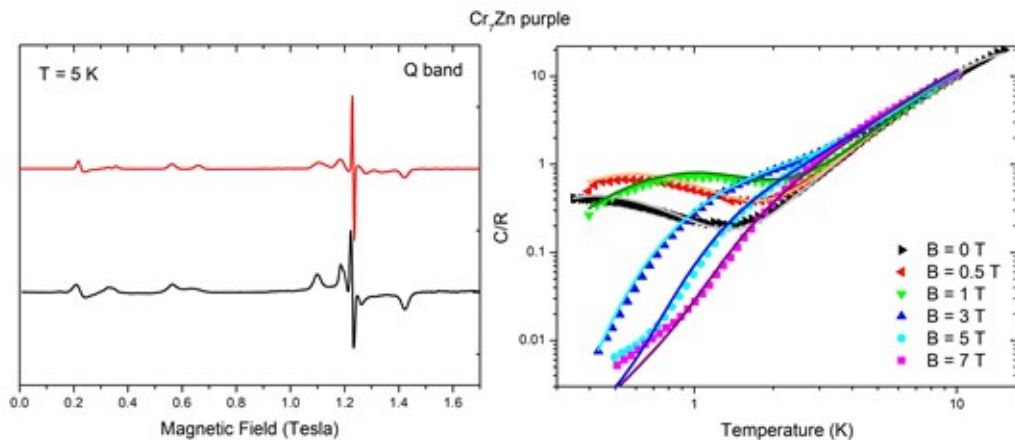
Figure 6.11: Left panel: Experimental (black line) and calculated (red line) EPR Q band (ν = 34.1212 GHz) at T = 5 K of Cr_7Zn purple ring. Right Panel: specific heat of Cr_7Zn purple ring as a function of temperature for different applied magnetic fields.
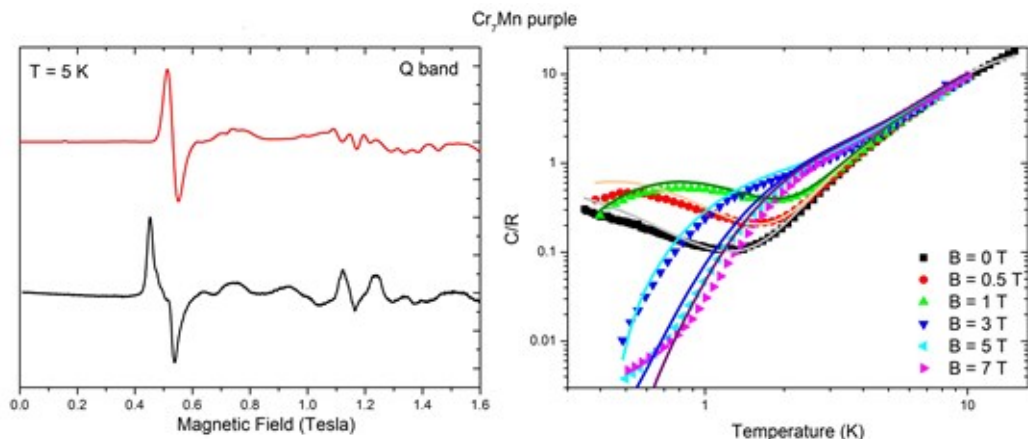

Figure 6.12: Left panel: Experimental (black line) and calculated (red line) EPR Q band (ν = 34.1580 GHz) at T = 5 K of Cr_7Mn purple ring. Right Panel: specific heat of Cr_7Mn purple ring as a function of temperature for different applied magnetic fields.

are not sensitive to differences between local anisotropies. Future ab initio calculations [146] will allow us to confirm this scenario and to have a deeper insight onto local crystal fields of purple rings.

Cr_7Mn purple Q band spectrum can be well reproduced considering an isotropic gyromagnetic tensor for both Cr and Mn $g_{Mn}^{xx} = g_{Mn}^{yy} = g_{Mn}^{zz} = 2$, as expected for S ions like Mn^{2+}. In order to reproduce all the features of the spectrum we have to include also a small rhombic parameter to the local crystal field of the Mn ion, e_{Mn} = -0.008 K.

The Cr_7Ni purple ring spectrum is characteristic of a ground-state doublet (Fig. 6.13-left panel), with lines sharper than those measured in Cr_7Ni green (Fig. 6.13-right panel): This might be due to the F-substitution, that reduces the hyperfine-induced decoherence. Since the spectrum involve the ground state doublet only, it doesn't give us enough in-
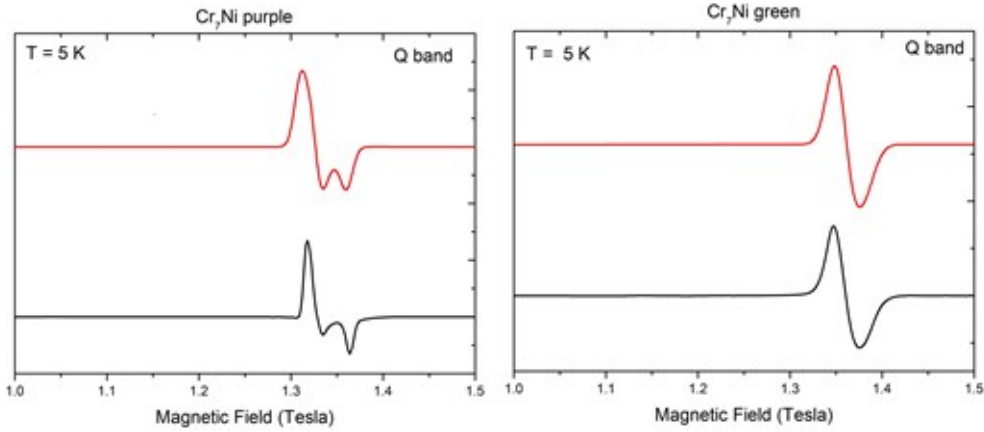
Figure 6.13: Experimental (black line) and calculated (red line) EPR Q band (ν = 34.1587 GHz) at T = 5 K of Cr$_7$Zn purple (left panel) and green ring (right panel).

formation to determine the rhombic parameter of the Ni ion, which have been set to zero. The spectrum can be reproduced by assuming a slightly anisotropic Ni gyromagnetic tensor: $g_{Ni}^{xx} = g_{Ni}^{yy}$ =2.16 and g_{Ni}^{zz} = 2.22.

Specific heat of the two Cr$_7$M purple rings has been measured at low-temperature and with different applied magnetic fields. Theoretical curves have been calculated as:

$$\frac{C}{R}(T) = \frac{\sum_i E_i^2 e^{-\beta E_i} \sum_i e^{-\beta E_i} - \left(\sum_i E_i e^{-\beta E_i}\right)^2}{\left(\sum_i e^{-\beta E_i}\right)^2},$$ (6.3)

where the sums run over all the eigenvalues of the Spin Hamiltonian in Eq. 6.1 with the parameters of Tab. 6.1[2]. We have also taken into account the vibrational contribution to the specific heat, calculated as:

$$\frac{C_{vib}}{R}(T) = \frac{243 r T^3}{(\Theta + \delta T^2)^3},$$ (6.4)

where r is the number of atoms per molecule and $\Theta_D = \Theta + \delta T^2$ is the Debye temperature. Graphs in Figs. 6.11 and 6.12 show that with the Spin Hamiltonian parameters obtained from the comparison with INS and EPR data we can also simulate specific heat measurements with a very good agreement with experiments. At high temperature the vibrational contribution to the specific heat dominates in both rings. At low fields (B = 0 - 0.5 T) Schottky anomalies are visible for both Cr$_7$Zn and Cr$_7$Mn below T = 1 K, which are mainly due to intra-multiplet energy splittings in the ground states. By increasing the magnetic field, Schottky anomalies move to higher temperatures and become less sharp, due to further splittings induced by higher magnetic fields.

6.1.4   Conculsions

Cr$_7$Zn, Cr$_7$Mn and Cr$_7$Ni purple rings have been completely characterised. Magnetic transitions have been measured with inelastic neutron scattering in polycrystalline sam-

---

[2]For specific heat calculations we have assumed isotropic **g** tensors: g$_{Cr}$ = 1.98 and g$_{Mn}$ = 2.

ples. Spin Hamiltonian parameters have been determined from the comparison of our calculations with INS data. The spectroscopic assignment of the main magnetic transitions have been confirmed by the Q dependence of the INS peaks for Cr$_7$Mn and Cr$_7$Ni. The set of parameters obtained from INS have allowed us to reproduce also EPR and specific heat measurements with a very good agreement between experiments and calculations. From EPR data we have also determined gyromagnetic tensor components.

Purple rings have the same structure of the energy spectra shown by their green analogues: They have the same magnetic ground state and the states with minimal energy for each S values form a parabolic band, which closely follows the Land*é* interval rule. Purple rings are characterised by stronger exchange interactions (both for Cr-Cr and Cr-M couplings), inducing wider gaps between different total-spin multiplets. Local crystal field parameters in purple rings have the same order of magnitude as in green ones, leading to similar intra-multiplet splittings. However they have a stronger rhombic character due to the lower symmetry of the local surrounding of Cr^{3+} ions.

As we will explain in the following section, purple and green rings can be also directly linked together. Thus, this characterization of single purple rings represents a first step in the description of these new purple-green entangled dimers.

6.2 Entanglement in a Cr$_7$Ni purple - Cr$_7$Ni green Dimer

In this Chapter we start the characterization of a new family of entangled AF rings. These new super-molecular clusters are obtained by linking a green and a purple single rings together. As already explained in the introduction of this chapter, the AF exchange coupling between two such rings is tailored by super-molecular chemistry and is small enough to leave unaltered the magnetic properties of each ring but sufficiently large to induce finite-temperature entanglement in experimentally reachable conditions. Cr$_7$Ni green dimers have been already synthesized and characterised [21]. The novelty of Cr$_7$M purple ring is that the rings can be *directly* linked together without requiring additional magnetic ions in the linker. In the Cr$_7$Ni purple dimer, for instance, the magnetic coupling between the rings arises from the pyridyl groups that link directly the Ni ions [143]. As we can see form Fig.6.14, in purple-green dimers the divalent M^{II} ion of the purple ring directly interact with the M ion and with a Cr ion of the green one.

All the possible combinations of Cr$_7$M purple - Cr$_7$M' green dimers have been synthesized (with M,M' = Zn, Mn or Ni). In the following we start our investigations on these new dimers from the characterization of Cr$_7$Ni purple-green dimer. Magnetic properties of Cr$_7$Ni green rings have been already widely investigated. As reported in the previous section, Cr$_7$Ni purple ring has been completely characterised from INS, EPR and specific heat data. Since the coupling between the rings is small enough to leave unaltered the magnetic properties of each ring, from the comparison of our calculations with EPR and specific heat measurements we can determine the AF exchange interaction between the two rings.

6.2.1 Theoretical Description

Purple and green single rings are described by Eqs. 6.1 and 5.2 respectively. The microscopic intermolecular coupling between the two rings in the dimer is described by an isotropic Heisenberg term given by:

$$\mathcal{H}_{pg} = J_{pg}\mathbf{s}_{Ni}^{p} \cdot \left(\mathbf{s}_{Ni}^{g} + \mathbf{s}_{Cr}^{g}\right),$$
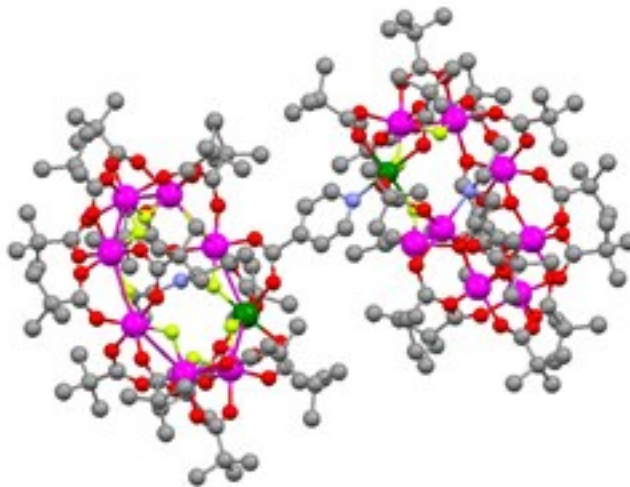
(6.5)

Figure 6.14: Molecular structure of a Cr₇M purple-green dimer: magenta = Cr, green = M (Zn, Mn, Ni), red = O, yellow = F. The dimer is obtained by linking a green (left) and a purple (right) single rings. The divalent M^{II} ion of the purple ring interact with the M ion and with one Cr ion of the green one.

where s_i^n are single ion spin operators of the ith ion of the ring n, projected onto the product Hilbert space $H_p \otimes H_g$.

In order to calculate the low-energy properties of the dimer, we first diagonalize the single-ring Hamiltonian. The coupling Hamiltonian $\mathcal{H}_{pg}$ is then represented on the product basis $|i_p\rangle \otimes |j_g\rangle$, being $|i_p\rangle$ and $|j_p\rangle$ the single-ring eigenstates of the respective Hamiltonians. Since $J_{pg} \ll J_{\text{Cr-Cr}}, J_{\text{Cr-Ni}}$ of both rings, the low-energy eigenstates are well approximated by truncating the product basis to include only the two lowest-lying multiplets of the single rings.

The presence of a sizeable exchange interaction between the two rings leads to entangled states for the super-molecular dimer. States that cannot be written as product states, are entangled states. Thus, if a generic state of the dimer can be written as:

$$|\psi\rangle_{pg} = \left(\sum_i c_i |i_p\rangle \right) \otimes \left(\sum_j c_j |j_g\rangle \right), \tag{6.6}$$

where $|\psi\rangle_p = \sum_i c_i^p |i_p\rangle$ and $|\psi\rangle_g = \sum_j c_j^g |j_g\rangle$ are states of the single rings, the state is not entangled.

6.2.2   EPR and Specific Heat

In Fig. 6.15 we report EPR (left panel) and specific heat (right panel) measurements and calculations for Cr₇Ni purple-green dimer. Specific heat theoretical curves have been calculated with Eqs. 6.3 and 6.4, while for the EPR spectrum simulations we have exploited Eq. 2.67. As we can see from the graphs, both data set can be well reproduced with the well-known single ring Hamiltonians in Eqs. 6.1 and 5.2 and with a J$_{pg}$ = 0.75 K
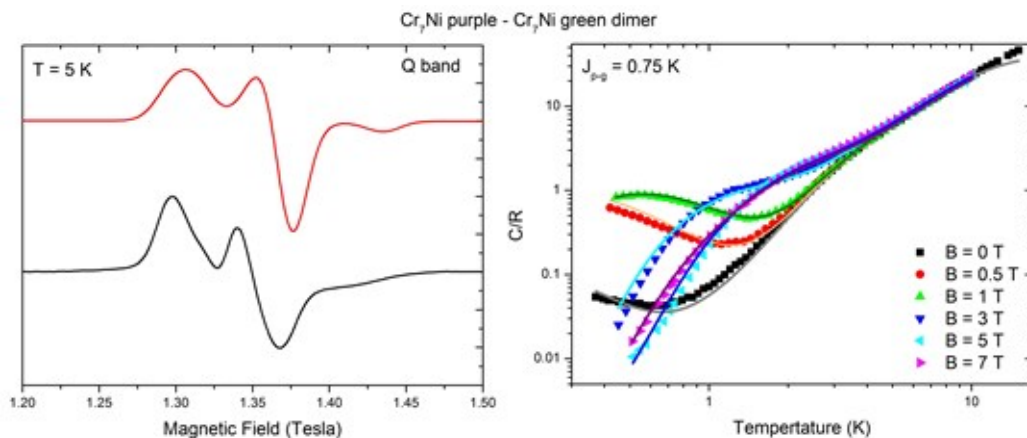
Figure 6.15: Left panel: Experimental (black line) and calculated (red line) EPR Q band (ν = 34.1587 GHz) at T = 5 K of Cr₇Ni purple-green dimer. Right Panel: specific heat of Cr₇Ni purple-green dimer as a function of temperature for different applied magnetic fields.

for the exchange Hamiltonian in Eq. 6.5, thus demonstrating the presence of an effective interaction between the two rings. Furthermore, if we compare the EPR spectrum in Fig. 6.15 with single ring spectra in Fig. 6.13, we can see that the dimer spectrum shows new features in respect to the mere sum of the two single rings spectra. These EPR and specific heat measurements can be therefore considered as a first evidence of the entanglement between the two dimers.
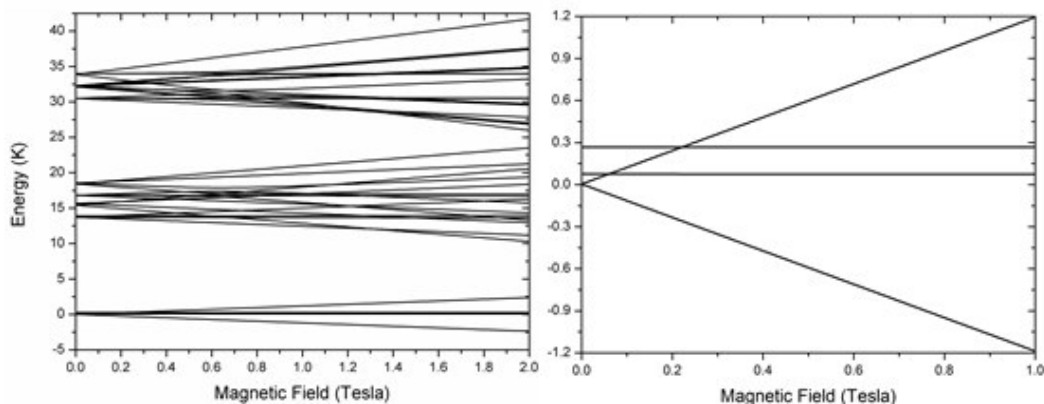
Figure 6.16: Left panel: Magnetic field dependence of the lowest-lying energy levels of the Cr₇Ni purple-green dimer. Right Panel: energy of the ground state multiplet as a function of the applied magnetic field.

In Fig. 6.16 we show the calculated energy levels of the Cr₇Ni purple-green dimer as a function of the applied magnetic field. In the low-energy spectrum there are three distinct groups of levels (see Fig. 6.16-left panel). The lowest-lying ones correspond to states where both rings are in their S = 1/2 ground states: Thus, the ground state of

the dimer is a S = 1 state, split by single rings anisotropies into $|S = 1, M = \pm 1\rangle$ and $|S = 1, M = 0\rangle$ states, with a first excited singlet S = 0 (see Fig. 6.16-right panel). The $|S = 1, M = 0\rangle$ and the S = 0 states are entangled Bell states. In fact, they can be written as:

$$|S = 1, M = 0\rangle \quad = \quad \frac{1}{\sqrt{2}} \left(|\uparrow\rangle|\downarrow\rangle + |\downarrow\rangle|\uparrow\rangle \right) \tag{6.7}$$

$$|S = 0\rangle \quad = \quad \frac{1}{\sqrt{2}} \left(|\uparrow\rangle|\downarrow\rangle - |\downarrow\rangle|\uparrow\rangle \right),$$

where $|\uparrow\rangle$ and $|\downarrow\rangle$ are the spin-up and spin-down states of the S = 1/2 ground state of each ring. At higher energy there are two other groups of levels: The levels of the second group correspond to states where one ring is still in its S = 1/2 ground state and the other one is in the first excited multiplet S = 3/2, whereas the levels of the third group are states where both rings are in the first excited multiplet S = 3/2.

6.2.3 Conclusion

Cr_7Ni purple-green dimer has been studied and characterised. EPR and specific heat measurements have allowed us to estimate the AF exchange interaction between the two rings. The very good agreement of our calculations with experimental data demonstrates the presence of an effective interaction between the two rings, leading to entangled states for the super-molecular dimer. This analysis represents a first step in the characterization of these new family of dimers. Other combinations of Cr_7M purple - Cr_7M' green dimers, already synthesized, will be investigated and new measurements and calculations will be performed, in order to describe and quantify the entanglement in these super-molecular systems and to study their application in the field of quantum computation.

General Conclusions

In this Thesis magnetic properties, spin and relaxation dynamics of Molecular Nano-magnets (MNMs) have been investigated. MNMs have been described with the Spin Hamiltonian theoretical approach and their relaxation dynamics have been studied with the Master Equations formalism. Specific *Fortran90* codes have been developed in order to build the Spin Hamiltonian of each system with the irreducible tensor operators technique and different diagonalization methods have been implemented. Relaxation dynamics have been investigated by assuming a magneto-elastic spin-phonon coupling within these molecules, which is responsible for an irreversible dynamics toward equilibrium, described by Rate Master Equations. Several experimental technique have been applied to the study of these molecules: Inelastic neutron scattering (INS), nuclear magnetic resonance (NMR), electron paramagnetic resonance (EPR) and X-rays magnetic circular dichroism (XMCD). In this Thesis proper computational techniques have been developed in order to simulate the experimental behavior of MNMs. In fact, from the comparison of theoretical calculations with experimental data it is possible to obtain the parameters of the Spin Hamiltonian and to study static and dynamical properties of the system.

In particular, we have studied frustration induced properties in MNMs, since geometrical magnetic frustration due to competing antiferromagnetic (AF) interactions is at the origin of many exotic phenomena. We have analysed the static and dynamical magnetic properties of the Ni_7 molecular nanomagnet, which has been an excellent model system to investigate the effects of magnetic frustration. The latter leads to a magnetization process displaying two double jumps, associated with multiple level crossings induced by the external field, involving states with three different total-spin quantum numbers (whereas in other MNMs crossing involves only two states). We have also verified that if we include crystal field anisotropy the crossings turn into anticrossings. Physically this effect corresponds to quantum oscillations of the total-spin length among the three different values, which could be detected by measuring the macroscopic torque at the anticrossing fields. We have also analysed Ni_7 relaxation dynamics induced by the spin–phonon coupling. The temperature and field dependence of these dynamics is again atypical and reflects the large degeneracies induced by frustration of the underlying energy levels.

With the study of the three cluster Fe_7, Fe_6 and Mn_6 we have shown how AF competing interactions lead to low-spin ground states and low-lying excited levels. Furthermore, we have investigated the phonon-induced relaxation dynamics of the Fe_7 cluster, to study the effects of competing AF interactions on the spin dynamics of MNMs. We

have found that several relaxation times contribute to the decay of the molecular magnetization of Fe_7 even at low temperature. We have also verified the multiple-times character of the relaxation dynamics is a direct consequence of the structure of the energy spectrum and that it is due to the topology of the competing AF interactions. We have measured the temperature dependence of its spin-lattice relaxation rate $1/T_1$ by ^{1}H NMR measurements, in order to determine the spin-phonon coupling strength and to set the scale factor of the relaxation dynamics timescales. We have also developed a model to calculate the nuclear spin-lattice relaxation rate $1/T_1$ taking into account also the wipeout effect.

MNMs can also display an enhanced magnetocaloric effect (MCE) and they are considered promising materials for magnetic refrigeration. Within the established recipe to synthesize MNMs with an enhanced MCE, clusters with competing AF exchange interactions are among the best candidates, together with 3d-4f heterometallic complexes, due to their large maximal entropy variation ΔS_{max}. The crucial point of our work has been to show that even if ΔS_{max} is large it is not obvious that it can be fully exploited in refrigeration cycles. In this work we have considered explicitly Carnot cycles and performed calculations in ideal model systems to understand the characteristics of a MNM yielding an efficient MCE between T = 10 K and the sub-Kelvin region. We have demonstrated that the best molecular MCE refrigerants in this temperature range are those based on molecules containing magnetic ions strongly ferromagnetically coupled, contrarily to the common belief. Hence, molecules without RE ions can be excellent magnetocaloric materials.

In this Thesis another important sub-group of MNMs have been studied: AF rings. We have carried on the investigation of Cr_7Ni green cluster. Cr_7Ni is a very promising system to encode a qubit, since it behaves as an effective spin 1/2 at low temperature and can be manipulated in times much shorter than the measured decoherence time. In this work we have studied Cr_7Ni with ^{53}Cr-NMR, with the aim of establishing the distribution of the local spin density in the ring. Indeed the latter plays a key role in the scheme proposed for obtaining time dependent qubit–qubit couplings in the presence of permanent exchange interactions between two AF rings. ^{53}Cr-NMR signal observed at high magnetic field values and at T = 1.6 K on Cr_7Ni is in excellent agreement with the local magnetic moments calculated theoretically. The local spin density distribution in Cr_7Ni is rather uniform, with a staggered spin configuration along the ring. Furthermore, from the comparison between results with two orthogonal directions of the applied magnetic field we have evinced that the Cr^{3+} spins are characterized by a sizable local easy-axis anisotropy.

Cr_7Ni AF rings can be also successfully grafted on surfaces in an ordered fashion. We have investigated the origin of magnetic anisotropy of these rings using XMCD compared with our theoretical calculations. Deep analysis of the angular dependence of XMCD spectra of ordered monolayers of Cr_7Ni rings have allowed us to elucidate the relationship between the magnetization of the single ions and that of the entire molecule. Experimentally, at 8 K and 5 T, the magnetic moment of Ni tends to align along the axis perpendicular to the ring plane, whilst the total magnetic moment of the molecule prefers to align within that plane. This apparent discrepancy is due to the fact both Ni and single-Cr magnetic moments have easy-axis anisotropy. Projecting these anisotropies on the S = 3/2 multiplet, which dominates in our experimental conditions, we obtain an easy-plane anisotropy for the magnetization of the whole molecule, in perfect agreement of our experimental findings. Experimental and theoretical results have evidenced a weak anisotropy of the magnetic moments at the Cr sites, that is a further element for the easy manipulation of the molecular spin as required for the use of these

molecular spin clusters for quantum information processing.

In the last part of this Thesis we have introduced AF *purple* rings and Cr_7Ni purple-green dimers. Cr_7M (M = Zn, Mn, Ni) purple rings have been originally synthesized in order to facilitate the linking of two or more AF rings. Furthermore, the substitution of bridging fluorides of green rings with alkoxide groups in purple ring can reduce the hyperfine-induced decoherence , making them attractive candidates for applications in quantum-information processing. Cr_7Zn, Cr_7Mn and Cr_7Ni purple rings have been completely characterized. Intra-multiplet and inter-multiplet magnetic transitions have been measured with INS in polycrystalline samples. Spin Hamiltonian parameters have been determined from the comparison of our calculations with INS and EPR data and the same set of parameters have allowed us to reproduce also specific heat measurements with a very good agreement between experiments and calculations. From EPR data we have also determined gyromagnetic tensor components. Purple and green rings can be also directly linked together. Thus, the characterization of single purple rings represents a first step in the description of these new purple-green entangled dimers. EPR and specific heat measurements on Cr_7Ni purple-green dimer have allowed us to estimate the AF exchange interaction between the two rings. The very good agreement of our calculations with experimental data demonstrates the presence of an effective interaction between the two rings, leading to entangled states for the super-molecular dimer.

Bibliography

[1] D. Gatteschi and R. Sessoli, Angew. Chem. Int. Ed. **42**, 268 (2003).

[2] D. Gatteschi, R. Sessoli, and J. Villain, *Molecular Nanomagnet* (Oxford University Press, New York, 2006).

[3] A. Abragam and B. Bleaney, *Electron Paramagnetic Resonance of Transition Ions* (Claredon Pres, Oxford, 1970).

[4] C. Sangregorio, T. Ohmand, C. Paulsenand, R. Sessoli, and D. Gatteschi, Phys. Rev. Lett. **78**, 4645 (1997).

[5] W. Wernsdorfer, C. R. Chimie **11**, 1086 (2008).

[6] N. Ishikawaand, M. Sugitaand, T. Ishikawaand, S. Koshiharaand, and Y. Kaizu, J. Am. Chem. Soc. **125**, 8694 (2003).

[7] S. D. Jiang, B. W. Wang, G. Su, Z.-M. Wang, and S. Gao, Angew. Chem. Int. Ed. **122**, 7610 (2010).

[8] J. D. Rinehart and J. R. Long, Chem. Sci. **2**, 2078 (2011).

[9] M. Boulon, G. Cucinotta, J. Luzon, C. Degl'Innocenti, M. Perfetti, K. Bernot, G. Calvez, A. Caneschi, and R. Sessoli, Angew. Chem. Int. Ed. **52**, 350 (2013).

[10] M. Gonidec, R. Biagi, V. Corradini, F. Moro, V. DeRenzi, U. del Pennino, D. Summa, L. Muccioli, C. Zannoni, D. B. Amabilino, et al., J. Am. Chem. Soc. **133**, 6603 (2011).

[11] A. Caneschi, A. Cornia, A. C. Fabretti, S. Foner, D. Gatteschi, R.Grandi, and L. Schenetti, Chem. Eur. J. **2**, 1379 (1996).

[12] K. L. Taft, C. D. Delfs, G. C. Papefthymiou, S. Foner, D. Gatteschi, and S. J. Lippard, J. Am. Phys. Soc. **116**, 823 (1994).

[13] A. Caneschi, A. Cornia, A. C. Fabretti, and D. Gatteschi, Angew. Chem. Int. Ed. **38**, 1295 (1999).

[14] S. P. Watton, P. Fuhrmann, L. E. Pence, A. Caneschi, A. Cornia, G. L. Abbati, and S. J. Lippard, Angew. Chem. Int. Ed. **36**, 2774 (1997).

[15] J. van Slageren, R. Sessoli, D. Gatteschi, A. Smith, M. Helliwell, R. E. P. Winpenny, A. Cornia, A. L. Barra, A. G. M. Jansen, E. Rentschler, et al., Chem. Eur. J. **8**, 277 (2002).

[16] R. H. Laye, M. Murrie, S. Ochsenbein, A. R. Bell, S. J. Teat, J. Raftery, H. U. Güdel, and E. J. L. McInnes, Chem. Eur. J. **9**, 6215 (2003).

[17] G. A. Ardizzoia, M. A. Angaroni, G. LaMonica, F. Cariati, M. Moret, and N. Masciocchi, J. Chem. Soc. Chem. Commun. p. 1021 (1990).

[18] J. Schnack and M. Luban, Phys. Rev. B **63**, 014418 (2000).

[19] F. K. Larsen, E. J. L. McInnes, H. E. Mkami, J. Overgaard, S. Piligkos, G. Rajaraman, E. Rentschler, A. A. Smith, G. M. Smith, V. Boote, et al., Angew. Chem. **115**, 105 (2003).

[20] C. J. Wedge, G. A. Timco, E. T. Spielberg, R. E. George, F. Tuna, S. Rigby, E. J. L. McInnes, R. E. P. Winpenny, S. J. Blundell, and A. Ardavan, Phys. Rev. Lett. **108**, 107204 (2012).

[21] G. A. Timco, S. Carretta, F. Troiani, F. Tuna, R. J. Pritchard, C. A. Muryn, E. J. L. McInnes, A. Ghirri, A. Candini, P. Santini, et al., Nature Nanotech. **4**, 173 (2009).

[22] Y. Furukawa, K. Kiuchi, K. Kumagai, Y. Ajiro, Y. Narumi, M. Iwaki, K. Kindo, A. Bianchi, S. Carretta, G. A. Timco, et al., Phys. Rev. B **78**, 092402 (2008).

[23] A. Bianchi, S. Carretta, P. Santini, G. Amoretti, T. Guidi, Y. Qiu, J. R. D. Copley, G. Timco, C. Muryn, and R. E. P. Winpenny, Phys. Rev. B **79**, 144422 (2009).

[24] O. Waldmann, S. Carretta, P. Santini, R. Koch, A. G. M. Jansen, G. Amoretti, R. Caciuffo, L. Zhao, and L. K. Thompson, Phys. Rev. Lett. **92**, 096403 (2004).

[25] S. Carretta, P. Santini, G. Amoretti, F. Troiani, and M. Affronte, Phys. Rev. B **76**, 024408 (2007).

[26] G. Lorusso, V. Corradini, A. Candini, A. Ghirri, R. Biagi, U. del Pennino, S. Carretta, E. Garlatti, P. Santini, G. Amoretti, et al., Phys. Rev. B **82**, 144420 (2010).

[27] K. A. van Hoogdalem and D. Loss, Phys. Rev. B **88**, 024420 (2013).

[28] C. Schroeder, H. Nojiri, J. Schnack, P. Hage, M. Luban, and P. Koegerler, Phys. Rev. Lett. **94**, 017205 (2005).

[29] J. Schnack, H. Schmidt, J. Richter, and J. Schulenburg, Eur. Phys. J. B **24**, 475 (2001).

[30] L. F. Chibotaru, L. Ungur, and A. Soncini, Angew. Chem., Int. Ed. **47**, 4126 (2008).

[31] L. Ungur, S. K. Langley, T. N. Hooper, B. Moubaraki, E. K. Brechin, K. S. Murray, and L. F. Chibotaru, J. Am. Chem. Soc. **134**, 18554 (2012).

[32] T. Kaelberer, V. A. Fedotov, N. Papasimakis, D. P. Tsai, and N. I. Zheludev, Science **330**, 1510 (2010).

[33] M. Leuenberg and D. Loss, Nature **410**, 789 (2001).

[34] F. Troiani, M. Affronte, S. Carretta, P. Santini, and G. Amoretti, Phys. Rev. Lett. **94**, 190501 (2005).

[35] P. Santini, S. Carretta, F. Troiani, and G. Amoretti, Phys. Rev. Lett. **107**, 230502 (2011).

[36] S. Carretta, A. Chiesa, F. Troiani, D. Gerace, G. Amoretti, and P. Santini, Phys. Rev. Lett. **111**, 110501 (2013).

[37] H. Schmidt, J. Phys.: Condens. Matter **47**, 434201. (2008).

[38] A. Soncini and L. F. Chibotaru, Phys. Rev. B **77**, 220406 (2008).

[39] D. I. Plokhov, A. I. Popov, and A. K. Zvezdin, Phys. Rev. B **84**, 224436 (2011).

[40] K. Marinov, A. D. Boardman, V. A. Fedotov, and N. Zheludev, New J. Phys. **9**, 324 (2007).

[41] M. Trif, F. Troiani, D. Stepanenko, and D. Loss, Phys. Rev. Lett. **101**, 217201 (2008).

[42] L. Bogani and W. Wernsdorfer, Nature Materials **7**, 179 (2008).

[43] Y. I. Spichkin, A. K. Zvezdin, S. P. Gubin, A. S. Mischenko, and A. M. Tishin, J. Phys. D **34**, 1162 (2001).

[44] M. Affronte, A. Ghirri, S. Carretta, G. Amoretti, S. Piligkos, G. A. Timco, and R. E. P. Winpenny, Appl. Phys. Lett. **84**, 3468 (2004).

[45] J. Schnack, R. Schmidt, and J. Richter, Phys. Rev. B **76**, 054413 (2007).

[46] M. Evangelisti and E. K. Brechin, Dalton Trans. **39**, 4672 (2010).

[47] G. Amoretti, *Formulazione Microscopica delle Interazioni Fondamentali nel Magnetismo* (L'Aquila, 1990), dispense presentate al XXII corso del G.N.S.M.

[48] A. Messiah, *Mécanique Quantique*, vol. 2 (Dunod, Paris, 1960).

[49] A. Bencini and D. Gatteschi, *EPR of Exchange Coupled Systems* (Springer Verlag, Berlin, 1990).

[50] J. Jensen and A. R. Mackintosh, *Rare Earth Magnetism* (Claredon Pres, Oxford, 1991).

[51] E. Liviotti, S. Carretta, and G. Amoretti, J. Chem. Phys. **117**, 3361 (2002).

[52] B. S. Tsukerblat, *Group Theory in Chemistry and Spectroscopy: a Simple Guide to Advanced Usage* (Dover Publications, Mineola, New York, 2006).

[53] E. Liviotti, S. Carretta, and G. Amoretti, J. Chem. Phys. **117**, 3361 (2002).

[54] C. Lanczos, J. Res. nat. Bur. Stand. **9**, 255 (1950).

[55] G. H.Golub and C. V. Loan, *Matrix Computation* (Johns Hopkins University Press, Baltimore, 1996).

[56] J. Jaklič and P. Prelovšek, Phys. Rev. B **49**, 5060 (1994).

[57] J. Jaklič and P. Prelovšek, Adv. Phys. **49**, 1 (2000).

[58] F. Troiani, V. Bellini, and M. Affronte, Phys. Rev. B **77**, 054428 (2008).

[59] K. Blum, *Density Matrix Theory and Applications* (Plenum Press, New York, 1981).

[60] L. Spanu and A. Parola, Phys. Rev. B **72**, 212402 (2005).

[61] P. Santini, S. Carretta, E. Liviotti, G. Amoretti, P. Carretta, M. Filibian, A. Lascialfari, and E. Micotti, Phys. Rev. Lett. **94**, 077203 (2005).

[62] S. Carretta, P. Santini, G. Amoretti, M. Affronte, A. Candini, A. Ghirri, I. Tidmarsh, R. Laye, R. Shaw, and E. McInnes, Phys. Rev. Lett. **97**, 207201 (2006).

[63] A. J. Würger, J. Phys.: Condens. Matter **10**, 10075 (1998).

[64] R. Caciuffo, G. Amoretti, A. Murani, R. Sessoli, A. Caneschi, and D. Gatteschi, Phys. Rev. Lett **81**, 4744 (1998).

[65] M. L. Baker, T. Guidi, S. Carretta, J. Ollivier, H. Mutka, H. U. Güdel, G. A. Timco, E. J. L. McInnes, G. Amoretti, R. E. P. Winpenny, et al., Nature Phys. **8**, 906 (2012).

[66] S. W. Lovesey, *Theory of Neutron Scattering from Condensed Matter*, vol. 2 (Oxford University Press, New York, 1984).

[67] O. Waldmann, Phys. Rev. B **68**, 174406 (2003).

[68] R. Caciuffo, T. Guidi, G. Amoretti, S. Carretta, E. Liviotti, P. Santini, C. Mondelli, G. A. Timco, C. A. Muryn, and R. E. P. Winpenny, Phys. Rev. B **71**, 174407 (2005).

[69] M. A. Adams, W. S. Howells, and M. T. F. Telling, *The IRIS User Guide, 2nd edition* (ISIS Facility, Rutherford Appleton Laboratory, Chilton Didcot (UK), 2001).

[70] T. Moriya, Prog. Theor. Phys. **16**, 23 (1956).

[71] A. G. Redfield, IBM J. **1**, 19 (1957).

[72] C. P. Slichter, *Principle of Magnetic Resonance* (Springer-Verlag, Berlin, 1978).

[73] A. Abragam, *The Principle of Nuclear Magnetism* (Oxford University Press, London, 1961).

[74] E. Fermi, Z. Phys. **60**, 320 (1930).

[75] A. J. Freeman and R. E. Watson, *Hyperfine Interactions in Magnetic Materials Magnetism*, vol. IIA (G T Rado and S Suhl, New York: Academic, 1967).

[76] R. K. Wangsness and F. Bloch, Phys. Rev. Lett. **89**, 728 (1953).

[77] G. van Veen, J. Magn. Reson. **30**, 91 (1978).

[78] G. Morin and D. Bonnin, J. Magn. Reson. **136**, 176 (1999).

[79] J. Stör, J. Magn. Magn. Mater. **200**, 470 (1999), and references within.

[80] J. P. Crocombette, B. T. Thole, and F. Jollet, J. Phys.: Condens. Matter **8**, 4095 (1996).

[81] E. Goering, Philos. Mag. **85**, 2895 (2005).

[82] V. Corradini, F. Moro, R. Biagi, U. del Pennino, V. DeRenzi, S. Carretta, P. Santini, M. Affronte, J. C. Cezar, G. Timco, et al., Phys. Rev. B **77**, 014402 (2008).

[83] V. Corradini, A. Ghirri, U. del Pennino, R. Biagi, V. A. Milway, G. Timco, F. Tuna, R. E. P. Winpenny, and M. Affronte, Dalton Trans. **39**, 4928 (2010).

[84] A. Ghirri, G. Lorusso, F. Moro, V. Corradini, M. Affronte, C. Muryn, F. Tuna, G. Timco, and R. E. P. Winpenny, Phys. Rev. B **79**, 224430 (2009).

[85] J. S. Gardner, M. J. P. Gingras, and J. E. Greedan, Rev. Mod. Phys. **82**, 53 (2010).

[86] T. H. Diep, *Magnetic systems with competing interactions* (World Scientific, Singapore, 1994).

[87] J. Schnack, Dalton Trans. **39**, 4677 (2010).

[88] Y. Furukawa, K. Kiuchi, K. Kumagai, Y. Ajiro, Y. Narumi, M. Iwaki, K. Kindo, A. Bianchi, S. Carretta, P. Santini, et al., Phys. Rev. B **79**, 134416 (2009).

[89] E. K. Brechin, S. G. Harris, S. Parsons, and R. E. P. Winpenny, Angew. Chem. Int. Edn. **36**, 1967 (1997).

[90] J. S. Gardner, M. J. P. Gingras, and J. E. Greedan, Rev. Mod. Phys. **82**, 53 (2010).

[91] J. Villain, Z. Phys. B **33**, 31 (1979).

[92] K. Penc, N. Shannon, and H. Shiba, Phys. Rev. Lett. **93**, 197203 (2004).

[93] M. E. Zhitomirsky, Phys. Rev. B **67**, 104421 (2003).

[94] S. Ma, W. B. Cui, D. Li, N. K. Sun, D. Geng, X. Jiang, and Z. D. Zhang, Appl. Phys. Lett. **92**, 173113 (2008).

[95] S. Carretta, P. Santini, G. Amoretti, T. Guidi, J. R. D. Copley, Y. Qui, R. Caciuffo, G. Timco, and R. E. P. Winpenny, Phys. Rev. Lett. **98**, 167401 (2007).

[96] S. Carretta, P. Santini, E. Liviotti, N. Magnani, T. Guidi, R. Caciuffo, and G. Amoretti, Eur. Phys. J. B **36**, 169 (2003).

[97] C. J. Milios, R. Inglis, R. Bagai, W. Wernsdorfer, A. Collins, S. Moggach, S. Parsons, S. P. Perlepes, G. Christou, and E. K. Brechin, Chem. Commun. p. 3476 (2007).

[98] C. Cañada-Vilalta, T. A. O'Brien, E. K. Brechin, M. Pink, E. R. Davidson, and G. Christou, Inorg. Chem **43**, 5505 (2004).

[99] H. Weihe and H. Güdel, J. Am. Chem. Soc., **119**, 6539 (1997).

[100] S. M. Gorun and S. Lippard, Inorg. Chem **30**, 1625 (1991).

[101] S. M. Gorun, G. C. Papefthymiou, R. B. Frankel, and S. J. Lippard, J. Am. Chem. Soc. **109**, 3337 (1987).

[102] D. M. Kurtz, Chem. Rev. **90**, 585 (1990).

[103] A. Bianchi, S. Carretta, P. Santini, G. Amoretti, J. Lago, M. Corti, A. Lascialfari, P. Arosio, G. Timco, and R. E. P. Winpenny, Phys. Rev. B **82**, 134403 (2010).

[104] F. Borsa, A. Lascialfari, and Y. Furukawa, in *Novel NMR and EPR Techniques* (Springer, Berlin Heidelberg, 2006).

[105] M. Belesi, A. Lascialfari, D. Procissi, Z. H. Jang, and F. Borsa, Phys. Rev. B **72**, 014440 (2005).

[106] S. H. Baek, M. Luban, A. Lascialfari, E. Micotti, Y. Furukawa, F. Borsa, J. van Slageren, and A. Cornia, Phys. Rev. B **70**, 134434 (2004).

[107] S. Carretta, P. Santini, G. Amoretti, M. Affronte, A. Candini, A. Ghirri, I. S. Tidmarsh, R. H. Laye, R. Shaw, and E. J. L. McInnes, Phys. Rev. Lett. **97**, 207201 (2006).

[108] R. D. McMichael, J. Ritter, and R. D. Shull, J. Appl. Phys. **73**, 6946 (1993).

[109] M. Evangelisti, O. Roubeau, E. Palacios, A. Camón, T. N. Hooper, E. K. Brechin,

and J. J. Alonso, Angew. Chem. Int. Ed. **50**, 6606 (2011).

[110] G. Lorusso, M. Jenkins, A. A. P. Gonzalez-Monje, J. Ses'e, D. Ruiz-Molina, O. Roubeau, and M. Evangelsiti, Adv. Mater. **25**, 2984 (2013).

[111] V. Corradini, A. Ghirri, A. Candini, R. Biagi, U. del Pennino, G. Dotti, E. Otero, F. Choueikani, R. J. Blagg, E. J. L. McInnes, et al., Adv. Mater. **25**, 2816 (2013).

[112] R. Sessoli, Angew. Chem. Int. Ed. **51**, 43 (2012).

[113] I. A. Gass, E. K. Brechin, and M. Evangelisti, Polyhedron **52**, 1177 (2013).

[114] M. Manoli, A. Collins, S. Parsons, A. Candini, M. Evangelisti, and E. K. Brechin, J. Am. Chem. Soc. **130**, 11129 (2008).

[115] M. Evangelisti, A. Candini, M. Affronte, E. Pasca, L. J. de Jongh, R. T. W. Scott, and E. K. Brechin, Phys. Rev. B **79**, 104414 (2009).

[116] M. Evangelisti, A. Candini, A. Ghirri, and M. Affronte, Appl. Phys. Lett. **87**, 072504 (2005).

[117] S. K. Langley, N. F. Chilton, B. Moubaraki, T. Hooper, E. K. Brechin, M. Evangelisti, and K. S. Murray, Chem. Sci. **2**, 1166 (2011).

[118] J. W. Sharples, Y. Z. Zheng, F. Tuna, E. J. L. McInnes, and D. Collison, Chem. Commun. **47**, 7650 (2011).

[119] Y. Z. Zheng, M. Evangelisti, and R. E. P. Winpenny, Angew. Chem. Int. Ed. **50**, 3692 (2011).

[120] T. N. Hooper, J. Schnack, S. Piligkos, M. Evangelisti, and E. K. Brechin, Angew. Chem. Int. Ed. **51**, 4633 (2012).

[121] J. Liu, T. Gottschall, K. P. Skokov, J. D. Moore, and O. Gutfleisch, Nature Materials **11**, 620 (2012).

[122] A. M. Tishin and Y. I. Spichkin, *The Magnetocaloric Effect and Its Applications* (Institute of Physics Publishing, Bristol(UK) and Philadelphia (USA), 2003).

[123] A. Kitanovski and P. W. Egolf, Int. J. Refrig. **29**, 3 (2006).

[124] M. D. Kuz'min and A. M. Tishin, J. Phys. D: Appl. Phys. **24**, 2039 (1991).

[125] G. Rajaraman, J. Cano, E. K. Brechin, and E. J. L. McInnes, Chem. Commun. p. 1476 (2004).

[126] M. J. Martinez-Perez, O. Montero, M. Evangelisti, F. Luis, J. J. Ses'e, S. Cardona-Serra, and E. Coronado, Adv. Mater. **24**, 4301 (2012).

[127] D. Gatteschi, A. Caneschi, R. Sessoli, and A. Cornia, Chem. Soc. Rev. **25**, 101 (1996).

[128] G. A. Timco, E. J. L. McInnes, R. G. Pritchard, F. Tuna, and R. E. P. Winpenny, Angew. Chem. Int. Ed. **47**, 9681 (2008).

[129] E. Micotti, Y. Furukawa, K. Kumagai, S. Carretta, A. Lascialfari, F. Borsa, G. A. Timco, and R. E. P. Winpenny, Phys. Rev. Lett. **97**, 267204 (2006).

[130] G. C. Carter, L. H. Bennet, and D. J. Kahan, in *Progress in Material Science vol.20* (Pergamon, New York, 1977).

[131] Y. Furukawa, Y. Nishisaka, K. Kumagai, P. Kögerler, and F. Borsa, Phys. Rev. B **75**, 220402(R) (2007).

[132] S. Carretta, P. Santini, G. Amoretti, T. Guidi, J. R. D. Copley, Y. Qiu, R. Caciuffo, G. A. Timco, and R. E. P. Winpenny, Phys. Rev. B **72**, 060403(R) (2005).

[133] M. Mannini, F. Pineider, P. Sainctavit, C. Danieli, E. Otero, C. Sciancalepore, A. M. Talarico, M. A. Arrio, A. Cornia, D. Gatteschi, et al., Nat. Mater. **8**, 194 (2009).

[134] M. Mannini, F. Pineider, C. Danieli, F. Totti, L. Sorace, P. Sainctavit, M. A. Arrio, E. Otero, L. Joly, J. C. Cezar, et al., Nature **468**, 417 (2010).

[135] M. Cavallini, J. Gomez-Segura, D. Ruiz-Molina, M. Massi, C. Albonetti, C. Rovira, J. Veciana, and F. Biscarini, Angew. Chem. Int. Ed. **44**, 888 (2005).

[136] A. Cornia, M. Mannini, P. Sainctavit, and R. Sessoli, Chem. Soc. Rev. **40**, 3076 (2011).

[137] M. Mannini, E. Tancini, L. Sorace, P. Sainctavit, M.-A. Arrio, Y. Qian, E. Otero, D. Chiappe, L. Margheriti, J. C. Cezar, et al., Inorg. Chem. **50**, 2911 (2011).

[138] A. Ghirri, V. Corradini, V. Bellini, R. Biagi, U. del Pennino, V. D. Renzi, J. C. Cezar, C. A. Muryn, G. A. Timco, R. E. P. Winpenny, et al., ACS Nano **5**, 7090 (2011).

[139] V. Corradini, F. Moro, R. Biagi, U. del Pennino, V. D. Renzi, S. Carretta, P. Santini, M. Affronte, J. C. Cezar, G. Timco, et al., Phys. Rev. B **77**, 014402 (2008).

[140] F. Troiani, A. Ghirri, M. Affronte, S. Carretta, P. Santini, G. Amoretti, S. Piligkos, G. Timco, and R. E. P. Winpenny, Phys. Rev. Lett. **94**, 207208 (2005).

[141] V. Corradini, A. Ghirri, E. Garlatti, R. Biagi, V. D. Renzi, U. del Pennino, V. Bellini, S. Carretta, P. Santini, G. Timco, et al., Adv. Funct. Mater. **22**, 3706 (2012).

[142] V. V. M. Wiesniak and C. Brukner, New J. Phys. **7**, 258 (2005).

[143] A. Candini, G. Lorusso, F. Troiani, A. Ghirri, S. Carretta, P. Santini, G. Amoretti, C. Muryn, F. Tuna, G. Timco, et al., Phys. Rev. Lett. **104**, 037203 (2010).

[144] P. Christian, G. Rajaraman, A. Harrison, J. J. W. McDouall, J. T. Rafterya, and R. E. P. Winpenny, Dalton Trans. p. 1511 (2004).

[145] O. Waldmann, Phys. Rev. B **65**, 024424 (2001).

[146] A. Chiesa, S. Carretta, P. Santini, Amoretti, and E. Pavarini, Phys. Rev. Lett. **110**, 157204 (2013).

List of Publications

Refereed publications

K. Mason, J. Chang, E. Garlatti, A. Prescimone, S. Yoshii, H. Nojiri, J. Schnack, P.A. Tasker, S. Carretta and E. K. Brechin: *Linking [Fe$_3^{III}$] triangles with "double-headed" phenolic oximes*, Chem. Commun. **47**, 6018–6020 (2011).

E. Garlatti, S. Carretta, M. Affronte, E. C. Sañudo, G. Amoretti, P. Santini: *Magnetic properties and relaxation dynamics of a frustrated Ni$_7$ molecular nanomagnet*, J. Phys.: Condens. Matter **24**, 104006 (2012).

K. Mason, J. Chang, A. Prescimone, E. Garlatti, S. Carretta, P. A. Tasker, E. K. Brechin, *Linking [M$_3^{III}$] triangles with "double-headed" phenolic oximes*, Dalton Trans. **41**, 8777 (2012).

V. Corradini , A. Ghirri , E. Garlatti, R. Biagi, V. De Renzi, U. del Pennino, V. Bellini, S. Carretta, P. Santini, G. Timco, R. Winpenny, M. Affronte, *Magnetic Anisotropy of Cr$_7$Ni Spin Clusters on Surfaces*, Adv. Funct. Mat. **22**, 3706-3713 (2012).

C. M. Casadei, L. Bordonali, Y. Furukawa, F. Borsa, E. Garlatti, A. Lascialfari, S. Carretta, S. Sanna, G. Timco and R. Winpenny, *Local spin density in the Cr$_7$Ni antiferromagnetic molecular ring and ^{53}Cr-NMR* , J. Phys.: Condens. Matter **24**, 406002 (2012).

E. Garlatti, S. Carretta, P. Santini, G. Amoretti, M. Mariani, A. Lascialfari, S. Sanna, K. Mason, J. Chang, P. Tasker and E. K. Brechin, *Relaxation dynamics in a Fe$_7$ nanomagnet*, Phys. Rev. B **87**, 054409 (2013).

E. Garlatti, S. Carretta, J. Schnack, G. Amoretti and P. Santini, *Theoretical design of molecular nanomagnets for magnetic refrigeration*, Appl. Phys. Lett. **103**, 202410 (2013).

L. Bordonali Y. Furukawa, M. Mariani, K.P.V. Sabareesh, E. Garlatti, S. Carretta, A. Lascialfari and F. Borsa, *Low temperature spin dynamics in Cr$_7$Ni-Cu-Cr$_7$Ni coupled molecular rings*, J. Appl. Phys. **115**, 17E102 (2014).

Publications under review

L. Bordonali, <u>E. Garlatti</u>, C. M. Casadei, Y. Furukawa, A. Lascialfari, S. Carretta, F. Troiani, G. Timco, R. E. P. Winpenny, F. Borsa, *Magnetic properties and hyperfine interactions in Cr_8, Cr_7Cd and Cr_7Ni molecular rings from ^{19}F-NMR*, submitted to J. Chem Phys..

Publications in preparation

M. A. Albring, <u>E. Garlatti</u>, M. L. Baker, R. J. Doherty, H. Mutka, T. Guidi, G. F. S. Whitehead, G. A. Timco, F. Tuna, S. Carretta, P. Santini, M. Affronte, E. J. McInnes, D. Collison and R. E. P. Winpenny, *Spin dynamics of Cr_7M purple Rings*.

Acknowledgments

I would like to express my sincere gratitude to all the people who supported me during these three years of Ph.D. fellowship.

Foremost, I would like to thank my supervisor Prof. Alessandro Lascialfari, for giving me the opportunity to work with him in Milano and to start my research career, for his advices and priceless discussions. I strongly hope to carry on collaborating with him in the next years, wherever I will be: It has been a pleasure to study and work with such a professional and trustworthy supervisor.

I also would like to thank my co-supervisor Prof. Paolo Santini, for his brilliant comments, invaluable suggestions and constructive feedbacks. Ever since he was my master-degree thesis supervisor, I have always admired his ability to summarize many ideas and results in one clear and accurate overall view. Thanks are owed to all his group of the University of Parma.

Many special thanks to Prof. Stefano Carretta for his enthusiasm, motivation, brilliant ideas and continuous support: Without his assistance in these three years, I could not have been so proud of my Ph.D. project and results as I am now.

I will forever be thankful to Prof. Giuseppe Amoretti for his priceless advices and unsurpassed knowledge. He has been my bachelor-degree thesis supervisor and he introduced me to the attractive research field of molecular magnetism. Since then, I can't consider my targets accomplished and my results achieved without his reviews and approval.

I also would like to thank Prof. Lascialfari's collaborators in Milano and Pavia, Prof. Ferdinando Borsa, Dr. Paolo Arosio, Dr. Lorenzo Bordonali and Dr. Samuele Sanna, for their hard work on NMR and all the data on molecular nanomagnets provided in these years.

Special thanks to Prof. Juergen Schnack for welcoming me in Bielefeld in September 2012, for his enthusiasm and priceless advices.

Many thanks to other collaborators: Dr. Tatiana Guidi, for her assistance on neutron scattering techniques during the experiment at ISIS in Oxford, and all the people in the group of Prof. Marco Affronte of the University of Modena and Reggio Emilia and of the S3 CNR-NANO National Research Center, for their useful discussions and experimental data. I also would like to thank all the chemists, the group of Prof. Richard Winpenny and Prof. Euan Brechin.

Last but not least, many thanks to my Ph.D. collegues of the "Area 51" office of the Department of Physics in Parma, for their patience and company: Pietro, Tiziano and Mattia (my buddies), Alessandro (I'm sure we'll do new exciting research together in the

next years), Giacomo (thank you for the essential discussions about the magnetocaloric effect) and Matteo. And many thanks also to all the other Ph.D's and Post-docs from Parma! Special thanks to the Ph.D. collegues of the IMEM-CNR Institute: Nicola, Matteo, Davide and Giacomo. Without you all guys life would have been harder in these three years!

<div align="right">

Elena Garlatti
January 2014

</div>